Design, manufacturing and characterization of a microfluidic chip for droplet trapping

Auteur : Maltez Cavalheiro, Kévin
Promoteur(s) : Gilet, Tristan
Faculté : Faculté des Sciences appliquées
Diplôme : Master en ingénieur civil physicien, à finalité approfondie
Année académique : 2022-2023
URI/URL : http://hdl.handle.net/2268.2/18201

University of Liège
Faculty of Applied Sciences

Design, manufacturing and characterization of a microfluidic chip for droplet trapping

Supervisor: Tristan Gilet

Kévin Maltez Cavalheiro

Master's thesis completed in order to obtain the degree of Master of Science in Physics Engineering

Academic year 2022-2023

Remerciements

J'aimerais tout d'abord prendre le temps de remercier mon promoteur, M. Gilet, qui m'a soutenu tout au long de cette année. Je tiens à lui exprimer ma gratitude pour l'investissement qu'il a pu mettre dans ce projet. Sa prévenance, sa patience et ses encouragements m'ont poussé à donner le meilleur de moi-même. Au-delà de l'aspect purement académique, il a également su trouver les mots pour m'aiguiller sur de nombreux sujets. Il a été à l'écoute et a su se rendre disponible, parfois même à des heures improbables.

Mes remerciements vont également aux membres du laboratoire de microfluidique que j'ai appris à découvrir et à apprécier. Ils m'ont offert un bon accueil et m'ont guidé grâce à leurs remarques constructives, contribuant ainsi à l'amélioration constante de la qualité de mon travail. Tout particulièrement, je tiens à remercier Malik, qui m'a grandement aidé à assimiler le sujet initial et a développé ma curiosité pour envisager toutes les pistes de recherche.

Je tiens également à remercier mon comité de lecture composé de Mme Van Loo, M. Dorbolo et M. Vanderbemden pour le temps qu'ils consacreront à la lecture de ce mémoire. Merci également à M. Arnst pour son remplacement dans le rôle de président de jury.

Il me tient particulièrement à coeur de remercier mes amis pour leur présence et leur soutien depuis d'innombrables années. Notamment, merci à Dorian et Joseph pour avoir partagé mon bureau cette année. Et merci à l'ensemble du GRASP pour avoir toléré la présence d'un renégat dans leur département.

Tout particulièrement, j'adresse un grand merci à Anthony. Malgré nos personnalités opposées, nous partageons une ambition et une volonté de sortir des sentiers battus, ainsi qu'une passion pour nous investir dans toutes sortes de projets. Tu es toujours attentif et prêt à me prodiguer les conseils adéquats pour me pousser à prendre davantage d'initiatives.

Je souhaite également remercier Laura pour son empathie et son soutien indéfectible. Ton analyse, assortie de ta curiosité sans limite et de ta patience, te permet de cerner les véritables enjeux dans toutes les situations. Tes précieux conseils m'ont aidé à surmonter de nombreuses épreuves. Et, plus que quiconque, tu as su guider mes décisions lors de choix difficiles.

Je tiens aussi à remercier Matteo pour son énergie inépuisable et sa bonne humeur quotidienne qu'il parvient à transmettre. Ton dynamisme et ta motivation nous poussent à aller de l'avant, peu importe les échecs. Tu sais certainement accélérer mes prises de décisions en me poussant à l'action, bien que parfois un certain manque de tact puisse se faire sentir.

Même si je suis incapable de citer tout le monde, je n'oublie pas l'ensemble des personnes et des amis qui m'ont apporté leur aide tout au long de ce parcours.

Enfin, je voudrais remercier ma famille pour leur soutien total depuis le tout début.

Contents

Symbol	Signification	Units	Constant Value
ρ	density of the fluid	kg/m^3	
$\boldsymbol{v}$	velocity	m/s	
$\boldsymbol{\sigma}$	Cauchy stress tensor	Pa	
$\boldsymbol{b}$	external volume force	m/s^2	
p	pressure	Pa	
μ	dynamic viscosity	Pa.s	
ν	kinematic viscosity	m^2/s	
Q	flow rate	m^3/s	
Re	Reynolds number	/	
Ca	Capillary number	/	
Bo	Bond number	/	
γ	Surface tension	N/m, J/m^2	
λ_c	Capillary length	m	
g	acceleration of gravity	m/s^2	9.81
l	length or characteristic length	m	
w	width	m	
h	height	m	
R	hydraulic resistance	$Pa.s/m^3$	
H	chamber height	m	
W	well depth	m	
D	well diameter	m	
i	interwell distance	m	
V	droplet volume	m^3	
A	droplet area	m^2	
κ	mean curvature	m^{-1}	
$\boldsymbol{n}$	unit outward normal	/	
M	wettability coefficient	/	

Symbol	Signification	Units	Constant Value
$\mathcal{A}$	absobance	/	
$\mathcal{T}$	transmitance	/	
r_i	internal droplet radius	m	
r_e	external droplet radius	m	
$\mathcal{R}$	radius of curvature	m	
ε	error	/	
ϵ	eccentricity	/	
C_n, n $\in \mathbb{N}$	constant	Problem-dependent	

Part I

Introduction

Chapter 1

Introduction

This master thesis is part of the drug testing and screening process on cells within a microfluidic chip. The process is automated within the chip using droplets, enabling rapid and reproducible testing and screening on a large scale. The article by Brouzes [1] provides a general description of this method. Other examples can be found in [2–4].

To begin, it is necessary to specify the context in which this work is carried out. This project aims to design a microfluidic chip for successively trapping two populations of droplets, and thereby providing a new platform to a variety of applications involving cell assays (e.g., drug screening, cancer research, personalized medicine, medical diagnostics, etc.). A few recent publications have also revealed the promises of this technique [5, 6]. The Fig. 1.1 develops the key points of the above articles. The numbers are used to illustrate the different stages of the workflow. The first step is to form a first population of thousands of droplets containing cells (1). These droplets are then trapped in various ways within the microfluidic chip (2). In general, these droplets are isolated from each other to ensure the independence of each culture. The next step involves creating a second population of droplets within which either a drug or another cell population is introduced (4). Each of the droplets in this new generation must then be trapped in the same location as a droplet from the previous generation (5). Thus, each well contains one droplet of each population. For example, the first droplet could contain tumor cells, and the second could contain a drug whose action on these cells needs to be tested (6). To accomplish this objective, It is then necessary to merge the two droplets trapped in each well (7). At any point in this workflow, droplets could have to be kept in an incubator for several hours to several days to form spheroids (3). These are aggregates of cells that sediment at the bottom of the droplet. The droplet naturally takes on the shape of a potential well due to its curvature, and the cells then conglomerate into a mass called a spheroid. The final essential step would be to release the droplets from their trap and convey them outside the chip to analyze them (8). At any time (during trapping or after release), the interaction of the cells with their environment (drugs, other cells) can be observed, e.g., with fluorescence microscopy.

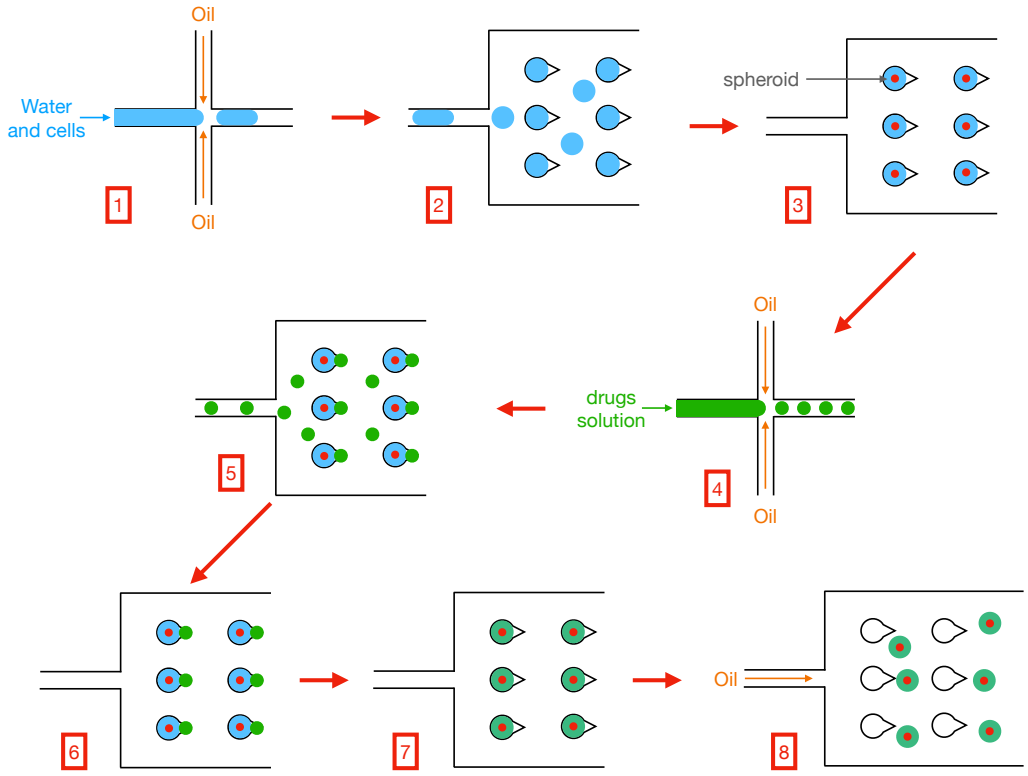

Figure 1.1: Project workflow. Generation of drops containing cells (1). Trapping of this first population (2). Incubation, and formation of spheroids (3). Generation of droplets containing cells or drugs to be tested (4). Trapping of this second population (5). Flushing the excess droplets (6). Fusion and start of the cell assay (7). Release of droplets (8).

This master thesis aims to build upon these works, reproduce their trapping techniques, and study them. Simultaneously, these techniques will be compared to other trapping methods encountered in the literature, allowing their efficiency to be highlighted. Fig. 1.1 illustrates the purpose of this project and shows its real utility. However, it should be emphasized that only the physical aspect related to droplet trapping will be considered in this master thesis. Other researchers specializing in the fields of biology and chemistry will be better suited to continue this work in its part dedicated to drug testing on spheroids.

Chapter 2

State of the art

1 Context

Microfluidics is a field of study situated at the intersection of physics, biology, and chemistry. It involves the manipulation of fluids at the micrometer scale. Its role is to automate and miniaturize complex processes that were originally performed manually. The objective is to increase the speed and precision of manipulations while reducing contamination errors and the amount of liquid used. Microfluidics finds numerous applications in medicine and the pharmaceutical industry. One branch of this technology is based on microfluidic chips made from a biocompatible material. These chips have channels and various micro-sized structures printed on them. The channels allow the desired manipulation and transport of liquids. Generally, each chip is dedicated to performing a specific task. As a result, a chip can replace a set of precise tasks that take place in a laboratory. This gives rise to the concept of lab-on-chip. It involves taking a sample and introducing it into the microfluidic chip. The sample is then mixed with a chemical agent and undergoes an incubation step. Finally, it becomes possible to detect and analyze a specific signal that allows drawing conclusions about the nature of the sample. It is necessary to maintain a general descriptive character since the applications of microfluidics are numerous and target various markets. The most common examples include clinical diagnostics (human or animal), pharmaceutical research, agro-food testing, environmental testing, drug delivery, optical actuation, flow chemistry, and more.

2 History

To introduce a brief historical context, microfluidics is a relatively recent advancement. Its origin can be traced back to the *1950s* in the inkjet printer manufacturing industry. However, it was not until the emergence of electronics that silicon wafers appeared. These wafers serve as the main substrate for printing the negative of the chip, which is then molded with the biocompatible material. In the *1980s*, the first micro-valves and micro-pumps were created. This advancement represented the first step towards modern microfluidics. The rest of the story unfolds with the specialization of the various possibilities offered by this new technology in the early *2000s*. Gradually, components enabling the manipulation, dosing, and parallel mixing of fluids at a reduced scale began to emerge.

3 Theoretical background

3.1 Navier-Stokes equations

The main equation governing fluid mechanics is the Navier-Stokes equation. It is essential to introduce it to characterize flows in channels at this scale. Assuming a continuous medium, it is possible to write the Cauchy momentum equation:

$$\rho \frac{d\boldsymbol{v}}{dt} = \nabla \cdot \boldsymbol{\sigma} + \rho \boldsymbol{b} \tag{2.1}$$

To obtain the formulation of the Navier-Stokes equations for most common fluids like water and oil in a microfluidic chip, it is considered that the fluid is incompressible. Thus, the continuity equation $\frac{d\rho}{dt} + \rho \nabla \cdot \boldsymbol{v} = 0$ reduces to $\nabla \cdot \boldsymbol{v} = 0$. Considering Newtonian fluids, the stress tensor is written as:

$$\boldsymbol{\sigma} = -p\boldsymbol{I} + \mu(\nabla \boldsymbol{v} + (\nabla \boldsymbol{v})^{\mathrm{T}}) \tag{2.2}$$

By injecting Eq. 2.2 into Eq. 2.1 and considering the incompressibility assumption introduced earlier, it leads to the general form of the Navier-Stokes equations:

$$\overbrace{\underbrace{\frac{\partial \boldsymbol{v}}{\partial t}}_{\text{Local}} + \underbrace{(\boldsymbol{v} \cdot \nabla)\boldsymbol{v}}_{\text{Convective}}}^{\text{acceleration}} = \underbrace{-\frac{1}{\rho}\nabla p}_{\text{Pressure gradient}} + \underbrace{\nu \Delta \boldsymbol{v}}_{\text{Viscous shear}} + \underbrace{\boldsymbol{b}}_{\text{Body forces}} \tag{2.3}$$

Comparing the different terms of the equation allows obtaining the famous dimensionless numbers. Only the Bond number will be relevant in this master thesis. The Bond number is expressed as:

$$Bo \equiv \frac{\text{Body forces}}{\text{Surface tension}} = \frac{\rho g l^2}{\gamma} = \frac{l^2}{\lambda_c^2} \tag{2.4}$$

Where $\lambda_c = \sqrt{\frac{\gamma}{\rho g}}$ represents the capillary length.

The surface tension does not appear directly in the Navier-Stokes equations since they describe the behavior of a fluid, while γ comes into play at the interface. Indeed, the origin of surface tension is related to the absence of interaction forces with neighboring molecules for those located at the interface. Therefore, the surface tension only comes into play in the boundary conditions of the stress tensor.

3.1.1 Hydraulic resistance

In a microfluidic chip during operation, the acceleration terms as well as the volume forces are generally negligible in describing the fluid flow within the channels. In this context, the Navier-Stokes equation, Eq. 2.3, reduces to the Stokes equation:

$$\mu \Delta \boldsymbol{v} = \nabla p. \tag{2.5}$$

The channels have a rectangular cross-section. The height is denoted by h, the width by w, and the length by l. The boundary conditions impose a zero velocity at the walls. Solving the Stokes equation while considering these parameters leads to:

$$\Delta p \approx \frac{12\mu l Q}{h^3(w - 0.63h)} \tag{2.6}$$

A detailed resolution of this problem is provided in the appendices 1. The approximation given here is only valid for the case of a channel where $w >> h$. When the cross-section approaches a square shape, the provided solution loses accuracy.

It is interesting to draw an analogy with the study of electrical circuits. Indeed, the flow rate Q and the pressure difference Δp can be respectively assimilated to the current and the electrical potential difference. The remaining term is equivalent to resistance in the hydraulic case. Ohm's law can thus be transcribed in microfluidics as follows:

$$R \equiv \frac{12\mu l}{h^3(w - 0.63h)} = \frac{\Delta p}{Q} \tag{2.7}$$

Through this analysis, it is possible to design the different channels by assigning them a specific resistance through modifications of their geometry, primarily their length. As a result, the channel circuit within the chip can be tailored to meet specific requirements.

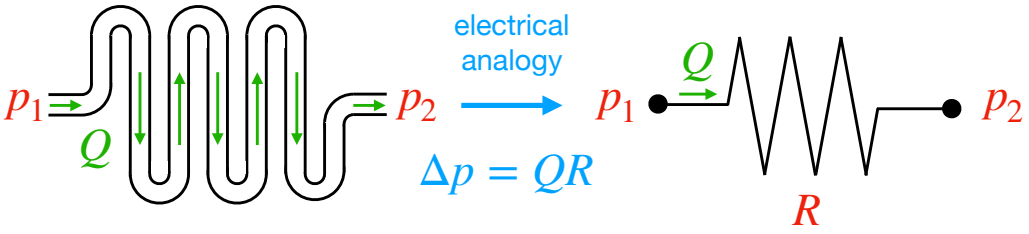

Figure 2.1: Diagram illustrating the analogy between a hydraulic resistance and an electrical resistance.

To be perfectly exhaustive, this model considers only one liquid within the channel. In practice, once the droplets are formed, the continuous phase of the medium and the discrete phase of the droplets share the volume of the channel in proportion. Thus, the resistance is modified based on the number and size of droplets in the channel. The assumption is made that the velocity of the droplets is approximately equal to that of the oil in the channel. Additionally, it is also assumed that there exists an additional resistance induced by the droplets in the channel. Hence, it is possible to deduce an empirical law for the resistance in the channels:

$$\Delta p = (R_c + N R_d)(whv_d) \tag{2.8}$$

R_c and R_d are the resistance of the channel and the additional resistance induced by the droplets, respectively. R_c represents the resistance due to Poiseuille flow of the continuous phase (often oil) in the channels, as shown in Eq. 2.7. N is the number of droplets present in the channel. v_d is the velocity of the droplets. h, w are, respectively, the height, and width of the channel.

The presentation of this formula seeks to highlight that a channel where droplets are circulating will experience an increase in resistance proportionally to the number of droplets compared to a channel where only the continuous phase flows.

For droplet trapping, they are often guided to move within a chamber. When the chamber has limited height and contains relatively large droplets, they move in a confined manner along a direction in space. Since the length and width of the chamber are much larger than its height, the movement between two liquids follows the theory of thin films. More specifically, this type of geometry is known as a Hele-Shaw cell in the literature. The study of the interaction between two immiscible fluids in this type of configuration has been investigated by Park [7]. For the specific case of droplets, a study of their gravity-induced movement can be found in this article [8] and a numerical study by finite elements in [9]. Finally, An approximation of droplet velocity in a Hele-Shaw cell can be found in [10, 11].

In a continuous pressure regime, only resistances play a role. However, capacitance and inductance may come into play in the case of time-varying pressures. For time scales $T >> \frac{L}{R} \simeq \frac{h^2}{10\nu}$, the inductance L can be omitted in the problem, which is the case here. The inductance is due to the fluid's inertia and is only relevant when there are significant accelerations. The capacitance allows for the storage of liquid volume through material deformation or by the presence of compressible gas pockets. Fig. 2.2 illustrates the operation of a capacitance within a microfluidic chip. In the context of this work, the material used for chip manufacturing is called PDMS (Polydimethylsiloxane). It is deformable and elastic. Its effect is generally reduced with geometric dimensions in the order of a few micrometers for the channels. However, further in this master's thesis, a very large chamber will be used to enable droplet storage in wells. Without caution, this chamber can act as a large capacitance. This issue will be further investigated in the section dedicated to the results.

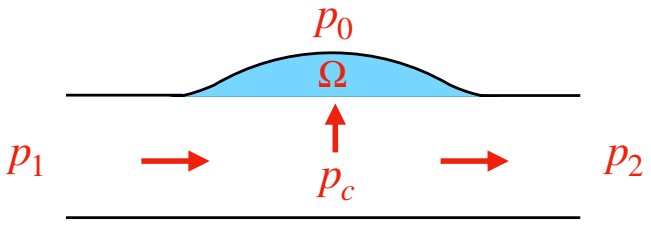

Figure 2.2: Diagram of a channel cross-section illustrating the possibility of storing a certain volume of liquid Ω through elastic deformation of PDMS.

For fluids, the mathematical expressions for the inductance and capacitance are given by:

$$L = \frac{6\rho l}{5wh}, \qquad C = \frac{\partial \Omega}{\partial(p_c - p_o)}. \tag{2.9}$$

3.1.2 Laplace equation

The Young-Laplace equation can be derived from the boundary conditions of the Navier-Stokes equations. It is possible to express these conditions for the normal and tangential components as follows [12]:

$$\begin{cases} \boldsymbol{n} \cdot \boldsymbol{\sigma_2} \cdot \boldsymbol{n} - \boldsymbol{n} \cdot \boldsymbol{\sigma_1} \cdot \boldsymbol{n} = \gamma \nabla \cdot \boldsymbol{n}, & \text{(2.10a)} \\ \boldsymbol{n} \cdot \boldsymbol{\sigma_2} \cdot \boldsymbol{t} - \boldsymbol{n} \cdot \boldsymbol{\sigma_1} \cdot \boldsymbol{t} = \nabla \gamma \cdot \boldsymbol{t}. & \text{(2.10b)} \end{cases}$$

By focusing on the normal component provided by Eq. 2.10a, it is possible to describe the interface between two immiscible fluids when they are in a state of hydrostatic equilibrium. This assumption allows the equality of tangential stresses at the interface, resulting in the

cancellation of Eq. 2.10b. Thus, in its most general form, the Laplace equation is written as:

$$\Delta p = \gamma \nabla \cdot \boldsymbol{n} = 2\gamma\kappa \tag{2.11}$$

Where κ is defined as the mean curvature. This parameter can be expressed in a general manner using the two principal radii of curvature of the surface, $\mathcal{R}_1$ and $\mathcal{R}_2$, characterizing the interface. More precisely, the expression of these radii of curvature satisfies a differential equation given by:

$$2\kappa = \left(\frac{1}{\mathcal{R}_1} + \frac{1}{\mathcal{R}_2}\right) = \nabla \cdot \left(\frac{\boldsymbol{e}_z - \nabla S}{\sqrt{1 + \|\nabla S\|^2}}\right) \tag{2.12}$$

The last equality could be obtained by assuming that the surface S can be described as a function of x and y such that $z = S(x, y)$. In an axisymmetric problem, the surface can be expressed as $z = S(r)$. In this situation, denoting $S_r = \frac{\mathrm{d}S}{\mathrm{d}r}$, the Young-Laplace equation becomes [13, 14]:

$$\Delta p = \gamma \left(\frac{-S_{rr}}{(1 + S_r^2)^{3/2}} + \frac{1}{S\sqrt{1 + S_r^2}}\right) \tag{2.13}$$

3.1.3 Young-Dupré equation

The Young-Dupré equation describes the contact angle between a liquid and a smooth surface in the presence of a gas phase. The details of its derivation may be found in [15], it can be written as follows:

$$\cos(\theta) = \frac{\gamma_{SG} - \gamma_{SL}}{\gamma_{LG}} \tag{2.14}$$

Where γ_{SG}, γ_{SL}, and γ_{LG} are the surface tensions between solid and gas, solid and liquid, and liquid and gas, respectively.

It is possible to define a wettability coefficient M such that $M < 0$ implies partial wetting, while $M \geq 0$ results in complete wetting.

$$M = \gamma_{SG} - (\gamma_{SL} + \gamma_{LG}) \tag{2.15}$$

This coefficient simply represents an energy difference per unit surface. Thus, if $M < 0$, it indicates that $\gamma_{SG} < \gamma_{SL} + \gamma_{LG}$ and, therefore, it is favorable to form an interface between the solid and gas phases. This will limit the spreading of the liquid. Conversely, when $M > 0$, it indicates that $\gamma_{SG} > \gamma_{SL} + \gamma_{LG}$, and it is favorable for the liquid to form an interface with the gas phase and the solid substrate, justifying its spreading. By substituting Eq. 2.14 into Eq. 2.15, the condition is rewritten as $M = \gamma_{LG}(\cos\theta - 1)$. The wettability angle θ defines the location of the contact line at the junction of the three phases. This angle is only defined for values of $M \leq 0$. The liquid will be considered as rather wetting in the situation where $\theta < \frac{\pi}{2}$ and rather non-wetting in the case where $\theta > \frac{\pi}{2}$. Fig. 2.3 illustrates this wetting phenomenon.

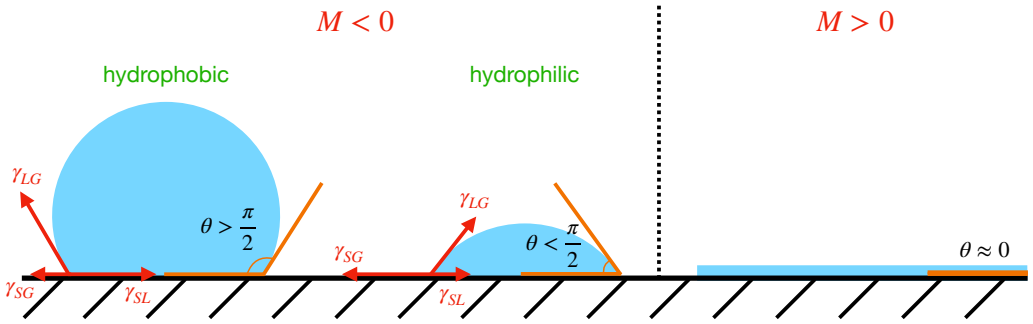

Figure 2.3: Diagram illustrating the wettability of a liquid on a smooth solid substrate. From left to right, the liquid is rather non-wetting, rather wetting, and completely wetting.

3.1.4 Surfactants

Surfactants are used in microfluidics to stabilize droplets and prevent their coalescence. If the droplets are packed and pushed against each other, the absence of surfactants can quickly lead to droplets of highly variable sizes and blockage of different channels, rendering the chip inoperable. These surfactants are composed of a hydrophilic head and a hydrophobic tail. They position themselves at the droplet's surface, with the head immersed in the aqueous medium and the tail in the surrounding oil. This oriented positioning at the interface prevents direct contact between droplets and, consequently, their coalescence. Their presence at the interface also lowers the surface tension between water and oil [16–18].

It is only possible to accumulate a certain number of surfactant molecules at the interface. Once the droplet's surface is completely covered with a monolayer of surfactant, excess molecules will form spherical clusters in the aqueous medium, with the hydrophilic heads oriented outward and the hydrophobic tails inward. These formations are called micelles. It is not clear whether the micelles are predominantly present in the water or in the surrounding oil since they are soluble in both. There are studies on the critical concentration threshold of surfactant before micelle formation in the oil [19, 20]. The effect of surfactants on cells is a subject of research, indicating their presence inside the droplet. Most microfluidic applications require surfactants that are biocompatible [21–23]. In practice, in this master's thesis, surfactants are used in a way to be close to the micelle formation threshold. It is necessary to prevent coalescence by covering the droplets' surface with surfactant as much as possible. However, since surfactants can be quite expensive, it is crucial to limit micelle formation, as they represent passive aggregates within the droplet. An illustration of the role of surfactants can be seen in Figure 2.4.

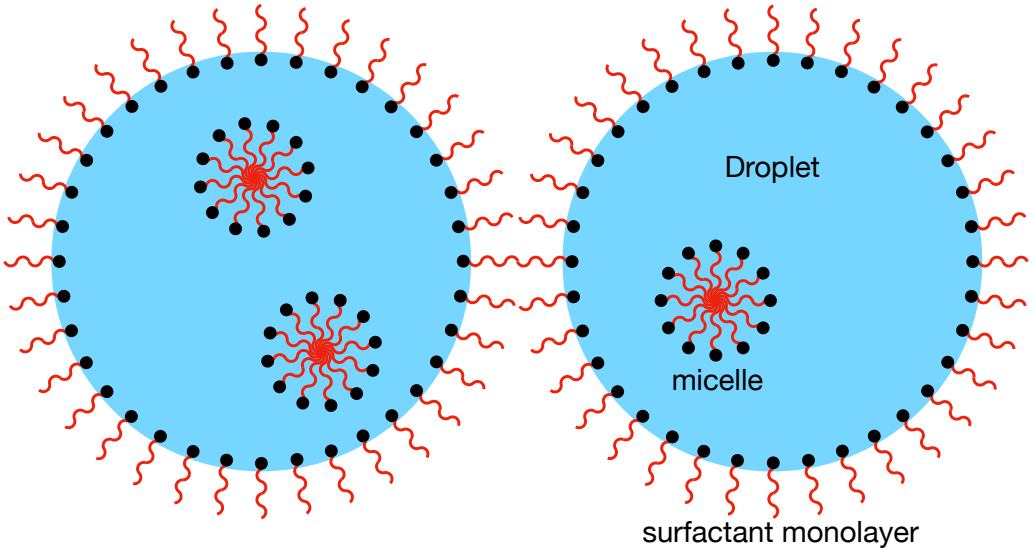

Figure 2.4: Diagram illustrating the action of surfactants and the prevention of coalescence between two droplets, each possessing a saturated monolayer.

4 Droplet microfluidics

This master's thesis aims to trap droplets within a microfluidic chip. Several major research directions are commonly encountered in the literature for manipulating droplets. To better understand the subsequent analysis, a brief introduction will be provided on these topics.

4.1 Droplet formation

Droplet formation often occurs through junctions that allow the meeting of water and oil (Fig. 2.5). This diagram shows only the main junctions, which are most commonly encountered in the literature. It should be noted that droplet formation is often a preliminary step for many articles in the field of microfluidics [16, 24–27].

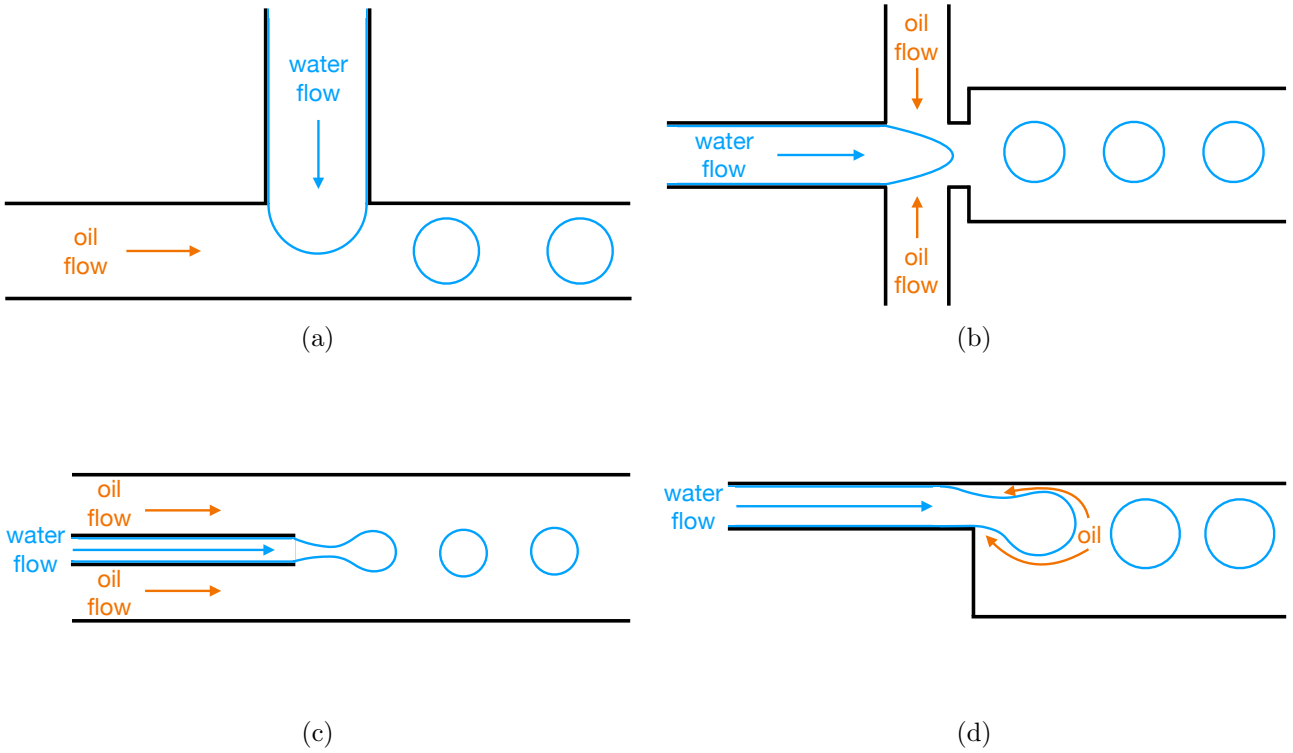

Figure 2.5: Diagram illustrating the different possibilities of droplet formation. (a) T-junction with flow directions perpendicular. A variation considers flows oriented in the same direction but with opposite directions. The perpendicular channel then collects the formed droplets. (b) Flow focusing (at high pressures, the regime transitions to dripping then jetting). (c) Co-flow. (d) Step emulsification. A synthesis of these droplet production techniques can be found in [24].

In this master's thesis, the preferred droplet formation technique is flow focusing (Fig. 2.5b). It involves a more complex geometry compared to other formation techniques, including two oil inlets. The advantage lies in the stability of the formation frequency and the size of the generated droplets. It should be noted that the oil and water inlet channels must have similar resistances to ensure they operate in the same pressure regime. These resistances are necessary to isolate the junction from noise and pressure fluctuations.

Completely unintentionally, the step emulsification technique (Fig. 2.5d) was also encountered in this work. It occurred when relatively large droplets transitioned from a channel height of 30 [μm] to an deeper chamber with an approximate height of 120 [μm]. This experiment aimed to release the droplets from confinement rather than generating new ones.

The various droplet formation techniques using junctions (Fig. 2.6). This figure presents experimental images taken from the literature for illustrative purposes.

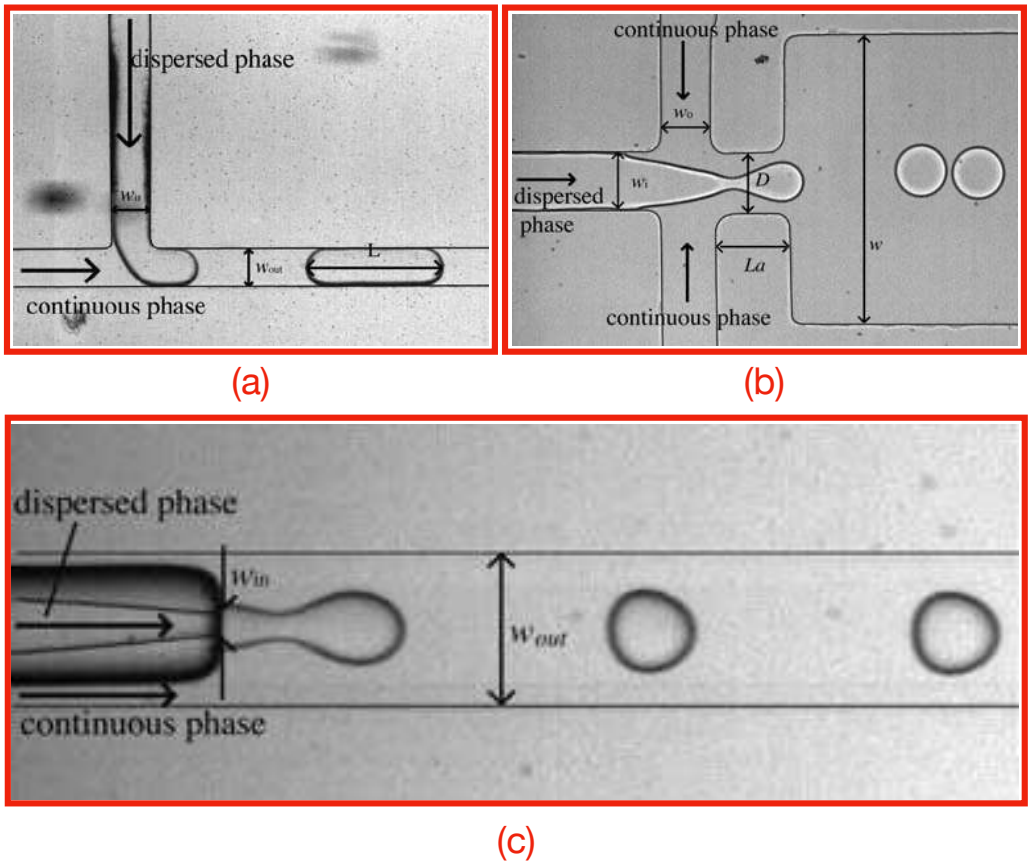

Figure 2.6: Experimental photos illustrating the different junction geometries. All images are taken from Baroud's article [28]. (a) T-junction, (b) Flow focusing, (c) Co-flow.

The formation of droplets depends on both the junction and the flow rates of the continuous and dispersed phases in the chip. Fig. 2.7 shows the different droplet sizes possible for the same junction by adjusting the flow rates or the fluid viscosity.

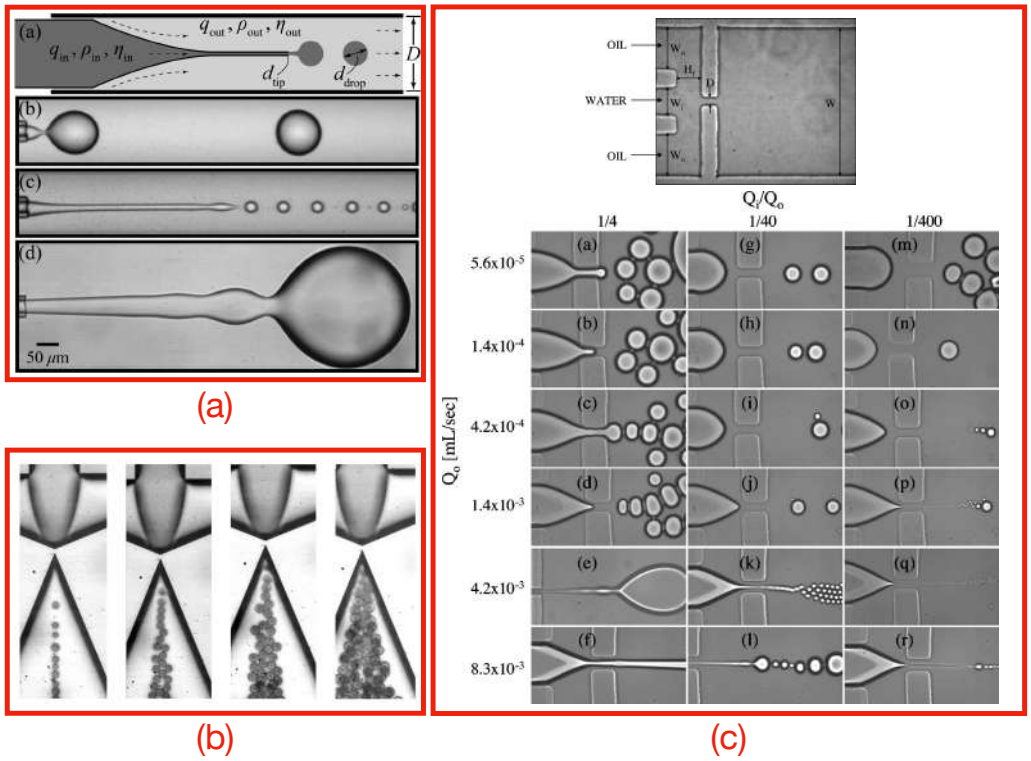

Figure 2.7: Experimental photos illustrating the different regimes of droplet formation for the same junction. The modification concerns only the flow rates or viscosity of the liquids. (a) Photo from [3, 29]. (b) Photo from [30, 31]. (c) Photo from [3, 32, 33].

4.2 Droplet merging

Droplet coalescence presents a significant challenge as surfactants are often used to prevent their coalescence after they have been generated. The goal is to achieve targeted coalescence of specific droplets at precise locations within the chip. In this section, targeted coalescence techniques will be briefly presented.

4.2.1 Geometry confinement

Some techniques commonly encountered in the literature involve modifying the geometry of a channel to drain the oil separating two successive droplets [34]. Once this step is completed, the two droplets come into contact. If the surfactant concentration is low and the droplets are strongly pressed together, coalescence between them becomes possible. Coalescence can also be facilitated if the droplets collide with a certain velocity. These techniques have the advantage of being passive, without the need for external devices to enable fusion [16]. However, a major drawback is often the complexity of this geometry, as they require advanced microfabrication techniques. Additionally, these geometries are prone to droplet misalignments or can be rendered ineffective by the arrival of debris. Fig. 2.8 illustrates two fusion techniques involving modification of the channel geometry.

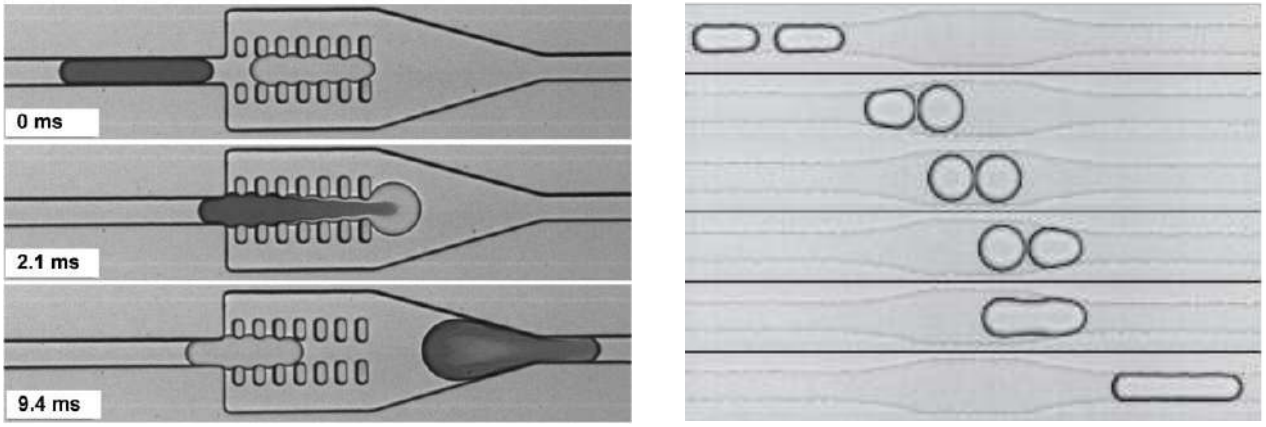

(a) (b)

Figure 2.8: Experimental photos illustrating droplet coalescence passively. These two examples are taken from Baroud's article [28]. (a) Comb drop merging device from the article [33, 35]. (b) Droplet fusion by channel widening from [36].

4.2.2 Electrocoalescence

Electrocoalescence is a fusion technique that relies on the application of an electric field. This field induces electrical charges on the droplet surfaces and polarizes them. Electrostatic forces appear and promote contact between the droplets. As a result, the two contacting membranes possess opposite charges. The thin oil film separating the droplets is gradually drained. The charges present on the surface also reduce the surface tension. Thus, the membrane eventually disappears locally, allowing contact between the two droplets and enabling their fusion. Fig. 2.9 shows various applications of this technique from the literature.

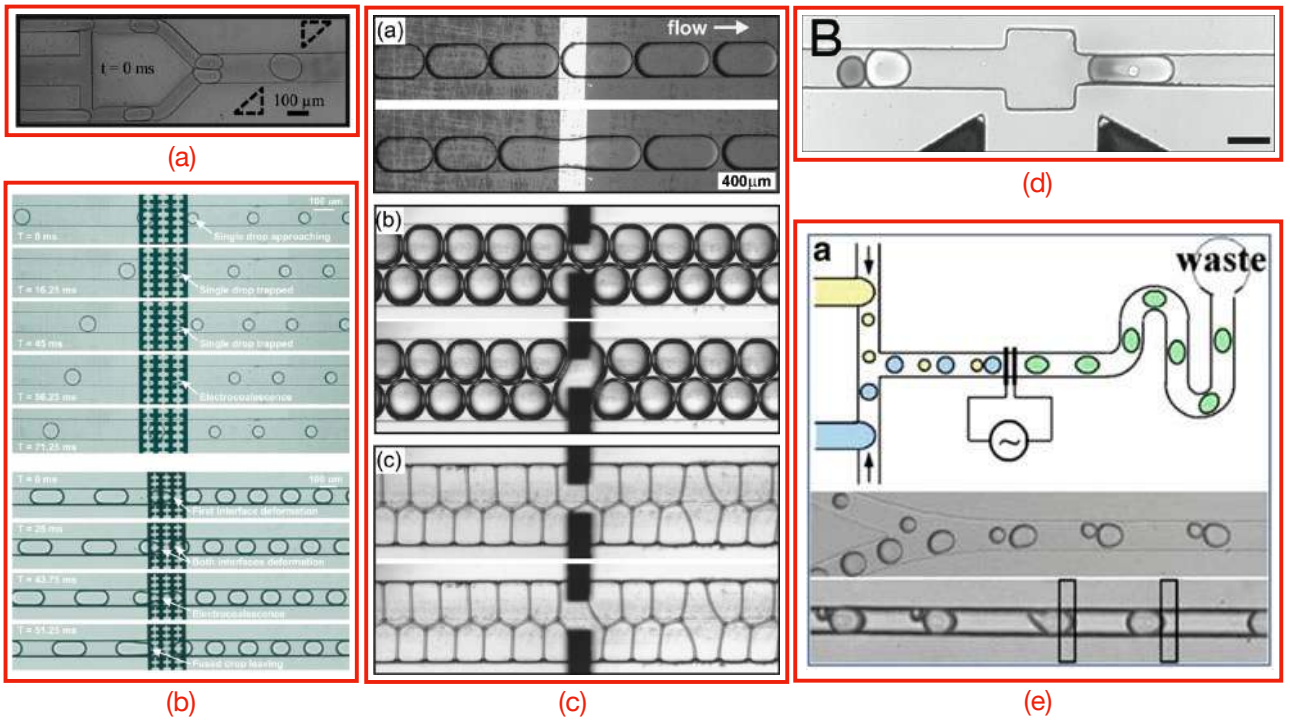

Figure 2.9: Experimental photos from the literature of droplet fusion by electrocoalescence: (a) Dashed triangles represent the electrodes. The image is from [24, 37]. (b) Photo from [38, 39] showing the different stages of fusion. (c) Photo from [31, 40] demonstrating electrocoalescence for various droplet size regimes. (d) Zoomed-in image of electrocoalescence fusion within an enlarged channel from [1]. (e) Schematic and experimental image from [33, 41] illustrating the fusion of two populations of droplets of different sizes.

This merging technique was also encountered in the article [42], which focuses on trapping and electrocoalescence of two droplets using a high-speed camera.

4.2.3 Laser merging

One famous droplet fusion technique involves the use of a laser. The laser is directed at the point where the two droplet membranes come into contact. The localized heating reduces the surface tension and leads to droplet coalescence. One major advantage of this technique is the ability to perform it at any point on the chip. No specific chip fabrication is required, as the laser can be controlled and adjusted directly from the outside. However, a drawback is the local heating of the droplets, which can lead to damage to their contents. Cells or chemical compounds may be affected. The Fig. 2.10 shows a sample of laser-induced fusion from the literature.

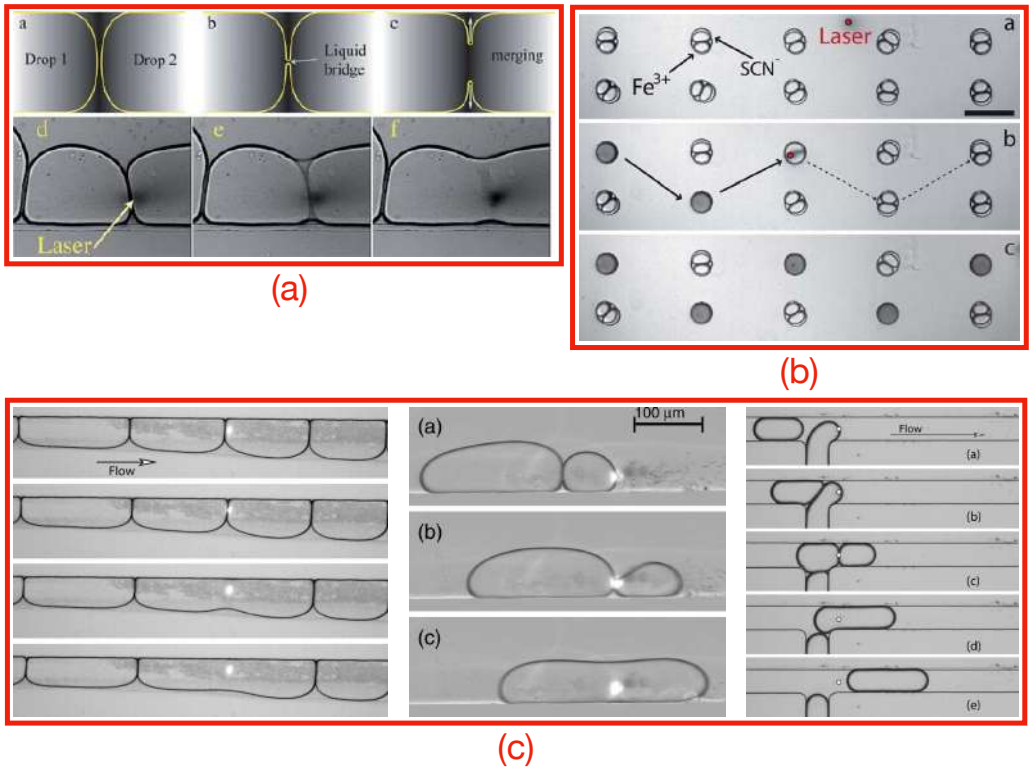

Figure 2.10: Experimental pictures from the literature illustrating droplet fusion by laser. (a) Image from the article by [28] highlighting the different stages of fusion between two droplets. (b) Photos from [43] showing laser-induced fusion of trapped droplets inside wells. (c) Various photos from [44] demonstrating laser-induced fusion in different situations.

A more specific article focuses on trapping two droplets of different compositions and their fusion by laser [45]. It then tests the diffusion time for the final droplet to reach a homogeneous composition.

The laser is not only used for droplet fusion but also for their manipulation. Indeed, the laser beam has the ability to release droplets, sort them by directing them in one direction or another, or even temporarily stop them, as illustrated in numerous articles [6, 24, 43, 46–51].

4.2.4 PFO merging

This last fusion technique is the one used in this master thesis. It uses a destabilization agent that reduces the surface tension of the droplets by acting on the surfactant layer at the interface. It destabilizes this layer so that the droplets in contact eventually merge. A common agent is called PFO (perfluoro-octanol) and is used in [52–54]. Both the advantage and disadvantage of this method are its action on the entire chip, as all the droplets in contact with the PFO merge. As a result, fusion occurs very quickly throughout the chip. Unfortunately, targeted fusion does not seem possible with this method. It is also possible that the experiment may fail due to the merging of excess droplets located in different undesired locations. In this situation, these droplets form a large aqueous environment that can disrupt the proper functioning of the channels and wells. An illustration of this droplet fusion method (Fig. 2.11).

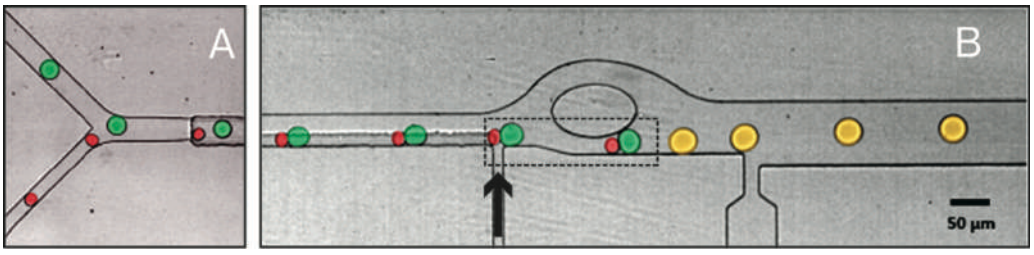

Figure 2.11: Experimental photo from [53] illustrating droplet fusion using PFO in a microfluidic chip.

4.3 Droplet trapping

This section aims to present the literature related to droplet trapping. The different methods will be discussed separately to better structure the various techniques encountered. A brief overview of the literature can be found in [55]. It is worth noting that there is not always a consensus on the name of a particular type of trapping. Some liberties have been taken in the nomenclature to better distinguish these trapping methods.

4.3.1 Oil flow trapping

This method uses an oil flow to trap the droplets. To distinguish this technique further, it is possible to divide this section into two distinct methods.

4.3.1.1 Static droplet array This technique uses an oil flow and channels to trap the droplets. The idea is to precisely guide the droplets using the channels. Circular shapes are designed to form traps. These traps are surrounded by a diversion channel and a direct channel. In the absence of droplets, the flow will be distributed between these two paths. By adjusting the size of the channels, the microfluidic resistance is also modified, allowing to find a balance in the flow between the main and diversion channels. When a droplet reaches the trap, it is more likely to enter it. Since the direct channel is narrower, the droplet cannot deform to enter it, provided that the oil flow is sufficiently limited. As a result, the droplet is trapped in the spot like in a funnel. It restricts the oil flow in the direct channel and increases the resistance in this part of the circuit. The next droplet cannot enter an already occupied trap and will preferentially choose the diversion channel. At the exit of this channel, the droplet faces a similar choice: enter an empty spot or take the diversion channel if it is already occupied. This process continues until the entire array of traps is filled. Any excess droplets will be redirected through all the diversion channels to the waste outlet.

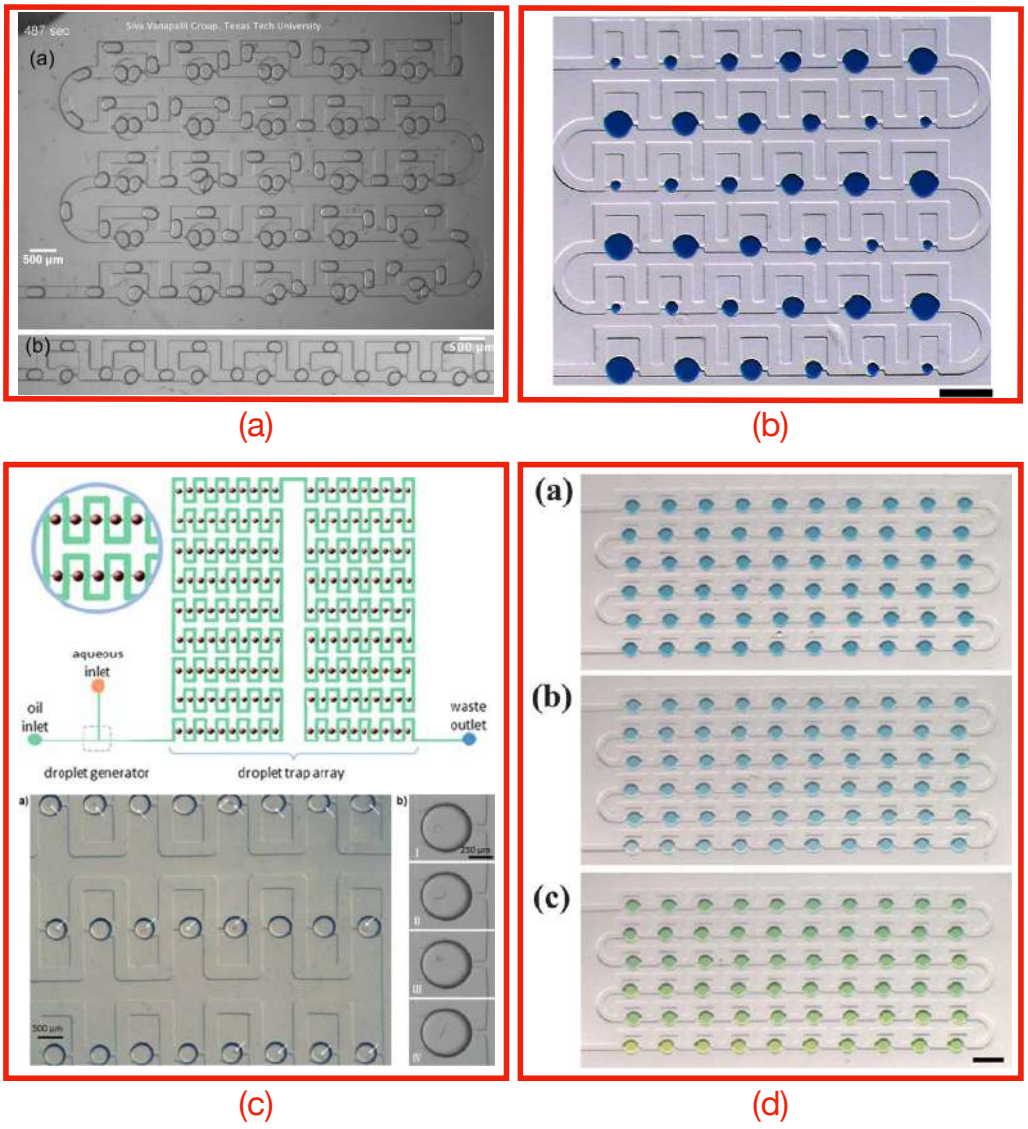

Figure 2.12: Experimental photos from the literature illustrating static droplet arrays: (a) Photo from [56] showing the chip in operation. In this test, two droplets have been trapped within each of the traps. (b) Photo from [24, 57] showing the trapping of droplets of different sizes. (c) In this image from [58–60], a schematic of a chip of this type is shown. In this experiment, the chip was used to trap droplets containing worms. (d) Photo from [61] illustrating trapping via static droplet arrays. A compound is gradually diluted to change the dye concentration and generate this color gradient.

Static droplet arrays are extremely common in the literature and are considered as a stable and well-established trapping method [62–70]. An unusual example of geometry can be found in [69]. In this example, there is an additional control over the traps through the use of multilayer microfabrication and the introduction of microfluidic valves [65].

4.3.1.2 U-shaped trapping array The second type of trapping that uses an oil flow involves U-shaped microstructures that allow droplets to infiltrate but not to exit, provided a slight oil flow is maintained. The major difference compared to the previous trapping method is the freedom given to the droplets. They are no longer constrained to move within channels but can autonomously move within the chamber. Fig. 2.13 provides an overview of the literature on this topic. Fig. 2.13a and Fig. 2.13b illustrate back-side traps. The simplified description of their

geometry consists of two U-shapes combined in opposite directions. One U-shape has longer branches than the other, allowing it to trap two and one droplet, respectively. The principle is to trap the first population of droplets with the small U-shape. Then, the oil flow is reversed so that these droplets are trapped in the large U-shape of the microstructure facing it. Finally, the second population of droplets can be generated while maintaining the same direction of oil flow. Since the large U-shape already contains one droplet from the first generation, it can capture a droplet from the second generation but not more. This results in two droplets from two distinct populations trapped within the same well. In this scenario, the droplets from both distinct generations have the same size. This type of trapping is very common in the literature [18, 42, 71–78].

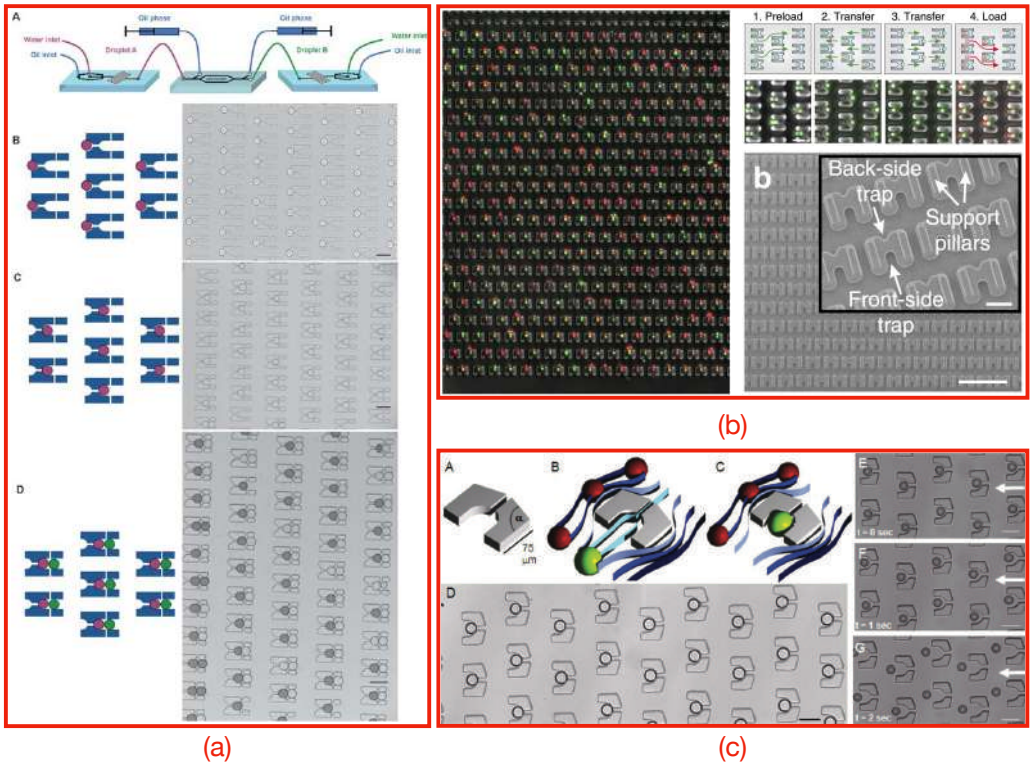

Figure 2.13: (a) Array of a back side U-shaped trap [60, 79]. The illustration of how this type of trap works has been retained in the image. (b) Array of a back side U-shaped trap [80]. (c) Simple U-shaped trap [24, 33, 81].

4.3.2 Phase substitution trapping

This type of trapping is rare and quite unique since no droplet generation is required. The idea is to completely fill the chamber with the aqueous phase. In this situation, the traps are actually wells with a depth greater than the height of the chamber. The next step is to flush the chip with oil. The aqueous phase is gradually removed, except for the wells, which serve as important anchoring points. As a result, the aqueous phase is trapped inside the wells, and droplets are formed. This technique imposes the same composition on all the wells and requires a large quantity of the aqueous phase. It is also challenging to release these droplets or even capture a second population of droplets using this method. Fig. 2.14 illustrates this phase substitution trapping.

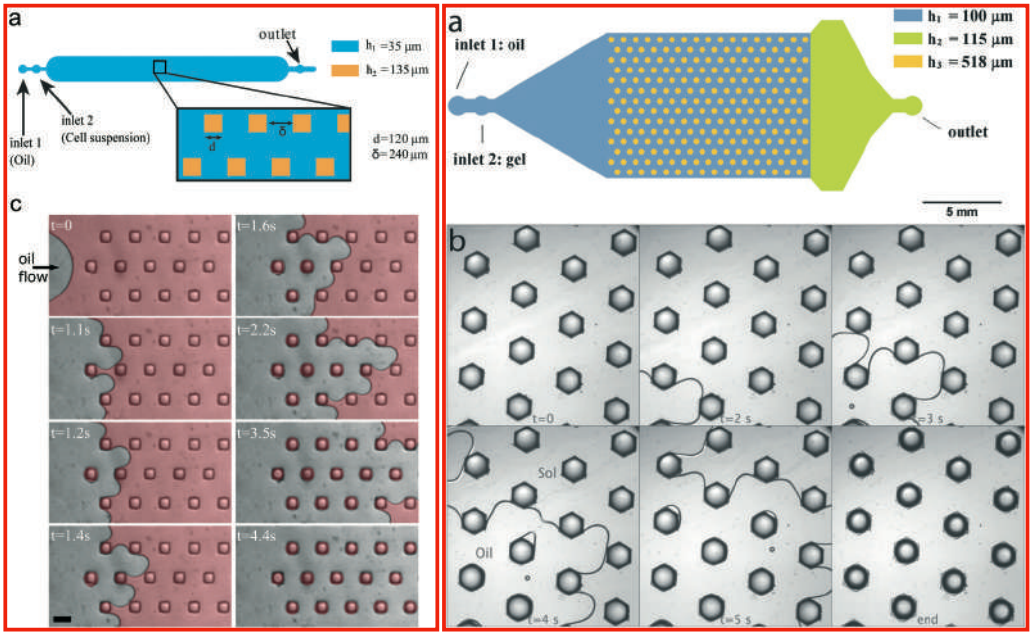

(a) (b)

Figure 2.14: (a) Photo illustrating different moments of the flushing of the aqueous phase using a difference in coloration [48].(b) Another illustration of the flushing of the aqueous phase [82].

4.3.3 Pillars trapping

This trapping technique is unique in its design, as the capture is achieved using pillars that surround the droplet. In the references consulted, a set of six pillars is necessary to capture one droplet. These pillars are arranged at each corner of a hexagon. This hexagonal pattern is replicated to form a network. As a result, droplets can be captured in each of the hexagons of the network. Fig. 2.15 illustrates this trapping method.

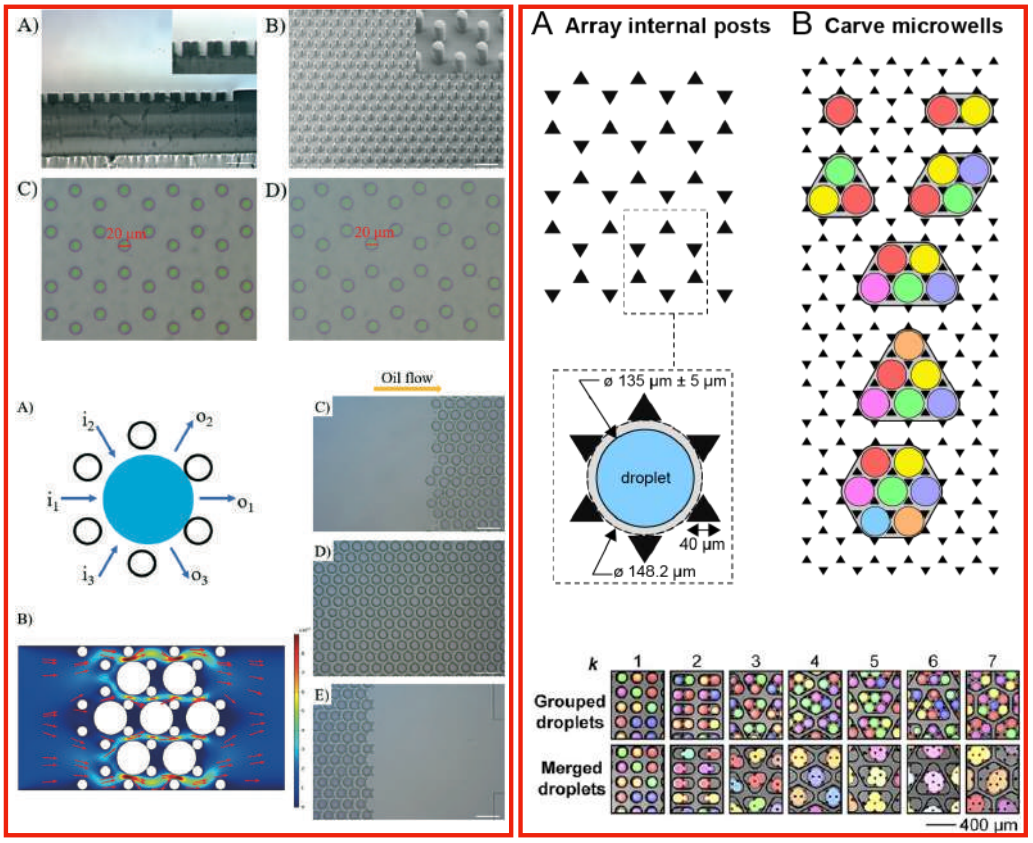

Figure 2.15: (a) Images showing the pillars and the hexagonal pattern under a microscope. The pillars are circular in shape. The different stages of droplet trapping are also presented [83]. (b) Images showing a similar trapping using triangular-shaped pillars [84, 85]. In this example, droplet clusters are formed by etching a contour between a set of adjacent hexagons.

In the article by He[83], there is a droplet size threshold for which one or two droplets are trapped within the same hexagon. Unfortunately, it does not seem possible to confine two droplets from different generations in this example.

4.3.4 Dropspots

Dropspots are a trapping technique based on the deformation of droplets. Certain regions, called spots, are circular and have a diameter slightly larger than the diameter of the droplet. These spots are separated by constrictions where the cross-section is narrower. Under these conditions, a droplet can adopt a circular shape within a spot, minimizing its total surface area at a constant volume. To dislodge the droplet, it will be necessary to deform it to make it pass through a narrower section. This process will increase its surface area and will not be spontaneous. To achieve this, there can be the arrival of a new droplet or a significant increase in the oil flow rate. The first possibility is used to gradually place the droplets into the spots, while the second allows the recovery of all droplets. Since the spots are placed successively in a channel, when droplets are dislodged, the resistance decreases, and the flow rate increases, which dislodges the remaining droplets. Indeed, the spots act as important anchoring points for the droplets, drastically increasing the channel's resistance. Fig. 2.16 illustrates this trapping method using dropspots. In all the examples encountered in the literature [60, 86–88], only one droplet per spot has been observed.

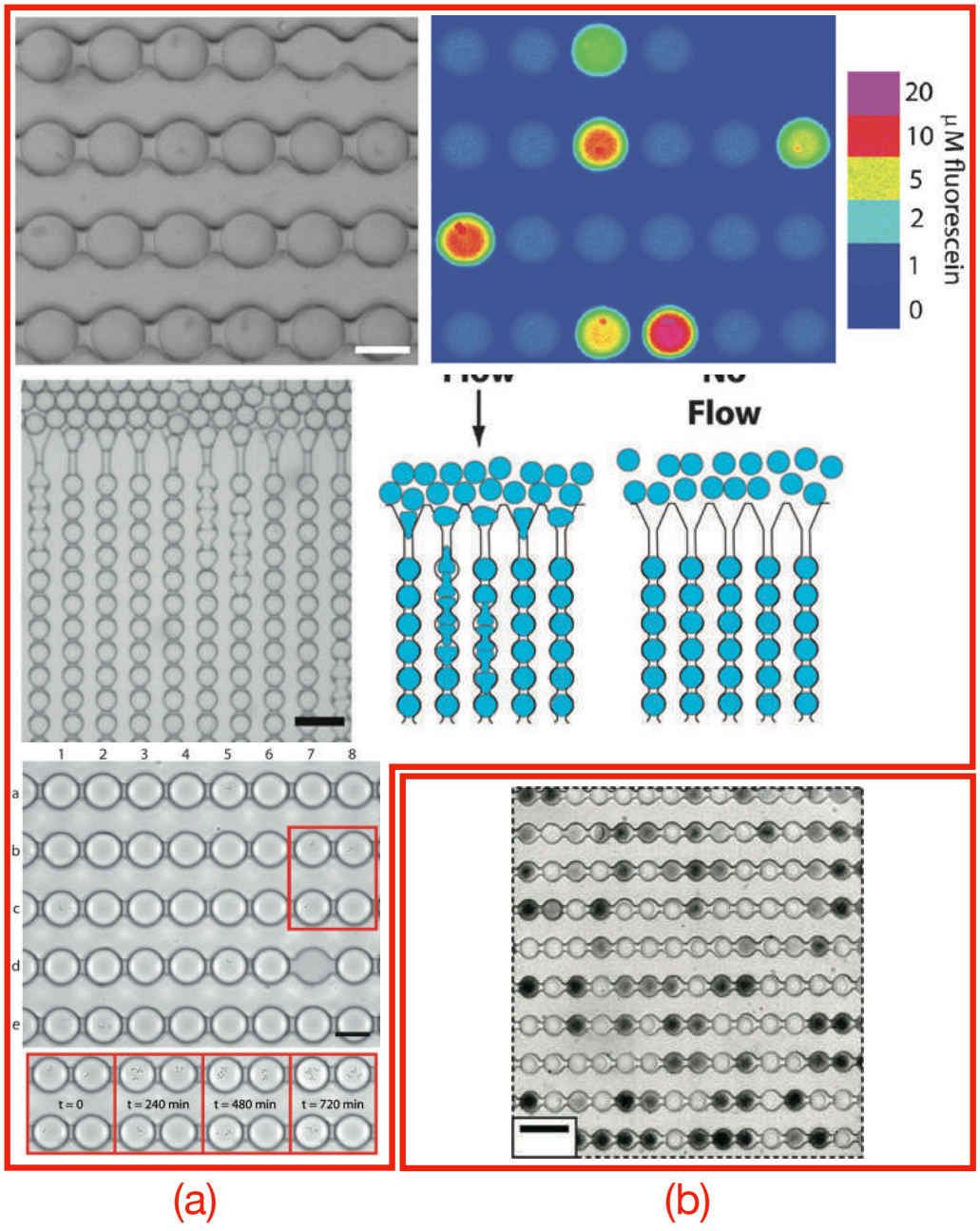

Figure 2.16: (a) Photos from [86], the dropspots are adjacent. The arrival of a new droplet requires pushing the entire chain. (b) Another illustration from [60, 87] based on the same principle.

4.3.5 Anchor trapping

To achieve trapping with a classic anchor, the droplet needs to be flattened inside a chamber. Thus, the confinement occurs only in one direction. The anchor is a well with a significantly smaller diameter than the diameter of the flattened droplet. When the droplet encounters the anchor, it deforms and takes a cap-shaped form inside the anchor [89]. This shape allows the droplet to minimize its surface. To release the droplet, the cap must flatten again or the droplet must split. The latter phenomenon occurs for droplets with a considerable diameter compared to that of the anchor. For droplets slightly larger than the anchor's diameter, they can be released by increasing the oil flow rate or by the arrival of a new droplet, as the trapping force is relatively limited. For this type of trapping, only the capture of one droplet per well has been

observed in the literature. Fig. 2.17 provides an overview of anchor trapping in the various encountered articles. A peculiar example of anchor trapping can be found in [90].

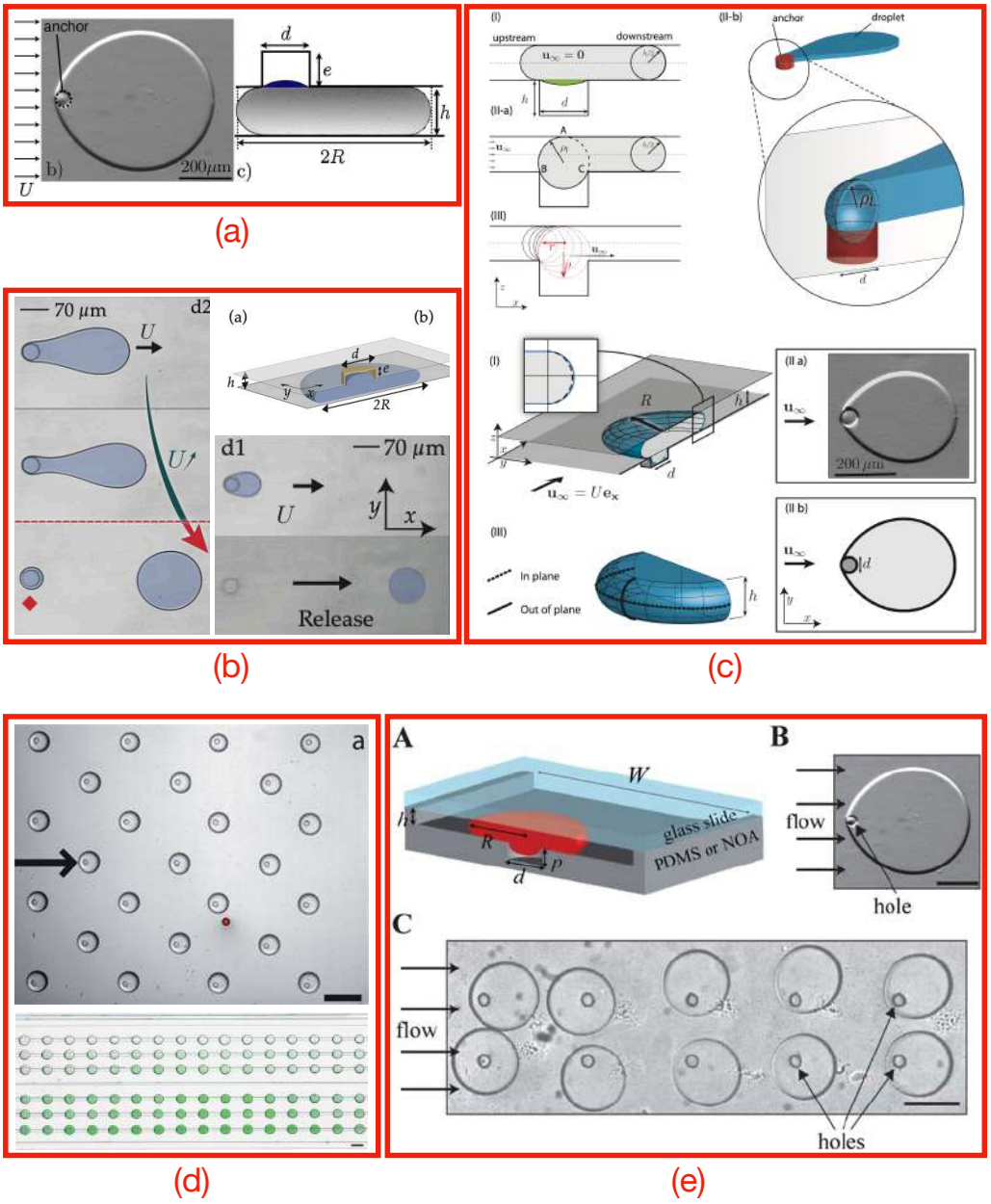

Figure 2.17: (a) Photo and cross-sectional diagram of the anchor trapping [91]. (b) 3D diagram illustrating the anchor trapping along with experimental photos showing the splitting of a large droplet under increased oil flow [92]. (c) Diagrams illustrating the physical study of anchor trapping and various approximations to characterize the droplet deformation within the anchor [93]. (d) Experimental photos of an array of anchor traps where the trapping occurs. The second photo combines anchor trapping with rails that allow droplet guidance through deformation and minimization of surface energy [43]. (e) 3D diagram and experimental photos illustrating an array of anchor trapping [94].

4.3.6 Capillary trapping

This trapping technique is particularly widespread in the literature [6, 43, 47, 85, 95–107]. It is based on the same principle as anchor trapping 4.3.5. In this case, the well has a greater

depth and diameter. The droplet remains flattened in the chamber and is still confined in one direction of space, adopting a pancake-like shape. When the droplet passes under a well, it can deform completely and enter it. This configuration is favored as it greatly minimizes the droplet's surface energy. Consequently, the droplet ends up occupying a large part of the well's volume and is firmly trapped. The trapping force is generally much stronger than in the case of anchor trapping. The disadvantage is the difficulty in releasing the droplets at a later time. Depending on the volume and depth of the well, the droplets can take a spherical shape or be flattened between the well's bottom and the chamber's floor. Fig. 2.18 illustrates various examples of capillary trapping from the literature.

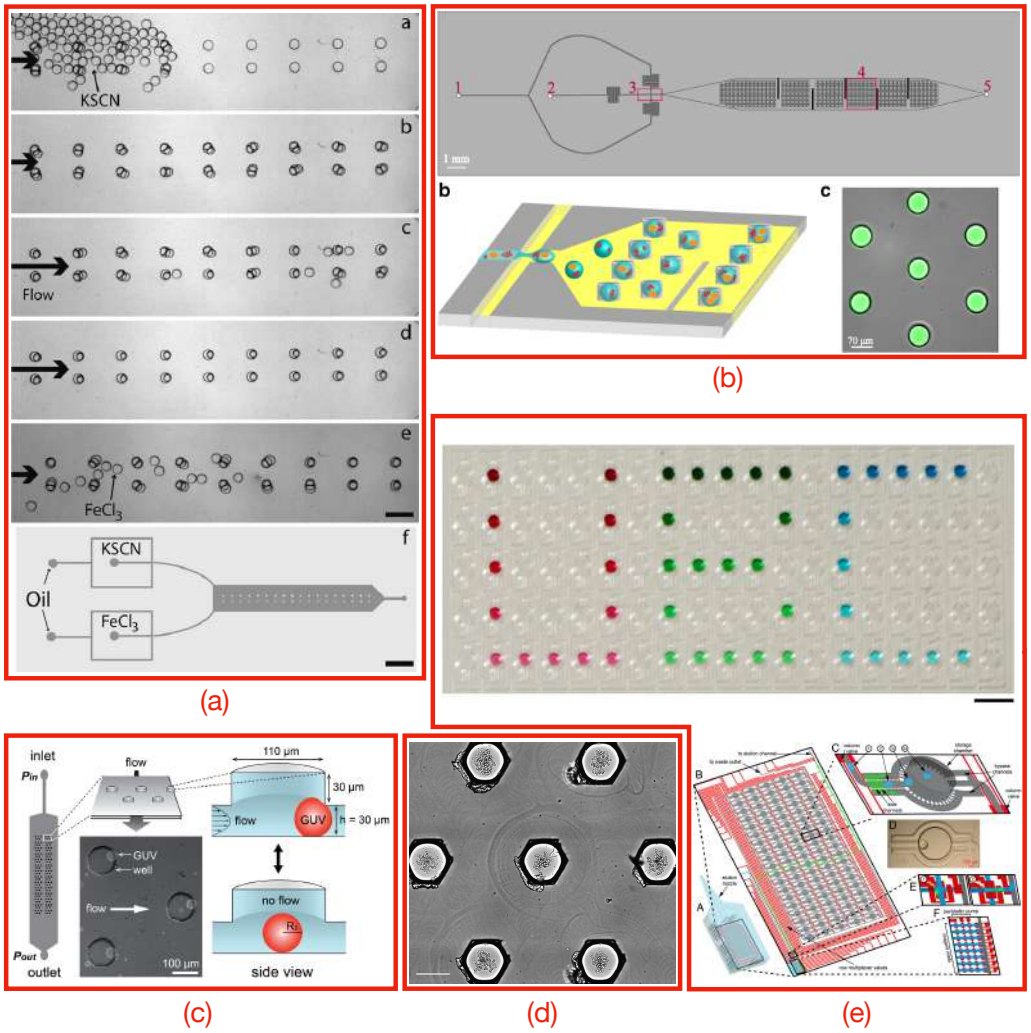

Figure 2.18: (a) Experimental photos illustrating the different stages of trapping. By adjusting the oil flow rate, excess droplets can be flushed out. The remaining droplets are trapped in the same manner as in an anchor, as they cannot enter an already occupied well. This allows trapping of two distinct populations [43]. (b) Schematics and experimental photos showing capillary trapping. The chip diagram shows walls in the trapping area that ensure proper distribution of the droplets [98, 99]. (c) Counterexample of droplets experiencing weak trapping forces. The droplet diameter is barely larger than the chamber's height. Giant Unilamellar Vesicles (GUVs) are used to simulate cell behavior [100]. (d) Capillary trapping is widely used in spheroid formation [47]. (e) Schematics and experimental photos illustrating capillary trapping in a microfluidic chip with sophisticated design. It offers precise control over droplet movement, allowing the university initials in which it was developed to be traced [24, 108].

4.3.7 Buoyancy trapping

Buoyancy trapping shares similarities with capillary trapping 4.3.6. Droplets retain their freedom to move within a chamber. However, the major difference compared to capillary trapping lies in the fact that the droplets are not confined in a specific direction of space. Instead, they maintain their spherical shape and have minimal surface energy. The deeper chamber also allows for better distribution of droplets, resulting in a more homogeneous dispersion. The traps, in this case, are similar to circular wells. When a droplet passes under a trap, buoyancy displaces it inside, leading to trapping. The significant advantage of this method is the ease of recovering the droplets by simply flipping the chip. The buoyancy force then operates in the opposite direction, releasing the droplets from the traps. A low oil flow can guide these droplets towards the exit. This technique has only been found recently in the literature [95, 109–111]. Notably, the article by Labanieh [109] represents the starting point of this master thesis. An illustration of the available content in the literature for this trapping method is provided in Fig. 2.19.

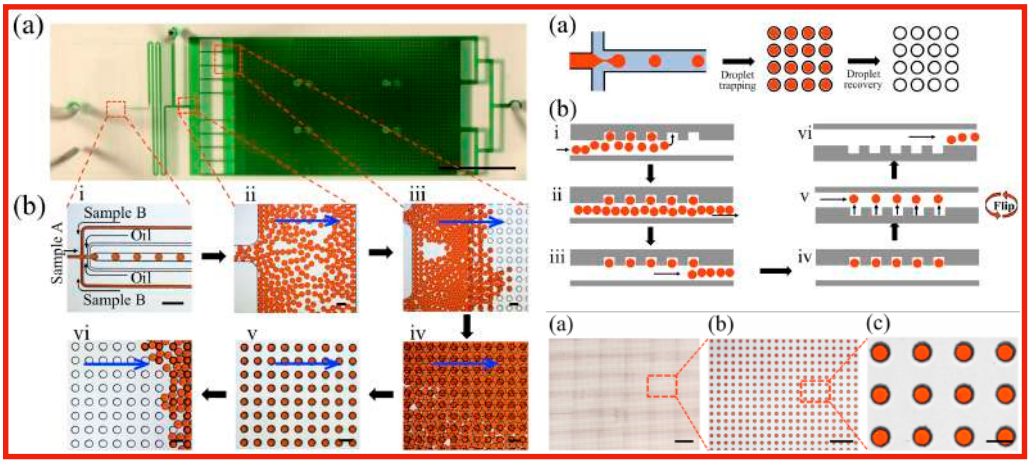

(a)

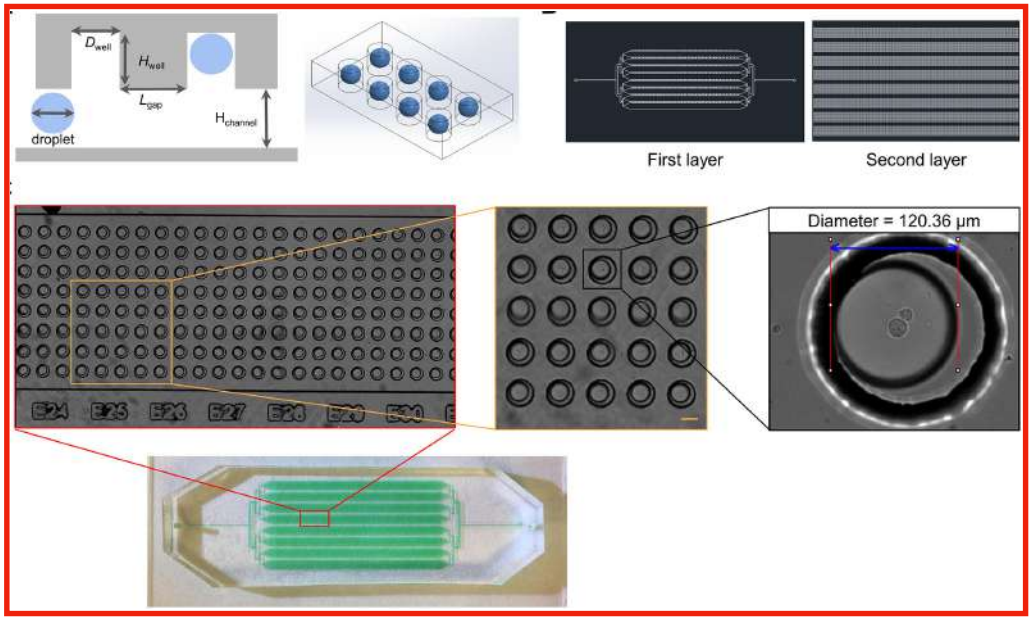

(b)

Figure 2.19: (a) Experimental photos and diagrams illustrating the trapping and release of droplets using buoyancy from Labanieh's article [109]. (b) Another example from the literature of buoyancy trapping [110]. The particularity of this chip is that it doesn't have a single chamber but several. The aim is to allow good diffusion of droplets from the channel originating in their production zone.

4.3.8 Asymmetric trapping

Unlike the trapping methods encountered so far, this technique does not bring anything innovative. The idea is to combine the previous trapping methods to trap multiple droplets from different populations within the same well. To achieve this, the trick is often to introduce an asymmetry in the initial shape of the circular or hexagonal well. In parallel, it is possible to play with the depth of the wells using multi-layer microfabrication techniques. With this approach, a single well can have two distinct depths targeting a specific type of droplet. Fig. 2.20 from Tomasi's article [5, 52] illustrates this analysis.

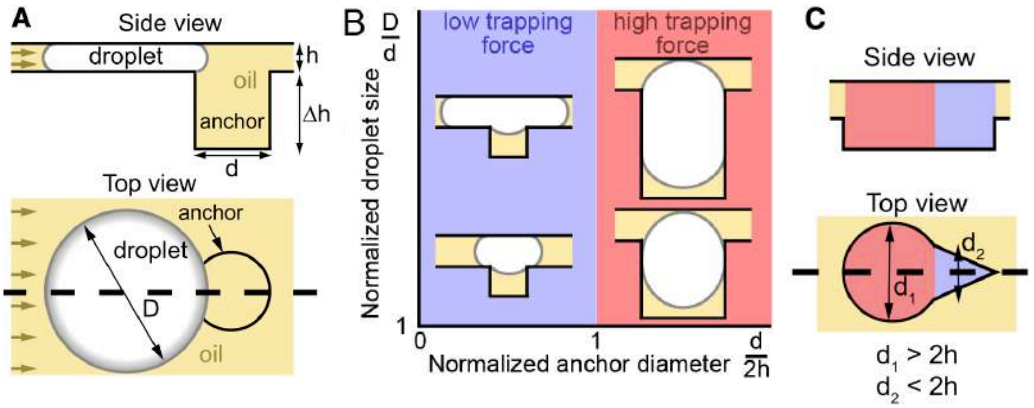

Figure 2.20: Diagram illustrating an example of capturing droplets from different populations by manipulating the asymmetry of the well. In this situation, the well combines both capillary trapping and anchor trapping techniques. Consequently, the first droplet experiences a strong trapping force, while the other can be easily released.

To concretely illustrate the capture of two droplets from distinct populations in a single well, a sample of images from the literature is provided (Fig. 2.21). The references demonstrating this type of trapping can be summarized in [5, 52, 95, 97, 104].

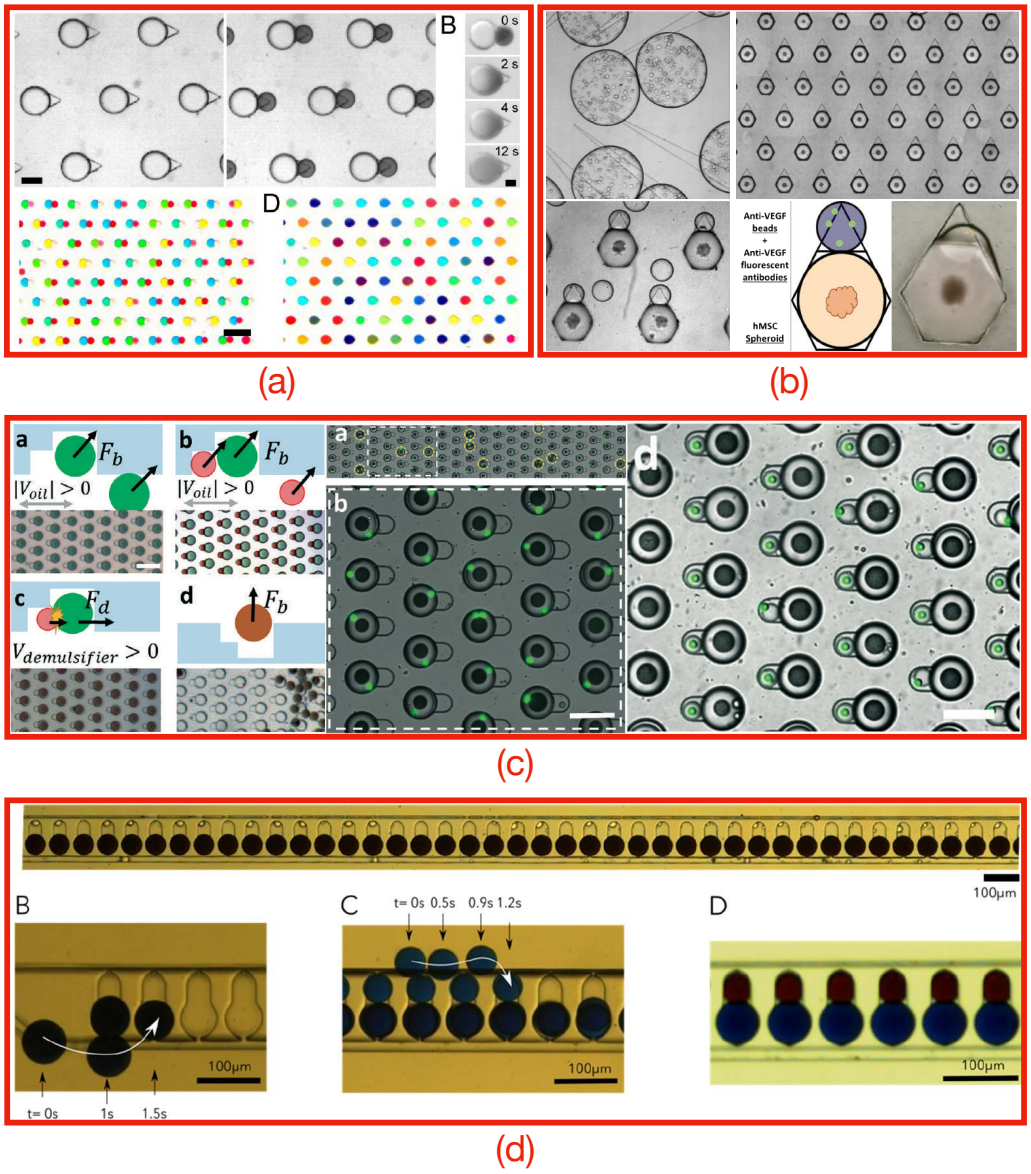

Figure 2.21: (a) Experimental photos from Tomasi's article [5, 52] illustrating the capture of the first population of droplets by capillarity and the second one by anchor, achieved by introducing a tip on the well shape and modifying the droplets' size. This photo also illustrates the fusion using PFO. (b) This example is similar to (a) but with hexagonal-shaped wells [97]. To enable anchor trapping, the well is also equipped with a tip. However, the tip is shallower than the rest of the well to ensure that the droplet cannot enter it deeply and thus maintain trapping by anchor. (c) In this example, trapping occurs in an enlarged chamber, allowing buoyancy trapping [95]. To capture two populations, they are generated with different sizes. In this type of trapping, droplets maintain a spherical shape. The main well is large and circular, serving as the capture point for the first population. A smaller rounded eccentricity is added to it, enabling the capture of the second population of smaller droplets. (d) In this example, the wells have the same shape as (c) but have a single depth [96]. The chamber is small, and droplets are trapped by capillarity. To ensure proper trapping, the droplets are sorted by size and guided along a rail on the side of the well where they are supposed to settle.

4.3.9 Other Techniques

In order to be concise in this section, many innovative and exotic techniques could not be presented. Readers interested in exploring this topic further can look into *Slipchip* [60, 112,

113], *Lock & shift* [114, 115], *Electrostatic potential well* [24, 116], and *Sedimentation* [117]. Regarding fusion, a unique technique can be found in [33, 118].

4.4 Spheroid

This section dedicated to spheroids aims to illustrate their formation through various articles encountered in the literature [5, 6, 47, 52, 97, 104]. To form spheroids, the aqueous phase must contain a high density of suspended cells. This liquid is used to generate droplets. Once trapping is performed, the droplets are brought to a stop for a period ranging from several hours to several days. During this time, the cells undergo sedimentation, accumulate at the bottom of the droplet, and eventually aggregate into a spheroid.

The spheroid has a limited lifespan since its environment consists of the small volume of liquid in the droplet. Under these conditions, nutrients are quickly depleted, preventing the spheroid from surviving in the long term [6]. To counteract this issue, a common strategy is to gel the droplets and then substitute the surrounding oil phase with some nutrient-rich aqueous phase [6, 47].

To test the action of a drug on spheroids, it is important to develop a tool that can highlight successful tests. The number of droplets is substantial as it is proportional to the number of tests. And these tests are often maximized to discover as many effective drugs as possible. To evaluate the validity of each test within each of these countless droplets, fluorescence detection is often used. Thus, a signal will only appear if the test is successful and the spheroid has survived. This process of detection through signal acquisition can be automated. As a result, the time spent on this analysis is drastically reduced compared to a similar manual operation. This final step marks the end of the cell screening process [2–4, 31, 110, 119–122].

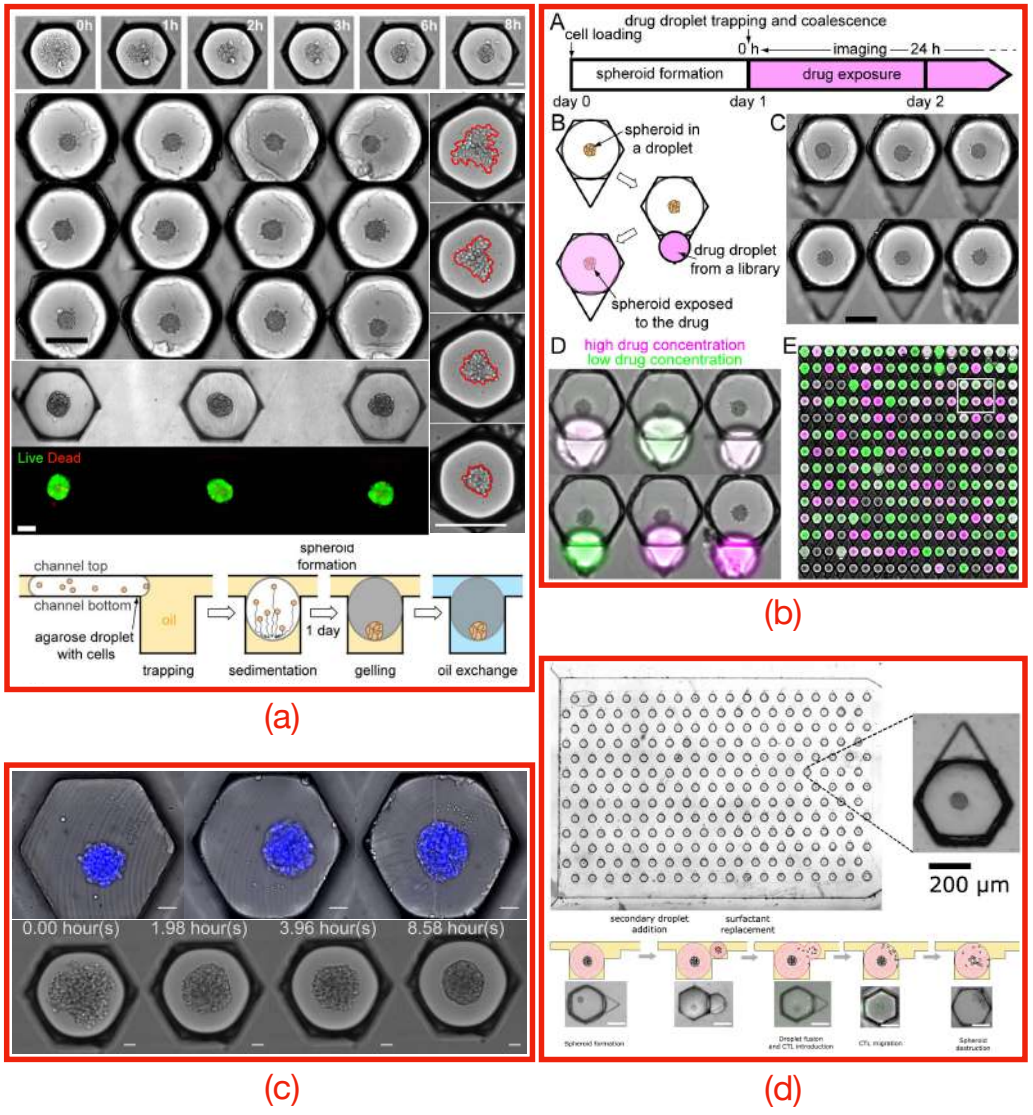

Figure 2.22: (a) Experimental photos and diagrams simply illustrating the formation of spheroids and highlighting the agglomeration process [47, 123]. (b) Experimental photos and diagrams showing the formation of spheroids. A droplet containing a test drug is then introduced into the same well and fused with the droplet containing the spheroid. Finally, testing and screening are carried out to visualize the action of different drugs on a large scale [5, 52]. (c) Experimental photos and timelapse showing the formation of spheroids [104]. (d) Experimental photos showing the chip with the cell assay. A diagram depicts the cross-section of a well and the various stages of drug delivery to the spheroids [97].

Part II

Methodology

Chapter 3

Micro-fabrication

In this section, the details of chip manufacturing will be discussed. The subject of this thesis is essentially based on the use of microfluidic chips, this part aims to describe how they were created.

1 Chip architecture

To begin, it is necessary to introduce the essential parts of microfluidic chips dedicated to trapping, which will be used later on. A general diagram can be seen in Fig. 3.1.

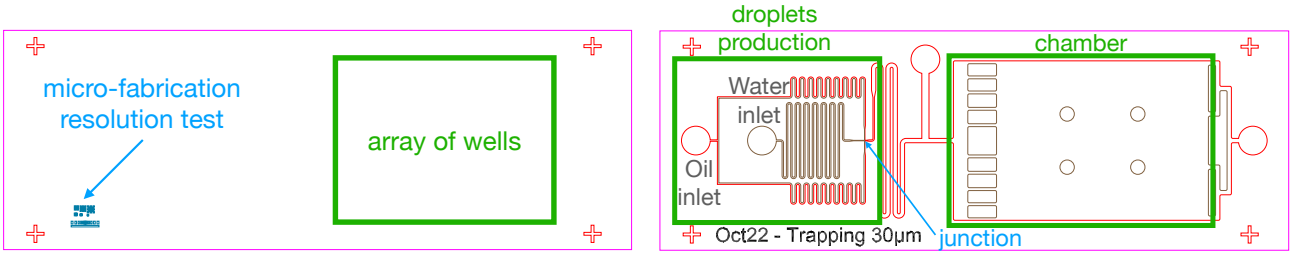

(a) (b)

Figure 3.1: Diagram illustrating the (a) upper and (b) lower parts of the final chip for droplet trapping.

The vast majority of chips designed thereafter will be composed of an assembly of two PDMS (Polydimethylsiloxane) half-chips (Fig. 3.1). These will be assembled to form the final chip. This configuration is peculiar as traditionally chips are assembled on a glass slide. The upper part consists of a well array that can be uniquely and creatively designed for droplet trapping (Fig. 3.1a). It overlays a chamber where the droplets are free to move (Fig. 3.1b). Additionally, there is a dedicated area for droplet generation on the same chip. The generation part of the chip is designed to be as compact as possible to maximize the space available for trapping. This production junction is called flow-focusing (Fig. 2.5) and was presented in section 4.1. It consists of microfluidic channels with matching resistances that meet at a cross-section. The oil is divided into two symmetrical channels, unlike the water, which arrives via a single channel. The objective is twofold: first, since oil is the dominant phase, two channels allow a higher flow rate. Second, the stability of the droplets formed is superior to a simple T-junction.

2 Chip manufacturing

2.1 Photo-lithography

First of all, it is necessary to create the design of the chip. This is done with the help of the software `AutoCAD`. This allows to build the chip geometrically through a vector drawing. The conditions for making the drawing are to always draw closed loops strictly included in each other without any possible intersections.

Once the geometry of the chip is complete, a mask is made. This is transparent in some areas and completely opaque in others. The principle of closed loops defined above allows each of these areas to be separated topologically. The principle being that each loop inside another is only a deformed circle. Thus, the first loop will contain an opaque zone, all the internal loops will define transparent zones. At subsequent stages, the pattern will alternate between opaque and transparent zones each time a loop is crossed. In practice, the transparent areas will be the places defined as hollow and where a liquid could theoretically flow. For example, this is the case for the various channels. In practice, a different color is assigned to each of these loops in the `AutoCAD` design (Fig. 3.1).

The creation of the mask requires a very precise transition between a transparent and opaque area. In theory, this transition should be as abrupt as possible to prevent any limitation of the microfabrication by the mask. Indeed, the smallest structures appearing in a chip have dimensions of the order of a few micrometers. This is valid in the literature for the most advanced research groups. The transition must therefore take place on a scale that is smaller than a micrometre.

In the case of this thesis, the mask could not be made directly at the university since the machine used to make it suffers from some accuracy problems and has been described as capricious. As the making of the mask is the starting point of any good microfabrication, the task was delegated to a specialised company in England. In one hand, the masks obtained were therefore of very good manufacture. On the other hand, they were rather expensive compared to home production. The second problem was of course the waiting time for orders.

The next step involves printing the various structures of the chip designed in `AutoCAD`, which are now visible on the mask. This consists of creating the negative of the final chip on silicon wafers from the semiconductor industry. The reason for this choice is the technological advance of this field with respect to microfluidics, since it was only developed much later. The idea is to make a mould that can be used several times so that the same chip can be reproduced multiple times. This part of the process takes place in a clean room.

The use of a glass wafer as a substrate, which at first sight seems more accessible, is in fact a misleading idea. The main reason is that glass is a transparent material. During the UV exposure process which will be explained later, light can pass through the glass layer and undergo reflection on the substrate underneath. As a result, opaque areas on the mask could be exposed by this undesired reflection, leading to a significant loss of the pattern of the structures.

The compound used to print the structures on the substrate is called SU-8 photoresist. It is at the core of the photolithography process. SU-8 is a photosensitive polymer from the thermoset

family. This means that it undergoes irreversible curing. In this case, curing is achieved through exposure to UV light and heat. The principle is to cross-link the polymer chains so that they form an infusible and insoluble network. SU-8 exists in different viscosities depending on the desired application but the composition remains the same. Only the length of the polymer chains varies.

The beginning of the process involves depositing a sufficient amount of SU-8 onto the silicon substrate. The substrate is then placed in a centrifuge to allow for the spreading of the SU-8 into a homogeneous and uniform layer. The viscosity of SU-8 increases with the average number of monomers in a chain. Thus, the choice of SU-8 viscosity allows for control over the final thickness of the chip during this spin coating process.

The wafer is then transferred onto a baking plate. After a defined curing time, it is placed under UV lamp. The mask is introduced between the wafer and the lamp. Thus, only the transparent areas will be exposed to UV light. The wafer is then again transferred to a hot plate. The wafer is then immersed in a bath of SU-8 developer which will allow the dissolution of the SU-8 which has not been exposed to UV. This finally allows the negative of the designed structures to appear on the chip. The wafer is rinsed with isopropanol and placed in the oven. This step concludes the fabrication of the wafer.

As a final remark, an optional technique involves pre-coating the silicon wafer. The principle being that the adhesion of future structures on the silicon wafer is not optimal due to the difference in properties between the two materials. The pre-coating is therefore carried out with the materials that will be used to print the rest of the chip which is SU-8. A small amount of SU-8 is poured onto the silicon wafer and then centrifuged to spread the SU-8 evenly. This last one must be as homogeneous as possible to avoid any important fluctuation of thickness along the chip. The initial idea was to create a thin, uniform and homogeneous layer of SU-8. Once this step has been completed, the wafer is then placed on a hot plate, which will harden the SU-8. The wafer is then exposed to a UV lamp. The UV light will prevent the SU-8 from being dissolved and will leave the pre-coating intact. After exposure, a second pass over the hot plate should be performed. This completes the pre-coating step.

Finally, before being able to fully utilize the wafer, it is necessary to ensure that the PDMS will not adhere to it. The direct analogy would be butter in a mold that allows for easy separation of the cake after baking. To fulfill this role, a release agent is applied to the wafer. The layer should obviously be as thin as possible. To achieve this, the wafer is placed under vacuum simultaneously with the application of the release agent. Thus, through the process of chemical vapor deposition (CVD), the wafer is coated with this agent. Once this step is completed, the wafer is ready to be used.

2.2 SU-8 thickness measurement

Throughout this master thesis, it is assumed that the microfabrication process achieves the expected SU-8 height. Thus, two heights have been considered in this work, namely 30 [μm] and 80 [μm]. In reality, this height is not perfectly exact. Within the same chip, there are slight fluctuations in thickness. To give an order of magnitude, chips designed theoretically at 30 [μm] actually had an average height of 29.94 [μm] with a standard deviation of 1.17 [μm]. The chip with a theoretical thickness of 80 [μm], on the other hand, had an actual average height of 78

[μm].

The characterization of the height was performed immediately after the microfabrication in the cleanroom. A probe applies a very slight force on the surface, and by moving the wafer using a micrometer screw, different regions can be traversed. The force applied to the probe varies depending on the height of the SU-8. This allows the characterization of the surface height. To avoid damaging the essential structures of the chip, this operation is often performed on the edges or in regions of low interest.

Recently, the laboratory acquired a laser for characterization purposes. However, this technology emerged too late to be used in this work. One of the advantages is that no contact with the wafer is required, reducing the risk of damaging the channels. Additionally, this equipment is readily available in the laboratory. The initial method could only be accessed in a cleanroom at Technifutur, which limited the study possibilities. One disadvantage of the laser, however, is the beam width of 50 [μm]. The average height is evaluated within this disk. For structures smaller in size, this method cannot be used.

2.3 Limitations of micro-fabrication

Microfabrication achieves high precision starting from the `AutoCAD` design. The order of magnitude of the mask error is below a micrometer. However, the true limitation arises from the thickness of the deposited SU8 layer which greatly influences the maximum achievable resolution. Although for simplicity, the assumption was made that the structures rose straight and uniformly over the thickness, a detailed analysis of the chip reveals that this is not the case. To confirm this, a predetermined pattern is inserted on each chip designed in `AutoCAD` (Fig. 3.1). Microscopic analysis of this pattern, with increasingly finer and adjacent structures, allows to determine the order of magnitude of the fabrication error by examining the smallest discernible structure. This error tends to increase dramatically with the height of the deposited SU-8 layer. For some chips, the different structures are only partially printed and, therefore, do not fulfill their intended function. The section 9 dedicated to failures illustrates this problem. This phenomenon is attributed to bevelled wall growth instead of straight growth as assumed, resulting in an undesired slope. The characteristic angle of this inclination is estimated to be around 10° based on the analysis of other doctoral students. As an example, the cross-section of an intended rectangular channel would actually be trapezoidal in shape.

The exact origin of this phenomenon remains somewhat mysterious. The error could come from the transition between a transparent and opaque zone on the mask. Even though this transition aims to be as abrupt as possible, there is a limitation in terms of resolution at the interface. The passage of light through this blurry and somewhat ambiguous zone could influence its direction and ultimately result in the creation of these inclined walls. Another hypothesis could be the partial reflection of UVs on the silicon substrate, which could degrade the quality of the transition between a clear and opaque area, thus potentially causing an error in wall resolution. As a result of all this, to ensure functional microfabrication, it is recommended to design structures in `AutoCAD` that have a width at least equivalent to the height of the deposited SU-8 layer.

2.4 PDMS molding and coating

Once the wafer is created, the final step is therefore the creation of the real chip that will host the different liquids. This part does not need to be done in a clean room because it is easy and inexpensive to start over in case of error. The material used for the chips is known as PDMS (Polydimethylsiloxane). It has the advantage of being bio-compatible, which allows the study of living organisms in the chips such as cells. It is also transparent and flexible. These are two essential qualities for both the observation and the connection of the different inlets and outlets.

PDMS is derived from a polymer family called elastomers. Elastomers are composed of long chains of molecules that are slightly cross-linked, allowing them to be in a solid state at room temperature. PDMS is supplied in a liquid state and is composed of long chains of molecules. However they do not interact sufficiently with each other to form a solid state. By adding one unit of curing agent to ten units of PDMS, the links between the chains of molecules can be establish and enables PDMS to solidify. Thanks to these long chains of molecules, PDMS exhibits excellent flexibility. It is essential to use the curing agent as it alone can initiate the interaction between the chains and facilitate the state change of PDMS to become an elastomer. The assiduous mixing of the two compounds introduces a significant amount of air. The mixed PDMS is placed under vacuum to remove any residual air. This step is essential since air bubbles could change the design of the printed patterns on the chip. It could also clog the channels. While the PDMS is under vacuum, an aluminum foil cover is made around the silicon wafer with adhesive paper. The aim is simply to contain the PDMS. After being under vacuum, the PDMS is poured on the wafer and the whole is sent to cure for 45 minutes at 85°C. The PDMS is then unmolded and the wafer is recovered for future use. The PDMS is cut to split the different chips gathered on the wafer. Typically, one wafer can contain up to seven microfluidic chips. In the situation of this thesis, one wafer is dedicated to the up part, i.e. the wells, while another wafer is dedicated to the down part, i.e. the chamber and channels. Each chip must be assembled with its twin, unlike the traditional process which simply consists in gluing the chip on a glass slide in order to form the fourth side and close the channels. In order to assemble the chips, it is first necessary to clean them. This step is done with an isopropanol bath, followed by a rinse with demineralized water. This step allows a better adhesion afterwards. The chip is then dried with compressed air. The respective surfaces of the two chips to be assembled undergo a final check. In order to avoid any possible dust, sticky paper is applied on each of these faces. The tape is then removed and the bare surfaces of each chip are directly exposed to the corona-gun for one minute. The latter allows to ionize and to promote the adhesion between the two PDMS pieces. The exposure is longer than usual because the alignment of the two chips is a difficult process to perform quickly. Prolonging the exposure ultimately improves the bonding between the two chips a bit. Another advantage is that the cohesion between PDMS and PDMS is better than between PDMS and glass. Directly after being assembled, the final chip is sent to the oven at 85° for one hour. This will allow to permanently glue the two chips together. After this period, the chip is removed and the holes corresponding to the different inlets and outlets are punched. It is important to note that this step is usually done before assembly. However, due to the difference in density between water and oil, the well chip must be located at the top to allow trapping by buoyancy force. The same goes for the different pipes for the classical observation under the microscope. Therefore, the two chips must be assembled to make sure that the holes are aligned with their locations on the bottom chip, the one containing the channels. Another particularity of the design developed in this thesis is the chamber which represents a huge non-adhesive space. During assembly, it can happen that the

top and bottom chips meet in the chamber. The oven passage definitively glues these two parts and the chip becomes unusable. If the holes are not punched before putting the assembled chip in the oven, the air contained in the chamber expands under the action of the heat. This air has no way to get out, the chamber acts as a huge microfluidic capacity, swells and prevents the top chip from sticking to the bottom chip.

Before the chip can be used, a flushing with `Aquapel` is done followed by a second one with `FC40`. The first one treats the channels and makes them hydrophobic in order to form nice droplets. The second one is used to remove the excess `Aquapel` because it is not good to let it dry in excess in the channels. The `FC40` is an oil which has the particularity of not evaporating. It fills the chip, prevents air from infiltrating the microstructures and makes it easier to use afterwards. A second, much more efficient flushing technique could be used in the latest results. The product replacing `Aquapel` is called `Novec`. It is much simpler to use and does not need to be flushed from the channels afterwards, which greatly limits the risk of damaging the chip. It is also much better in the final rendering, the formed droplets are nicer than with `Aquapel`. The procedure is to flush it inside the channels and then place the chip in the oven for 20 minutes at 135°C. After that, the chip is ready to be used.

To conclude this section dedicated to chip microfabrication, a summary of all the steps performed so far are presented (Fig. 3.2).

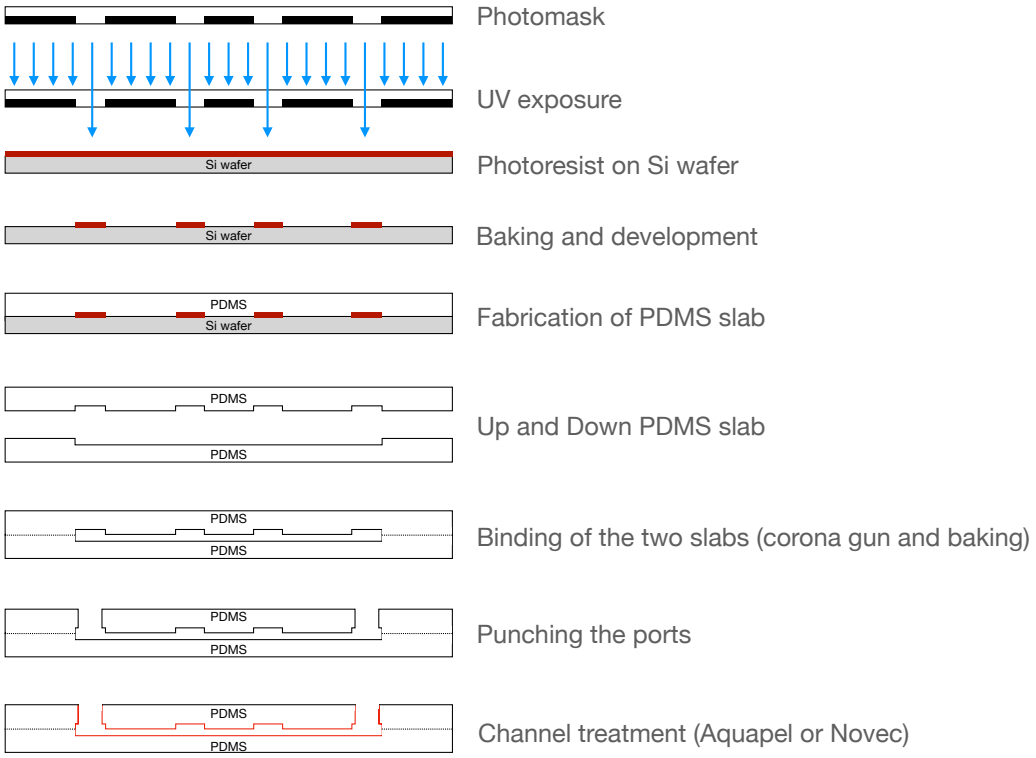

Figure 3.2: Diagram illustrating the chip manufacturing workflow. The design was inspired by [121]

3 Chip design

This section is dedicated to the development of the chip design used throughout this master thesis. In total, two chip fabrication runs were carried out.

3.1 First design

The first chip design was intended to be a validity test (Fig. 3.3). The goal was to adhere as closely as possible to the article by Labanieh [109]. The primary objective was to reproduce their results, use them, and ultimately continue analyzing trapping beyond this initial technique.

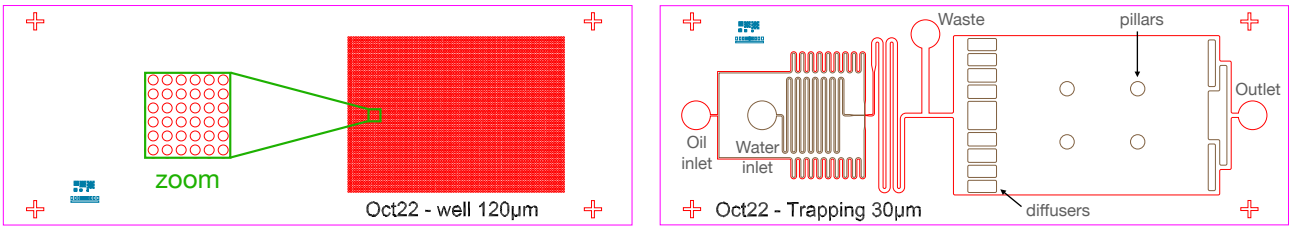

(a) (b)

Figure 3.3: Schematic representation of the initial chip design for droplet trapping. (a) The upper part displaying an array of wells. (b) The lower part featuring the chamber, channels for droplet generation and guidance, as well as the layout of various inlets and outlets.

The operation of the junction for droplet production has already been explained in section 1. Once the droplets have been generated, they leave the production zone and flow through a larger cross-sectional channel for good dispersion while ensuring disconnection of the chamber from the generation area. The channel located between the chamber and droplet generation serves as the waste outlet, allowing the evacuation of the first droplets that do not meet the expected requirements during chip startup. As the wells capture the first generated droplets, their regular size must be ensured before trapping them. In the chamber, several adjacent blocks can be observed, playing the role of diffusers for good droplet distribution within the chamber to achieve uniform trapping. In the middle of the chamber, there are four pillars that support the roof of the chamber, which is formed by the other chip. Indeed, the chamber represents a large vacuum space that expands as a capacitance when the chip is under pressure. Conversely, since the top of the chamber is only separated from the bottom by 30 [μm], these two parts can touch. If this occurs during the microfabrication step where the two PDMS chips are assembled into one, the top of the chamber can become permanently glued to the bottom, rendering the entire chip unusable. The outlet is located at the far right of the chip and is connected to the rest of the chamber by several large-section channels positioned according to the chamber's width to better evacuate the droplets. As explained earlier, the final chip is composed of two parts. It results from the assembly of the bottom chip (Fig. 3.3b) and the top chip (Fig. 3.3a).

The top chip consists of an array of circular wells. Only one well size is represented here, corresponding to wells with diameters of 120 [μm] (Fig. 3.3a). The other sizes, also designed, are 30, 40, 50, 60, 80, and 100 [μm]. For this first test, the spacing between the wells was adjusted to 50 [μm]. This choice proved to be both a problem and an opportunity since this distance is comparable to the size of the wells and droplets. This implies that there is an additional parameter in the system and that the wells are not independent of each other. The total number of wells varies from one chip to another. To give an order of magnitude, the chip with wells of 30 [μm] diameter had approximately 25000 of them, while the one with wells of 120 [μm] diameter had around 5000 wells. The number is simply determined by the size of the chamber since the entire network of wells must be able to overlay on it.

The chip containing the wells is located on the top, while the chamber belongs to the bottom

chip. This configuration was adopted because unlike typical oil, the one used in microfluidics is denser than water. It is Fluo-oil from the brand `Emulseo` and the typical density is close to $\rho_o = 1610$ [kg/m^3]. The surfactant concentration used is 1% for all experiments. Therefore, for the trapping of droplets by buoyancy force, it is necessary to have the wells in the upper layer, hence the adopted configuration.

Crosses are placed at the different corners of the chip to help with alignment. Indeed, a particularity of trapping is to align an up chip containing the wells with a down chip where the chamber resides. A pattern can also be spotted on the chips, which defines the quality of the microfabrication as explained in section 2.3.

3.2 Second design

The second chip design aimed to bring some improvements compared to the initial sketch (Fig. 3.4). Another objective was to open up the possibility of testing new trapping methods.

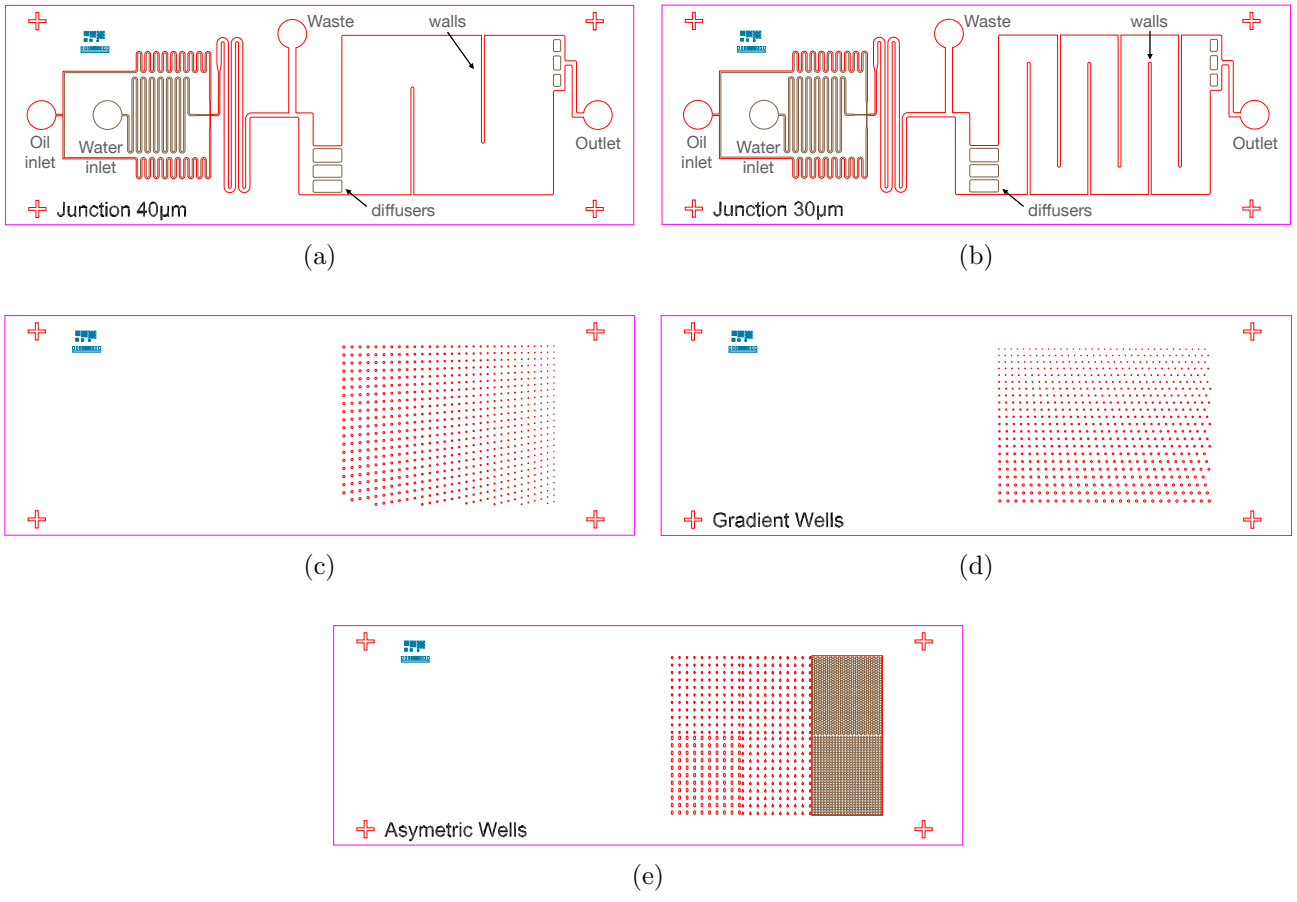

Figure 3.4: Schematic representation of the second chip design. (a) and (b) Lower section featuring the chamber with serpentine structures for droplet guidance and roof support. This design also includes channels for droplet generation and guidance, along with the layout of various inlets and outlets. (c) and (d) Upper section displaying an array of wells with gradually varying sizes in two spatial directions. (e) Upper section featuring asymmetrical well designs enabling the trapping of two populations of droplets.

Fig. 3.5 highlights the asymmetrical wells referenced in Fig. 3.4e by zooming in on the six different designs created.

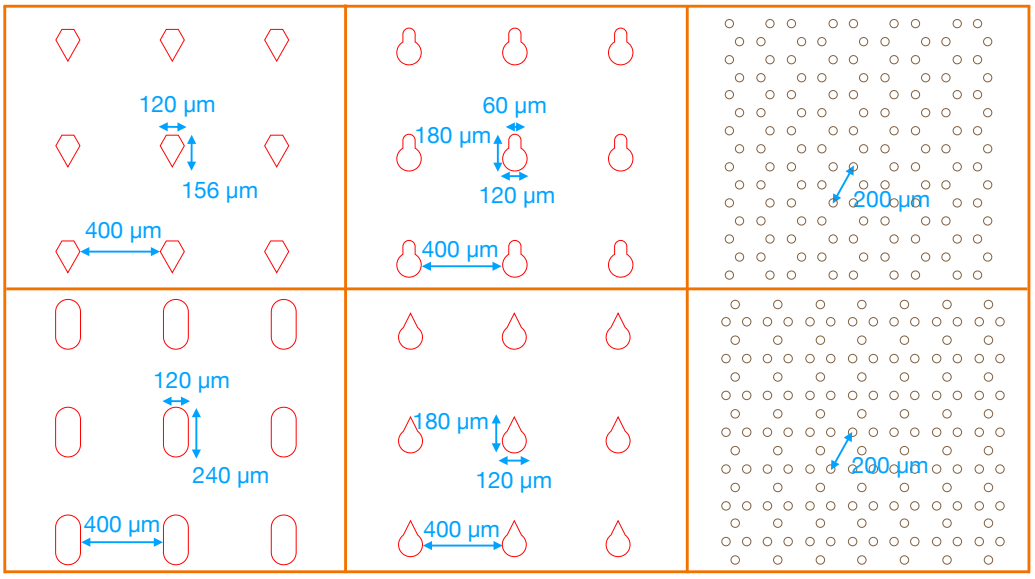

Figure 3.5: Zoomed-in view showcasing the six distinct designs of asymmetrical wells in the up part of the chip. Each design exhibits unique features for droplet trapping, enabling the trapping of two distinct populations of droplets.

On the bottom chips (Fig. 3.4a and Fig. 3.4b), the part dedicated to droplets generation has been kept identical. The water and oil inlets, as well as the waste outlet, still fulfill their respective roles as assigned in the previous design. An adaptation concerns the proper distribution of droplets within the chamber. The pillars used in the initial version of the chips could be ineffective in the case of capillary trapping. It sometimes happened that the droplets followed the edges until reaching the outlet without passing through the middle of the chamber where the wells are located. The introduction of walls has helped to limit this effect. Fig. 3.4b has six walls, while Fig. 3.4a has only two. Indeed, to be prepared for any potential issues, two distinct designs were developed, differing only in the number of walls. These walls help to form a wide canal that meanders inside the chamber, ensuring a good distribution of the droplets. For the sake of clarification, this solution was indeed better but far from perfect. There were strong velocity gradients in the turns leading to droplet releasing. Furthermore, the droplets would either form clusters or, on the contrary, not enter the areas where the flow rate was low. Lastly, in both cases, the chip outlet consists of a diffuser, just like the inlet. Although their existence may be questioned, they aim to prevent strong flows. Large velocity gradients in the chamber can cause droplets to become untrapped. Additionally, during experiments, the waste channel and the outlet allow for direct control of inlets and outlets in the chamber. Thus, they can be used in reverse, with the outlet serving as the inlet and the waste as the outlet. This way, droplets can be transported from the outlet to the inside of the chamber.

To correct some problems with the previous design, two major adaptations are implemented on the upper part of the chip. These top chips are depicted in Fig. 3.4c and Fig. 3.4d. First, considering the previous issues of droplet interactions due to proximity of the wells, it was chosen to increase the inter-well distance to 400 [μm]. The second main change concerns the size of these circular wells. Devoting an entire chip to studying a single well diameter seemed inefficient. Therefore, the chip was equipped with wells whose size varies gradually in both directions of the chamber. In this approach, theoretically no two wells have the same size. This double gradient aims to visualize the transition between different trapping regimes. The only difference between these two chips lies in the traversal direction of the two gradients. The

objective was to avoid any design errors by varying the well positions.

Fig. 3.4e(with a zoom in Fig. 3.5) shows a more specific chip design. The shape of the wells has been modified to enable trapping of two distinct populations of droplets. To achieve this, six well designs were developed.

It was only after testing the first design that knowledge of another recipe emerged, allowing for the modification of the SU8 height on the wafers. As a result, the top wafers containing the wells in this design were produced in two versions: one with a height of 30 [μm] and the other at approximately 80 [μm]. This final approach is less well-controlled and is affected by greater microfabrication errors associated with a larger SU8 height. Since the well diameters are on the order of 80 [μm] or even smaller for some, this limits the quality of microfabrication as discussed in section 2.3.

4 Experimental set-up

The role of this section will be to explain how the experiments are conducted. Since the chip fabrication is complete, the discussion now revolves around the equipment to be used for testing.

Firstly, the various inlets and outlets of the chip need to be connected to a set of tubes for the delivery and removal of different fluids. The tubes are cut to the desired length and have a sufficiently large cross-section to neglect their resistance in calculations. The connection is made using cut pieces of pipette tips, where the narrower end is inserted into the tube, while the other end is inserted into the chip through the specially designed holes made during the fabrication process. Both the tubes and the chip's PDMS (Polydimethylsiloxane) possess elastic properties, allowing for a sealed junction. The other end of the inlet tubes is individually connected to a liquid reservoir. In the case of this work, only water with or without dye, oil with or without a surfactant, and PFO (perfluoro-octanol) have been delivered into the chip. The outlet tubes are left open to the air and placed in a container to collect the outgoing fluids. At the inlet side, the liquid reservoirs are connected to an individual pressure system. The pressure range can vary from 0 to 1000 [mbar] above atmospheric pressure, with an adjustment accuracy of one millibar. The model used is from the Fluigent LineUP & FlowEZ brand.

Once the chip is connected, it needs to be placed under a microscope to visualize the processes taking place inside. The microscope used is an inverted fluorescence microscope Zeiss AxioVert A1. It can also highlight cells through fluorescence under the influence of certain substances. However, this aspect will not be considered within the scope of this master's thesis. This microscope naturally enables direct visualization. However, to record the different results, a Phantom MIRO110 camera or a Photron UX100 camera was initially used. They were retained for capturing rapid phenomena since they have a high frames-per-second (fps) capability. However, for timelapse and actions not requiring more than 60 fps, a Canon EOS 5D MKIII camera was used. It offers better ergonomics, making it easier to use, facilitating video capture, and improving compatibility with the computer. It also provides higher resolution.
Images of the experimental setup can be seen in Fig. 3.6.

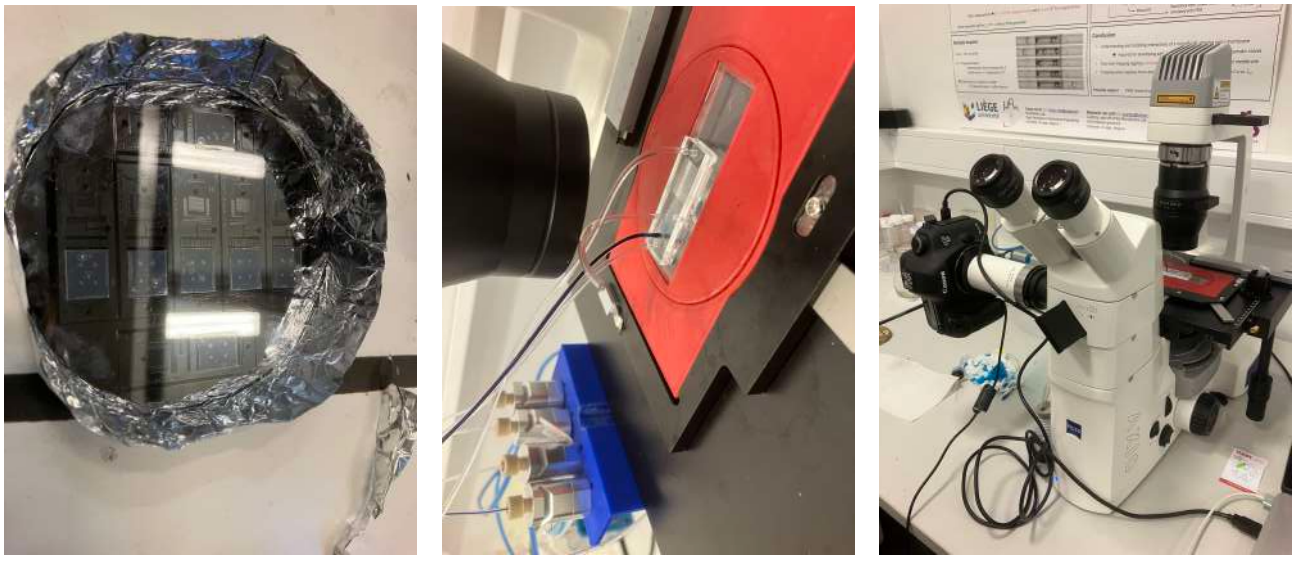

(a) (b) (c)

Figure 3.6: Experimental set-up. (a) Image of the SU-8 wafer (with the chamber covered by adhesive paper to make it deeper, see section 5). The wafer is encapsulated in aluminum and coated with PDMS to create the different structures and fabricate the chip after demolding. (b) Microscope image of the functioning chip, connected to various reservoirs for liquid delivery. (c) Overview image of the experimental set-up, highlighting the microscope and the camera used.

During the various trapping experiments, it was necessary to test whether the droplets could be released. To achieve this, a device capable of filming the chip when it was flipped over needed to be set up. Fully flipping the microscope was challenging due to the weight and size of the microscope itself, which would require a robust, complex, and costly structure. Additionally, the different pressure reservoirs for the liquids cannot function when inverted. While simply flipping the chip under the microscope may seem like the most logical idea, it also presents some difficulties. The connections of the different tubes located on the upper part of the chip end up on the lower part. This requires lifting the chip, adding thickness, and preventing the microscope from focusing on the area of interest.

When all these options were exhausted, the focus shifted to flipping the chip. Indeed, once the droplets are trapped, the chip can be delicately manipulated with certain precautions. The chip is placed on a plate equipped with micrometer screws for planar movement. This plate is attached to a metal arm, with the other end including fixtures for the camera and the objective lens. It turned out that the camera used with the most powerful lens, a Canon macro lens MP-E65, provided sufficient zoom for visualizing the droplets within the chip. Once the camera, the lens, and the chip are aligned on the same axis, the chip could be attached to a bearing connected to a fixed axis, allowing for a complete filmed rotation of the chip.

Unfortunately, no photos of this flipping device can be provided. The reason is that it was constructed using `Thorlabs` equipment. The author did not think to take photos at the time, and the equipment was quickly recycled for use in other experiments. Instead, a quick hand-drawn sketch can be seen in Fig. 3.7.

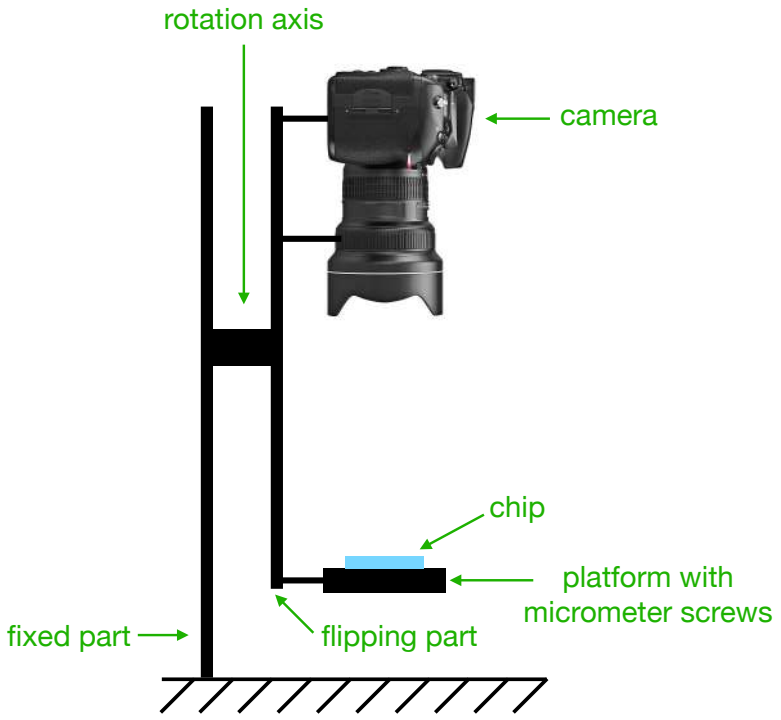

Figure 3.7: Diagram of the experimental setup used to flip the chip and visualize the droplet release under the Archimedes regime.

As a general note, hundreds of videos and photos were taken. Only the most beautiful and relevant ones have been included in this master thesis. It is evident that many other phenomena could have been observed. Additionally, each experiment represents a technical challenge. It is necessary to obtain the correct droplet size and avoid any errors in the pressure regime, as there is a risk of either completely flooding the chamber or being invaded by droplets of varying sizes. Depending on the scenario, the first droplets can be trapped without a simple means of untrapping, which leads to errors in patterns and analysis. Air also poses a significant problem in the experiments. For chips aiming to trap two different populations and merge them, all of these delicate steps accumulate. There is also the need to disconnect and reconnect tubes to the chip's inlets and outlets in order to change the droplet color to simulate ths two populations and inject the PFO for fusion. This causes sudden pressure variations and leads to untrapping. This list of manipulation concerns is by no means exhaustive. Any mistake made at any stage of the experiment results in a complete halt and the cleaning of the chip before being able to restart the manipulations. The amount of wasted oil during this year in the realization of this master thesis will remain a secret kept by the author.

Chapter 4

Droplet volume calculation

The problem of estimating the volume of a droplet confined in one dimension is not trivial. In this section, different approaches will be considered in order to estimate this volume with different degrees of accuracy. To begin with, it is relevant to adopt an empirical approach that abstracts from the physics and has the advantage of a simple implementation. Since this is an axisymmetric problem, it is simpler to focus on a cross-section of the droplet in two dimensions.

1 Empirical estimation

1.1 Cylindrical approximation

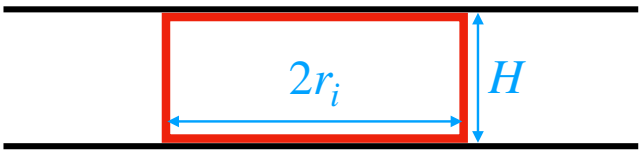

Figure 4.1: Schematic representation of a 2D cross-section of a droplet confined between two walls, approximated as a cylinder.

The simplest idea to implement is to approximate the flattened droplet to a cylinder (Fig. 4.1). Therefore, the edge of the droplet is completely omitted. All curvature at the edge is reduced to a simple straight section. The advantage of this approach is the formidable simplicity of the calculation of the surface area and the volume through:

$$A = 2\pi r_i(H + r_i), \qquad V = \pi r_i^2 H. \tag{4.1}$$

The disadvantage is that this approximation leads to a non-negligible error. Indeed, for example, an unconfined droplet will adopt a spherical shape. Its volume is given by $V_s = \frac{4}{3}\pi r_i^3$. A cylindrical approximation of this sphere is equivalent to keeping the radius of the sphere for the base of the cylinder and using $H = 2r_i$ for the height. Thus, the volume of the cylinder is given by $V_c = 2\pi r_i^3$. It is possible to calculate the relative error $\varepsilon = \left|\frac{V_c - V_s}{V_s}\right|$ which is 50% in this situation. The relative error on the volume is minimal when the radius of the squeezed droplet is large since only the edges will be poorly approximated. Conversely, at the transition between a free and confined droplet, the relative error increase. Unfortunately, this is an essential case study for this work and it is relevant to look for better models.

1.2 Cut Sphere approximation

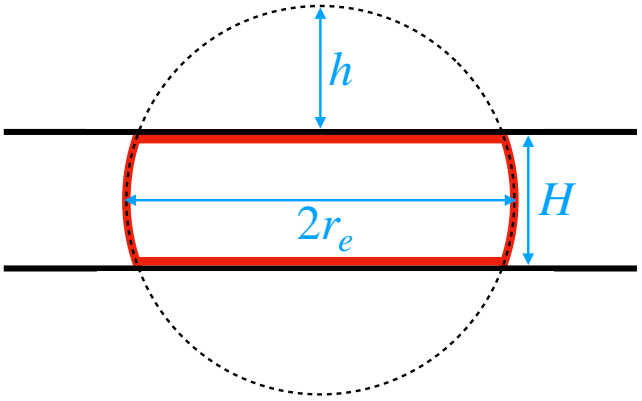

Figure 4.2: Schematic representation of a 2D cross-section of a droplet confined between two walls, approximated as a truncated sphere.

The next step is to try to take more account of the true shape of the droplet and add a curvature effect. The simplest technique is to use a sphere with the spherical caps removed symmetrically on either side, beyond the height of the chamber (Fig. 4.2). After some mathematical manipulation, it is possible to write the surface area and volume as:

$$A = 4\pi r_e^2 - 4\pi r_e h, \qquad V = \frac{4}{3}\pi r_e^3 - \frac{2\pi h^2}{3}(3r_e - h). \tag{4.2}$$

Here, the approximation is better due to the inclusion of the curvature, but the derivative is discontinuous at the connection between the cap and the inner part of the droplet. This model is rather poor and it is possible to do better quite easily.

1.3 Circular caps approximation

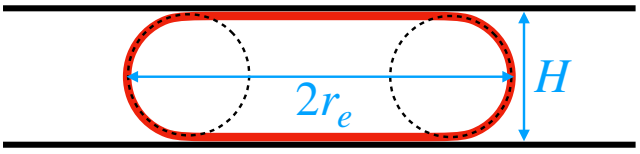

Figure 4.3: Schematic representation of a 2D cross-section of a droplet confined between two walls, approximated as a cylinder with a half-torus added around the perimeter.

The best technique for approximating the volume of a flattened droplet consists of taking an inner cylinder to which the outer part of a torus is grafted (Fig. 4.3). More specifically, due to the axisymmetry, the idea is to start from shape of the curve in two dimensions and use integration via rotational symmetry to obtain the surface area and the volume of the droplet. In two dimensions, the problem discussed above reduces to a simple rectangle for the inner part to which two half disks are attached on either side of the unconfined sides. Thus, the calculation of the surface area and the volume is performed using the formula for the solid of revolution for the circular caps around the y axis:

$$A = 2\pi \int_{-\frac{\pi}{2}}^{\frac{\pi}{2}} x(s)\sqrt{\frac{\mathrm{dx(s)}}{\mathrm{ds}} + \frac{\mathrm{dy(s)}}{\mathrm{ds}}}\,\mathrm{ds}, \qquad V = \int_{-\frac{\pi}{2}}^{\frac{\pi}{2}} \pi x(s)^2 \frac{\mathrm{dy(s)}}{\mathrm{ds}}\,\mathrm{ds}. \tag{4.3}$$

The use of integration around the y-axis to obtain the surface area and the volume of the solid of revolution was done with the help of a parametrization, which is given by:

$$\begin{cases} x(s) = r_i + \dfrac{H}{2}\cos(s), \\ y(s) = \dfrac{H}{2} + \dfrac{H}{2}\sin(s). \end{cases} \tag{4.4}$$

With r_i defined as the internal radius. This method has the advantage of being very simple to implement, corresponds well to the physics of the problem and suffers from reduced error. Although the only way to demonstrate this is through empirical results. A comparison between these different methods of approximating the volume of a flattened droplet can be found in [124]. It is important to note that all the approaches considered so far estimate the volume of the droplet by looking for a model that best fits the observed shape of the droplet. The question of why the droplet adopts this shape and what the true shape of the caps is is completely ignored.

2 Nodoids

2.1 Theoretical developments

In this part, the problem of volume estimation will, this time, be considered from a physical point of view. The idea is no longer simply to assemble various solids of known volumes in order to approximate the silhouette of the droplet but rather to start from Laplace's equation. Ideally, it would then be possible to compare this theoretical model with the empirical model considered earlier. In this way, the error could be highlighted. It would then be possible to justify or not the use of empirical models to estimate the volume of the droplet.

The most direct technique to obtain the Laplace equation in an axisymmetric model is the Lagrange multipliers. This is the most general formalism that could easily be extended to other geometries. Moreover, even if it is a complex problem which will not be studied in this work, the Lagrangian approach allows a stability study of the solution. This would not be possible with more classical approaches based only on geometry. The idea of the Lagrange multiplier is based on the variational principle which states that physics always seeks to minimize a certain quantity. In the particular case of droplets, the quantity to be minimized is nothing else than the contact surface between the two fluids for a droplet constant volume. Let us introduce the functional G:

$$G = \gamma A - \lambda V. \tag{4.5}$$

Here λ represents the Lagrange multiplier and has the units of a pressure. This one is the parameter to optimize in this problem. The theory developed by Hamilton shows that G must minimize the action integral to satisfy the true physics of the problem. This is equivalent to the solution given by the Euler-Lagrange equations 4.8.

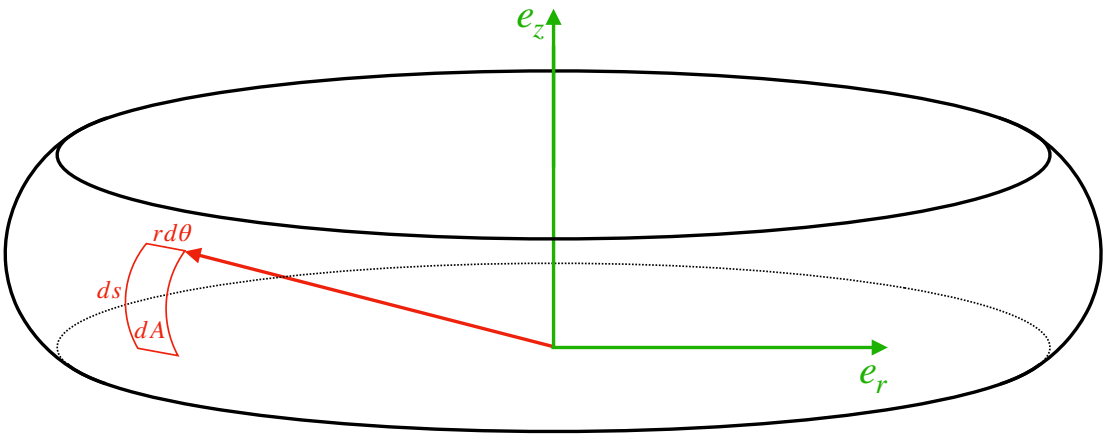

Figure 4.4: Schematic representation of a droplet confined between two walls, highlighting the coordinate system and parameterization for analytical calculation

To begin with, the expressions for the droplet surface and volume in cylindrical coordinates are given respectively by (Fig. 4.4):

$$A = 2\pi \int_{z_1}^{z_2} r\sqrt{\dot{r}^2 + 1}\,\mathrm{dz}, \qquad V = \pi \int_{z_1}^{z_2} r^2\,\mathrm{dz}. \tag{4.6}$$

By introducing these two expressions in the functional G, it comes that:

$$G = \gamma A - \lambda V = \int_{z_1}^{z_2} \left(\gamma 2\pi r\sqrt{1+\dot{r}^2} - \lambda\pi r^2\right)\,\mathrm{dz} = \int \mathcal{L}(\mathrm{r}, \dot{\mathrm{r}})\,\mathrm{dz}. \tag{4.7}$$

The integrant of this expression is therefore the Lagrangian and it must satisfy the Euler-Lagrange equations:

$$\frac{\mathrm{d}}{\mathrm{dz}}\left(\frac{\partial \mathcal{L}}{\partial \dot{r}}\right) + \frac{\partial \mathcal{L}}{\partial r} = 0. \tag{4.8}$$

By isolating λ, one finally find Laplace's equation in differential form in its axisymmetric version through Eq. 4.9. The parameter to be optimized λ is effectively the pressure difference across the interface:

$$\Delta p \equiv \lambda = \gamma\left(\frac{1}{r\sqrt{1+\dot{r}^2}} - \frac{\ddot{r}}{(1+\dot{r}^2)^{\frac{3}{2}}}\right). \tag{4.9}$$

This differential equation is nonlinear; therefore, a complete analytical solution seems unlikely. However, by introducing a change of variable $U = (1+\dot{r}^2)^{-\frac{1}{2}}$, it is possible to obtain a first integration [14]. The mean curvature is represented through the constant $\kappa = \frac{1}{2}\left(\frac{1}{\mathcal{R}_1} + \frac{1}{\mathcal{R}_2}\right)$, where $\mathcal{R}_1$ and $\mathcal{R}_2$ are the main radii of curvature. Next, by noticing that the derivative of a product appears, it is thus possible to integrate this equation a first time, that leads to:

$$-\frac{\ddot{r}}{(1+\dot{r}^2)^{\frac{3}{2}}} + \frac{1}{r\sqrt{1+\dot{r}^2}} = \frac{\Delta p}{\gamma} = \pm 2\kappa, \tag{4.10}$$

$$\iff C_1 = \frac{r}{\sqrt{1+\dot{r}^2}} \pm \kappa r^2, \tag{4.11}$$

$$\iff F = 2\pi\gamma C_1 = 2\pi\gamma r\sin\varphi \pm \Delta p\pi r^2. \tag{4.12}$$

where C_1 is an integration constant. For the last equivalence, the Eq. 4.11 has been multiplied by $2\pi\gamma$. Using Laplace's equation with the notion of mean curvature introduced earlier, it can be rewritten as $\Delta p = \pm 2\gamma\kappa$. It is possible to see that $(1+\dot{r}^2)^{-1}$ is nothing more than $\sin\varphi$. Multiplying the integration constant C_1 by $2\pi\gamma$ results in the total force acting on a slice of the drop. This first integral thus transcribes the fact that each slice of the drop is in hydrostatic equilibrium. This one can be seen as a succession of planar volumes of infinitesimal thickness stacked on each other. There must be equality in the internal stresses and in the surface stresses for the droplet as a whole to remain in hydrostatic equilibrium (Fig. 4.5).

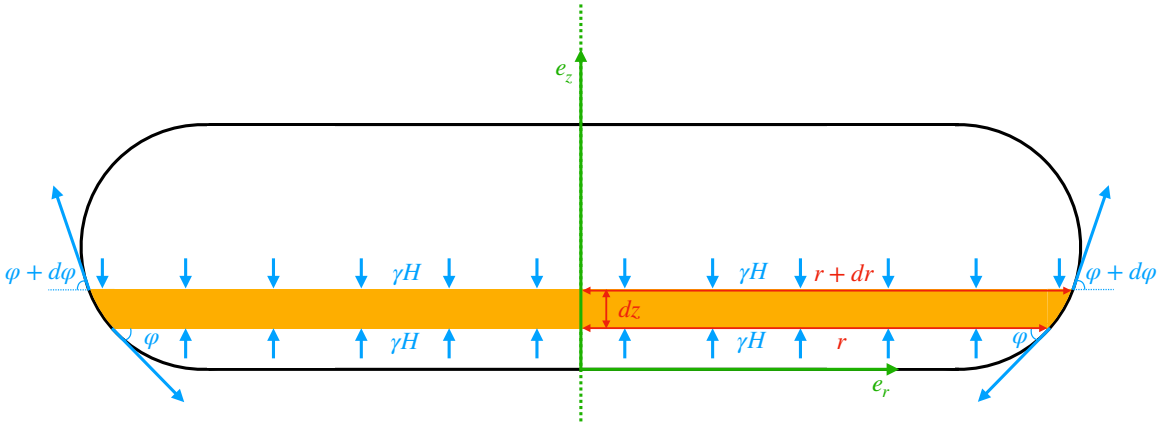

Figure 4.5: Schematic representation of pressure and surface tension equilibrium within a droplet squeezed between two walls in hydrostatic equilibrium. This 2D cross-section diagram illustrates the balance resulting from the first integral of the Laplace equation in an axisymmetric model.

Noether's theorem states that there is a connection between the symmetries of a physical system and the associated Lagrangian. This results in a conserved quantity. The obtained first integral relates to the conservation of momentum in the z-direction and corresponds to the independence of the Lagrangian with respect to the variable z. The time-independence of the Lagrangian corresponds to the conservation of energy.

Starting again from the Eq. 4.11, simply isolate the term $\dot{r}$ and then use the inverse derivative theorem so that the unknown function is now $z(r)$ through $\dot{z}$ [13]:

$$\frac{\mathrm{dz}}{\mathrm{dr}} = \frac{2C_1 - \kappa r^2}{\sqrt{4r^2 - (2C_1 - \kappa r^2)^2}}. \tag{4.13}$$

2.1.1 Delaunay surfaces

This section aims to be a brief digression on the mathematical foundation that governs the studied physics [125]. For this approach, the following change of variable will be adopted, $a = \frac{1}{\kappa}$ and $b^2 = \frac{2C_1}{\kappa}$ By reinjecting this in Eq. 4.13, it comes that:

$$\frac{\mathrm{dz}}{\mathrm{dr}} = \frac{b^2 \pm r^2}{\sqrt{4a^2r^2 - (b^2 \pm r^2)^2}}. \tag{4.14}$$

The purpose of this change is to emphasize a specific mathematical object known as "Delaunay surfaces." They are a type of surface of revolution. One of their particularity is to have a constant mean curvature κ. The type of curve will depend on the sign of κ, so it is considered positively,

negatively or equal to zero at this stage of development. The action of the rotation of the curve around an axis gives rise to Delaunay surfaces. These curves are obtained by applying the roulette to an ellipse, a parabola or a hyperbola. All these curves depend only on the eccentricity. Taking the example of an ellipse, the associated curve through the roulette, called an unduloid, is obtained by rolling it without slipping on the ground. In this mathematical universe, the ground is represented by the abscissa axis. By observing the trajectory followed by one of the foci in this situation, the resulting curve appears (Fig. 4.6).

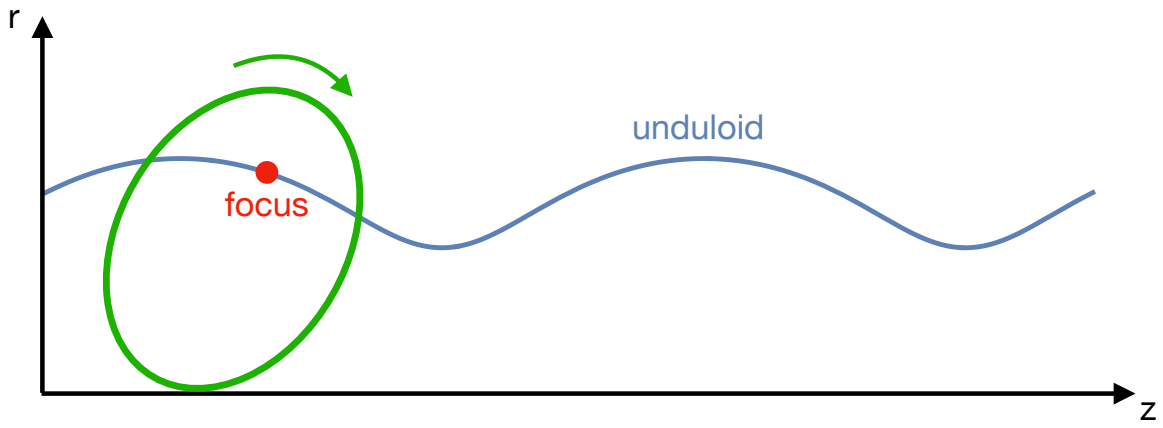

Figure 4.6: Illustration of the trajectory followed by one of the foci of an ellipse when it undergoes a rolling motion without slipping on the ground. The resulting curve is an unduloid.

This process can be repeated with a hyperbola and a parabola, although the analogy is not as immediate. The trajectory of a focus will yield respectively either a nodoid or a curve called a catenary, which appear in many problems in physics. Here, a and b represent the semi-major and minor axis of the different conics. The change in sign of the numerator in Eq. 4.14 allows defining the curve that undergoes the roulette, namely an ellipse, a hyperbola, or a parabola. To further push the analysis, it is needed to ensure that the argument under the square root is positive or zero to ensure that the result is real:

$$4a^2r^2 - (b^2 + r^2)^2 \geq 0, \tag{4.15}$$

$$-r^4 + (4a^2 - 2b^2)r^2 - b^4 \geq 0. \tag{4.16}$$

Equality occurs when:

$$r = \pm\left(a \pm \sqrt{a^2 - b^2}\right). \tag{4.17}$$

It is possible to introduce the parameter ϵ which represents the eccentricity of the conic. This one is a function of the principal half axes of the conic a and b. In the particular case of nodoids, the conic used is a hyperbola. Thus, ϵ can be expressed as:

$$\epsilon = \sqrt{1 - \frac{b^2}{a^2}}. \tag{4.18}$$

As a final step, only roots containing a positive semi-major axis are retained. Thus, only two roots are relevant in the problem and are named root_1 and root_2 for simplicity. It is also possible to re-express these two roots in terms of eccentricity only, which is shown by:

$$\begin{cases} \text{root}_1 & \equiv a(1-\epsilon) = a - \sqrt{a^2 - b^2}, \\ \text{root}_2 & \equiv a(1+\epsilon) = a + \sqrt{a^2 - b^2}. \end{cases} \tag{4.19}$$

The objective of this calculation was to define the conditions for the existence of the desired solution. Thus, $r \in [\text{root}_1, \text{root}_2]$ to obtain a real solution.

2.1.2 Limit case

Starting from Eq. 4.13, it is possible to highlight specific cases of Delaunay curves. It is simpler to reason in terms of physics rather than adopting a mathematical viewpoint for this section. Under these conditions, it is relevant to re-express the eccentricity of Eq. 4.18 in terms of a physical variable:

$$\epsilon = \sqrt{1 - 2\kappa C_1}. \tag{4.20}$$

Special cases occur when the eccentricity is equal to one. This happens in two situations. Either the mean curvature κ is equal to zero, or the integration constant C_1 representing the resultant force applied to the edges is equal to zero. In the first situation, Eq. 4.13 becomes:

$$\frac{\mathrm{dz}}{\mathrm{dr}} = \frac{2C_1}{\sqrt{4r^2 - 4C_1^2}} \Longleftrightarrow z(r) = \frac{1}{C_1} \operatorname{arcCosh}\left(\frac{r}{C_1}\right) + C_2 \tag{4.21}$$

Where C_1 and C_2 are arbitrary constant. As shown, this expression is analytically solvable. The result is a hyperbolic cosine characteristic of a catenary, which appears in many constrained optimization problems.

The second case to consider is when the integration constant C_1 is equal to zero. In this situation, Eq. 4.13 is rewritten as:

$$\frac{\mathrm{dz}}{\mathrm{dr}} = \frac{-\kappa r}{\sqrt{4 - \kappa^2 r^2}} \Longleftrightarrow z(r) = \frac{\sqrt{4 - \kappa^2 r^2}}{\kappa} + C_2 \tag{4.22}$$

Where $C_1 = 0$ and C_2 are arbitrary constant. In this scenario, once again, there is an analytical solution. The final result happens to be well-known as it represents the equation of a circle.

In the final analysis, it has been shown that the specific case where $\kappa = 0$ corresponds to a catenary. Regarding the other solutions of Eq. 4.13, when $\kappa > 0$, it results in a nodoid. Conversely, when $\kappa < 0$, the studied curve corresponds to an undoloid. In this master thesis, only nodoids will be analyzed in detail. Indeed, in the case of a droplet flattened in an axisymmetric model, the Laplace equation will always have a positive mean curvature κ.

2.1.3 Change of variable

The rest of the reasoning will consist in the parametrization of the differential equation through the s variable which represents the curvilinear coordinate of the curve. Then, by integration, the original differential equation will be transformed into an integral equation. Thus, the variables r and z coupled in the differential equation will become linked by becoming both functions of s. This can be achieved through the introduction of elliptic integrals. However, in the specific case of nodoids, a more elegant formulation has been found [100, 126] and developed in [125]. The first step in this process is to pose a change of variable for $r(s)$. Its explanation is not obvious and it is justified by the fact that it works. Here is the application of the above transformation:

$$r(s) = a\sqrt{1 + \epsilon^2 + 2\epsilon \sin s}. \tag{4.23}$$

where the variables a and ϵ are the same as those introduced earlier.

To obtain the component $z(s)$, it is sufficient to transform Eq. 4.13 in such a way as to obtain $\frac{\mathrm{dz}}{\mathrm{dr}} = \frac{\mathrm{dz}}{\mathrm{ds}}\frac{\mathrm{ds}}{\mathrm{dr}}$ and integrate this result. The final parametric curve describing the height of a nodoids is then given by:

$$z(s) = a\int_0^s \frac{(1+\epsilon\sin\tilde{s})}{\sqrt{1+\epsilon^2+2\epsilon\sin\tilde{s}}}\,\mathrm{d}\tilde{s}. \tag{4.24}$$

It should be noted, that there is obviously no analytical solution to this result, only the form has changed compared to the Eq. 4.13. However, the usefulness besides the elegance of this expression compared to the previous ones is its ease of numerical implementation. The rest of the project will be done on the notebook `Mathematica` in order to obtain the function describing the true shape of the droplets via a numerical integration.

2.2 Boundary conditions

In the previous section, the equation for the radius and height of a droplet confined between two walls was demonstrated. This approach led to the introduction of the nodoids whose solution involves the resolution of an elliptic integral provided by Eq. 4.24. This section aims to solve these equations numerically, it is therefore necessary to find the boundary conditions that will allow to find the nodoid corresponding to the droplet confined in a channel of a given height. To determine the first integration constant, it is necessary to start again from the differential equation given by Eq. 4.13. The droplet confined in a channel has a continuous derivative at the junction of the nodoid and the walls. Thus, this condition can be translated by the fact that $\frac{\mathrm{dz}}{\mathrm{dr}} = 0$ when $z = 0$ and $z = H$. By the inverse derivative theorem, this amounts to the condition $\frac{\mathrm{dr}}{\mathrm{dz}} = \dot{r} = \infty$ which can be injected into Eq. 4.11. This will allow to link three parameters, the force through C_1, the mean curvature through κ and the internal radius of the nodoid through r_i. The latter corresponds to the radius of the nodoid at the top and bottom of the channel where the droplet is located. Finally, the boundary condition can be written:

$$C_1 = \frac{-\kappa r_i^2}{2}. \tag{4.25}$$

This implies that the combination of two parameters, κ and r_i, determines the integration constant C_1. These two parameters are expressed as a and ϵ in the final formulation presented in Eq. 4.24 and 4.23. At this step, there is one degree of freedom left, which is the pressure inside the droplet. This pressure is related to the mean curvature through the Laplace equation. In theory, it should be necessary to look for the mean curvature κ which generates the nodoid whose height corresponds to the size of the chamber. However, thanks to this extra degree of freedom, a trick can be used to avoid this search for the corresponding curvature of the problem. In a first step, it is allowed to fix this parameter κ. Let's now look at when $\frac{\mathrm{dz}}{\mathrm{dr}}$ cancels. This condition can be re-expressed through a parametric formulation:

$$\frac{\mathrm{dz}}{\mathrm{dr}} = \frac{\frac{\mathrm{dz}}{\mathrm{ds}}}{\frac{\mathrm{dr}}{\mathrm{ds}}}. \tag{4.26}$$

Since $\frac{\mathrm{dr}}{\mathrm{ds}} \neq 0$ in $z = 0$ and $z = H$, it is sufficient to start from the parametric formulation given by Eq. 4.24 and to evaluate $\frac{\mathrm{dz}}{\mathrm{ds}} = 0$. In practice, $z(s)$ is an increasing function in which the derivative cancels periodically. Consequently, it is possible to keep only two successive

cancellations of the derivative to obtain a single nodoid. This nodoid does not a priori satisfy the imposed boundary conditions since the mean curvature which represents the second parameter is fixed at an arbitrary value at this stage. To avoid having to search for the right curvature that satisfies the height of the chamber, the idea is to use a scaling of the nodoid found by multiplying $r(s)$ and $z(s)$ by the right constant so that it fits the height of the chamber. This condition can be expressed as $z(s_2)-z(s_1) = H$, where s_2 and s_1 have been determined using the derivative cancellation method explained above. This modifies the mean curvature κ imposed at the beginning. However, it will also change the radius of the droplet and therefore the radius of the nodoid. This does not matter since the modification of κ leads to the modification of r_i. When re-scaling, a droplet size is imposed since these two parameters are linked and must satisfy Eq. 4.25. Therefore, by fixing C_1 and κ initially, the internal radius of the nodoid r_i is also determined thanks to Eq. 4.25 multiplied by the scaling factor α:

$$r_i = \sqrt{-\frac{2C_1}{\kappa}}\alpha. \tag{4.27}$$

By modifying the mean curvature to satisfy the problem studied through the first boundary condition, κ and α are now fixed. Therefore, there remains only one degree of freedom. There exists a unique proportionality relation between C_1 and r_i. Fixing one will determine the value of the other parameter uniquely. The underlying significance of this condition is the conservation of volume. Indeed, for a given radius, it is possible to calculate the volume of the corresponding nodoid. In practice, it was not necessary to find the value of C_1 for a specific nodoid. During the experiments, the volume varies between the studied droplets. The trick is simply to vary the value of C_1 and find the proportionality relation with the volume. Then, by reversing the relation, it is possible to retrieve the value of C_1 corresponding to the studied volume. The illustration of the shape of the droplet by solving the Laplace's equation is provided in Fig. 4.7.

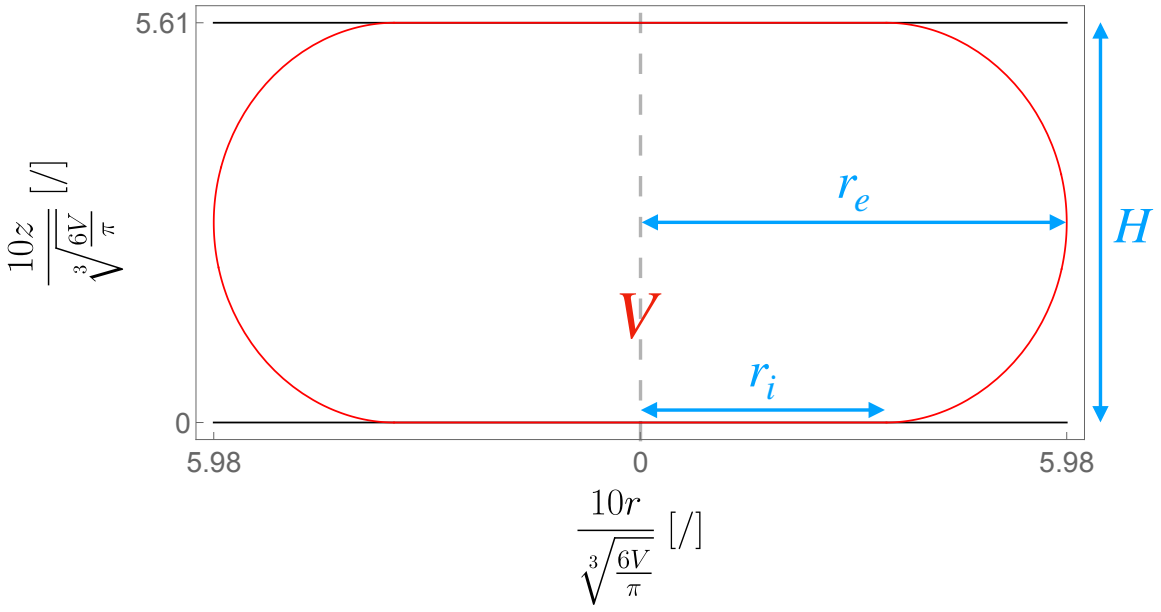

Figure 4.7: Simulation of the Laplace equation to obtain the true shape of the droplet. Chamber height: $H = 30$ [μm], droplet volume: $V = 80.27$ [pL].

2.3 Comparison between nodoids and circular caps

The theoretical resolution of the Laplace equation allowed highlighting the true shape of the droplet. Previously, in the section 1, the shape of the droplet could be approximated in various ways. The most advanced model was that of circular caps. In this part, an order of magnitude can be established with respect to the exact solution which constitutes that of nodoids. This will allow the calculation of the error and evaluate the quality of the approximation. Starting from the limiting case of a free droplet whose volume gradually increases, the solution starts from a particular case of nodoid whose eccentricity is zero. This corresponds to the sphere as discussed in section 2.1.2. As the droplet grows, it is possible to evaluate the relative error between the volume of the nodoid whose curvature changes with the volume and the circular caps which maintain their curvature (Fig. 4.8).

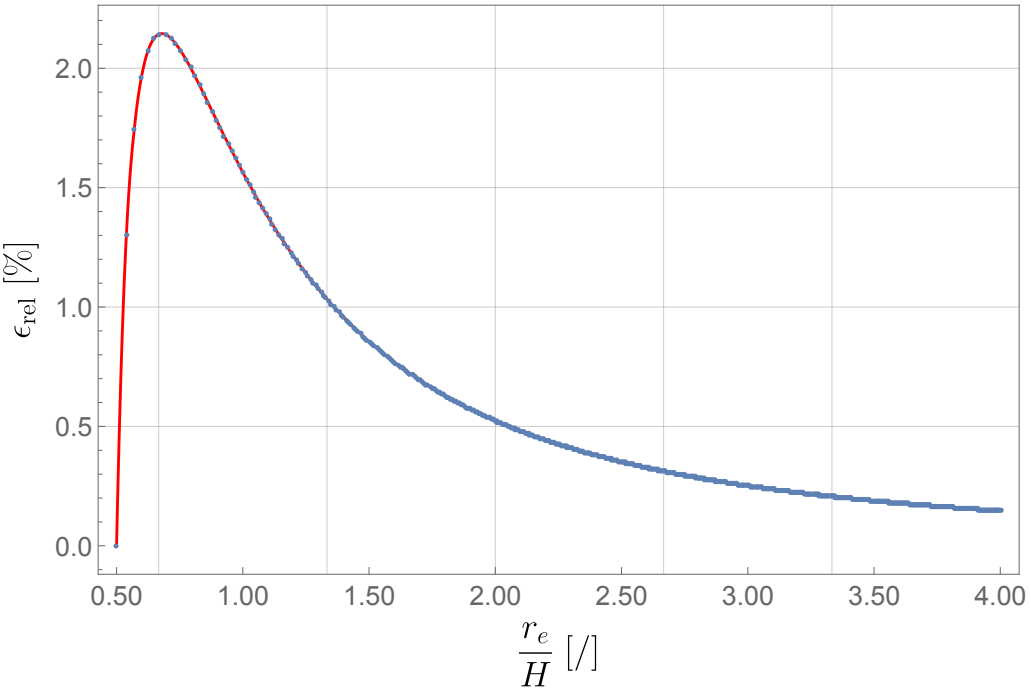

Figure 4.8: Relative volume error between the Laplace equation solution and the circular caps approximation. Chamber height: $H = 30$ [μm].

To carry out this study, it was assumed that the measured radius was the maximum one located at the center of the droplet (Fig. 4.8). This implies that there is a correspondence between the external radii r_e, but the internal radii r_i are different because the contact point of the circular caps and nodoids with the walls of the chamber varies. This point of view implies that the measured radius in the experiments is indeed r_e. In the Fig. 4.9, it is possible to observe the exact solution of the nodoid in orange. In green, it is possible to see the approximation using circular caps for the scenario where the external radius r_e matches that of the nodoid. Consequently, $r_{i,n}$ and $r_{i,c}$ correspond to the internal radius of the nodoid and the circular caps, respectively.

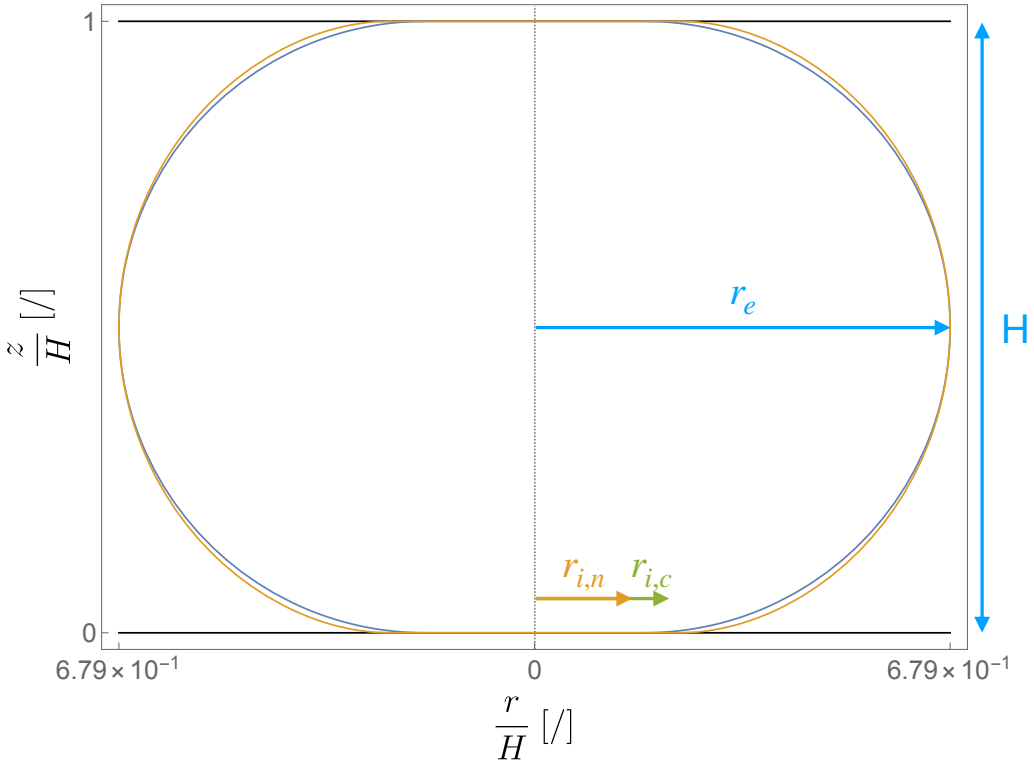

Figure 4.9: Result of the Laplace equation simulation for the true shape of the droplet and the approximation using circular caps at the radius where the error is maximal. The radius is $r_e = 20.4$ [μm] and the chamber height is $H = 30$ [μm].

In practice, this condition of measuring r_e will be more or less verified depending on the focus of the camera. Under these conditions, Fig. 4.8 shows that the error made on the volume is the most important shortly after the transition between the state of sphere and the flattening of the droplet. This is also the moment when the physics is the most interesting and when the developed model makes the most sense. Indeed, the larger the radius, the less the volume contained in the caps will be comparable to the volume contained inside the droplet. For large droplets, the shape of the edge will play only a negligible role. It is therefore normal to observe that the relative error tends towards zero as the radius of the droplet increases. On the other hand, for droplets whose radius is of the order of magnitude of the height of the chamber, the difference in volume is more significant. The majority of the droplets studied in this study fall into this category. It should be noted in Fig. 4.8 that the maximum error occurs for $\frac{r_e}{H} = 0.68$ and reaches a value of $\varepsilon = 2.1\%$. Thus, the error can be considered low and validates the good approximation of the droplet by circular caps.

It is possible to quickly consider the worst-case scenario where the measured radius is the internal radius r_i. In this case, the external radius r_e of the nodoid and circular caps no longer correspond. The maximum error reached in this case occurs for a radius of $\frac{r_i}{H} = 0.14$ [μm] and the relative error reached is $\varepsilon = 20.2\%$. In this case, it is much more difficult to conclude that it is a good approximation. This analysis allows for a slight nuance of the previous conclusion dealing only with the perfect case. Experimentally, the latter is the one that is closest, however, a slight error on the focus can lead to a focus on an intermediate radius between the maximum and minimum radius. Under these conditions, the error is much higher than that considered in the first case.

It is interesting to note that the exact solution to the problem via nodoids was obtained by minimizing the surface at a given volume. Thus, the curvature evolves so as to always satisfy this physical condition. The approximation by circular caps does not take this physical property into account at all. Therefore, the radius for which the relative error between the surface of the nodoid and that of the circular cap is maximal does not coincide with the radius for which the relative error between the volumes themselves is maximal. For the surface, the maximal error occurs at $\frac{r_e}{H} = 0.7$ [μm] and has a value of $\varepsilon = 1.47$ [%]

In conclusion, this study demonstrates that approximating a droplet using circular caps is effective, particularly for large droplets. However, in the remainder of this master's thesis, the droplet volume will be evaluated using the nodoid solution, as the tool has been developed and aligns with the exact theoretical solution.

3 Droplet generation

It is important to focus on droplet generation, as this formation technique will remain constant for all trapping approaches adopted. This section aims to simply demonstrate the functioning of the flow focusing junction [24, 28], as explained in section 4.1 to show how the droplets are created (Fig. 4.10).

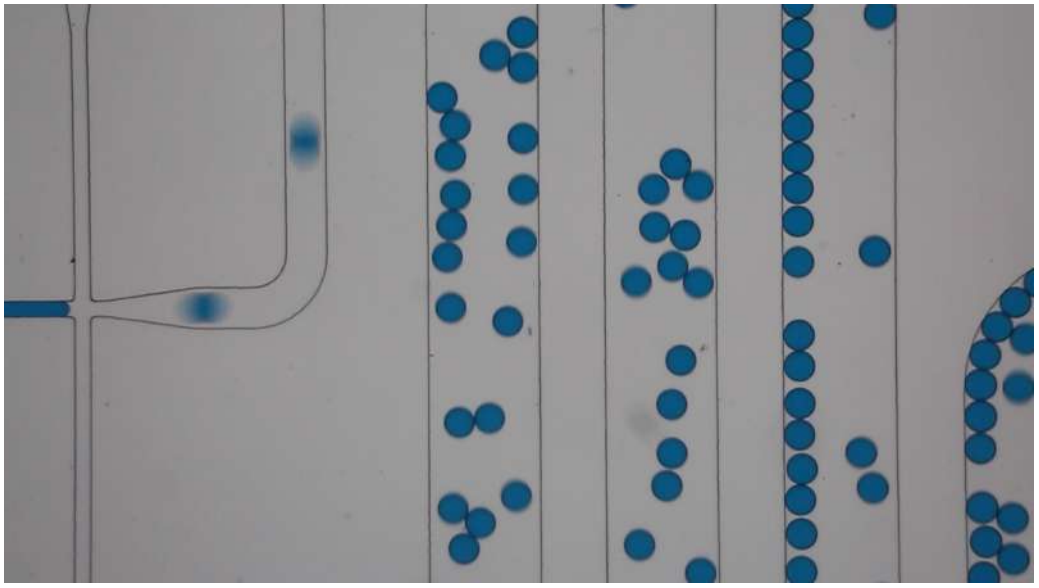

Figure 4.10: Operational chip view. The image highlights the cross-junction, responsible for droplet generation. The accompanying channels disperse and guide the droplets towards the chamber. The chip height is set at $H = 30$ [μm]

This kind of video is especially valuable for image analysis to determine the droplet radius and consequently the droplet volume, which is crucial for result analysis. Fig. 4.11 showcases an implementation of the Python code developed for examining the droplet radius. The volume of the droplets can then be determined through the development using the nodoid model presented in Section 2.

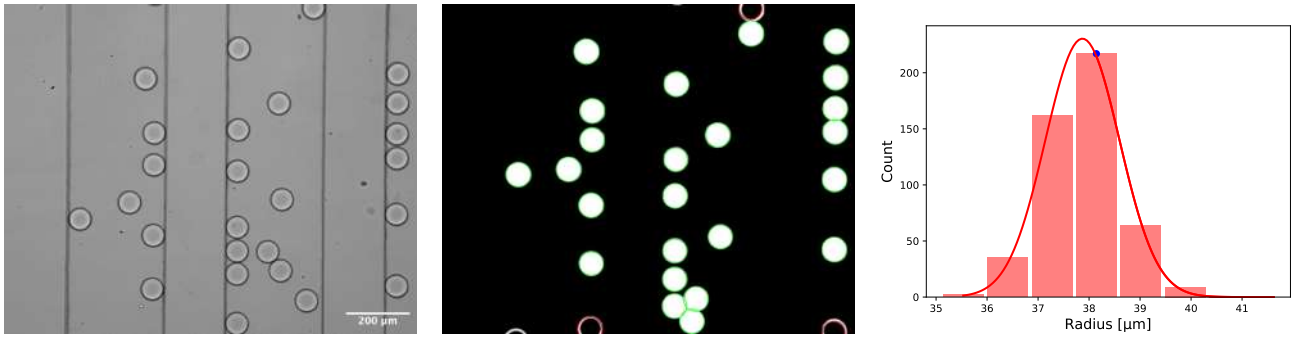

(a) (b) (c)

Figure 4.11: Image analysis of droplets. (a) Original image extracted from a video, showcasing the droplets moving within the channels immediately after generation. (b) Result of image processing, displaying the detected circles marked in green (validated) and red (rejected). (c) Histogram of the radii of the validated circles detected throughout the video, along with a Gaussian fit. The mean radius is determined to be 37.87 [μm], with a standard deviation of 0.73 [μm]. This leads to a mean droplet volume of 115 [pL]. The volume of the droplet for each end of the standard deviation is estimated at 111 [pL] and 120 [pL]. For this experiment $H = 30$ [μm]

Fig. 4.11a is obtained from a video. As a result, it was possible to evaluate the temporal median image and subtract it. This allowed for the removal of the background and highlighted only the moving objects, i.e., the droplets. The condition for a successful temporal median image subtraction relies on the value of a pixel. It should display the background value for more than half of the time. This implies that the number of droplets must be sufficiently limited for the condition to be met. The other parameters of the detection may vary from one video to another. However, a constant is the use of a Gaussian kernel to slightly blur the image and enable circle detection using the Hough transform algorithm [127]. In the current case, a dilation followed by an erosion was performed to close the majority of circles in the image. The next trick involved filling these circles. To consider a droplet as valid, it is sufficient to test the percentage of white pixels it contains against a sufficiently high threshold. Circles that do not meet this condition are marked in red and rejected. The distribution of detected radii can be observed in Fig. 4.11c.

It should be noted that the Hough transform can quickly reach its limits for circle detection, especially in the chamber that contains numerous droplets and wells. It is not easy to distinguish between the two, especially when the droplets are deformed. Other approaches would likely be more effective, but this was the first attempt at automation using a Python code. In the best cases, this approach allows us to avoid manual analysis in `ImageJ` [128] and obtain a much larger sample size by considering almost all the droplets in a video to determine their radius.

Chapter 5

Key parameters

The objective of this chapter is to present the key parameters that enable the study of various chip models introduced in Chapter 3. To initiate the exploration of different trapping designs, a synthesis of these key parameters for capturing droplets inside the chips is presented in Fig. 5.1. This diagram illustrates a single trapping technique for clarity, but variations in these key parameters will result in different forms of capture.

Figure 5.1: Illustrative schematic highlighting key parameters for the various trapping techniques. The parameters are: chamber height H, well diameter D, well depth W, droplet volume V, inter-well distance i. The presented example only serves to demonstrate the application of these parameters.

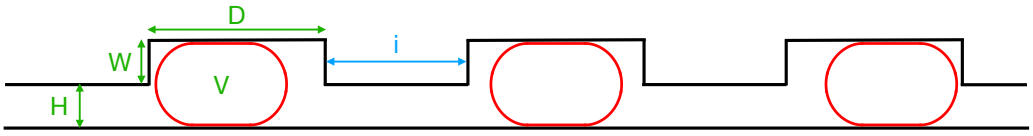

There are four variables of interest shown in Fig. 5.1. They are named H, W, D, V, corresponding to the chamber height, well depth, well diameter, and droplet volume, respectively. For the first chip design described in section 3.1 based on the Labanieh paper[109], a fifth parameter is involved through the distance between the wells, denoted as i for inter-well distance. This distance is comparable to the other characteristic dimensions, making the wells dependent on each other. The second design developed in section 3.2 aimed to eliminate this additional parameter. By considering only the first four parameters, the number of possible combinations is 24. By considering only the parameters related to the chip design, W, H, and D, the number of combinations decreases to 6. Thus, the number of chip configurations is limited enough to consider each of them individually. The droplet volume is the variable with the most flexibility, as it can be modified as desired during the chip testing phase.

To visualize the 6 possible chip design options more effectively, Fig. 5.2 presents a summary of the different possible geometries:

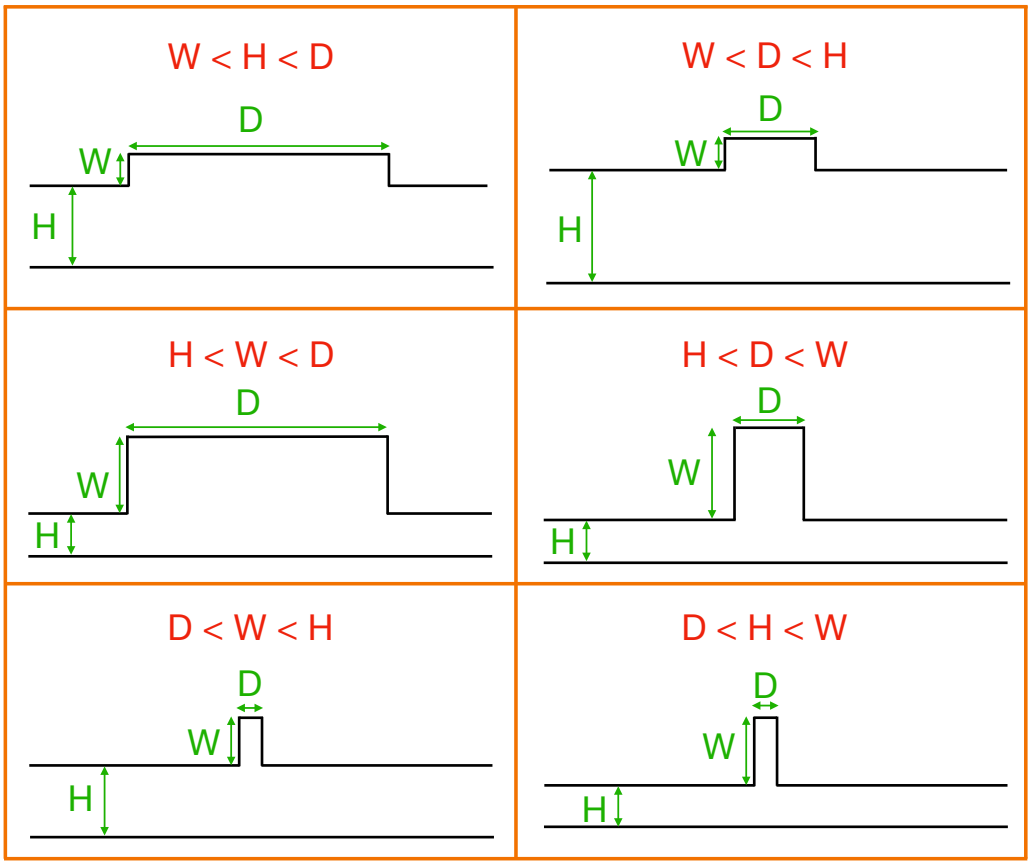

Figure 5.2: Summary of the six possible combinations of parameters H, D, and W. Exploring these possibilities enables the study of various trapping techniques using circular wells for a specific droplet volume.

All possible values for these parameters are summarized in Tab. 5.1.

	H	**D**	**W**	**i**
possible values [μm]	30, 120	30, 40, 50, 60, 80, 100, 120 [30, 166] incrementing by 0.2	30, 80	50, 400

Table 5.1. Illustration of the possible values of the main variables of interest, H, D, W, i, encountered in this master thesis.

The values of parameters affecting the thickness, H and W, are very difficult to modify as they depend on the microfabrication and the height of SU-8 that is applied over the entire wafer. Not all recipes are known to achieve a specific height. However, the combination of all available parameters allows for obtaining at least equality if not strict inequality. With this approximation, all the regimes could be tested.

Since the chamber is connected to the different channels for droplet production and guidance, any change in the chamber height, H, during microfabrication can lead to a drastic change in the generated droplets, especially their sizes. To address this issue, a workaround was implemented. The microfabrication process initially achieved a chamber height of $H = 30$ [μm], which is the most well-controlled recipe and also results in reasonably small droplet sizes. Then, to modify only the chamber height, pieces of adhesive tape were used. These rectangular-shaped pieces, matching the size of the chamber, were overlaid and bonded to it on the silicon wafer containing the SU-8 structures. This piece of adhesive tape has thus become an integral part of the silicon wafer, enabling the fabrication of PDMS chips. The main advantage of the chamber is that it is sufficiently wide to allow cutting a piece of adhesive paper by hand to its dimensions, in order to cover it and allow a modification of its depth. After this operation, the chamber height reached approximately $H \approx 120$ [μm]. To clarify a point, there is a technique in microfabrication processes called multilayering. This technique allows for the creation of structures at different levels and theoretically could have been used to increase the chamber height without modifying the channel heights. However, it is a more complex process that naturally increases the risk of errors during the microfabrication step. Additionally, it would have been too ambitious to undertake such a procedure in a master's thesis.

The width of the wells, denoted as D, is the most straightforward geometric parameter to modify. This dimension is defined in the horizontal direction rather than the vertical direction, as was the case for H and W. Under these conditions, it is simply necessary to modify the width of the wells using the design defined in `AutoCAD`. In the initial design described in section 3.1, the entire chip consisted of an array of wells of the same size. The size variation only occurred from one chip to another. In this configuration, the well diameters took on the following discrete values: $D = (30, 40, 50, 60, 80, 100, 120)$ [μm]. Subsequently, in order to explore all possibilities and visualize the changes in droplets behavior in a more gradual manner, the well arrays within each chip were modified to incorporate a double well gradient, each extending in a different plane direction. The different well sizes range from (30 to 165) [μm] with an increment of 0.2 [μm] from one well to the next. This increment is smaller than the typical microfabrication error, which is on the order of 2 [μm]. However, over the hundreds of generated wells, the increment gradually changes the well diameter. The minimum value of D at 30 [μm] actually represents the limits of microfabrication. For a defined height of SU8, the structures can at best have a width equal to this height as explained in section 2.3. The objective of this design was to approach a continuum of well sizes as closely as possible in order to observe the change in trapping regime.

To differentiate all these scenarios, the study will focus on the parameters W and H, which can only take a limited number of discrete values. The well diameter D and droplet volume V will be specified based on the experiments. Lastly, the distance between the wells in the first chip design is set at $i = 50$ [μm]. Subsequently, it is increased to $i = 400$ [μm] for the second chip design.

1 Bond number

An important dimensionless number for this study on droplet trapping in a microfluidic chip is the Bond number. In the wells, droplets are often at rest in a state of hydrostatic equilibrium.

In future analyses, it is often assumed that surface tension dominates over gravitational forces. To verify this, the Bond number can be calculated to compare the significance of these two quantities. It is defined as follows:

$$\mathrm{Bo} = \frac{\Delta\rho g l^2}{\gamma} = 1.2 \times 10^{-2}. \tag{5.1}$$

In this situation, $\Delta\rho = 610$ [kg/m^3] according to the datasheet presenting the density of the `Emulseo` oil. The characteristic length of a droplet can be approximated as $d_e = 200$ [μm] as a high value of the diameter. As a result, $\mathtt{Bo} << 1$, which implies the dominance of surface tension in the various conducted experiments and allows to neglect droplet deformation due to gravitational forces. In the case of trapping by Archimedes buoyancy, it is therefore reasonable to assume that the droplets retain a spherical shape.

Part III

Results

Chapter 6

Circular wells

1 Shallow chamber

To begin exploring all trapping regimes, the height of the chamber is set to its initial value of $H = 30$ [μm].

1.1 Shallow wells

In the following section, the well depth is set to a value of $W = 30$ [μm].

1.1.1 Interwell distance of 50 µm

To begin this analysis, the interwell distance is set to $i = 50$ [μm]. The well diameter is an element of the following list D =[30, 40, 50, 60, 80, 100, 120]. The different observed scenarios will be analyzed separately.

1.1.1.1 Capillary trapping A schematic cross-section of droplets in a capillary trapping regime (Fig. 6.1).

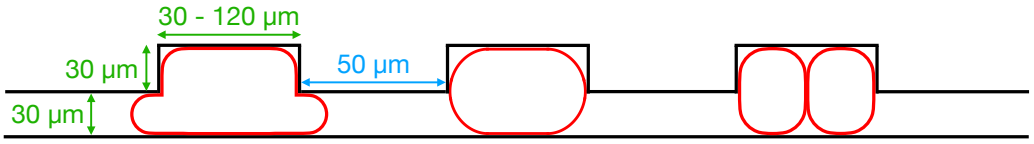

Figure 6.1: Schematic depicting the different possibilities of droplet trapping in chips with the following characteristics: $H = 30$ [μm], $W = 30$ [μm], $D = (30, 40, 50, 60, 80, 100, 120)$ [μm], and $i = 50$ [μm]

The droplet shape is a nodoid (section 2) as long as it entirely remains confined in the well. Droplets of volume larger than a critical value would invade the underlying chamber (Fig. 6.1-left). Their shape is still axisymmetric, and it can be approximated by a piecewise-continuous function corresponding to portions tangent to the walls of the well, connected to portions of nodoid. These nodoids can still be obtained by solving the axisymmetric Laplace equation.

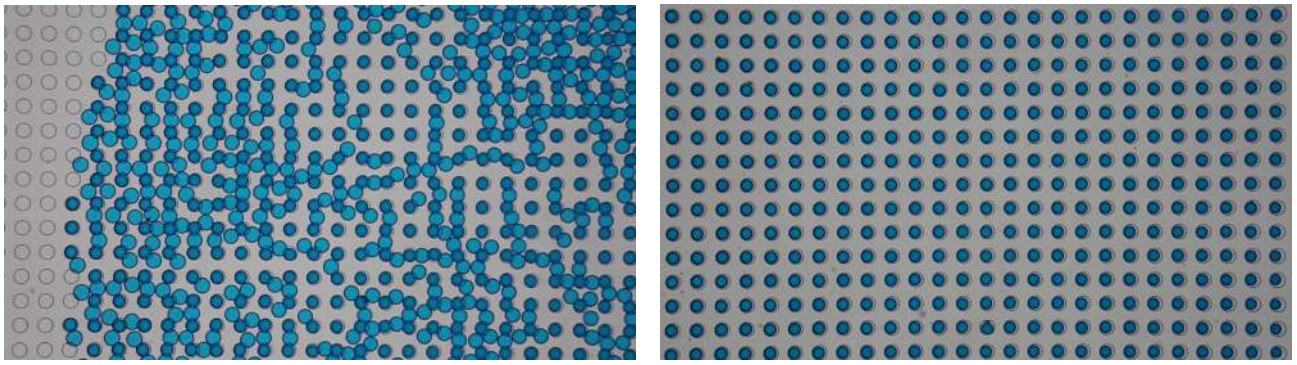

(a) (b)

Figure 6.2: Experimental snapshot showcasing capillary trapping in a chip with the following characteristics: $H = 30$ [μm], $W = 30$ [μm], $D = 60$ [μm], $i = 50$ [μm], and $V \approx 115$ [pL]. (a) Image captured during the filling of the wells. (b) Illustration of capillary trapping after the excess droplets have been evacuated.

In Fig. 6.2, droplets are generated in such a way that their volume allows them to occupy almost the entire available space once inside the well. Thus, it is not possible for a second droplet to fit in. The result is the trapping of a single droplet per well. Since the droplet is flattened both in the chamber and in the well, it is very challenging to release all the captured droplets afterwards. However, since the total height inside the well is twice the height of the chamber, it is energetically favorable for a droplet to confine itself within a well. To release it, one would have to be able to flatten the droplet again to remove it from the well and carry it into the chamber. This would require a significant oil flow. However, as the chamber acts as a very wide channel, the main flow follows the path with the lowest resistance, which goes through the space between the wells since the trapped droplets limit the flow. Thus, while trapping appears to be very regular, uniform, and efficient, the release of droplets becomes a challenging task in this scenario.

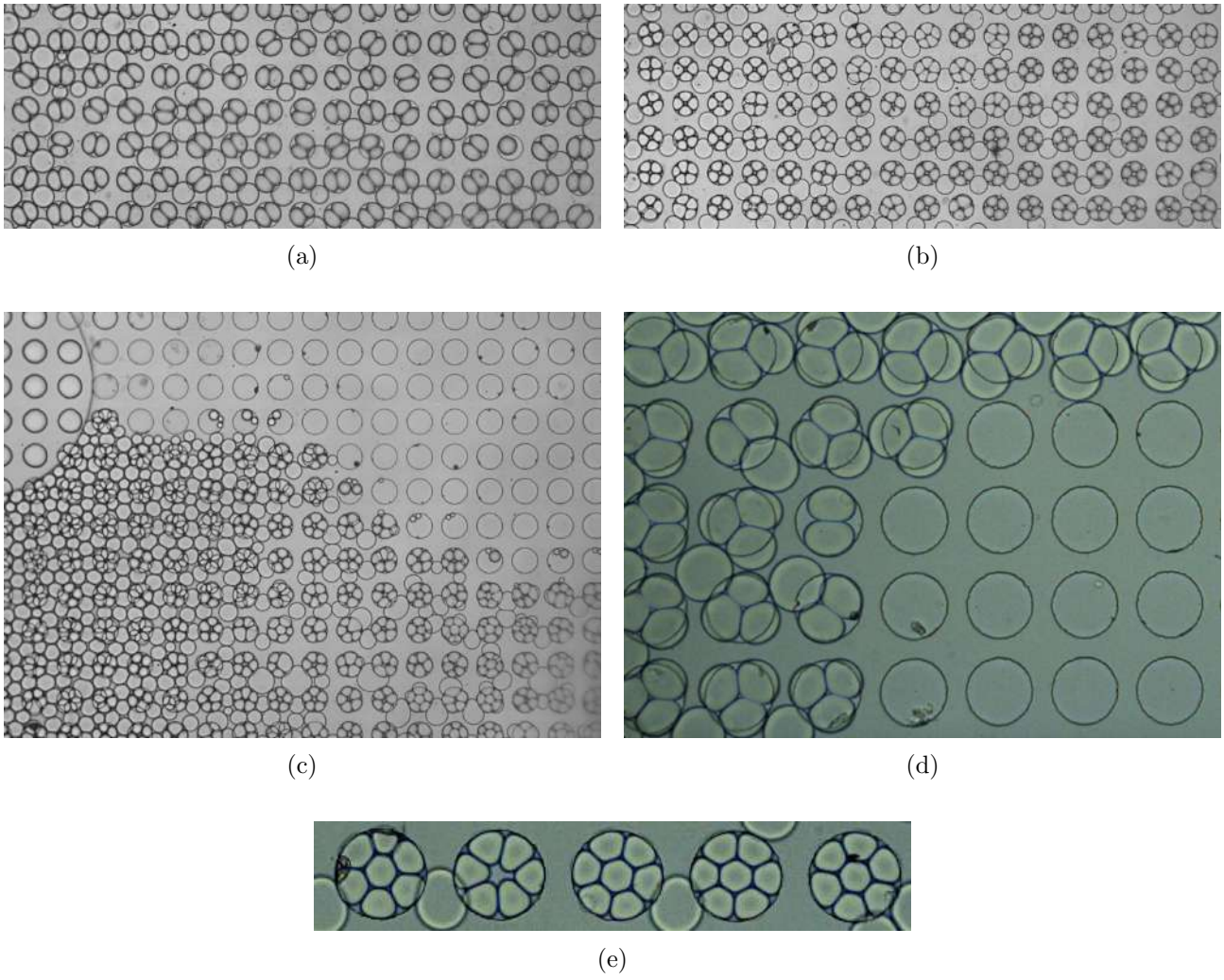

(a) (b) (c) (d) (e)

Figure 6.3: Experimental photographs showcasing droplet trapping by capillarity in a chip with the following characteristics: $H = 30$ [μm], $W = 30$ [μm], $i = 50$ [μm]. (a) Capture of two droplets per well with $D = 100$ [μm] and $V \approx 200$ [pL]. (b) Capture of four droplets per well with $D = 100$ [μm] and $V \approx 80$ [pL]. (c) Capture of five to six droplets per well with $D = 100$ [μm] and $V \approx 65$ [pL]. (d) Capture of three droplets per well with $D = 120$ [μm] and $V \approx 225$ [pL]. (e) Capture of seven droplets per well with $D = 120$ [μm] and $V \approx 80$ [pL].

In all Fig. 6.3, the number of droplets per well varies depending on the size of the droplets and the size of the wells. Since there is only one well size per chip, and the number of chips is limited to seven, the number of possibilities is relatively restricted. The adjustment of droplet size is also limited by the width of the junction. Moreover, not all generation regimes are possible in the present case. High input pressures cannot be used as it could result in excessive flow in the chamber leading to untrapping. It is also necessary to avoid regions of inhomogeneity with large velocity gradients. Trapping should be reproducible and uniform with identical conditions to achieve a similar pattern for all wells on the chip. Thus, by manipulating both the droplet size and well size, it is possible to trap from one to seven droplets per well.

1.1.1.2 Anchor trapping This experiment focuses on the chip with the smallest achievable well diameter, set at $D = 30$ [μm]. The height of the chamber, as well as the depth of the wells, are also fixed at $D = W = 30$ [μm]. The chip consists of an array of identical wells spaced 50 [μm] apart. Although the initial idea was to replicate Labanieh's[109] results with 30 [μm]

diameter droplets, it was not possible to create a junction as small as that in the article, thus limiting the minimum droplet size that can be produced. In this context, the obtained droplets are significantly larger than the size of the well. Trapping occurs through capillarity, with the well acting as an anchor. The droplet deforms and its upper part adopts a spherical cap shape. Thus, the total surface area of the droplet decreases. Therefore, it is favorable for the droplet to be confined within the anchor. A cross-section of the situation can be seen in Fig. 6.4.

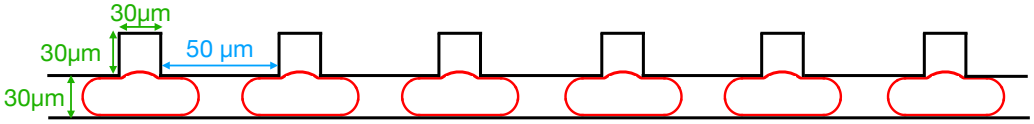

Figure 6.4: Schematic cross-section depicting droplet trapping using an anchor. The applied parameters are $H = 30$ [μm], $D = 30$ [μm], $W = 30$ [μm], and $i = 50$ [μm].

Fig. 6.5 shows the result of this experiment. The first important conclusion is the incredible regularity of trapping. The clusters of droplets are not errors but form a chain of movement. In this configuration, it is observed that the new droplets push the previous ones and take their place. The shifting occurs step by step and often involves multiple droplets. As a result, these clusters appear to emerge. They preferentially move diagonally. One of the great advantages of this trapping method is the ability to recover the droplets. The trapping force is weaker, which means that an increase in oil flow leads to a chain reaction, releasing all the droplets. Simultaneously, simply producing new droplets without modifying the pressure regimes causes the trapped droplets to gradually move towards the outlet, allowing their release.

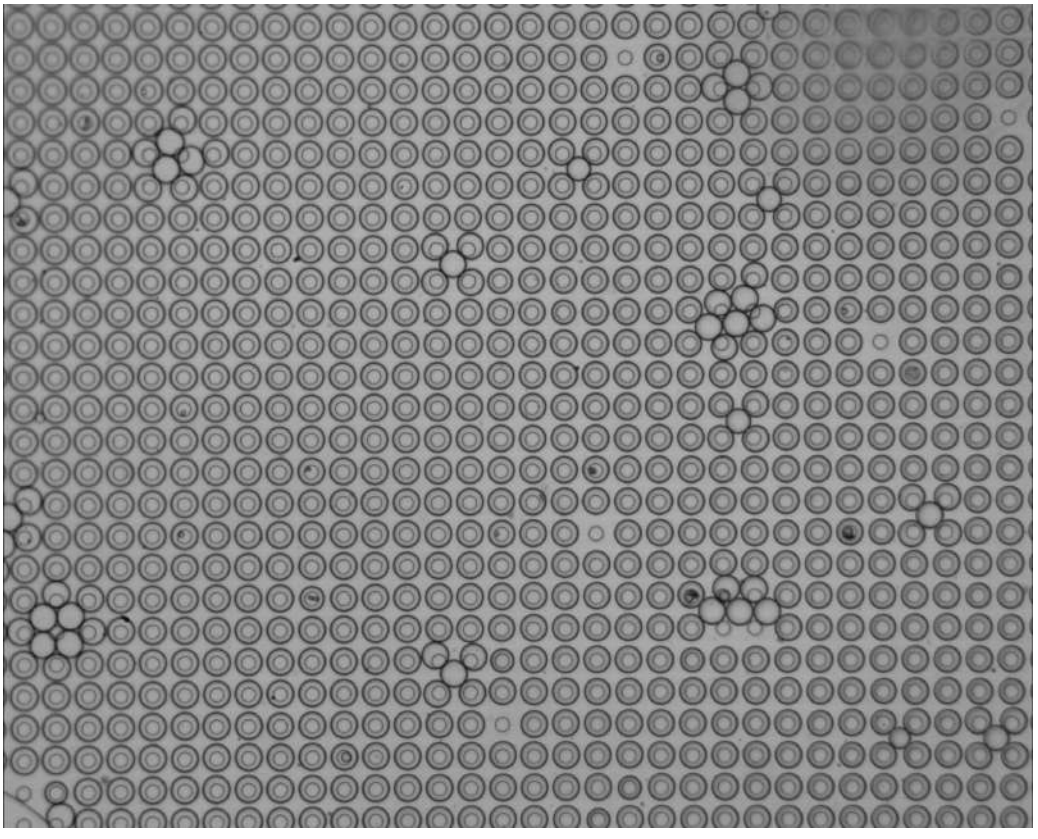

Figure 6.5: Experimental image showcasing droplet trapping using an anchor. The applied parameters are $H = 30$ [μm], $D = 30$ [μm], $W = 30$ [μm], and $i = 50$ [μm]. The approximate volume of the trapped droplets is measured to be $V \approx 88$ [pL].

The idea of demonstrating the difference in radius between an anchor-trapped droplet and a non-trapped one emerged. However, it was not possible to discern any difference because the objective used was not powerful enough. Additionally, the camera did not have sufficient resolution. Furthermore, this difference is of the same order of magnitude as the error in the size of the formed droplets and the error in approximating their circularity, as in practice, droplets in a functioning chip are often slightly deformed. All these factors prevented an accurate measurement of the radius difference.

For improved visibility, especially during the trapping tests of two droplet populations, dyes were introduced in the experiments. These dyes helped to highlight a phenomenon that was invisible in Fig. 6.5 and is evident in Fig. 6.6. Once the trapping was performed, the flow in the chip was stopped for a period ranging from 20 to 30 minutes. The phenomenon is rather slow, requiring a relatively long period of time. It would be possible to let the chip rest for more than half an hour, but there would be a risk of evaporation. During this period, the wells gradually took on a darker blue color, indicating that the droplet had invaded the well. Keeping in mind that the primary goal of this master thesis is to achieve trapping of two distinct populations of droplets, a second generation of droplets of the same size is produced. This represents a advantage compared to other techniques for trapping two populations, which often rely on asymmetric sizes of droplets. The new generation of yellow droplets will push and sever the anchored blue droplets in the wells. The part of the droplet in the chamber will be displaced while the part in the well remains trapped. Eventually, the droplet will break apart. Thus, all the blue droplets in the chamber will be replaced by yellow droplets. The difference now is that the wells are filled with blue droplets. Trapping the yellow droplets occurs in a similar manner to the trapping of the initial population of blue droplets. The yellow droplet deforms within the anchor, adopts a spherical cap shape, and minimizes its surface energy. It cannot enter an already occupied well, so there is contact between the yellow droplets and the small blue droplet trapped in the well (Fig. 6.7). Unfortunately, the experiment stopped at this stage as the phenomenon was completely unexpected. No attempts at fusion through PFO were carried out due to the proximity of the droplets, which made this type of fusion unsuitable.

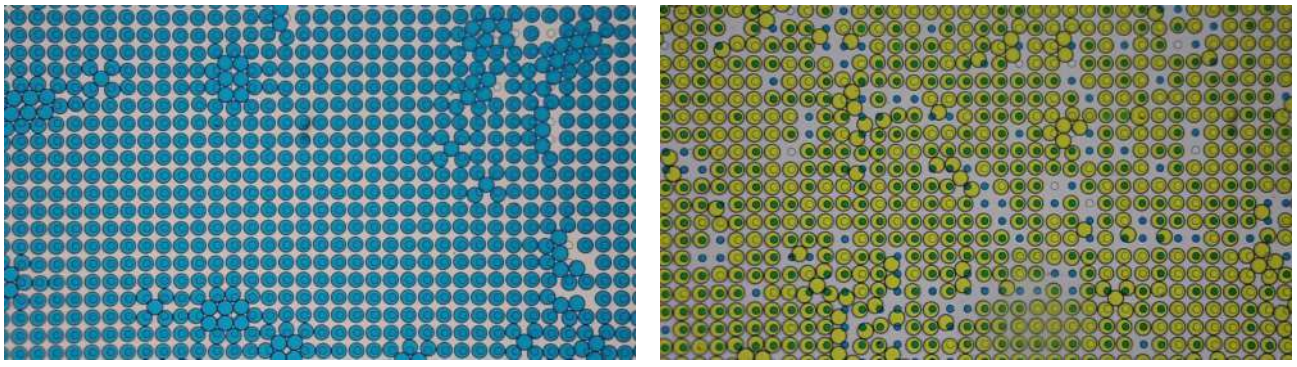

(a) (b)

Figure 6.6: Experimental picture illustrating droplet trapping using an anchor. (a) Trapping of the first droplet population. The chip is stopped for a duration of half an hour, during which the droplets wet the PDMS and invade the well. (b) Flushing of the first droplet population and subsequent trapping of the second population, also using an anchor. This results in the trapping of two distinct droplet populations within the same well. The applied parameters are $H = 30$ [μm], $D = 30$ [μm], $W = 30$ [μm], and $i = 50$ [μm]. The estimated volume of the droplets is $V \approx 105$ [pL].

To complement this analysis and better visualize the situation, a schematic of a cross-section of the chip is shown in Fig. 6.7. This is a simple hand-drawn representation of the observed result and may not perfectly reflect reality. The colors have been adjusted for better contrast. The small droplet within the well corresponds to the blue droplet in the previous explanation, while the one in the chamber represents the yellow droplet.

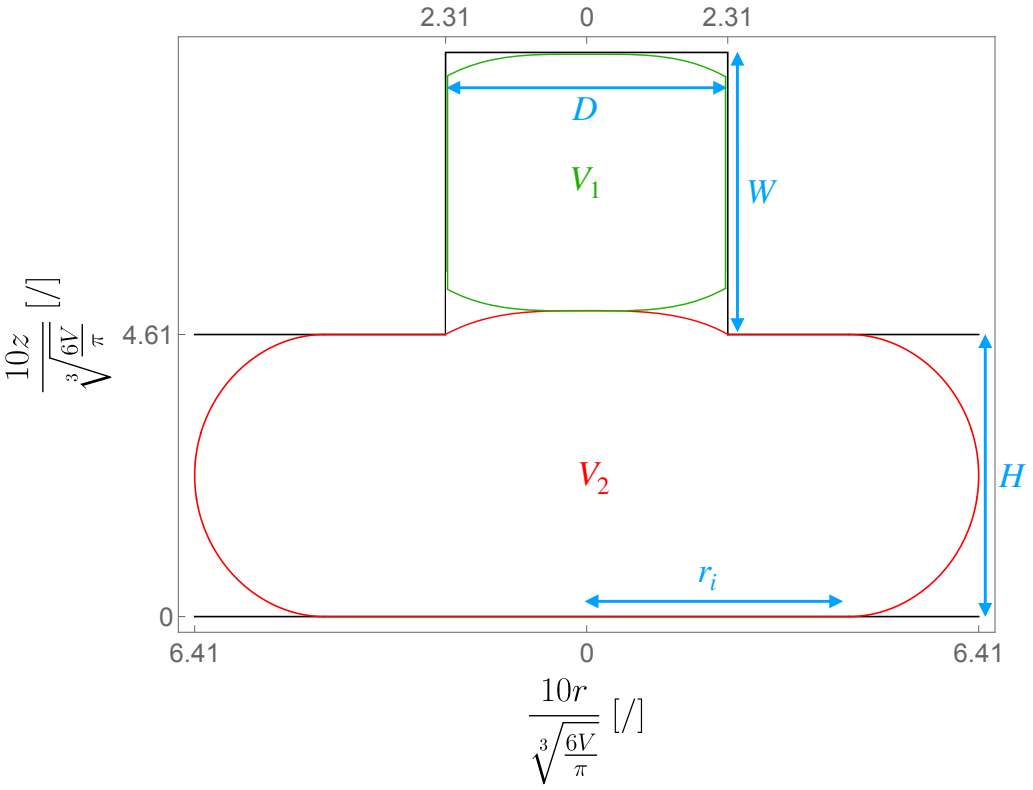

Figure 6.7: Cross-sectional view highlighting the capture of two distinct droplet populations within a single well. The first population is confined within the well and wets its surface. The second population is trapped by an anchor and resides in the chamber.

To complement this unexpected phenomenon, it was relevant to perform a duration test to study the stability of the experiment (Fig. 6.8).

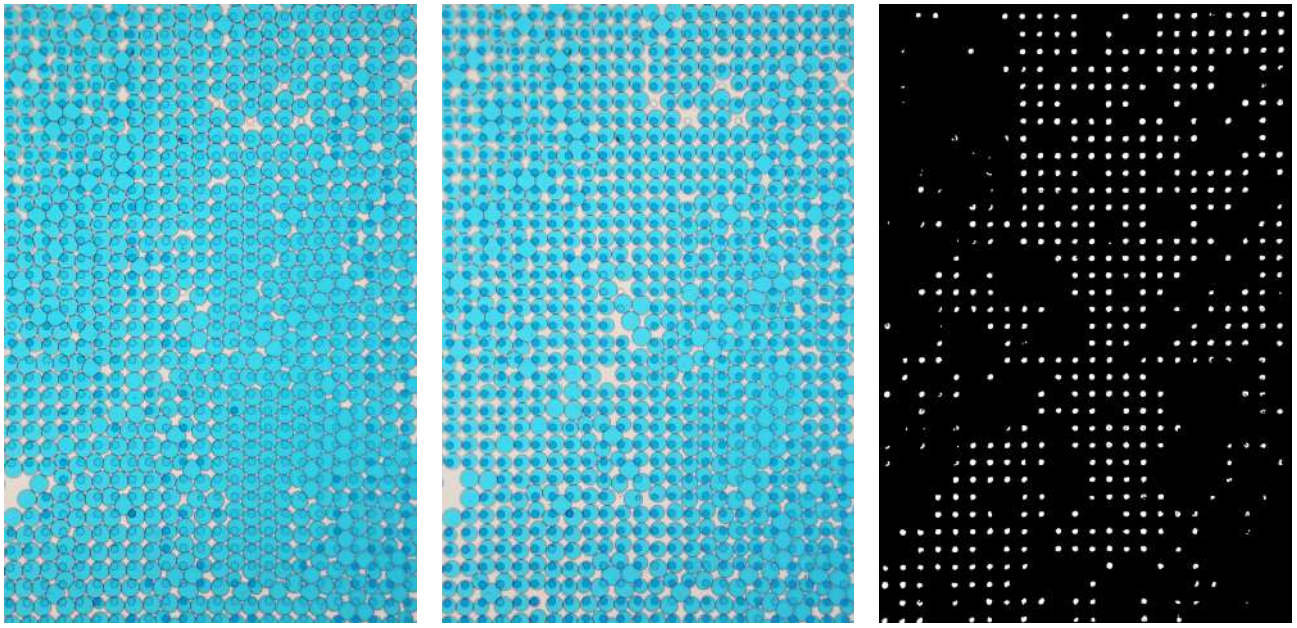

(a) (b) (c)

Figure 6.8: Timelapse of trapped droplets by an anchor over a duration of 30 minutes. (a) Initial state: Trapped droplets at $t = 0$ minutes. (b) Final state: Trapped droplets at $t = 30$ minutes. (c) Image difference: Highlighting the filling of the wells through `ImageJ` [128] analysis, showing the color change between the initial and final states.

Fig. 6.8 highlights the result of a timelapse. After more than half an hour, the wells appear much darker. To highlight this observation, a subtraction between the initial and final image is performed with some contrast adjustments (Fig. 6.8c).

A darker color cannot, a priori, mean only one thing: there is more liquid and therefore more dye within the well. To assess the amount of liquid that has filled the well, an image analysis is performed. The intensity of pixels for the RGB channels is evaluated in the background, on the droplet located in the chamber, and finally on the droplet within the well. The histograms are shown in Fig. 6.9.

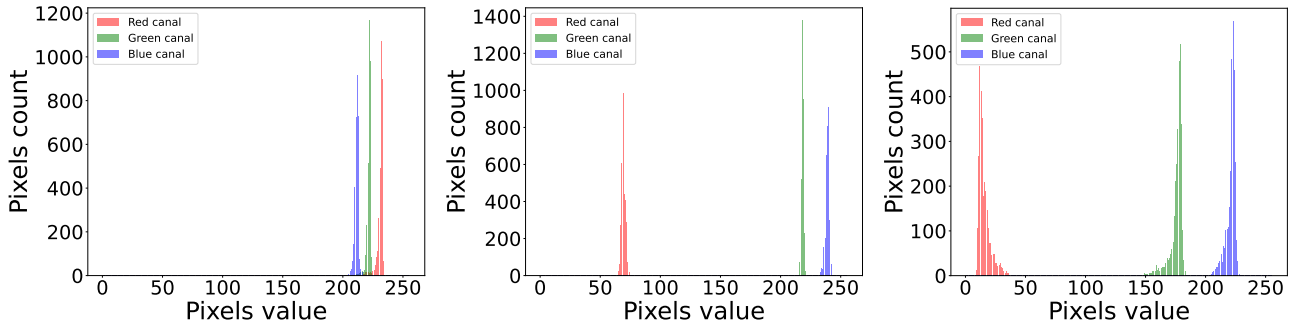

(a) (b) (c)

Figure 6.9: RGB histograms illustrating color distribution. (a) Background RGB histogram. The mean intensity per channel is as follows: R = 231, G = 222, B = 212. (b) RGB histograms of droplet color in the well and chamber at t = 0 minutes. The mean intensity per channel is as follows: R = 69, G = 218, B = 239. (c) RGB histogram of droplet color in the well at t = 30 minutes. The mean intensity per channel is as follows: R = 16, G = 176, B = 221.

Only the intensity of the red channel is strongly affected, which is consistent with the use of a blue dye. To deduce the difference in liquid thickness between the droplet in the chamber and the one in the well using this method, it is conventional to apply the Beer-Lambert law:

$$\mathcal{A} = -\log_{10} \mathcal{T}, \qquad \mathcal{A} = \xi l c. \tag{6.1}$$

Where $\mathcal{A}$ represents absorbance and $\mathcal{T}$ represents transmittance. ξ is the molar absorptivity of the material, c is the concentration, and l is the path length.

In this situation, both c and ξ are constant. As a result, absorbance is directly proportional to the thickness of the material traversed. For the droplet located in the chamber, the transmittance is calculated as the ratio of the received intensity to that of the background: $\mathcal{T} = \frac{69}{231}$. This leads to an absorbance of $\mathcal{A} = 0.52$, which corresponds to a thickness of 30 [μm], i.e., the height of the chamber. For the droplet located in the well, the same reasoning is applied. The transmittance is evaluated as $\mathcal{T} = \frac{16}{231}$, and the corresponding absorbance is $\mathcal{A} = 1.16$. Despite various errors and approximations, in terms of order of magnitude, the absorbance has approximately doubled. As absorbance is directly proportional to the thickness of the material traversed, it is possible to conclude that the colored water filled the well to its full depth of 30 [μm]. To be comprehensive, this analysis was performed on multiple wells to validate the general nature of this result.

However, finding the interpretation of this phenomenon is not trivial. The most intuitive idea would be to simply consider a deformation of the droplet. It would naturally introduce itself into the well (Fig. 6.10).

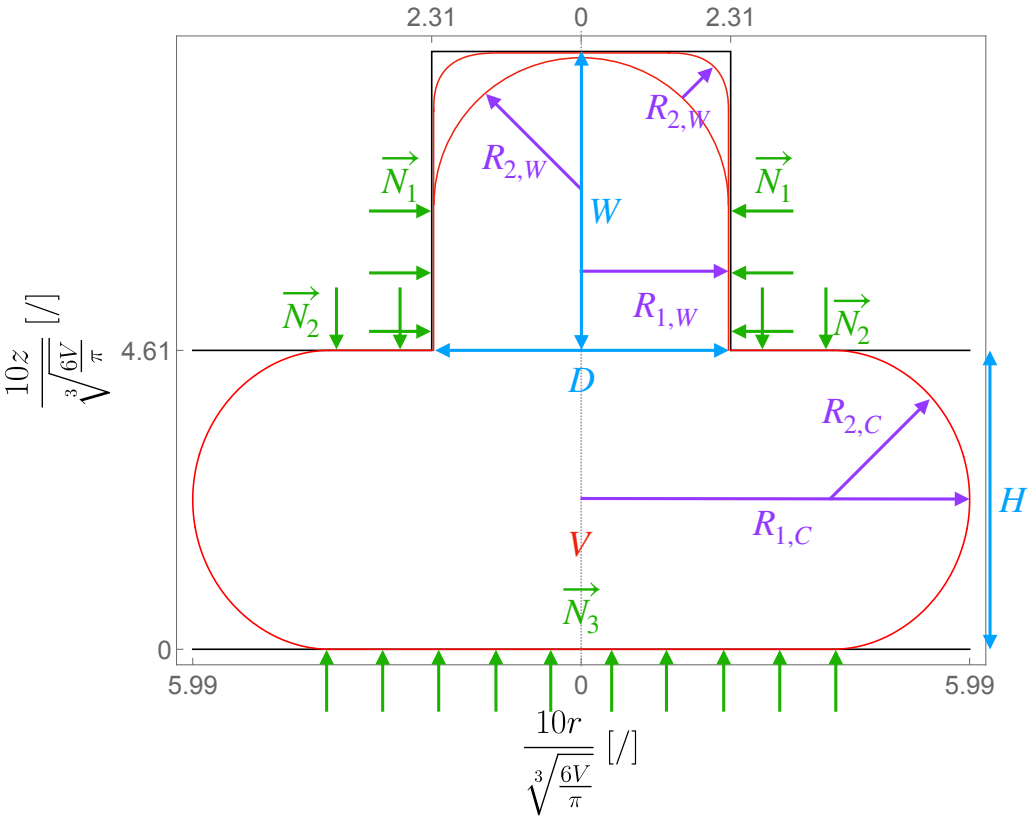

Figure 6.10: Schematic representation of a non-wetting droplet invading a well. The diagram illustrates the confinement of the droplet's shape by reaction forces from the wall and highlights the presence of unmatched principal radii of curvature, posing a paradox regarding the droplet's hydrostatic equilibrium and its mechanism of well invasion. The experimental parameters used are: $H = 30$ [μm], $D = 30$ [μm], $W = 30$ [μm], $V = 144.1$ [pL].

This trend would be motivated by the minimization of the surface energy of the droplet at a given volume. However, such reasoning quickly reaches its limits. By highlighting the radii of curvature within this trapped droplet, an inconsistency appears. The droplet is in a hydrostatic state, and therefore, there is no pressure gradient inside it. This means that the mean curvature κ must be constant. However, comparing the principal radii of curvature inside the chamber to those of the part of the droplet located in the well, it is impossible to find a way to equalize them. Physically, this means that the drop has no reason to locally pinch itself by increasing its surface and curvature to enter the well. On the contrary, it is preferable for the droplet to stay in the chamber to minimize its surface energy.

At the locations where the droplet is constrained by the walls, it undergoes a force from them and is compelled to deform. In these areas, one of the radii of curvature disappears. The example of the well is the most striking since below the cap, the droplet is forced to adopt a cylindrical shape. However, a cylinder only has one radius of curvature. To satisfy the Laplace equation at every point of the droplet, thus ensuring the hydrostatic equilibrium state, the wall must compensate for the missing radius of curvature by applying a force to the droplet.

Since the first attempt to explain the rise of water in the well seems unrealistic, a second approach must be considered. Now, the hypothesis is that the water eventually wets the PDMS. Under these conditions, a contact line is established between the water, oil, and PDMS in the

well. The spherical cap is no longer constrained to modify its curvature to enter the well. The contact line can simply move, and the droplet can gradually enter the well (Fig. 6.11).

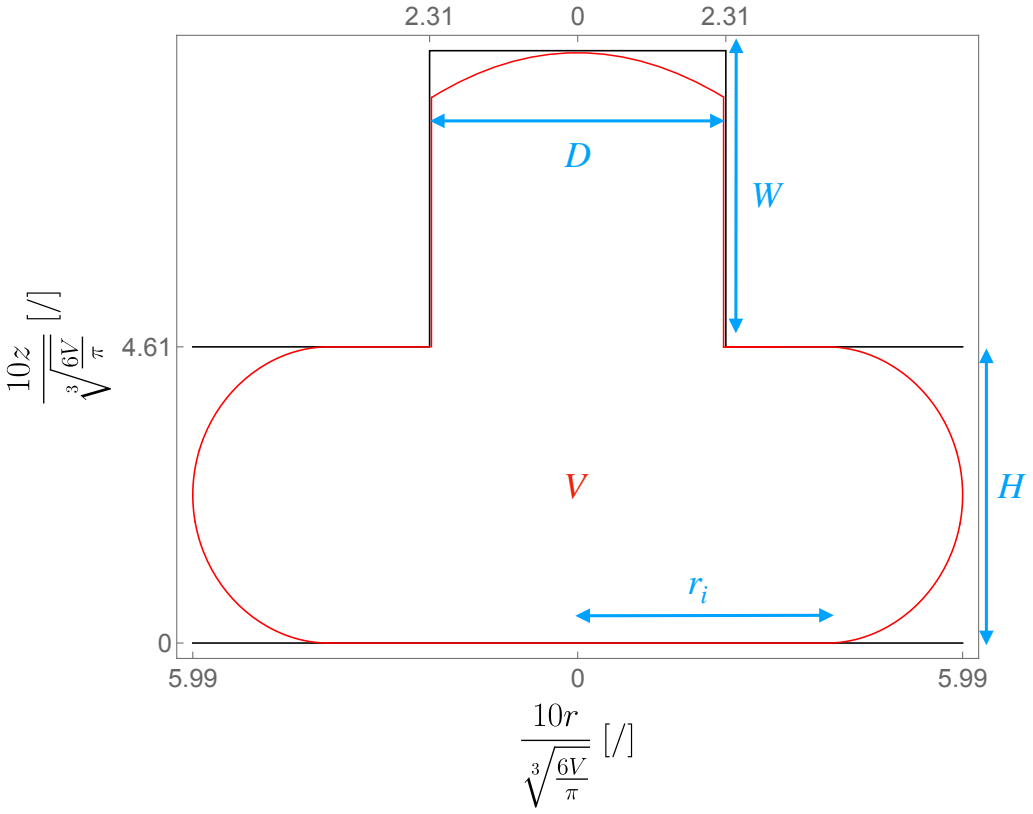

Figure 6.11: Schematic illustration of a droplet wetting the well walls and invading the well. The parameters used are: $H = 30$ [μm], $D = 30$ [μm], $W = 30$ [μm], $V = 144.1$ [pL].

According to the principle of least action, the droplet should only enter the well if it minimizes its surface energy. However, it should be noted that this energy is no longer directly proportional to the surface since the liquid wets the material. Under these conditions, there are two relevant interfaces. The first is that between water and oil, and the second is that between water and PDMS. Since the associated surface tensions are not the same, an increase in the total surface area can still lead to a minimum energy provided that water prefers to contact the PDMS rather than the oil. The surface energy can be written as:

$$E_\gamma = \gamma_{wo} S_{wo} + \gamma_{po} S_{po} + \gamma_{pw} S_{pw} = \gamma_{po}(S_{po} + S_{pw}) + \gamma_{wo} \underbrace{[S_{ow} - \cos(\theta) S_{pw}]}_{\tilde{E}_\gamma}. \tag{6.2}$$

where the relation $\cos\theta = \frac{\gamma_{po} - \gamma_{pw}}{\gamma_{wo}}$ was used as presented in section 3.1.3. Knowing that γ_{po}, γ_{wo}, and γ_{pw} represent the interfacial tensions between PDMS and water, between water and oil, and between PDMS and water, respectively. While the surface tension of water with oil is approximately $\gamma_{wo} \approx 31 \times 10^{-3}$ [J/m^2] [129, 130]. PDMS, has a surface tension with water of the order of $\gamma_{pw} \approx 40 \times 10^{-3}$ [J/m^2] [131]. PDMS exhibits rather hydrophobic properties. In open air, the contact angle between a water droplet and PDMS is approximately 110° [131–133]. The surface tension between the `Emulseo` HFE-7500 oil and PDMS, γ_{po}, could not be found in the literature.

However, this explanation must be contrasted with the fact that the chip was treated with NOVEC, which imparts hydrophobic properties to the walls. In this context, the exact wetting angle may be difficult to determine.

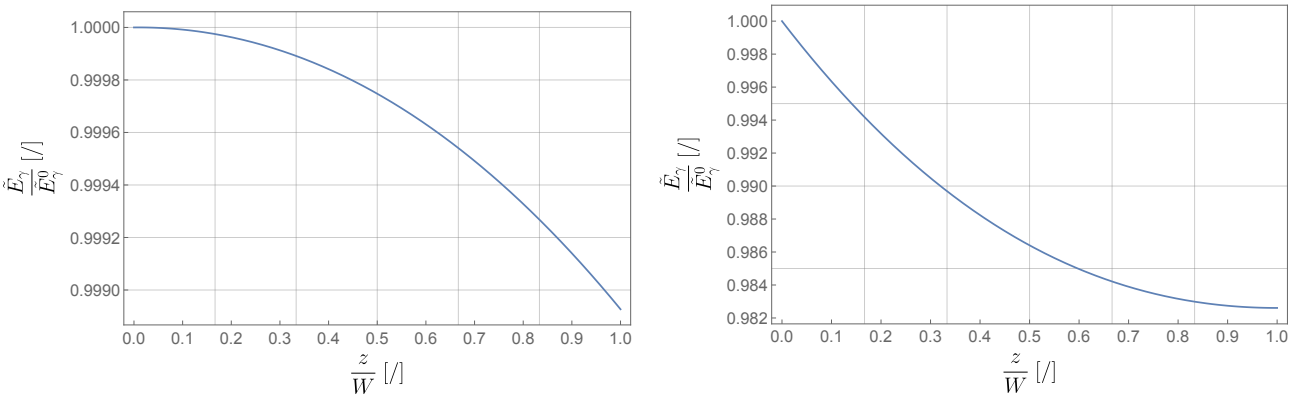

(a) (b)

Figure 6.12: Evolution of surface energy $\tilde{E}_\gamma$ with liquid height in the well at the critical wetting angle. (a) The well approximated as a cylinder. The critical angle is 130.68°, corresponding to the maximum energy at zero height. (b) The well approximated as a truncated cone with an inclination of 10°. The critical angle is 126.49°, corresponding to the energy minimum at $z = 30$ [μm].

The analysis is shown in Fig. 6.12. Using the Eq. 6.2 , it is possible to find the angle θ for which $\frac{\mathrm{dE}_\gamma}{\mathrm{dz}} = 0$ when $z = 0$ (Fig. 6.12a). This limiting angle is determined to be $\theta = 130.68°$. Indeed, starting from the Eq. 6.2 giving the surface energy, with the value of γ_{po} and γ_{wo} being constant, only the difference $S_{ow} - \cos(\theta)S_{pw}$ will count in the energy calculation. The term $(S_{po} + S_{pw})$ is constant since it represents the total solid surface. It should be noted that at the critical angle and for any angle below it, $\frac{\mathrm{dE}_\gamma}{\mathrm{dz}} < 0$ for increasing values of z. This means the associated surface energy decreases. Since the typical contact angle of water with PDMS is below this critical value, it seems reasonable to conclude that it is favorable for water to enter the well as long as it wets the PDMS. So far, the wetting phenomenon has only been considered in the well. It could potentially occur within the chamber as well, although this is more complex to demonstrate. In addition, the oil contained in the chamber is rarely inert, as is the case in the well. Except for long-term tests on spheroids or evaporation, a slight oil flow is maintained in the chamber. The layer of oil between the PDMS and the drop is thus maintained, limiting wetting.

To be completely rigorous, it would be necessary to take into account the microfabrication error to ensure that this phenomenon is not related to it. It has been observed that depending on the thickness of the SU8 layer used as a negative for PDMS molding, the structures do not rise perfectly straight but suffer from an inclination of about 10° as explained in section 2.3. However, this detail could be important in this situation since the wells were modeled with straight walls. Therefore, they can be assimilated to cylinders. To ensure that this simplifying assumption is not the cause of this unexplained phenomenon, simulations were conducted with inclined walls. The well is then comparable to a truncated cone. The result remains similar to what was shown previously, except for the changing limiting angle and the concavity in this configuration. According to this model, the angle decreases to a value of 126.49° (Fig. 6.12b). Below that, it is energetically favorable for the droplet to enter the well. Since the curvature is inverted, the critical angle corresponds to the minimum energy for the liquid to reach the 30 [μm] height of the well. In the case of non-inclined walls, the angle is taken such that zero

corresponds to a maximum energy.

To conclude this analysis with a more direct confrontation with the experimental results, a particular droplet from the image is considered using ImageJ [128]. Naturally, it must be ensured that the pattern is regular enough for the analysis to be extrapolated to all droplets in the image. In the well, when the timelapse begins in Fig. 6.8a, this droplet has a measured radius of $r_e = 41.7$ [μm]. However, at the end of the timelapse, the radius is only $r_e = 37.7$ [μm]. Nonetheless, starting from the initial radius, it is possible to calculate the volume of the droplet assuming that it has not yet penetrated the well. By assuming that the droplet completely invades the well, the volume of the well, approximated as a cylinder, is subtracted from the volume of the droplet. The last step is then to reverse the process by finding the corresponding r_e to this volume, which has been subtracted from the volume of the well. Thus, the radius found is $r_e = 38.6$ [μm]. This result leads to a rather immediate problem, since even assuming that the well has been completely filled by the droplet, the equivalent radius is higher than the experimentally measured one. This problem is not related to the model. The conclusion to be drawn is that the volume of the droplet is not conserved between the initial and final states. This can only occur if there has been evaporation or drainage of the water by the oil. These are significant issues in microfluidics focused on trapping, and they will be further examined in an upcoming section.

As a final clarification, the assumption was made that the wells were completely filled by the droplet. The wetting model is difficult to explain because it remains unclear where the oil contained in the wells disappeared. Furthermore, given the colorimetry of the image, all wells seem to be filled in the same way and are completely full.

It was possible to estimate approximately the volume of the trapped droplets inside the well. At the end of the experiment, the chamber was cleaned, and small taps were given to release the trapped droplets and allow for thorough cleaning. This process was quite aggressive, causing some droplets to separate. However, upon quickly placing the chip back under the microscope, it was observed that the majority of the released droplets originated from the wells as they had a similar size and were comparable to them. Using `imagej` [128], their radius was determined, followed by their volume. It was found that their volume was nearly identical to that of the wells, with some fluctuations around this value. This confirms, in a rough manner, the initial intuition that the entire well is filled with water.

Theoretical model The remainder of this section aims to develop a theoretical model on trapping by anchors. The goal is to extrapolate the theoretical model presented in section 2 to the specific case of anchor trapping, in order to discuss the shape adopted by the latter.

The well is assumed to be deep enough so that at the maximum of its deformation, the droplet does not touch the bottom. It is also assumed that the droplet is centered with respect to the well and therefore retains its axisymmetric shape. This allows to use again Young-Laplace equation of the axisymmetric model. Thus, the function describing the deformation of the droplet in the anchor is nothing else than a nodoid. The fundamental difference is that this time, the derivative is discontinuous at the exit of the well. This means that the nodoid does not have a tangent that vanishes at the boundaries as was the case before. Consequently, the boundary conditions will be different in this model. At first glance, it appears that it is necessary

to seek the tangent as an unknown in the problem. However, this is a false intuition because once the mean curvature, the force and the radius have been determined outside the well, by conservation of volume, these quantities will change to adapt to this new configuration. There exists a degree of freedom that allows for the choice of volume and, therefore, focusing on a droplet of a specific size. Once the volume is fixed, the portion of the droplet inside the chamber will adopt the shape of a nodoid as explained in section 2. This means that the droplet has a constant mean curvature κ. A simple reductio ad absurdum reasoning ensures this. If the mean curvature were not constant at every point of the droplet, there would be pressure gradients within it according to the Young-Laplace equation. However, this entire reasoning takes place within the framework of hydrostatic equilibrium, which refutes this possibility. Considering the droplet trapped in the anchor, the cap must possess the same mean curvature as the rest of the droplet. Therefore, the presumed degree of freedom concerning the tangent is not actually present and the cap is uniquely determined. Thus, once the volume is fixed, considering the boundary conditions in the chamber for the same droplet with the cap volume removed allows to determine the mean curvature. It is then used as a boundary condition for the unknown nodoid located in the anchor. The constant of integration of the Eq. 4.11 named C_2 for this second nodoid must be evaluated as previously but with a κ and a scaling factor α already fixed. It is easy to calculate the constant C_2 in this situation by remembering that it represents the force exerted on the droplet. To take into account the boundary condition of the first integral for this cap, it's enough to start from Eq. 4.11 and choose the position $r = 0$. Then, it is possible to notice that the force is null at the top of the droplet, which translates into the fact that $C_2 = 0$. At this stage, the shape of the nodoid is fixed. Only a portion of the nodoid will form the anchor. To determine this portion, it is sufficient to start from Eq. 4.13. By primitivizing on each side of the equality and knowing that the well has a width W, the function $z(r)$ can be determined:

$$z(r) = \int_0^r \frac{-\kappa}{\sqrt{\frac{4}{\tilde{r}^2} - \kappa^2}} \, \mathrm{d}\tilde{\mathrm{r}} = \frac{1}{\kappa}\sqrt{4 - \kappa^2 \mathrm{r}^2}. \tag{6.3}$$

where r varies in the interval $[0, \frac{W}{2}]$. This last equality corresponds to the equation of a circle. This demonstrates that the cap situated within the well is a specific case of nodoid that simplifies to a spherical cap, as discussed in section 2.1.2. In a completely analogous way, it is possible to achieve the same result through the parametric formulation which is needed for the numerical implementation. To do this, starting from Eq. 4.24, it is sufficient to find the s_1 for which $r(s_1) = 0$ and s_2 for which $r(s_2) = \frac{W}{2}$. Then, by taking the expression of z(s) in integral formalism, the shape of this second nodoid is given by the following parametric equations:

$$r(s) = \alpha a\sqrt{2(1 + \sin s)}, \qquad z(s) = \alpha a \int_0^s \sqrt{\frac{1 + \sin \tilde{s}}{2}} \, \mathrm{d}\tilde{\mathrm{s}}. \tag{6.4}$$

In this case where $\epsilon = 1$, the resulting nodoid is a spherical cap even if it is harder to spot with these parametric equations. This is consistent with the fact that there is no force exerted on the cap trapped in the anchor and therefore no curvature constraint imposed by external constraints. Under these conditions, since the pressure inside the droplet must be constant, the spherical cap will simply adapt its curvature to satisfy the pressure differential across the interface. In Fig. 6.13, it is possible to observe the variation of the internal radius r_i when the droplet initially in the chamber comes to anchor in a well. Due to volume conservation, a portion of the liquid composing the droplet will be stored in the spherical cap, which will cause a decrease in the droplet radius:

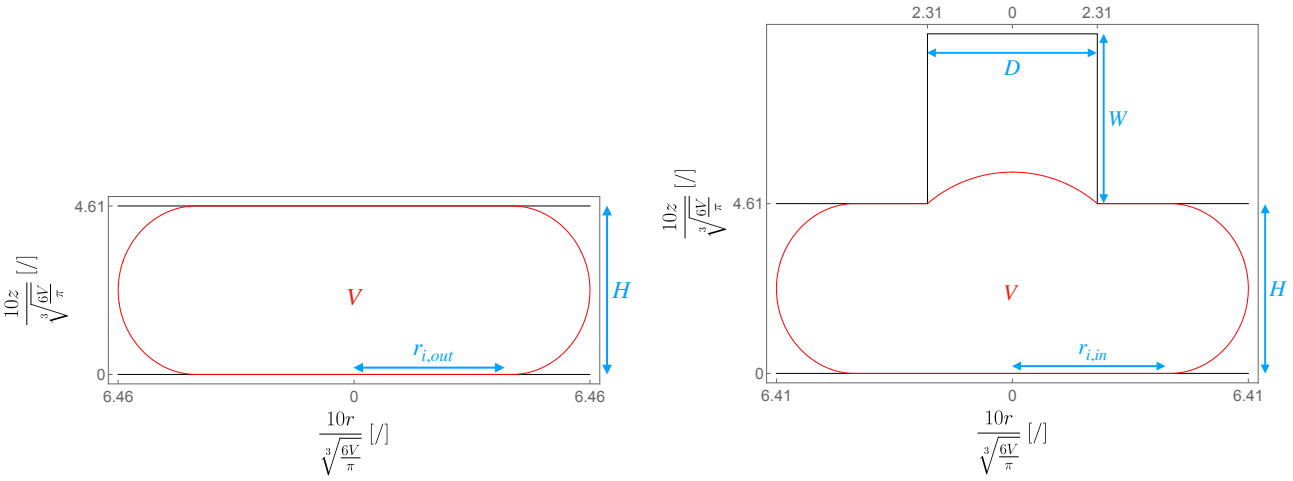

(a) (b)

Figure 6.13: Study of the droplet radius change as it enters the well. The droplet has a volume of $V = 144.1$ [pL]. (a) Droplet located outside the well with an internal radius of $r_{i,out} = 28.21$ [μm]. (b) Droplet located inside the well with an internal radius of $r_{i,in} = 27.94$ [μm]. The parameters used are $H = 30$ [μm], $D = 30$ [μm] and $W = 30$ [μm]

It should be noted that the model developed stipulates that the mean curvature must be constant for the entire droplet. Thus, fixing the pressure inside the droplet fixes its size and also fixes its mean curvature. From there, all the parameters of the spherical cap located in the well are adjusted. Therefore, the cap is unique and will depend solely on the pressure inside the droplet. It is possible to visualize the variation of the height of the cap and its volume as a function of the r_i of the droplet anchored in the well in Fig. 6.14:

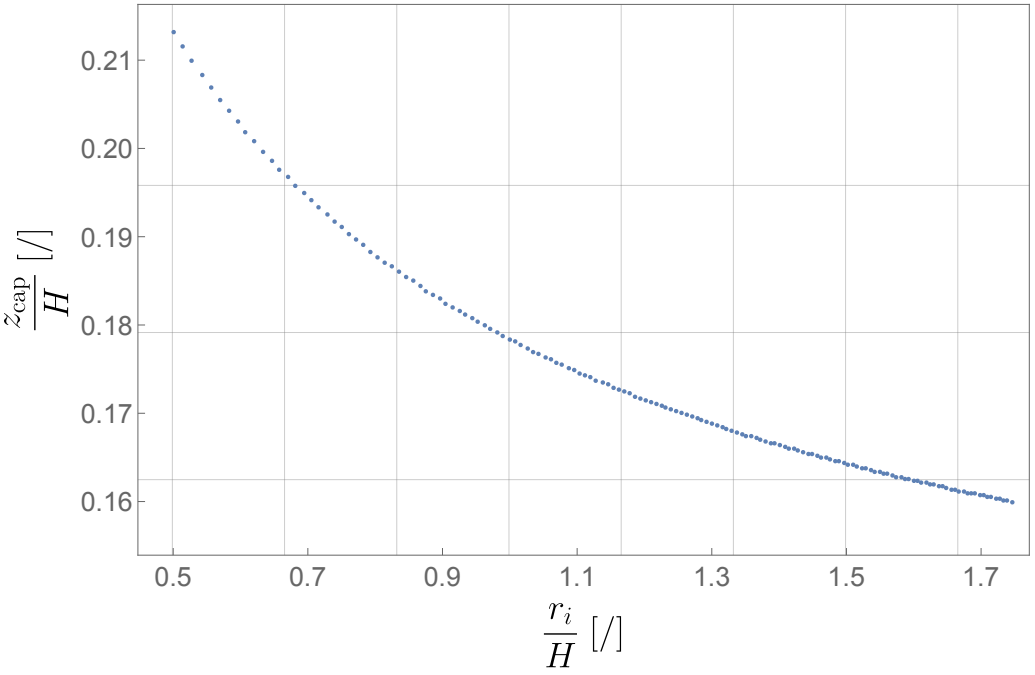

Figure 6.14: Study of the height of the spherical cap of the droplet inside the well as a function of its volume, expressed in terms of its inner radius r_i. The parameters used are $D = 30$ [μm] and $H = 30$ [μm].

This graph shows that as the internal radius of the droplet r_i increases, the maximum height of the cap decreases. This is consistent with the fact that the mean curvature will be higher for a smaller droplet compared to a larger one. Thus, the anchor will be more effective in the first situation. One way to analyze this is to understand that it is more difficult to deform a cap that is deeply sank in the well compared to one that is barely entered. Since a well with a diameter of $D = 30$ [μm] was used in this simulation, r_i cannot go below 15 [μm] to avoid transitioning to trapping via buoyancy force.

For the next developments, it may be interesting to check the relation between the internal radius when the droplet is outside the well compared to when it is anchored inside (Fig. 6.15).

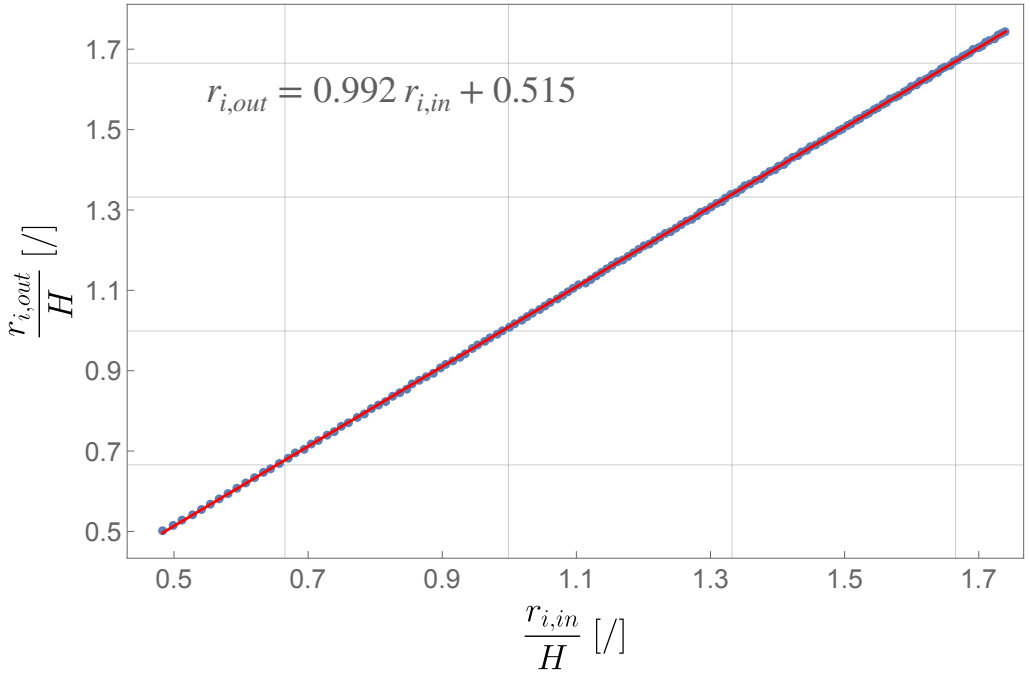

Figure 6.15: Relationship between the internal radius of the droplet when it is outside the well, $\frac{r_{i,out}}{H}$, and the internal radius when it is inside, $\frac{r_{i,in}}{H}$. Both radii are normalized by the height of the chamber, H. The parameters used are $\frac{D}{H} = 1$. A well with a diameter equal to zero indeed results in a linear relationship. As an illustration, for $D = 10$ and $D = 20$, the slope is given as 0.99994 and 0.99885, respectively.

Given the positioning of the points in these situation, it is appropriate to consider a linear fit in order to approximate these discrete results with a continuous curve. The result of this fit is displayed simultaneously with the points on the graph. Although the adjustment may appear perfectly linear, it is not exactly the case. Many parameters come into play in the trapping of the droplet in the well. It is expected that the variation in radius when the droplet is anchored in the well is significantly smaller than the radius itself. An estimation of the error of the least squares fit is given by 6.9×10^{-4}.

This next part aims to show that it is energetically favorable for a droplet to be located in a anchor rather than in a chamber. This means that the droplet must minimize its surface energy when it is located within the anchor. For this experiment, the volume of the droplet is kept constant. The surface energy is given by γ_S. Since the surface tension is a constant, the energy change is only given by the variation of the droplet surface. It is therefore sufficient to plot the

evolution of the droplet surface as a function of the volume in the case where it is trapped or not (Fig. 6.16).

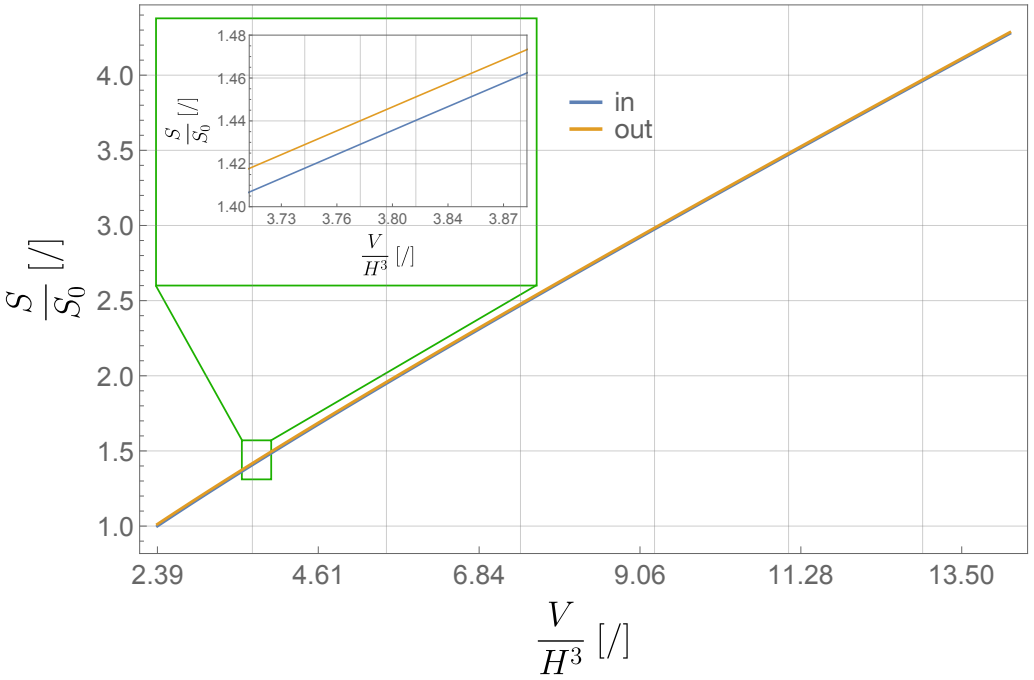

Figure 6.16: Comparison of the droplet surface when it is outside the well to the case when it is inside. The initial surface area is $S_0 = 8181.47$ [μm^2], and the chamber height is set at $H = 30$ [μm].

This graph shows the validity of the initial assumption since the droplet surface is lower when it is located in an anchor. This analysis also reinforces the validity of this model in light of what has been observed empirically. To better characterize the energy difference between the two droplet configurations, it is relevant to plot the evolution of the surface difference normalized by the initial total surface area as a function of the droplet volume. By plotting this result on a logarithmic scale, a linear decrease can be observed (Fig. 6.17):

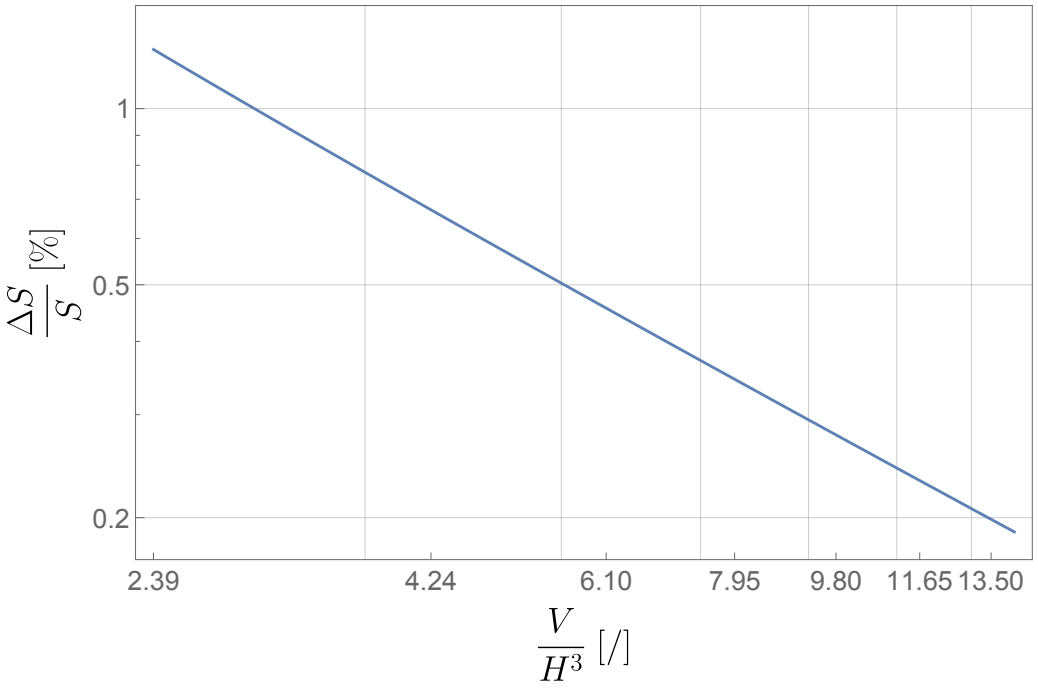

Figure 6.17: Percentage relative surface difference between a droplet located inside the well and outside, plotted as a function of droplet volume on a logarithmic scale. The parameter $H = 30$ [μm] is used.

An almost immediate observation is the monotonic decrease of this difference between the two surfaces. The slope of a linear fit was evaluated at -1.0668. The spherical cap inside the well sees its curvature decrease as the droplet volume increases. Consequently, the height and volume of liquid contained in the cap also decrease. If the cap is less deeply embedded in the anchor when the volume increases, this means that the anchoring force will be weaker for a large droplet than for a small one.

Attempting to evaluate the trapping force that keeps the droplet within an anchor is not straightforward. The force may be obtained by evaluating the energy gradient. This gradient can be approximated by the surface difference over the distance required to remove the droplet from the anchoring point. However, this approach can only provide the average force by completely neglecting the shape of the function between two points and approximating it by a straight line. The true force that matters in this problem is the maximum force encountered. It corresponds to the maximum slope encountered. However, no other index allows to bound this slope to a high value. It is only possible to assert that the maximum slope encountered must be equal to or greater than the average slope.

It has already been demonstrated that it was energetically favorable for a droplet to place itself in an anchor. However, from a certain point, it might be energetically more favorable for the droplet to fully deform and enter the well. Therefore, it is relevant to analyse how the surface of the droplet evolves according to the size of the well (Fig. 6.18). In this situation, a droplet whose volume is constant will be studied. Initially, it is confined between two walls with a total absence of wells. Subsequently, the size of the well will increase until it reaches $D = 30$ [μm]. This threshold may seem arbitrary; however, it corresponds to the point at which anchor trapping could be initially observed. If the well diameter increases in size further, it will exceed the height of the chamber, and therefore, the envisioned model is likely to reach its limits. Furthermore, to ensure staying within the acceptable range, the diameter of the well will not

exceed the radius of the sphere equivalent to the trapped droplet, i.e. $2r_i > D$ (Fig. 6.18).

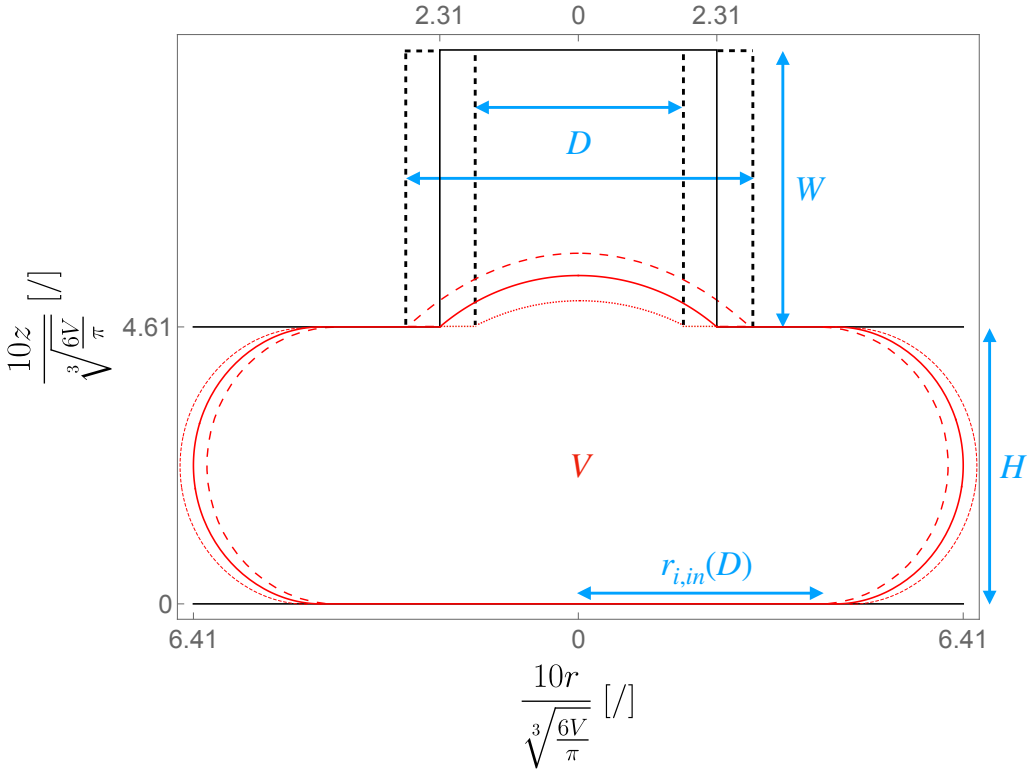

Figure 6.18: Schematic of a droplet trapped in a well. The diagram highlights the variation of the droplet inner radius r_i and thus the droplet surface as a function of the well diameter D.

The result of the evolution of the droplet surface as a function of the width of the well can be seen in Fig. 6.19.

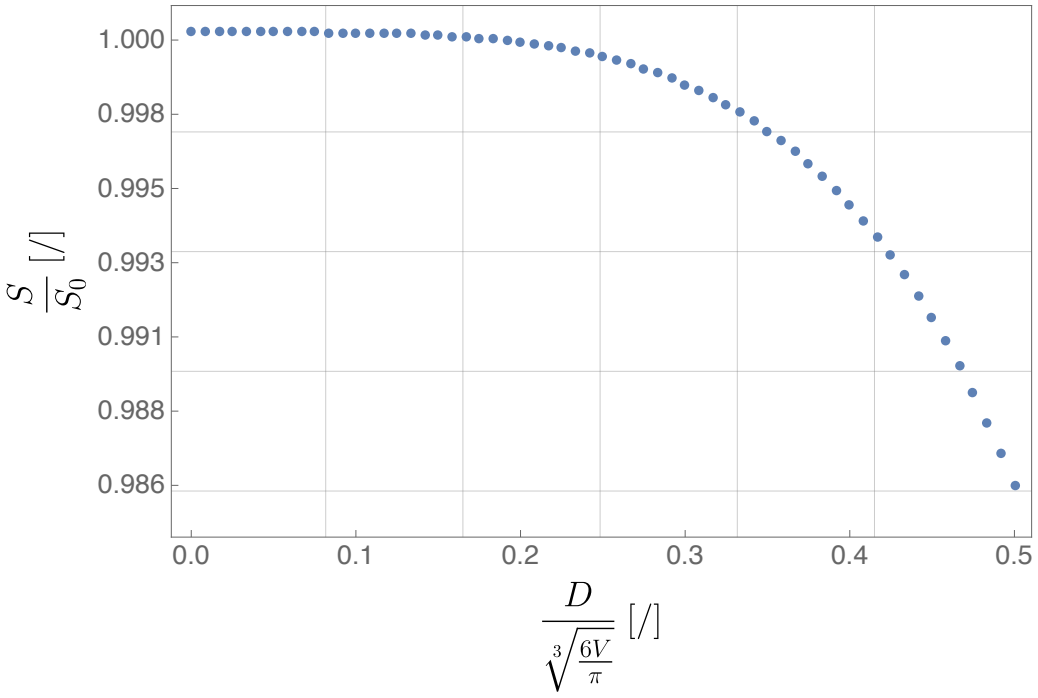

Figure 6.19: Simulation results showing the evolution of the droplet surface as a function of the well size D. The parameters used are $H = 30$ [μm] and $W = 30$ [μm] while maintaining a constant volume of $V = 144.1$ [pL].

The conclusion of this study is that the total surface area of the droplet decreases when the diameter of the well increases. Assuming that the droplet does not wet the PDMS but a thin layer of oil remains present, this means that the surface tension is constant and there is no contact line between water, oil, and PDMS. This assumption thus allows to affirm the direct proportionality relationship $E_\gamma \propto S$. Thus, with the same analyse, the surface energy associated with the droplet decreases as the diameter of the well increases, although this trend remains relatively marginal in Fig. 6.19. This implies that the trapping force on the droplet stabilized in an anchor will be relatively limited.

In this master thesis, the force of trapping by an anchor has not been studied in detail. This issue is not trivial and could be further explored in future works. However, it is possible to find an estimation of it among various studies in the literature [5, 52, 91–93].

Evaluation of the radius difference Following these theoretical developments, it would be interesting to try to assess the difference in radius between the droplet outside the well and the droplet trapped in an anchor. This outcome can be obtained by conserving the volume of the droplet between these two scenarios (Fig. 6.20).

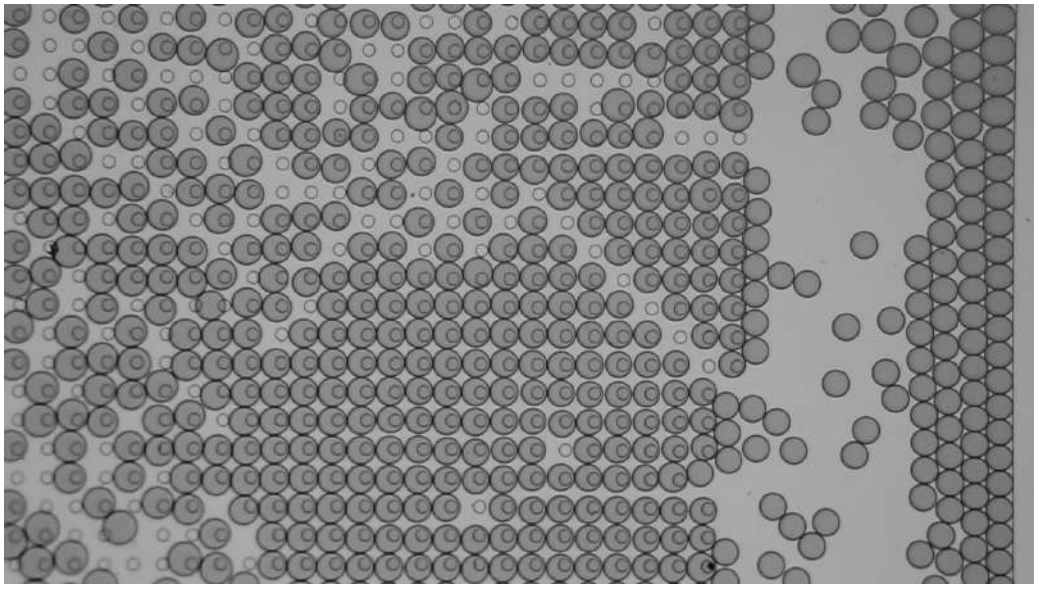

Figure 6.20: Transition between free droplets and their trapping by an anchor. The experimental parameters used are as follows: chamber height $H = 30$ [μm], well diameter $D = 30$ [μm], well depth $W = 30$ [μm], and droplet volume $V = 125.4$ [pL].

In this Fig. 6.20 from a video, there is a clear separation between trapped and free droplets. By image analysis and using the Hough algorithm in Python, it is possible to evaluate the average radius of droplets located beyond a certain x. Since the fit is not always perfect for an image of this type containing many adjacent circles, the results of this method were confirmed by a local analysis using `Imagej` [128]. For maximum precision, the best droplets are evaluated. By fitting the circle passing through the droplet contour, it is possible to determine its area and of course its corresponding radius while minimizing the error. This analysis found an average radius of $r_{out} = 39$ [μm]. Using this information and conservation of volume, the theoretical model can determine the equivalent radius of the trapped droplet. Following this analysis, the result gives $r_{in} = 38.8$ [μm]. The difference in radius is about one-fifth of a micrometer. It is impossible to highlight such a small variation. The device's resolution is at best one pixel per micron. To confirm this idea, the average radius of trapped droplets in Fig. 6.20 was evaluated using the same method as for free droplets. No significant difference could be established between the radii of the two populations of droplets. Thus, in this particular case, the model did not help to put a measurable radius difference into perspective. However, it was necessary to go through this step to ensure it.

1.1.1.3 Droplets interaction The strength and also the weakness of the wells spaced only 50 [μm] apart results in their interactions. To illustrate the challenge of the delicate interplay between all the parameters, Fig. 6.21 shows what happens when the droplet size is not suitable. In this situation, the space between the wells also becomes a trapping region. The regularity of the process could lead to new avenues to explore; however, this master thesis primarily focuses on trapping within the wells and seeks to study the physics of trapping independently. This type of chip indeed has a beautiful pattern and a large number of wells, but capturing two distinct populations and their fusion does not appear to be trivial at first glance.

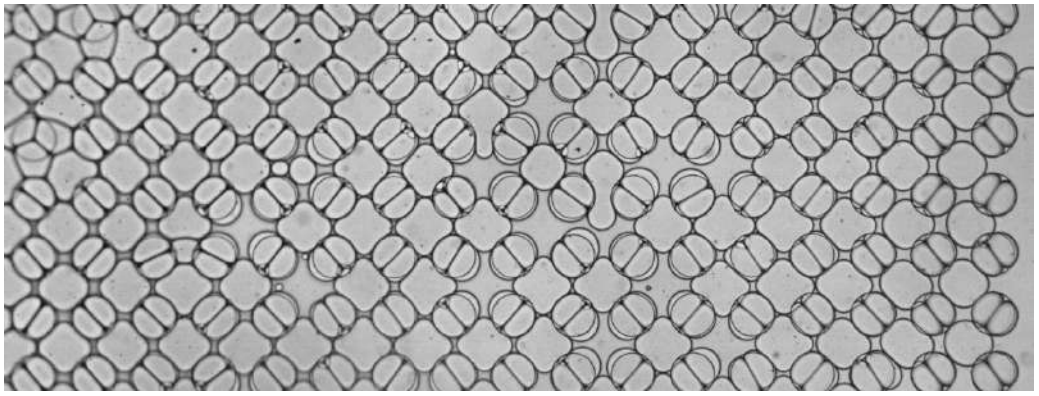

Figure 6.21: Illustration of the inter-well interaction due to the short distance between the wells set at $i = 50$ [μm]. The droplets are confined both within the wells and in the spaces separating them, hindering the proper functioning of the chip. The other parameters used are $H = 30$ [μm], $D = 100$ [μm], and $W = 30$ [μm]. The volume of the droplets is estimated to be $V \approx 300$ [pL].

1.1.2 Interwell distance of 400 µm

To prevent any interaction between the wells, the inter-well distance has been increased to $i = 400$ [μm]. Fig. 6.22 shows a cross-section of this new chip.

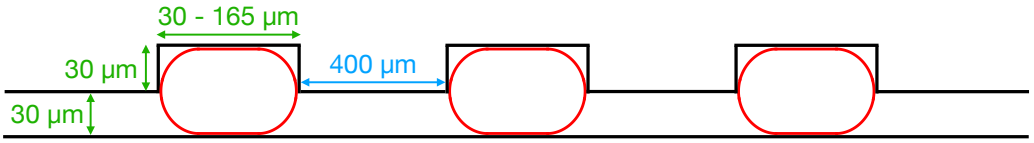

Figure 6.22: Schematic representation of a cross-section of the chip for capillary trapping. The parameters are set to $H = 30$ [μm], $i = 400$ [μm], and $W = 30$ [μm]. The diameter of the wells varies in the range $D = (30 - 165)$ [μm] with an increment of 0.2 [μm] between each well.

Regarding the results, they can be observed in Fig. 6.23. Depending on the size of the wells, the previous regimes can be encountered again. Trapping by the anchor technique appears for the smallest wells. Then, as the well diameter becomes sufficiently large, trapping by capillarity comes into play. This allows for gradually trapping one to five droplets. However, a new phenomenon appears in Fig. 6.23c. Between the trapping of one droplet per well and the trapping of two droplets per well, there is a transition. One of the droplets fully occupies the well while the second one can only enter partially. This regime could be particularly interesting to explore due to the asymmetry of the trapping force. The droplet confined within the well is much harder to extract than the one that has only partially entered, which can be considered as being trapped by an anchor. This characteristic could be exploited for trapping two distinct populations of droplets. However, in this situation, releasing the final droplet after fusion might be a challenging operation.

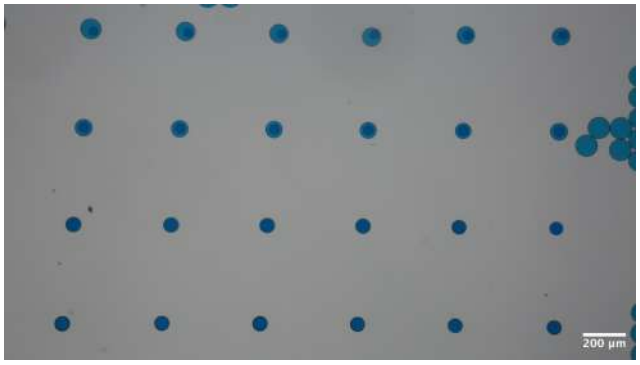

(a)

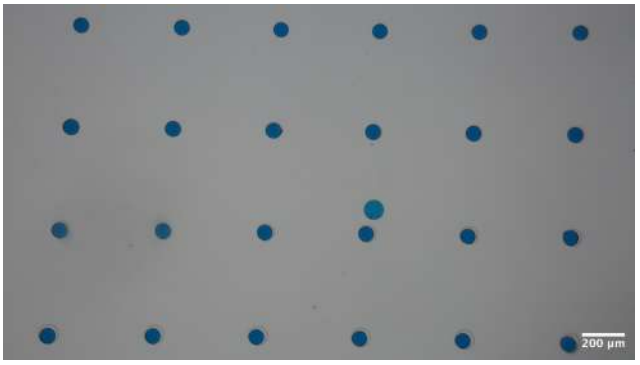

(b)

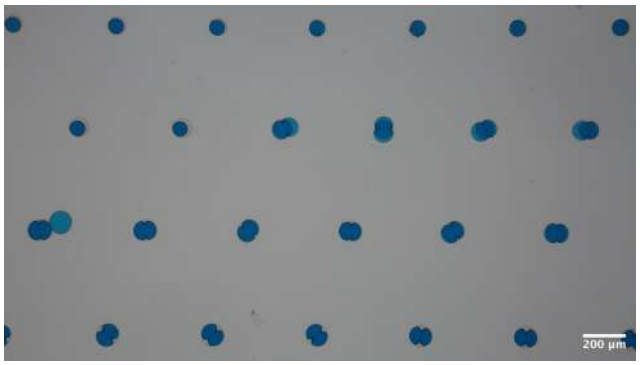

(c)

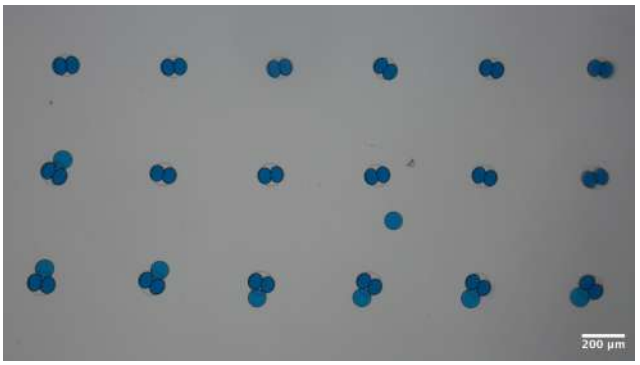

(d)

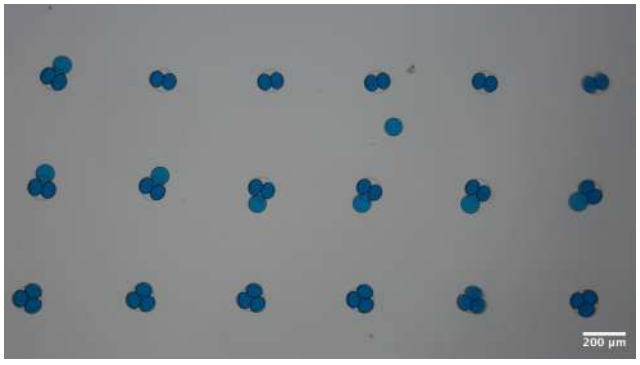

(e)

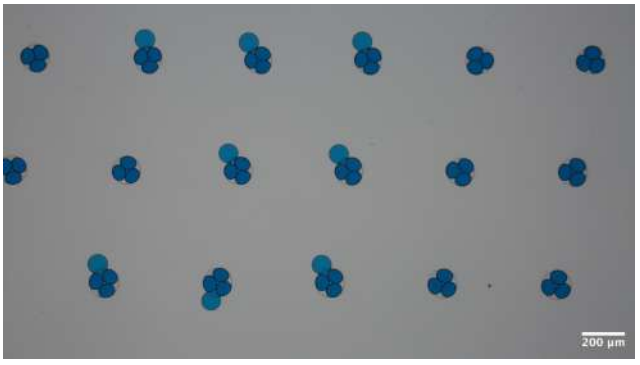

(f)

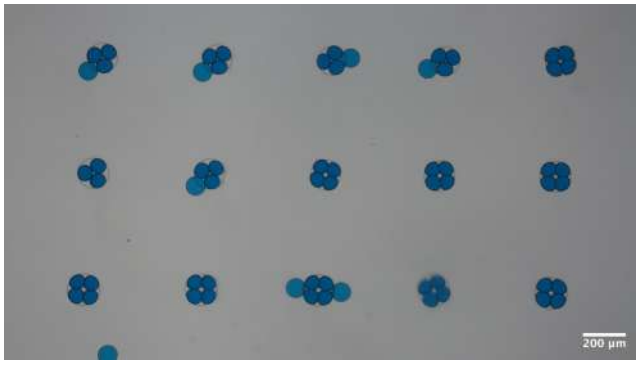

(g)

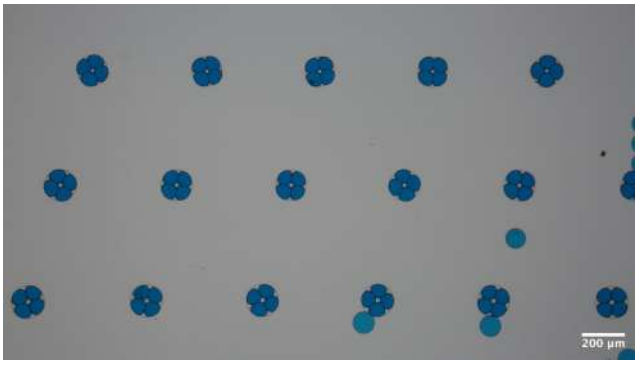

(h)

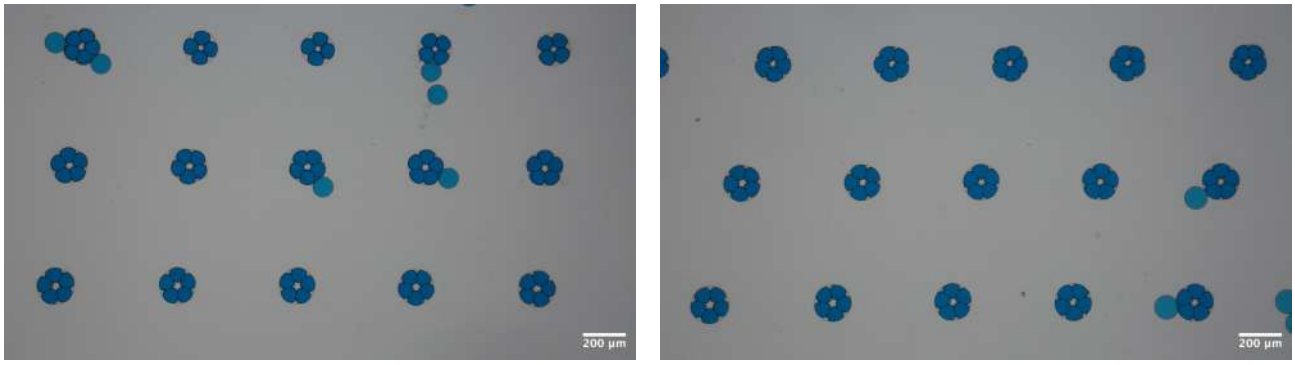

(i) (j)

Figure 6.23: Experimental photographs illustrating capillary trapping. The volume of the droplets, assumed to be constant, is estimated at $V \approx 215$ [pL], while the well sizes vary gradually from (a) to (j). The other parameters used are $H = 30$ [μm] and $W = 30$ [μm].

1.2 Deep wells

In this section, the chamber maintains a height of 30 [μm], but the depth of the wells increases from 30 to 80 [μm].

1.2.1 Interwell distance of 400 µm

This change in depth only applies to the second chip design as explained in section 3.2. Fig. 6.24 shows a cross-section of the chip and highlights the different possible trapping scenarios. It is a simplified representation, and not all scenarios are specifically depicted.

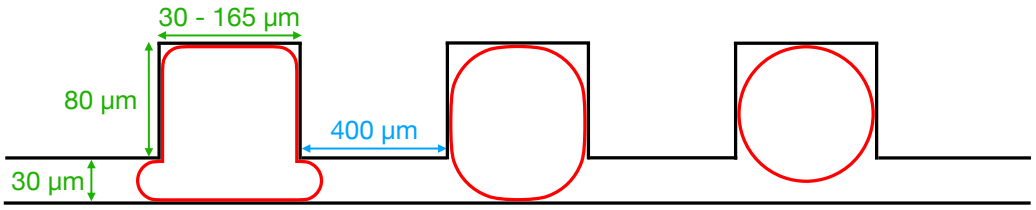

Figure 6.24: Schematic cross-section illustrating capillary trapping within deep wells. The droplet volume is adjusted to showcase different trapping possibilities. The parameters are set as $H = 30$ [μm], $i = 400$ [μm], and $W = 80$ [μm]. The well diameter varies within the range of $D = (30 - 165)$ [μm], with an increment of 0.2 [μm] between each well.

Fig. 6.25 displays the results of this experiment. Few differences can be observed compared to the same scenario but with wells of a depth of only 30 [μm] presented in section 1.1.2, even though the trapping appears nearly identical. Regarding trapping by an anchor, it appears again in this scenario. The depth of the well not influencing the result of the experiment. However, a notable difference is the absence of intermediate trapping. In the preceding analysis of section 1.1.2, it was highlighted that one droplet could partially fill the well while another occupied the remaining space, resulting in asymmetry in trapping. In this situation, the transition appears more abrupt, with no partial capture. Thus, trapping two populations seems to be a major challenge in this scenario. Furthermore, once a droplet is trapped in the well, it is extremely difficult to dislodge it. Therefore, the release of droplets also proves to be a complex task.

In the images, there is uncertainty as to whether the chip indeed possesses wells with a depth of 80 [μm]. The experiment was repeated to confirm this, and subsequently, the chip was disassembled to clarify its depth. This completely resolved the ambiguity. However, it's important to note that microfabrication quality can be significantly compromised for wells with such a thickness of SU-8. The size of the structure is comparable, if not smaller, than the height of the SU-8, which can lead to poor resolution, as discussed in section 2.3.

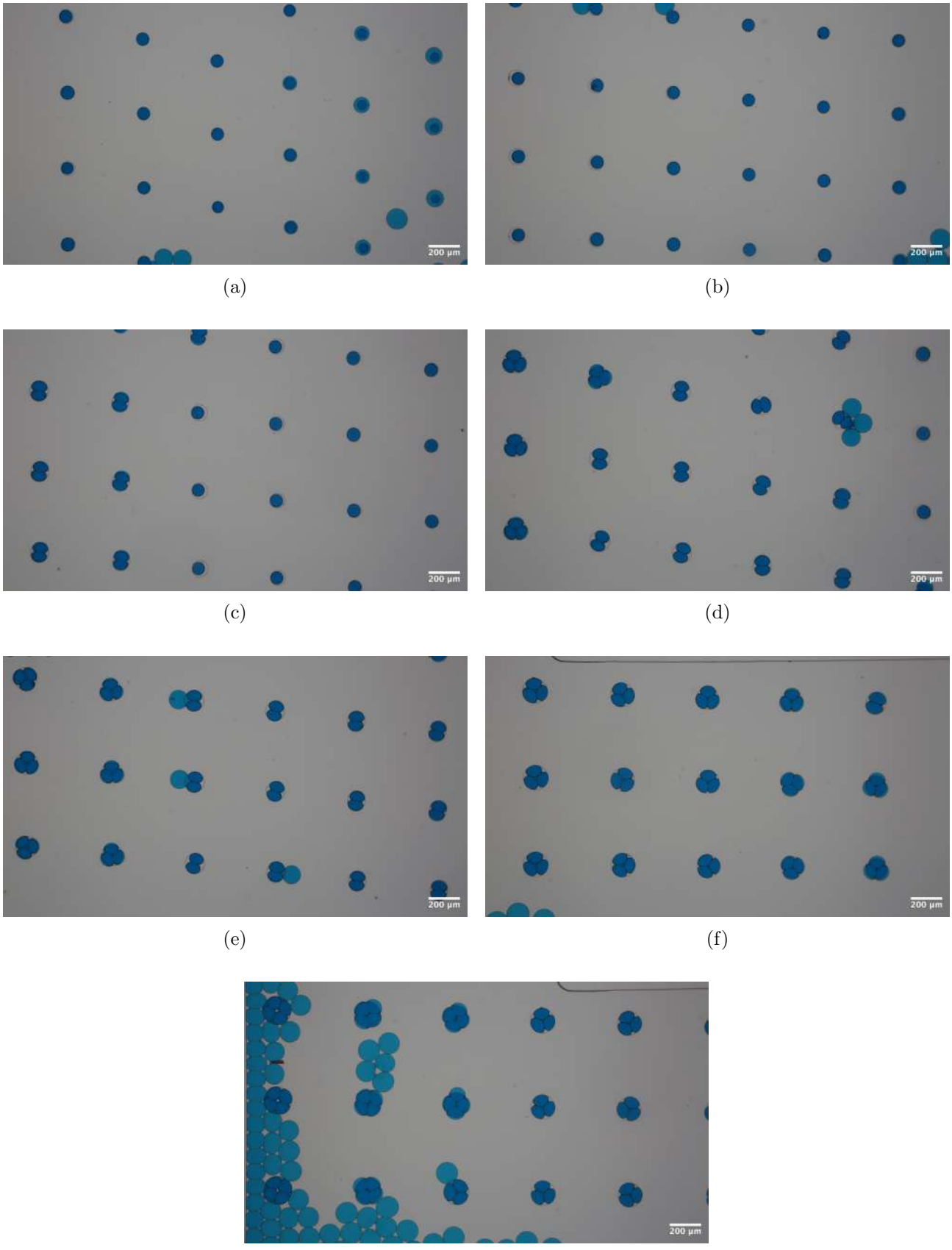

(a) (b) (c) (d) (e) (f) (g)

Figure 6.25: Experimental snapshots showcasing capillary trapping within deep wells. The parameters used include $H = 30$ [μm] and $W = 80$ [μm]. The well diameter ranges from image (a) to (g), covering $D = (30 - 165)$ [μm]. The droplet volume, assumed constant, is approximately $V \approx 380$ [pL].

1.3 Analysis of shallow chamber results

A graph presenting all the experimental data is shown in Fig. 6.26 to best summarize the results obtained for the different types of trapping in the shallow chamber. The problem involves too many parameters to hope to create a graph summarizing all the experiments. In an attempt to highlight a particular trend, it was chosen to normalize the droplet volume by the well volume on the x-axis. The goal is to compare the available space within the well with the space occupied by a droplet. On the y-axis, the choice was made to compare the diameter of the well with its depth. The idea is to quantify the geometric asymmetry of the well. Indeed, even if the well has the necessary volume to accommodate a droplet, it may not fit if the well is narrow and deep.

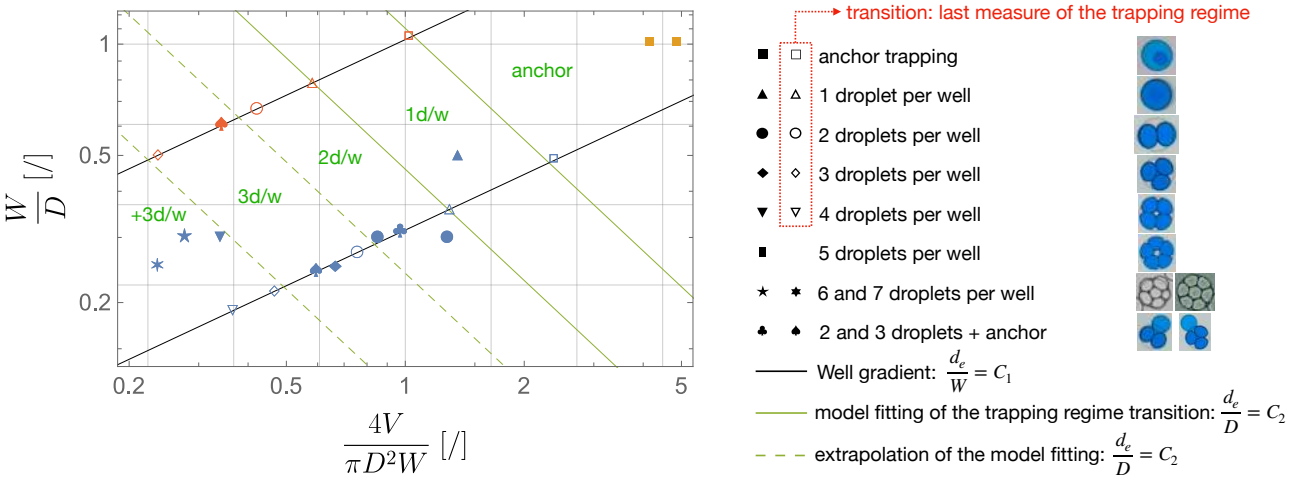

Figure 6.26: Logarithmic scale graph representing the experimental results of the shallow chamber ($H = 30$ [μm]). The blue and red data correspond to $W = 30$ [μm] and $W = 80$ [μm], respectively. The label "d/w" stands for droplet per well. The parameter $d_e \equiv 2r_e$ represents the major diameter of the droplet.

The solid black lines represent the evolution of the well gradient encountered in Fig. 6.23. In this experiment, both the droplet volume and the depth of the well are kept constant. Thus, by introducing C_1 as a constant, the condition is translated as follows:

$$\frac{d_e}{W} = C_1 \Longleftrightarrow \frac{W}{D} \propto \sqrt{\frac{V}{D^2 W}}. \tag{6.5}$$

Where it was used that $d_e^3 \propto V$. Thus, the well gradient leads to a power-law evolution of 1/2, which results in a straight line on a logarithmic scale. Along this gradient, only the points showing a regime transition have been displayed on the graph.

In the same vein, it is possible to define the transition from the anchor trapping regime to one droplet per well trapping regime by assuming that the diameter of the well must be equal to or larger than the diameter of the droplet. In practice, there are capillary forces that tend to deform the droplet. In this context, a constant C_2 is introduced, which is expected to be close to 1. Thus, it follows that:

$$\frac{d_e}{D} = C_2 \Longleftrightarrow \frac{W}{D} \propto \frac{D^2 W}{V}. \tag{6.6}$$

This last relationship is represented by a green line with a slope equal to -1 in Fig. 6.26. The two points marking the end of the anchor regime at $W = 30$ [μm] and $W = 80$ [μm] are used to determine the last parameter of the fit. Thus, the constant is fixed at $C_2 = 1.1$, which is of the same order of magnitude as the initial assumption. The fact that $C_2 > 1$ indicates that the transition occurs when the diameter of the droplet is greater than that of the well. This is coherent because the capillary forces will tend to deform the droplet and trigger the regime transition before reaching the equality of diameters.

This model was then extrapolated to the following trapping regimes. The transition between one and two droplets per well was well approximated and also plotted as a solid line. However, the quality of the fit seems to decrease as the number of droplets increases. To differentiate these regimes, the solid line has been changed to a dashed one. Unfortunately, such a small number of data points makes any attempt at justification difficult. Intuitively, the major difference beyond one droplet per well trapping regime would be the empty volume between the droplets within the well. The filling rate and the packing would change significantly and, of course, depend on W and V, which would explain this change in behavior.

1.4 Freed and squeezed droplet comparison

An interesting experiment with the confined droplet volume estimation model developed in section 2 is to test its range of validity against empirical results. For this purpose, a chip with a deeper chamber is used. Thus, the droplets within the chamber are in a free state and can be approximated by spheres. It is easy to ensure the extra degree of freedom by checking that the diameter of the droplet is smaller than the size of the chamber. A diagram of the situation can be seen in Fig. 6.27.

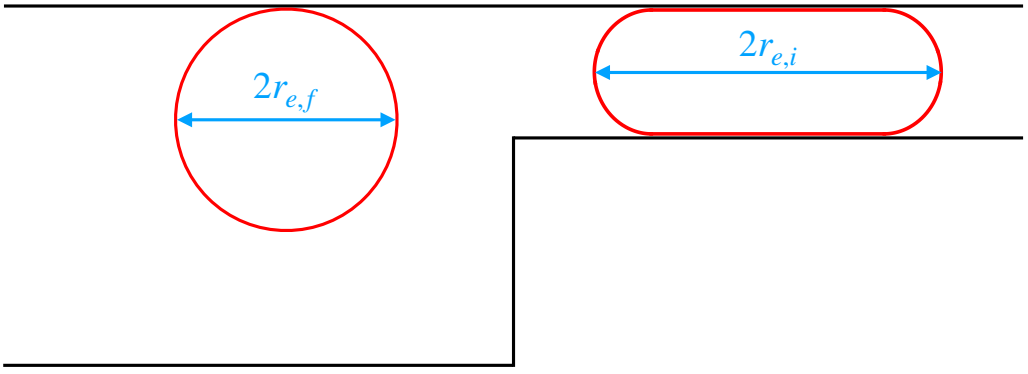

Figure 6.27: 2D cross-sectional schematic depicting the transition of a flattened droplet, when confined between two walls, to a freely spherical shape.

By filming the transition of the droplets at the entrance to the deeper chamber, it is possible to show two droplet radii. One corresponds to the state of a droplet confined between two walls and the second to the state of a free droplet. By subtracting the median and choosing the right parameters, it is possible to highlight the droplets using the Hough transform (Fig. 6.28).

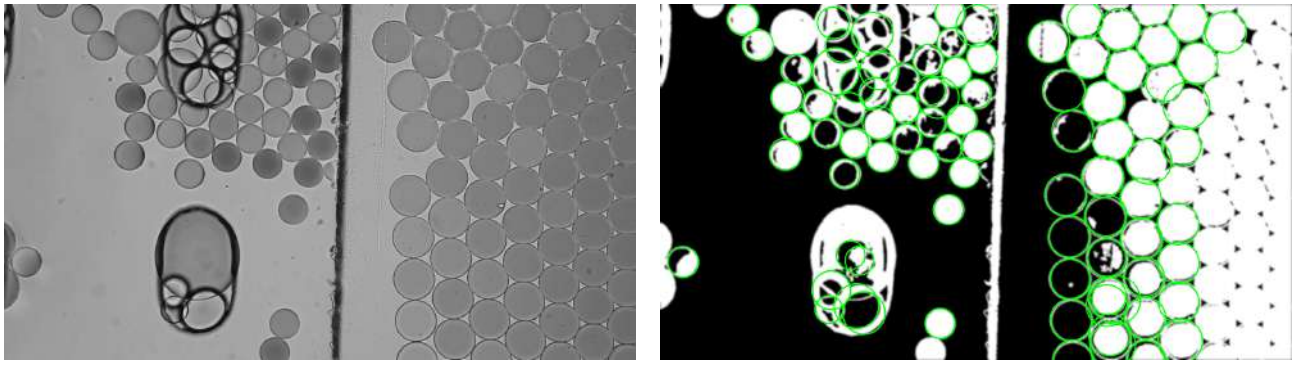

(a) (b)

Figure 6.28: Transition of confined droplets within a thickness of $H = 30$ [μm] to a free state in a deeper chamber. (a) Experimental photograph capturing the transition. (b) Highlighting the droplet contour detection achieved through image analysis using Python code.

It is possible to plot the histogram of the different droplet radii detected over the whole video (Fig. 6.29). Using the Python peak detection function with the correct prominence threshold, it is possible to detect the main peaks of the histogram. They correspond to the respective maxima of the two types of droplet population detected through their radii. The code then automatically separates the initial histogram into clusters according to the number of peaks detected. Using the peak as an initial estimate, it is possible to fit a Gaussian for each of the clusters.

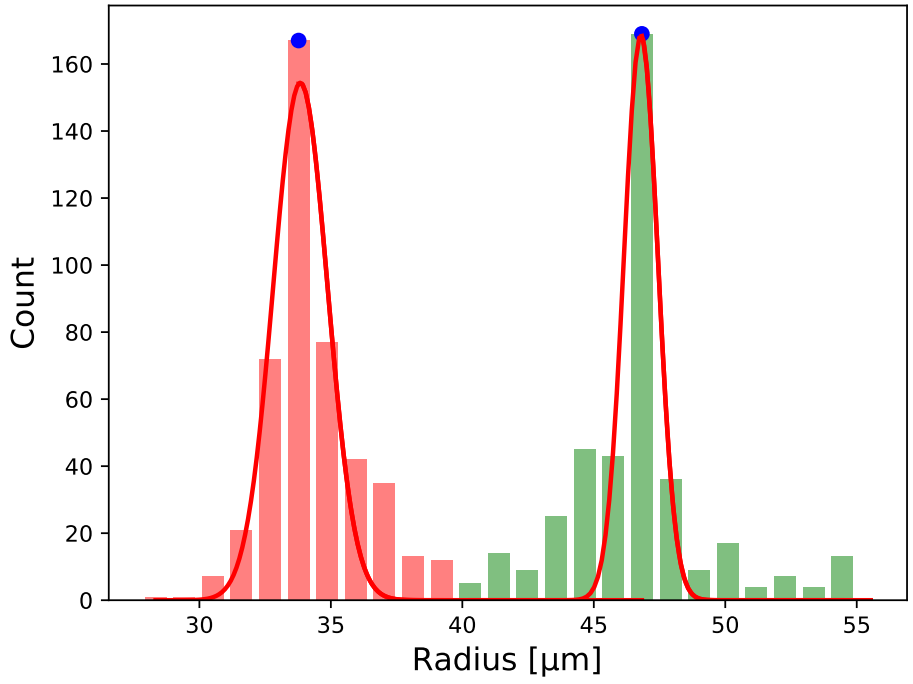

Figure 6.29: Histogram analysis of detected droplet radii between the initial and final states, highlighting peak identification, data clustering, and Gaussian fitting for each cluster. The average radii obtained are $r_{e,i} = 33.8$ [μm] with a standard deviation of $\sigma_i = 1.03$ [μm] for the first Gaussian (initial state), and $r_{e,f} = 46.8$ [μm] with a standard deviation of $\sigma_f = 0.65$ [μm] for the second Gaussian (final state).

In order to compare these observations with the most successful model of the nodoid developed previously, it is necessary to start from the average of the radii detected for the case of free droplets. This is estimated at 33.8 [μm] with a standard deviation of 1.03 [μm]. Via this radius, it is possible to find the volume of the spherical droplet $V = 162$ [pL]. By volume conservation and by using the previous nodoid developments, it is possible to find the correspondence between the volume and the maximum radius of the nodoid. The radius thus found is $r_e = 44.40$ [μm] using the mean value (with the standard deviation: 42.5 [μm] and 46.3 [μm]). Empirically, the average radius measured through the second Gaussian representing the droplets confined in the chamber is equivalent to $r_e = 46.8$ [μm] with a standard deviation of 0.65 [μm]. The error between theory and experiment is evaluated around 2.4 [μm]. To put this result in perspective, many approximations are made via image analysis on the empirical measurement of the radii. It is assumed that the droplets are perfectly circular and that all generated droplets have an identical size. This is not necessarily the case especially with motion. Furthermore, the focal plane must be centred on the maximum radius in both cases for an ideal resolution. However, the large radius of these two types of droplets is not located in the same focal plane (Fig. 6.27). Achieving the highlighting of the droplets to use the Hough transform also leaves a lot of freedom on the parameters to the user. The Hough transform itself is not perfect in this situation and generates errors in the detected circles. Finally, the estimation of the maximum radius in the initial state assume that the chamber had a height of 30 [μm]. However, the deposition of SU8 over a height of 30 [μm] during the fabrication of the wafer is an ideal case that is rarely perfectly achieved in practice, as mentioned in section 2.3. Fortunately, it is possible to give an order of magnitude for this parameter. Keeping the initial volume calculated for a free spherical droplet, it is possible to evaluate the evolution of its maximum radius in the case where it is crushed in a chamber of variable height (Fig. 6.30).

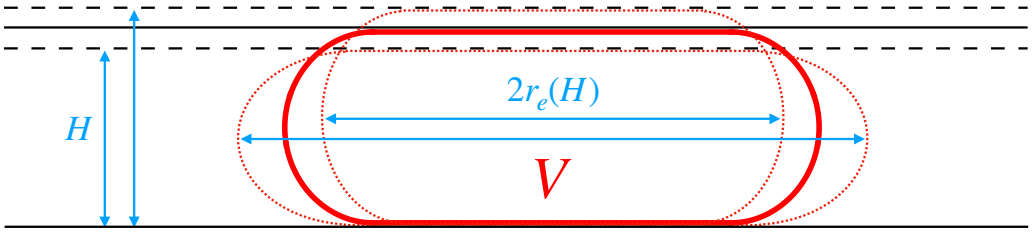

Figure 6.30: Schematic illustrating the variation of the diameter of a droplet with constant volume as a function of the chamber height.

The result of this study can be seen in Fig. 6.31.

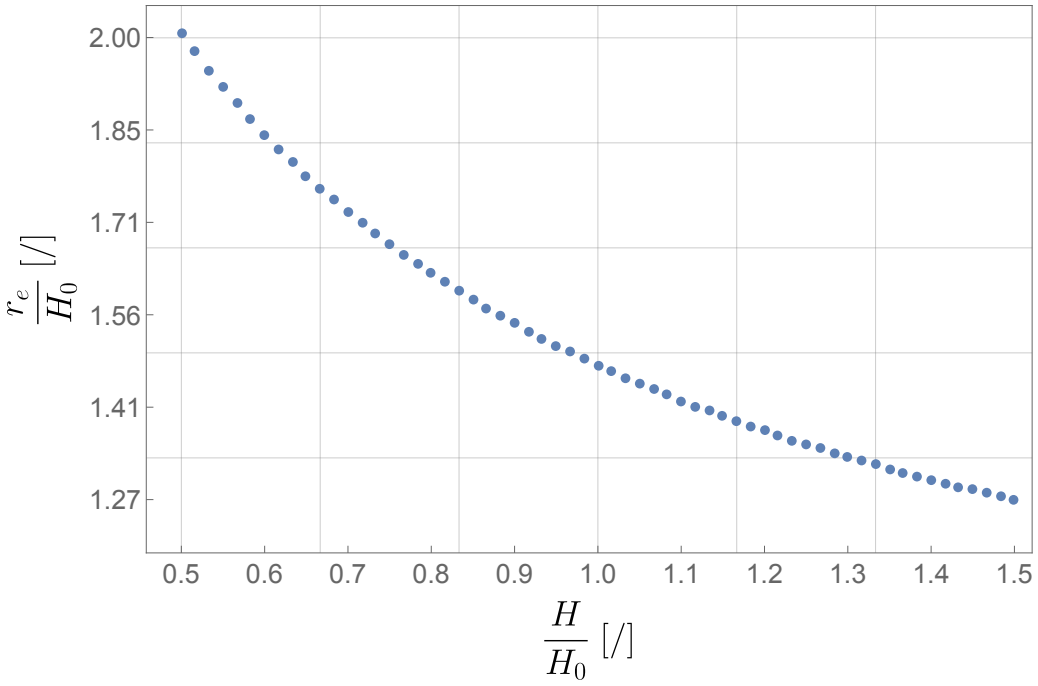

Figure 6.31: Variation of the droplet radius r_e as a function of the chamber height H at a constant volume $V = 162$ [pL]. The chamber height and the radius are normalized by the standard height $H_0 = 30$ [μm].

Using the empirical results from estimating the radius when the droplet is confined $r_e = 46.8$ [μm] and the volume when it is in the free state $V = 162$ [pL], it is possible to determine the required height of the chamber $H = 26.5$ [μm]. The characterization of this chip yielded an average height of $H = 29.94$ [μm], as explained in section 2.2. It's important to note that these measurements were not taken at the specific location considered in this analysis, but rather at the edges of the chip. However, despite this potential error in the thickness of the SU-8 layer, the discrepancy is too significant for it to have a meaningful impact.

2 Deep chamber

It is now time to test the case of the deeper chamber. In this entire section, trapping undergoes a radical change as it no longer relies on capillarity but rather on Archimedes' principle.

This deeper chamber no longer requires support pillars or walls to ensure spacing between the top and bottom of the chamber, as its depth has been extended to approximately 120 [μm]. The risk of the top chip adhering to the bottom of the chamber as it was the case in the shallow chamber becomes almost nonexistent. The thickness of 120 [μm] simply refers to the thickness of the adhesive tape used to enlarge the chamber, which is overlaid on the existing SU-8 layer. To ensure the chamber height, a rough characterization was performed.

In this section dedicated to the deeper chamber, the outlet position has been relocated. The hole was punched directly into the chamber. Since the droplets experience a completely free state within the chamber, it becomes challenging to coerce them to collapse back into the 30 [μm] high channels in order to reach the conventional outlet.

2.1 Shallow wells

The analysis begins with shallow wells of a depth of 30 [μm].

2.1.1 Interwell distance of 50 µm

Since the change only affects the part containing the chamber, all types of wells could be tested. The study starts with all arrays of identical wells spaced by 50 [μm]. A sketch of the situation is shown in Fig. 6.32.

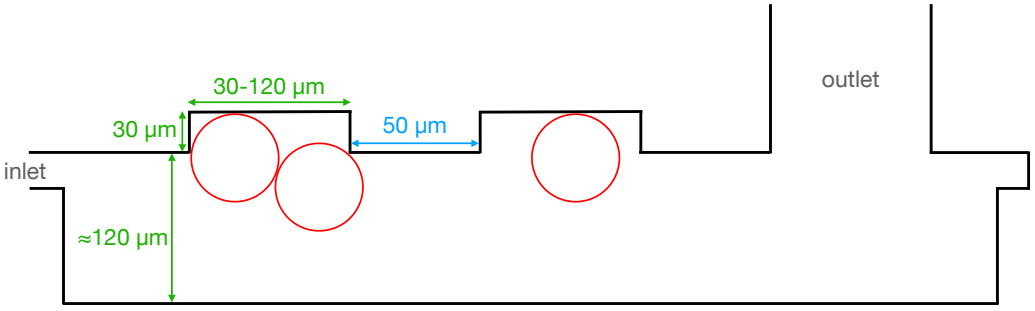

Figure 6.32: Schematic cross-section of the chip featuring a deep chamber and shallow wells. The outlet had to be relocated to allow the exit of spherical droplets. The chip parameters include $H \approx 120$ [μm], $W = 30$ [μm], and $i = 50$ [μm]. The diameter of the wells varies depending on the experiment and is selected from the list $D = (30, 40, 50, 60, 80, 100, 120)$ [μm].

This type of trapping is illustrated through Fig. 6.33. The first notable difference of this chip is the trapping efficiency. Dispersion of the droplets was quite challenging in the case of the shallow chamber in section 1; however, in this situation, it occurs naturally, leading to a more regular trapping. Furthermore, unlike the shallow chamber, the droplets enter the wells much more slowly. Additionally, they are not deformed and maintain a spherical shape. Moreover, simply flipping the chip allows for the release of the droplets due to the buoyancy force operating in the opposite direction. This contrasts with the shallow chamber where trapping did not allow for easy droplet release.

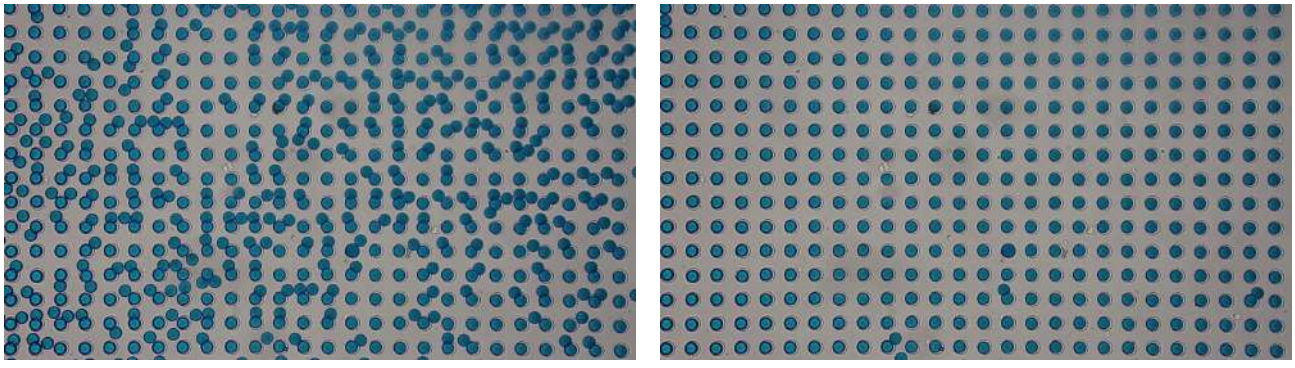

(a) (b)

Figure 6.33: Experimental pictures demonstrating the trapping of droplets in a deep chamber and shallow wells via buoyancy-driven forces. (a) Illustration of the chip during the trapping phase. (b) Image of the chip after flushing out the excess droplets, highlighting the trapped droplets in the wells. This scenario gives one droplet inside each well. The parameters used for this experiment are as follows: $H \approx 120$ [μm], $W = 30$ [μm], and $D = 80$ [μm]. The volume of the droplets is estimated to be $V \approx 175$ [pL].

In order to capture a maximum number of droplets, the chip consisting of an array of 120 [μm] wells was used (Fig. 6.34). The number of droplets is limited to two. They do not attempt to occupy the entire well as was the case with the shallow chamber in section 1. Instead, they continue their path rather than trying to fill the empty space. By carefully observing the image contrast, some droplets appear brighter than others. Specifically, each well is composed of both a bright droplet and a dark droplet. The cross-section shown in Fig. 6.32 illustrates the arrangement of droplets leading to this configuration. One droplet is completely inside the well and touches the bottom, while the second droplet has a point of contact on the edge of the well and another on the droplet already present inside. It is therefore mostly located in the chamber. Considering the asymmetry of the trapping, The droplet located on the surface of the well can be easily displaced simply by the arrival of new droplets, while the one trapped at the bottom of the well remains in place. This configuration could be particularly interesting to study when trapping two distinct populations of droplets. No difference in size is required between these two populations, and the well geometry consists of simple circular wells.

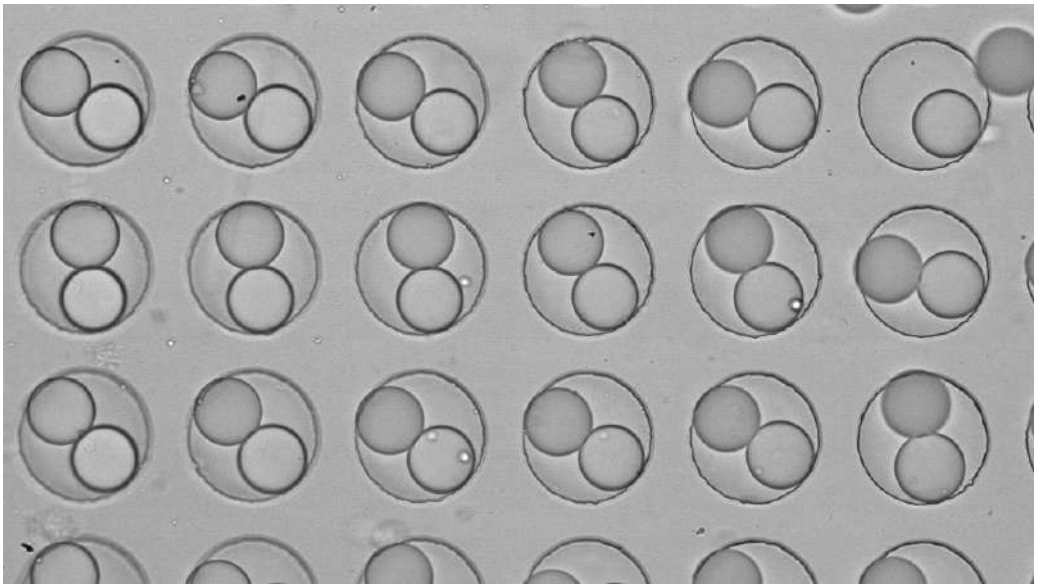

Figure 6.34: Experimental picture of the droplets trapping via buoyancy-driven forces inside a chip with deep chamber and shallow wells. The chip enables the capture of two droplets per well using the following parameters: $H \approx 120$ [μm], $W = 30$ [μm], and $D = 120$ [μm]. The volume of the droplets is estimated to be approximately $V \approx 155$ [pL].

2.1.2 Interwell distance of 400 µm

Following the same principle as the previous study on shallow wells, the distance between the wells has been increased to 400 [μm] to make them independent (Fig. 6.35). In order to highlight the transition between different trapping regimes, the diameter of the wells has been adapted according to a double gradient as explained in section 3.2.

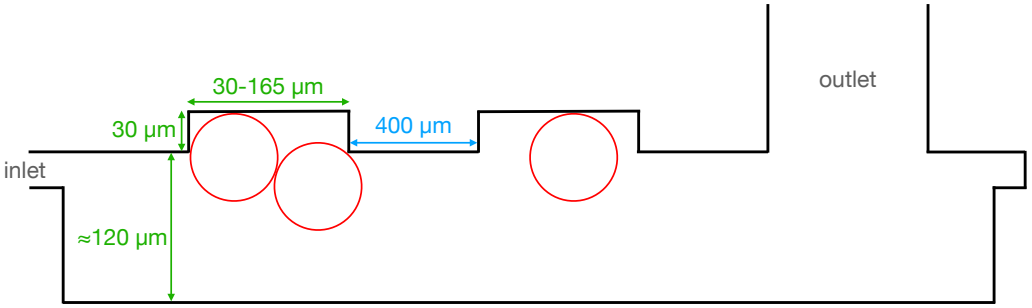

Figure 6.35: Schematic depicting the cross-sectional view of a chip with a deep chamber and shallow wells. The outlet had to be relocated to allow the exit of spherical droplets. The specific parameters of this chip are: $H \approx 120$ [μm], $W = 30$ [μm], and $i = 400$ [μm]. The well diameter varies within the range of $D = (30 - 165)$ [μm], with an increment of 0.2 [μm] between each well.

The result of this study can be seen in Fig. 6.36. A new droplet is admitted into a well only if the geometric structure formed by the spheres of the different adjacent droplets fits inside the well. Unlike the results of section 1, No deformation is observed, and there are empty spaces present in the wells. However, it occasionally happens that some droplets in the chamber adhere to the cluster of droplets present in the well, as can be observed in certain images. Although this adhesion is weak as the droplets can easily be dislodged with sufficient oil flow.

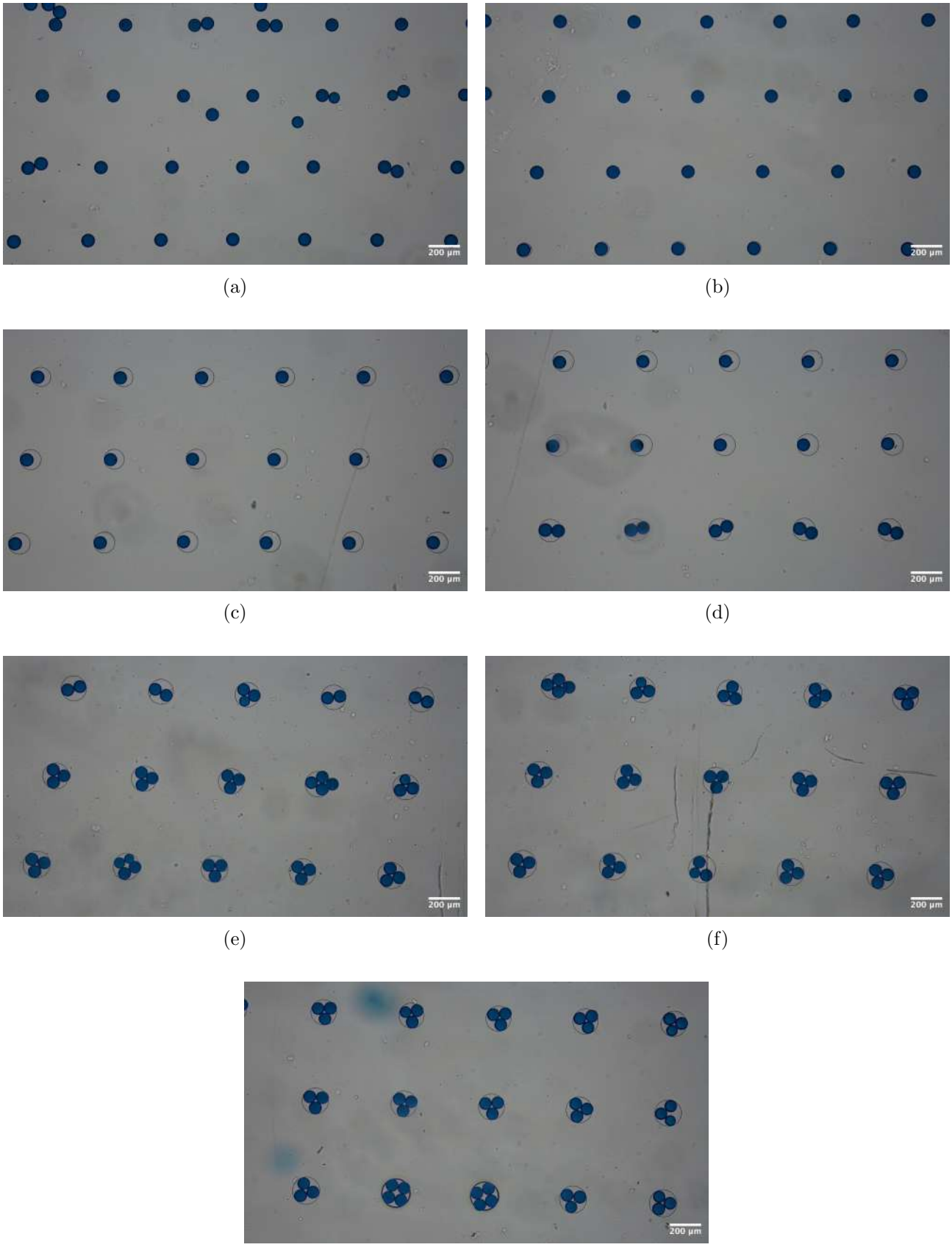

(a) (b)

(c) (d)

(e) (f)

(g)

Figure 6.36: Experimental images highlighting the trapping of droplets by buoyancy-driven forces. The chip features a well gradient between (a) to (g), enabling the visualization of the changing number of droplets per well. The other parameters used are $H \approx 120$ [μm] and $W = 30$ [μm]. The volume of the droplets is estimated to be 300 [pL].

Fig. 6.36c shows the example of one droplet per well, where the size of the well is significantly larger than that of the droplet.

In Fig. 6.36d, it is possible to observe the previous trapping regime of two droplets per well presented in section 1. Upon careful observation, there is again a droplet trapped at the bottom of the well and another one mostly located in the chamber for a certain range of well sizes. This demonstrates the full reproducibility of this previous regime.

Beyond a certain well size, two droplets can fit inside them. Furthermore, it is also possible to observe the transition to three and finally four droplets per well.

In Fig. 6.36a, even though the well diameter is smaller than the droplet diameter, the droplet is still trapped. This indicates that the anchor trapping regime encountered previously is still applicable for the deep chamber. The depth of the well has little importance in this situation; it just needs to be capable of accommodating the trapped droplet's spherical cap.

2.2 Deep wells

This last scenario combines wells with a depth of 80 [μm] with a deeper chamber with a height of approximately 120 [μm]. A diagram of the situation is depicted in Fig. 6.37:

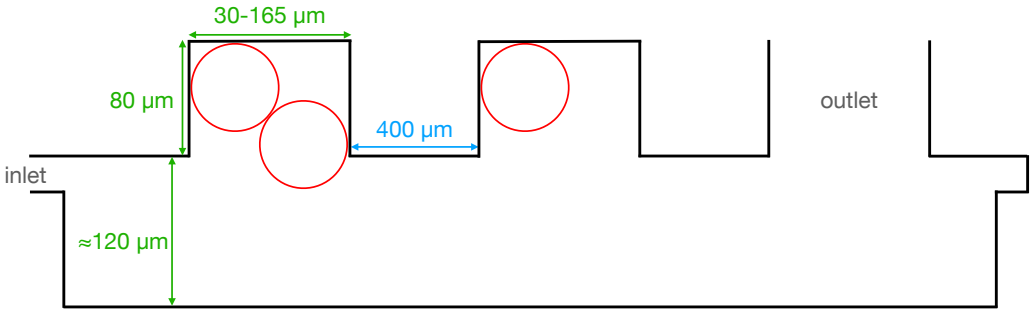

Figure 6.37: Schematic illustrating the cross-section of a chip enabling trapping by buoyancy-driven forces. The chip features a deep chamber and deep wells. The outlet has been relocated to allow for the evacuation of droplets in spherical form. The dimensions used are: $H \approx 120$ [μm], $W = 80$ [μm], $i = 400$ [μm]. The diameter of the wells varies in the range of $D = (30 - 165)$ [μm] with an increment of 0.2 [μm] between each well.

Regarding the Fig. 6.38, there is the significant number of droplets per well. In this situation, two distinct populations of droplets were introduced into the chip to assess the trapping efficiency. As suspected initially, the droplets located at the bottom of the well remain in place despite a significant flow of yellow droplets. However, the surface droplets can be displaced depending on the arrangement of the blue droplets within the well and the size of the well itself. Consequently, it is possible to create assemblies consisting mostly of blue droplets with a few yellow droplets. This suggests the possibility of a partially random filling model that could be used to combine x blue droplets with y yellow droplets. The resulting color after fusion could be analyzed to determine the proportions in which the droplets were combined.

In particular, in Fig. 6.38d, despite the limited droplet dispersion observed during this test in this region of the chip, it is possible to observe the trapping of two droplets within a single well. Each of these two droplets comes from a different population, which is indicated by the green

color of the well. The blue droplet appears to have settled at the bottom of the well, while the yellow droplet remains predominantly in the chamber. If both droplets entered the well, it would consist of two blue droplets that no yellow droplet could dislodge. For this reason, the yellow droplet can be displaced by new arrivals. This analysis is confirmed by calculating the diameter of the droplets relative to the depth of the well. However, the population of yellow droplets has a slightly larger size than that of the blue droplets. For this reason, it is difficult to determine if the two droplets are in contact within the well. It's possible that only the blue droplet can enter, while the yellow droplet might be trapped by an anchor, thus preventing it from penetrating deeply into the well.

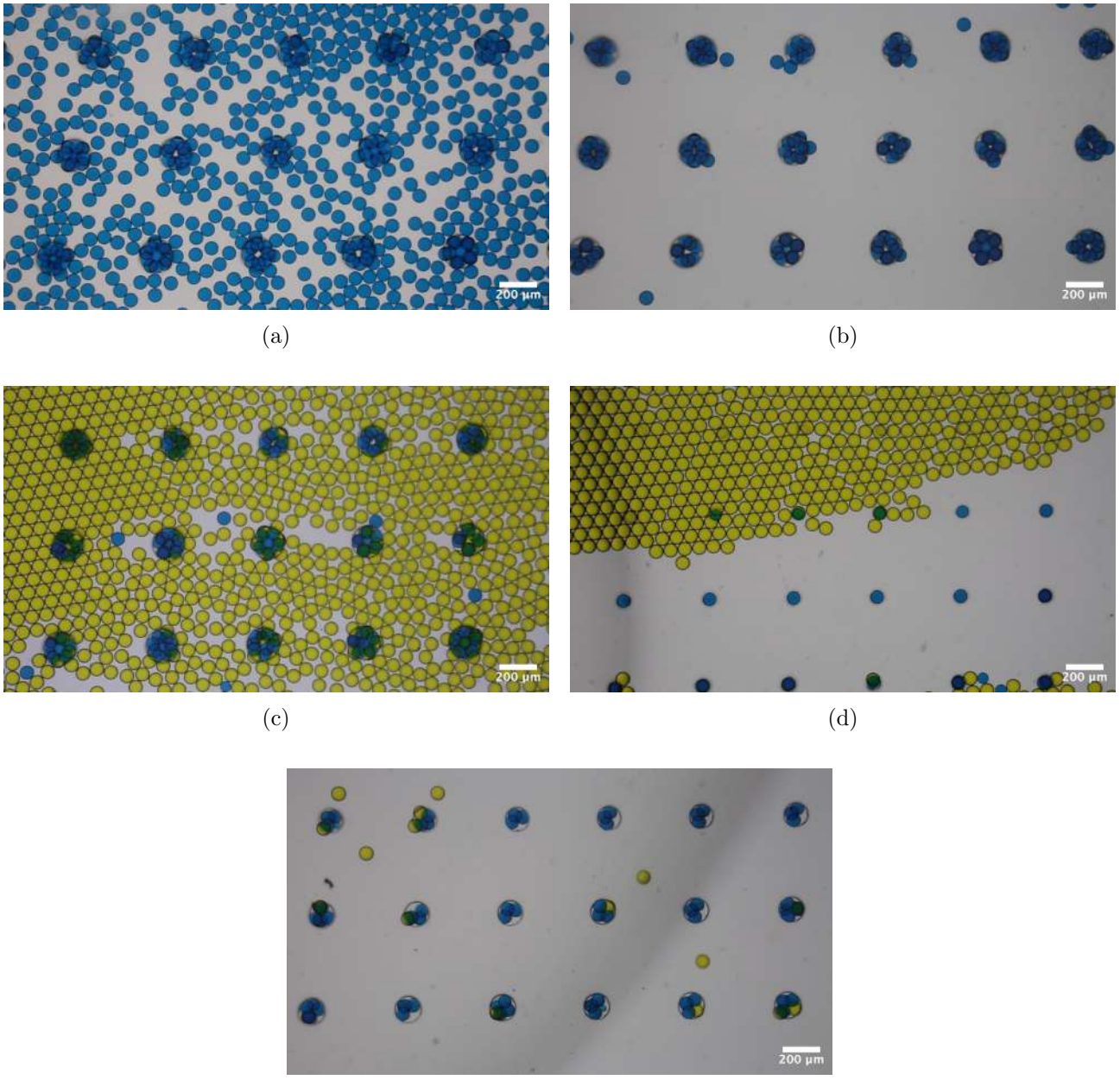

(a) (b)

(c) (d)

(e)

Figure 6.38: Experimental photos showcasing the trapping of two populations of droplets by buoyancy-driven forces within a chip featuring a deep chamber and deep wells. (a) Arrival of the first population. (b) Flushing of excess droplets. (c) and (d) Arrival of the second population. (e) Flushing of the second population, highlighting the trapped droplets. The diameter of the wells increases gradually by 0.2 [μm] across the chip and falls within the range of $D = (30 - 165)$ [μm]. The other dimensions are set to: $H = 120$ [μm] and $W = 80$ [μm]. The volume of the droplets is estimated to be $V_1 \approx= 170$ [pL] for the blue population and $V_2 \approx 210$ [pL] for the yellow one.

As a final remark, it should be noted that for all types of wells encountered so far, trapping always occurs. There is always at least one trapped droplet, whether it is due to an anchor, capillarity, or buoyancy force.

2.3 Releasing

To conclude this section, attention will be focused on the release of the droplets. Trapping by buoyancy allows for a simple release of the droplets by flipping the chip, as explained in Labanieh's article[109]. The challenge was to capture this phenomenon effectively. It was necessary to find a way to film the chip while flipping it. As explained in section 4, a setup was assembled using `Thorlabs` components for this purpose. It was not possible to focus on the flipped chip under the microscope due to the connections, which raised the chip in that orientation. Simply disconnecting the chip and flipping it to visualize the result under the microscope seemed like a feasible idea. However, to capture the moment of release as accurately as possible, the setup appeared more appropriate. In practice, it was not easy to manage the camera lens, which tended to collapse under its own weight. The chip also had a tendency to move during rotation. Lastly, controlling the lighting throughout the process was quite challenging. The result can be seen in Fig. 6.39. In this setup, flipping the chip is sufficient to trap and release the droplets repeatedly.

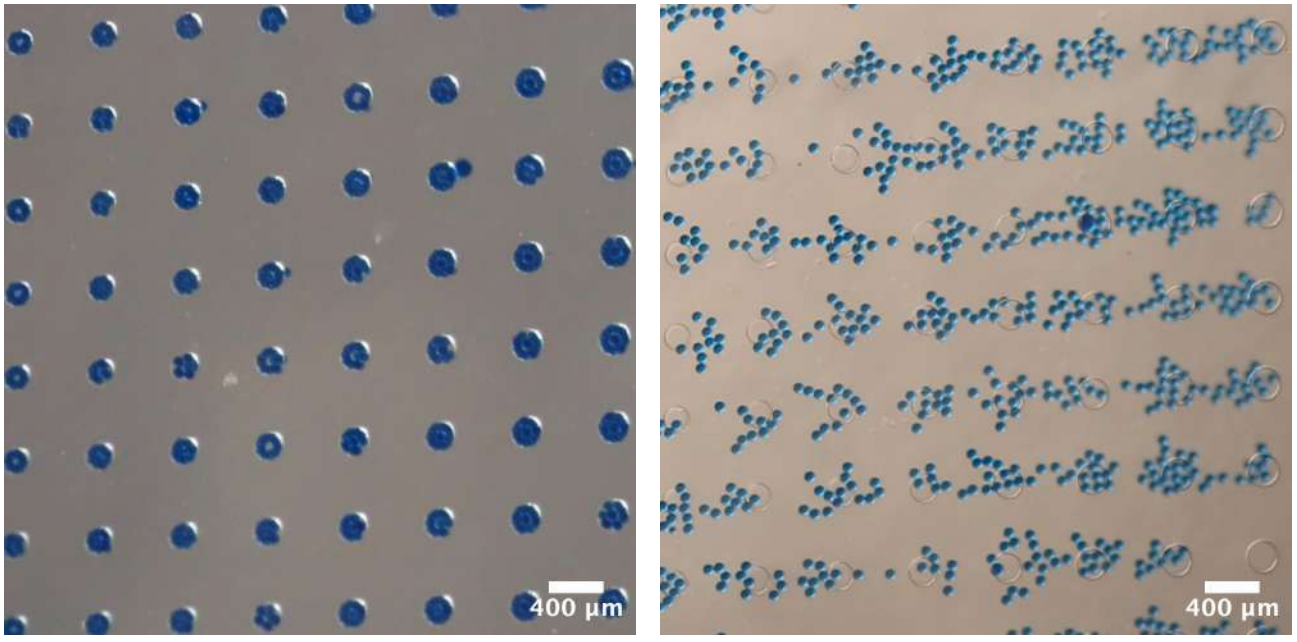

(a) (b)

Figure 6.39: Releasing of the droplets trapped by buoyancy-driven forces. (a) Trapped droplets. (b) Flipping the chip to enable droplet release. The chip parameters are set to: $H \approx 120$ [μm] and $W = 30$ [μm].

2.4 Analysis of deep chamber results

The analysis will be very similar to that performed for the shallow chamber 1.3. The major difference is the absence of capillary force. The droplets thus retain their spherical shape. By applying the reasoning from the previous analysis, the Fig. 6.40 shows the result obtained in this situation.

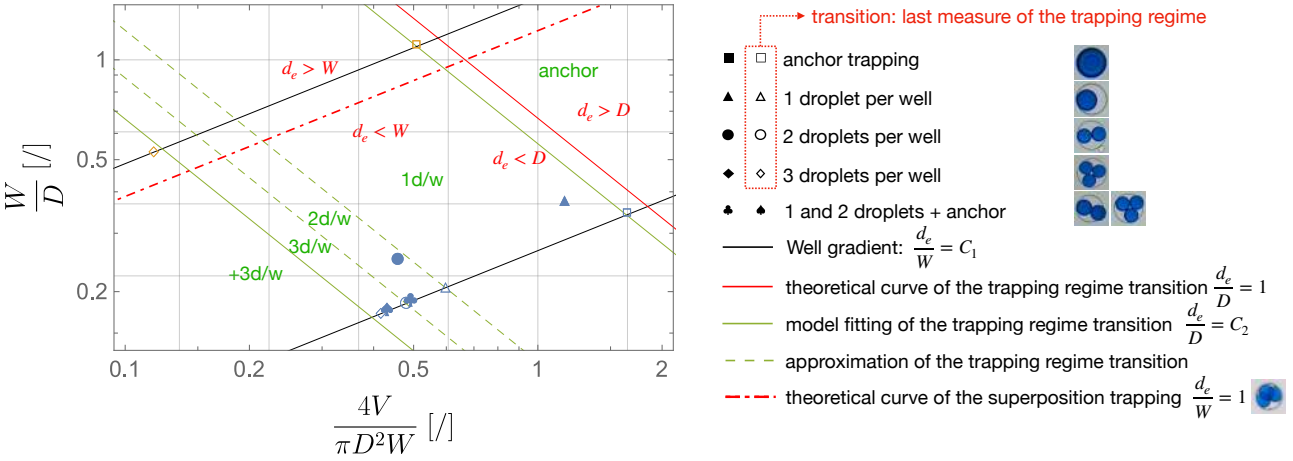

Figure 6.40: Logarithmic scale graph representing the experimental results of the deep chamber ($H = 120$ [μm]). The blue and orange data points correspond to $W = 30$ [μm] and $W = 80$ [μm], respectively. The label "d/w" indicates droplets per well. The parameter $d_e \equiv 2r_e$ represents the diameter of the spherical droplet.

Following the reasoning of section 1.3, the well gradient is represented by a straight line in logarithmic scale corresponding to $\frac{d_e}{W} = C_1 \iff \frac{W}{D} \propto \sqrt{\frac{V}{D^2 W}}$.

The transition from a droplet trapped by an anchor to a regime of Archimedes where it fully enters the well should result in the equivalence of diameters, and thus, the equality $\frac{d_e}{D} = 1 \iff \frac{W}{D} = \frac{2}{3}\frac{\pi D^2 W}{4V}$. Fig. 6.40 illustrates the corresponding straight line. In this situation, the constant can be fixed as the droplets maintain their spherical shape, and no capillary force comes into play to deform them. However, in practice, the constant is not perfectly equal to $\frac{2}{3}$. A fit has been performed on the observed experimental transition. The constant is evaluated in this case as $C_2 = 0.56$. This error can be partly explained by the difficulty in precisely observing the transition zone. In this case, the measurement represents a certain transition to another regime. However, there is a blurry zone of well diameters in which it is not possible to definitively determine the type of trapping.

Just like in the previous analysis, an attempt to extrapolate this model was made. However, only one data point was available for the transition to the following trapping regimes. Thus, the zone of trapping of two and then three droplets per well was adjusted along a line with the same slope as before. These fits are, of course, much more approximate and are only present to give a general idea of the transition zone. The transition to 4 droplets per well could be measured using two data points, and a line with the same slope was adjusted with a more rigorous fit.

The last model that seems relevant to consider is the transition $\frac{d_e}{W} = 1$. This equality marks the transition for which the well would be able to accommodate more than one droplet based on its depth. For very large depths, this analysis would be similar to the problem of packing spheres inside a cylinder.

Chapter 7

Asymmetric wells

This section marks the beginning of the second part of the experiments. So far, circular well designs have been considered. They represented the most basic shape to study and allowed for the development of analytical models on trapping analysis. This section aims to be more exploratory. For most designs, the objective is to achieve trapping of two different populations of droplets. It is also an opportunity to test various trapping ideas encountered in the literature and adapting them to the possibilities offered by the laboratory. Fig. 7.1 summarizes all the well geometries that will be encountered in this section, as well as the expected trapping outcomes for the two droplet populations whenever possible.

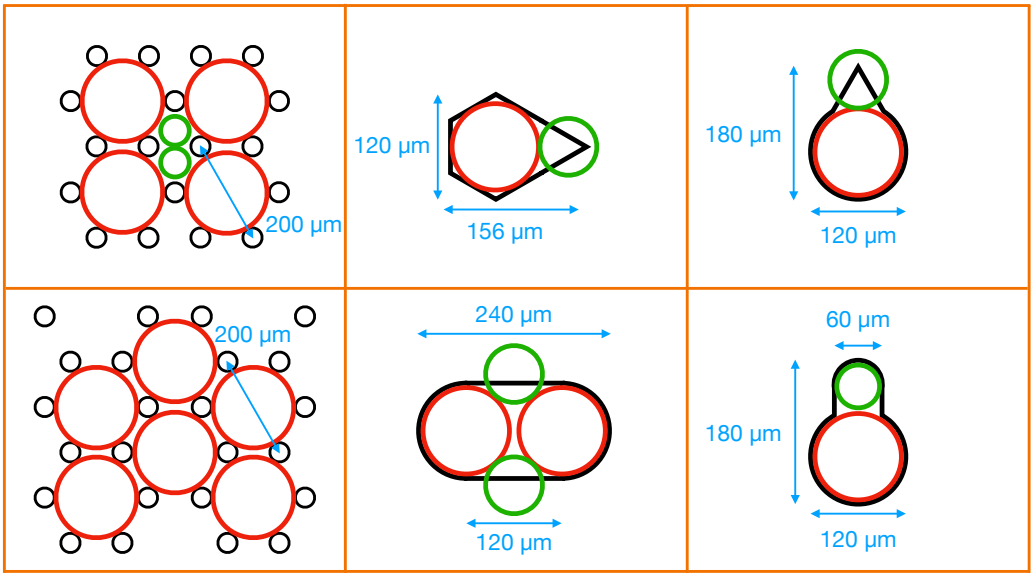

Figure 7.1: Schematic illustrating the six types of asymmetric wells used in this section and presented in section 3.2. The characteristic dimensions are indicated on the diagram and remain constant for all the wells. The inter-well distance is constant and set to $i = 400$ [μm] for all the wells. A theoretical sketch of the trapping operation for two distinct droplet populations is included on the diagram. The colors red and green are used to differentiate these populations

Like the previous study, four cases need to be considered. These involve combinations of a shallow or deeper chamber with two distinct well depths. Unlike what can be found in the literature [5, 52, 95], no attempt at multi-layer trapping within a single well has been made in this work.

1 Shallow Chamber

Maintaining the previous order, the analysis begins with the case of a chamber height of $H = 30$ [μm].

1.1 Shallow wells

The wells are also at a depth of $W = 30$ [μm] for this first case study.

Figure.7.2 shows the trapping of two droplet populations. This is achieved through the difference in size between these droplets. What is observed in Figure.7.2b is a common outcome. The expected droplets are trapped within the wells, but unfortunately, stray droplets adhere to those contained within the wells. Increasing the oil flow to flush them out can result in untrapping, either directly or through collisions between the stray droplets and the droplets in the wells. These stray droplets pose a problem as they may also participate in fusion by PFO. With a lot of patience, it is possible to achieve the result shown in Figure.7.2c. Unfortunately, one of the wells is missing the small yellow droplet. Among the wells where double trapping has worked, there is a variation in droplet size from one well to another. This is because it is difficult to create large droplets that are well-suited to the size of the large well using the junction employed in the chip. In reality, it was much easier to create the large droplets by merging small droplets already present in the wells, rather than struggling with the pressures to generate properly sized droplets through the junction. By reasoning, it seems that a cluster of small droplets occupies more space than an equally sized large droplet. Simply put, within the cluster of small droplets, there are empty spaces between them. Fusion allowed the release of this space and the introduction of a second droplet from the yellow population.

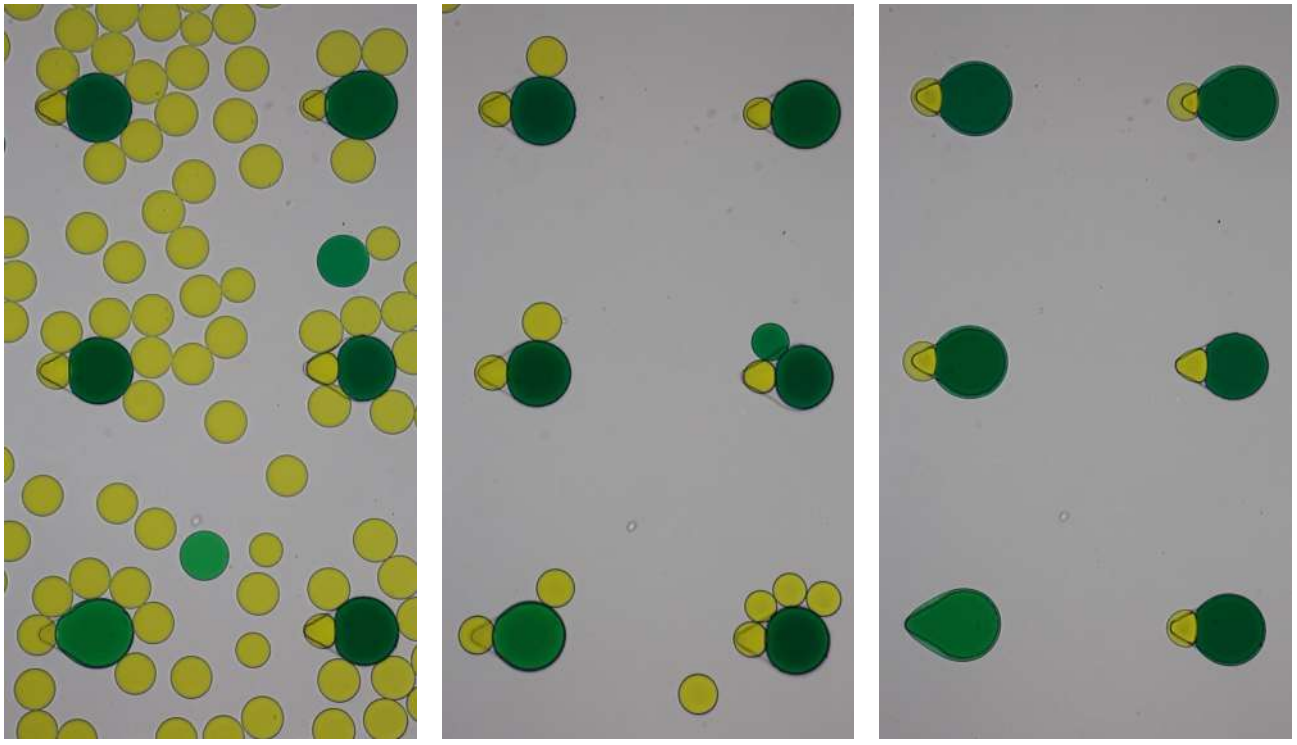

(a) (b) (c)

Figure 7.2: Experimental picture showing the trapping of two distinct droplet populations in a capillary regime. The dimensions of the chip are set to: $H = 30$ [μm] and $W = 30$ [μm]. The estimated volume of droplets is approximately $V_1 = 670$ [pL] for the first green population and $V_2 = 145$ [pL] for the second yellow population.

The next experiment involves a different type of well in which double trapping had also been successfully achieved (7.3). In the shallow chamber, the droplets are flattened, causing them to attempt to occupy a significant portion of the available space within the well. The trapping of large droplets initially leads to voids of insufficient size for another droplet of the same size to fit in. However, the second population consisting of small droplets can take advantage of these gaps to fit in. As the trapping is highly effective, it is easy to purge the chamber of excess droplets. It would then be possible to proceed with fusion. Not all wells contain the same quantity of droplets. As explained earlier, it is difficult to obtain large droplets of identical size with this junction. Addressing this issue, it would be pertinent to investigate reproducibility and verify the regularity of the pattern.

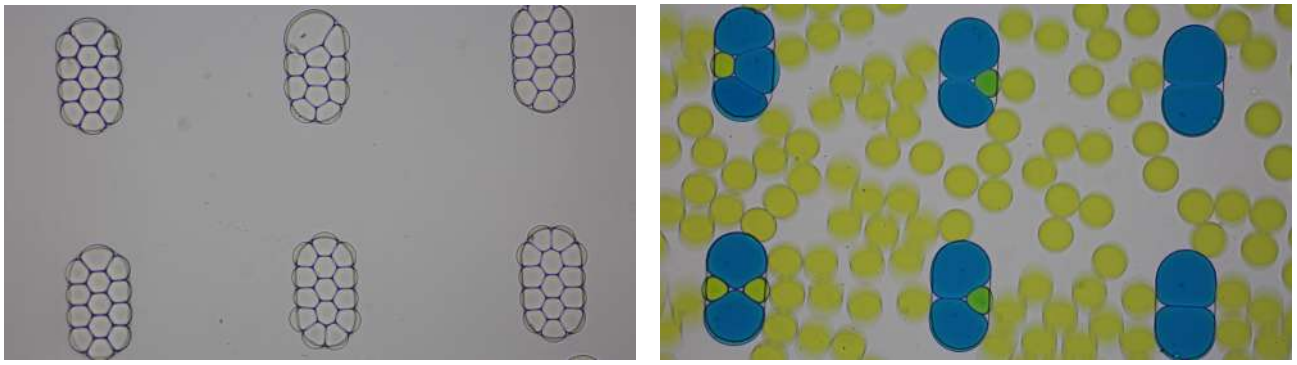

(a) (b)

Figure 7.3: Experimental picture showing trapping in capillary regime. The characteristic dimensions of the chip are: $H = 30$ [μm] and $W = 30$ [μm]. (a) Single population. The volume of droplets is estimated to be approximately $V \approx 120$ [pL]. (b) Two populations. The first population, colored in blue, has an estimated volume of $V_1 \approx 615$ [pL], while the second population, colored in yellow, has an estimated volume of $V_2 \approx 125$ [pL].

The final interesting test for this type of chip involves fusion using PFO. Figure.7.4 presents the best result obtained. The additional challenge of fusion using PFO arises from the fact that all parasite droplets must have been eliminated. Since fusion will occur for all droplets that have their surfaces in contact, it is necessary to ensure that fusion only occurs among the desired droplets.

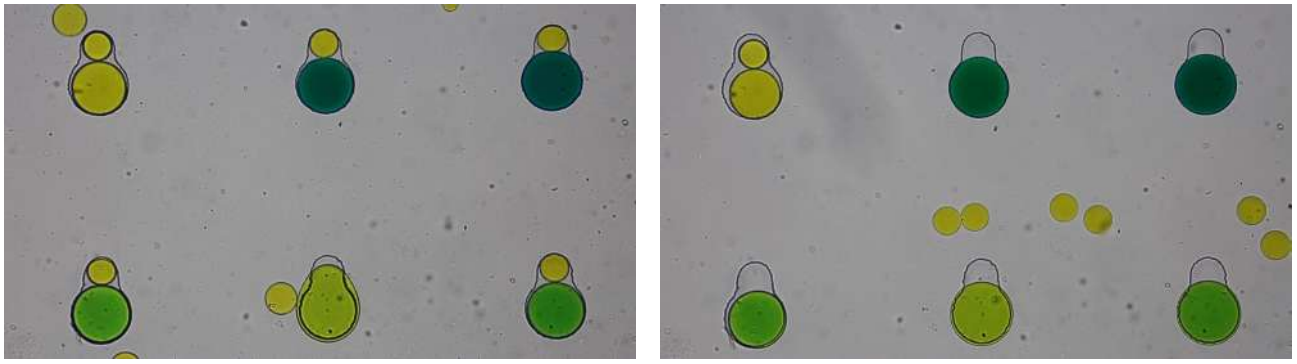

(a) (b)

Figure 7.4: Experimental picture showing capillary trapping of two droplet populations. The chip has the following dimensions: $H = 30$ [μm] and $W = 30$ [μm]. (a) Image taken before fusion. The first droplet population, colored in green, has an estimated volume of $V_1 \approx 670$ [pL], and the second droplet population, colored in yellow, has an estimated volume of $V_2 \approx 180$ [pL]. (b) Result of fusion using PFO. The volume of the final droplet is estimated to be $V \approx 850$ [pL].

1.2 Deep wells

This section will still focus on a chamber with a height of 30 [μm], but the depth of the wells has been increased to 80 [μm].

Fig. 7.5 shows the result for this chip. The initial goal was to create large droplets. Unfortunately, the trapped droplets were the first ones generated, and in this particular case, there was a significant size variation. However, this random size characteristic represents an interesting study parameter. In the case of the Fig. 7.5 study, a tapping pattern seems to emerge.

The asymmetry of the well has little importance in this situation since a maximum number of droplets seek to enter into the well to minimise their surface energy. Since the difference compared to the experiment conducted with circular wells is not significant, the test was not repeated with this chip to save time.

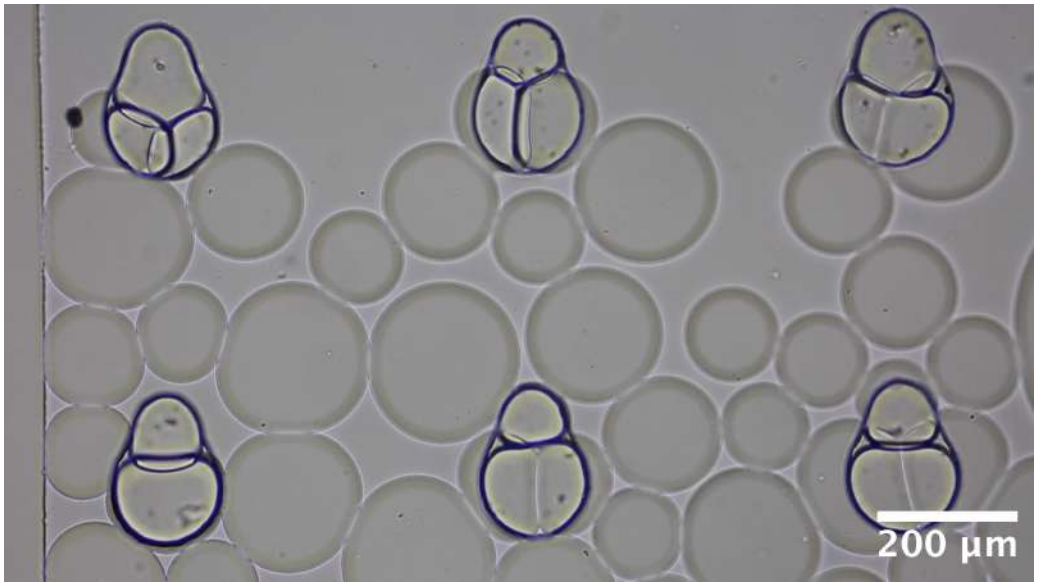

Figure 7.5: Experimental photo showing capillary trapping in a chip with deep wells. The generated droplets have random volumes ranging from approximately $V \approx (305 - 1080)$ [pL]. The chip has the following characteristics: $H = 30$ [μm] and $W = 80$ [μm].

Figure 7.6 presents a diagram that illustrates a novel trapping technique that was discovered through the use of this chip. To start, the water infiltrated the entire chamber, including the wells. By applying a flushing with oil, the aqueous phase can be removed. The wells act as important anchor points, and the water contained in them is difficult to extract. Eventually, they form isolated pockets by separating from the original aqueous phase. Each well ends up containing a water droplet occupying its entire volume.

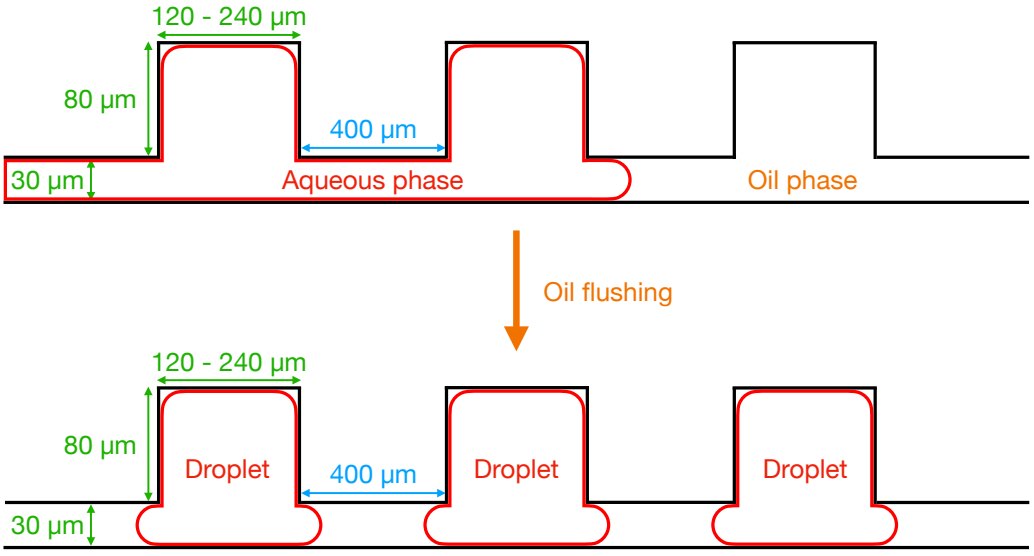

Figure 7.6: Schematic illustrating the oil flushing trapping technique. An aqueous phase fills the entire chip, and then oil displaces the water except within the wells, which serve as significant anchoring points. The dimensions used are $H = 30$ [μm], $W = 80$ [μm], $i = 400$ [μm], and $D = (120 - 240)$ [μm] depending on the well.

Fig. 7.7 demonstrates the implementation of this phenomenon. While it offers the advantage of adapting the droplet size to the well size, the issue of its release or fusion with another droplet population remains a complex subject. To support this hypothesis, the experiment was repeated with a second population of small blue droplets (Fig. 7.7b). As expected, they no longer have the opportunity to interact with the wells as they are already filled.

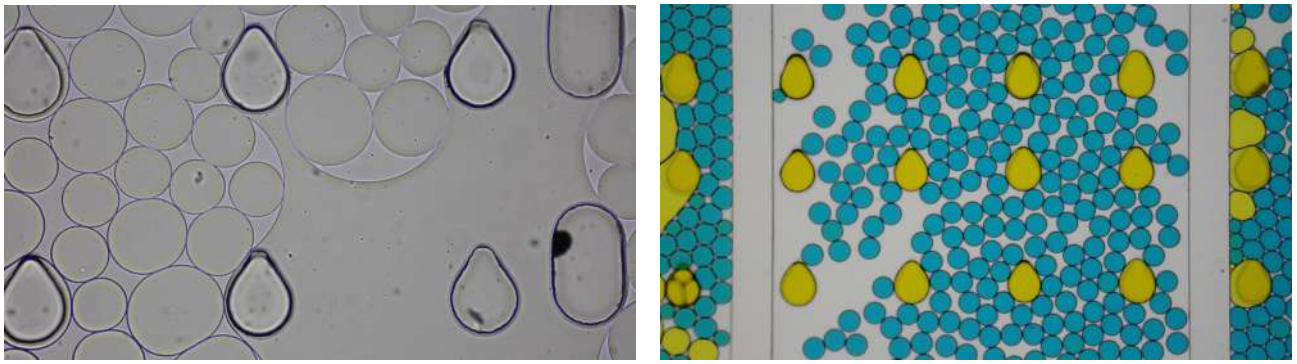

(a) (b)

Figure 7.7: Experimental pictures demonstrating the oil flushing trapping technique. (a) Generation of droplets at anchoring points by replacing the aqueous phase with oil in the surrounding environment. (b) Passage of a population of small droplets to highlight the robustness of trapping. The chip characteristics are $H = 30$ [μm] and $W = 80$ [μm]. The estimated volume of droplets is $V \approx 1200$ [pL] for those located in the yellow wells and $V \approx 180$ [pL] for the population of small blue droplets.

2 Deep Chamber

The study now takes place in the deeper chamber with an approximate height of 120 [μm]. A general observation about this section concerns the droplet size. The wells are of substantial size, often exceeding 120 [μm] in their principal axes. Since droplet production occurs in a

channel height of 30 [μm], the resulting droplet is flattened if it is intended to have a volume sufficient to fill the well afterwards. As the droplet passes through the chamber, it transitions from a pancake shape to a spherical shape, which reduces its radius from the camera's perspective. Therefore, it is very challenging to create well-adapted droplets through such a small junction. In addition to this problem, it should be noted that the transition into the deeper chamber occurs abruptly. As it was molded from a piece of adhesive tape, it was not possible to give softened edges to the chamber. When a droplet too large enters in the chamber, it simply splits apart by step emulsification as described in section 4.1.

It should also be mentioned that these types of wells have a single size unlike the previous circular wells, which were designed in a gradient form.

As a final detail, it is worth highlighting that generating large droplets requires a dominance of the aqueous phase at the junction. If water dominates over oil in proportion, it means that a large cluster of stuck droplets will be produced with oil present only between the droplets. This proximity leads to significant interaction between the droplets and affects trapping quality by limiting homogeneity and dispersion of the droplets in the chamber. Therefore, achieving two populations of droplets with suitable sizes to fit into the well, as was the case in section 6, was not possible in this scenario.

2.1 Shallow wells

This section combines wells with a depth of 30 [μm] along with a chamber of an approximate height $H \approx 120$ [μm]. The result of this study can be visualized in Fig. 7.8. As in the equivalent section of circular wells, a similar pattern emerges.

As mentioned earlier, generating large droplets with the available section at the junction can be challenging. Therefore, initially, medium-sized blue droplets were produced using a known pressure range (Fig. 7.8a). The picture was taken at the intersection of the four well designs to highlight the differences in trapping based on the well geometry. Some designs result in very regular and homogeneous trapping, while others are more uncertain in terms of the number of trapped droplets. A general trend is that the stability of the pattern decreases as the size of the wells increases. It's important to note that this observation is subject to change depending on the droplet volume.

In a second step, a population of yellow droplets was produced using the same pressure range as in the first generation. Fig. 7.8b shows the result for a single well category. It was the most interesting pattern, hence its emphasis. In several wells, it is possible to observe three blue droplets and an additional yellow droplet always positioned in the same way for all the considered wells. This droplet, located at the back of the well and easily replaceable, is an exciting discovery in the aim of trapping two different populations of droplets within the same well.

As a final test, the pressure range was modified to achieve the largest stable droplets possible with this chip (Fig. 7.8c). Obviously, the droplet sizes are much more uncertain at this stage since generating such large droplets was more challenging with such a small junction. However, a relatively regular pattern can be observed. One yellow droplet is accompanied by two blue droplets within a well. It was even possible to isolate a yellow droplet with a blue droplet within a well by slightly increasing the size. Obviously, the result would likely have been of

better quality if the large yellow droplets had been generated before the small blue droplets. By adjusting the technical details to achieve the right droplet size and being more rigorous, it would likely be possible to adopt the pattern of one droplet from each population per well in a much more regular and homogeneous manner.

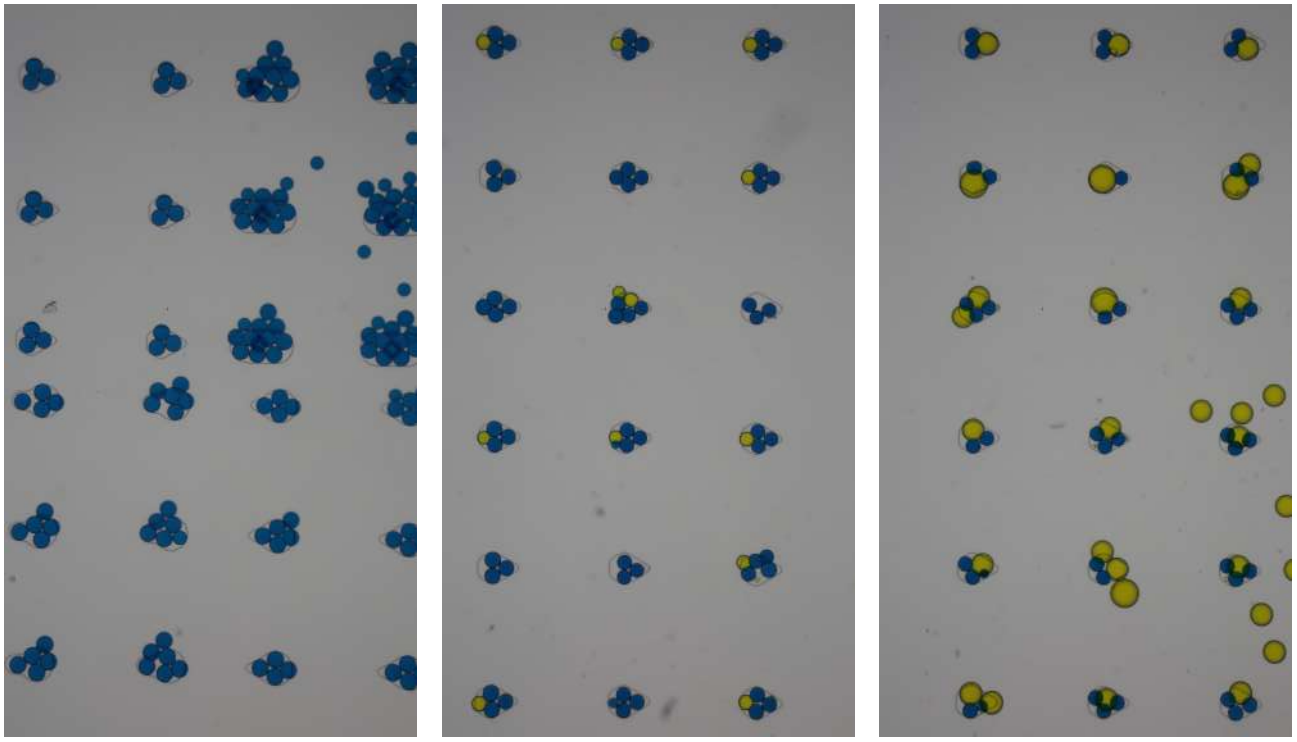

(a) (b) (c)

Figure 7.8: Experimental image illustrating trapping by Archimedes' buoyancy for two populations of droplets. The chip dimensions are $H \approx 120$ [μm] and $W = 30$ [μm]. (a) Trapping illustration for four well designs with a population of blue droplets with an estimated volume of $V_1 = 150$ [pL]. (b) Passage of a second population of yellow droplets with the same volume $V_2 = 150$ [pL]. (c) Illustration of trapping for a second population of larger yellow droplets. The estimated volume varies from $V_2 = (370 - 780)$ [pL].

2.2 Deep wells

As the final result of this section, a well depth of 80 [μm] in combination with a chamber height of approximately $H = 120$ [μm] will be considered.

Fig. 7.9a shows the initial production of a yellow droplet that was intended to be as large as possible. It was only in the later experiments that the idea of using yellow dye for the large droplets and blue dye for the small ones seemed more appropriate. Diluting a small amount of blue dye in a majority of yellow should be more aesthetically pleasing than the reverse situation.

As in section 2, since the droplets maintain their spherical shape, beyond a critical diameter, two droplets cannot be join in the well without deformation. One droplet then enters the well and prevents any other droplet from doing the same, as can be observed in Fig. 7.9a.

A second population of smaller blue droplets is introduced into the chip (Fig. 7.9b). The small

blue droplets find a way to fit into these larger wells thanks to the spaces left by the large yellow droplets. The droplets located in the area between the chamber and the well surface are easily removed by the arrival of the new flow of blue droplets, given the low-intensity trapping force at that location. This image also exhibits a complete anarchism in the size of the yellow droplets from the first population. It took some time to determine the maximum size that could be produced. Since the trapped droplets are none other than the first ones generated, the wells primarily capture the startup errors. The waste channel, presented in the section 3.1, helps to limit this effect. However, its use was limited by the sensitivity of the pressures required to create large droplets and the change in resistance between the junction and the chamber. Indeed, microfluidic resistance is subject to variation based on the number of droplets contained within a channel, as explained in section 3.1.1.

Once the chamber flushing is completed, Fig. 7.9c highlights what remains. Each well is composed of a unique and random cluster of yellow and blue droplets. By injecting PFO into the chip, each group of droplets merges into a single entity (Fig. 7.9d). This approach of random proportion of droplets could be used in practice, as the result of fusion within the final droplet provides a unique concentration of each population. Analyzing the colorimetry of the final droplet would be sufficient to retrieve the proportions of the mixture.

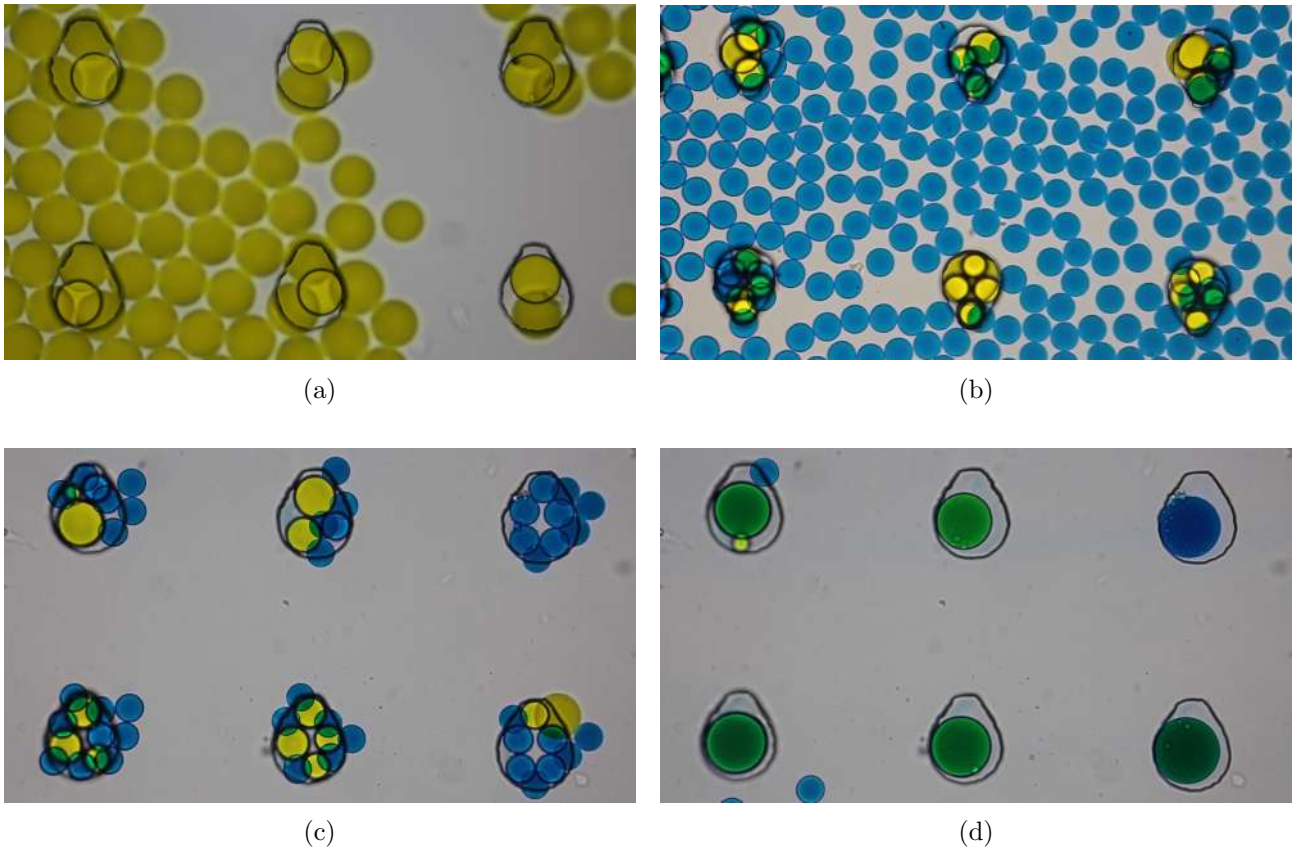

(a) (b)

(c) (d)

Figure 7.9: Experimental picture showing trapping by Archimedes' buoyancy in the case of deep wells with two populations of droplets. The chip dimensions are $H \approx 120$ [μm] and $W = 80$ [μm]. (a) Trapping of a first population of yellow droplets with an approximate volume of $V_1 = 800$ [pL]. (b) Passage and (c) Trapping of a second population of blue droplets with an estimated volume of $V_2 = 150$ [pL]. (d) Result after fusion by PFO. The volume of the final droplets varies in the range $V \approx (1100 - 2000)$ [pL].

Chapter 8

Liquid disappearance

1 Oil disappearance

An observation that remains quite mysterious is the disappearance of oil in a stopped chip. In Fig. 8.1, the quantity of droplets present in the chamber is very significant to the point where oil is only present at the interface between the droplets. Moreover, the droplets are deformed and take on a hexagonal shape, as seen in dry foams. Fig. 8.1b shows the reactivation of the chip, where the droplets regain their independence and return to a more circular shape as long as the thin oil film separating two attached droplets has not completely disappeared, which would result in their fusion. Knowing where, how, and why the oil has disappeared remains an open question. One possible explanation could be the permeability of PDMS to oil. If PDMS allows a small amount of oil to pass through, it could be the cause of its disappearance [134].

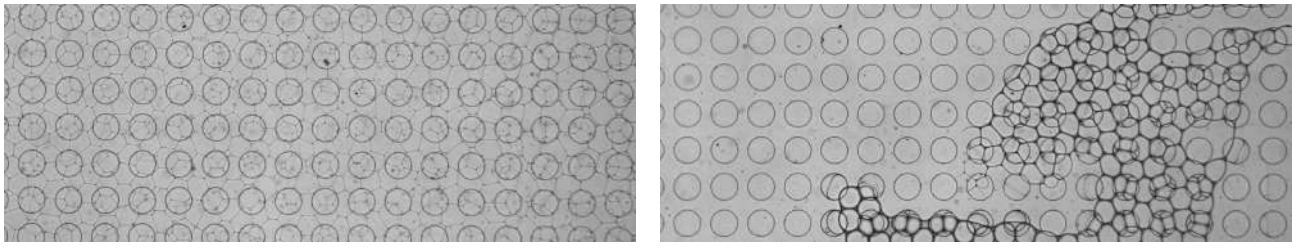

(a) (b)

Figure 8.1: Experimental picture showing the disappearance of oil within the chip. The characteristic dimensions are as follows: $H = 30$ [μm], $W = 30$ [μm], $D = 100$ [μm], $i = 50$ [μm]. (a) Photograph taken after one hour of chip shutdown, revealing the absence of oil. (b) Reactivation of oil flow, leading to the reformation of the initial droplets that did not fuse.

2 Evaporation

Another phenomenon to consider is the evaporation of water. PDMS is permeable to water, so trapping water droplets over a long period seems to be compromised. The droplets disappear after a few hours if nothing is done to counteract their evaporation. This problem is amplified in the application of these chips for spheroid formation since it requires incubation at 37°C. The literature offers various solutions, more or less complex to implement [135]. As a personal initiative, the chip was simply immersed in water. The idea was to saturate the PDMS with water so that it could not accept any more.

2.1 High water density

In this first scenario, the chip contained a large quantity of droplets. The dominant phase was therefore the aqueous phase. Fig. 8.2 shows the evolution of evaporation after 20 hours. No significant changes can be observed. With the PDMS saturated and the chamber predominantly filled with water, it is difficult to observe any leakage.

An important observation regarding Fig. 8.2 is the orientation of the wells. These images are the result of a time-lapse, yet the wells are not oriented in the same way. In reality, the chip adhered to the bottom of the water-filled dish through simple contact. As the different inlet and outlet tubes were not disconnected to prevent surrounding water from entering the chip, they gradually displaced the chip through tension.

Another remark concerns the background droplets that have moved between the two photos. The reason is that the chamber tends to expand when pressurized. It acts like a large fluidic capacitor as described in section 1. When the chip was stopped and the pressures were set to zero, the chamber gradually returned to its initial shape, displacing the droplets it contained. To confirm this, the focus was gradually lost between the two images. The lens had to be readjusted to obtain the final image.

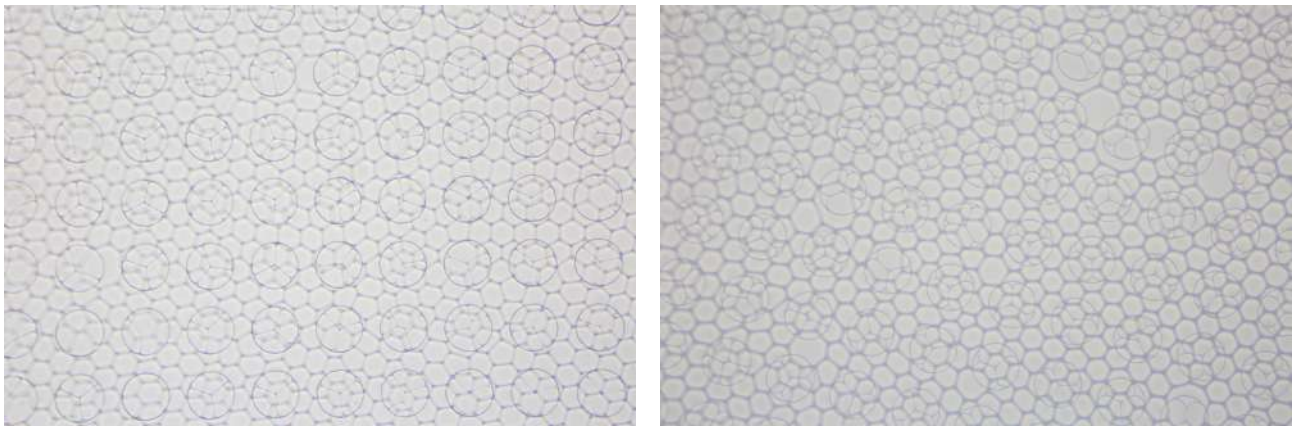

(a) (b)

Figure 8.2: Experimental image showing the evaporation of water within the chip when immersed, without emptying the chamber of excess droplets. The characteristic dimensions of the chip are: $H = 30$ [μm], $W = 30$ [μm], $D = 100$ [μm] and $i = 50$ [μm]. (a) Photograph taken at the initial moment of chip shutdown, showing the droplets within the wells with an estimated volume of $V \approx 77$ [pL]. (b) Photograph taken 20 hours after chip shutdown, with the same droplets showing a reduced volume estimated at $V \approx 62$ [pL].

2.2 Low water density

In contrast to the previous analysis, the experiment was repeated in the new chips. The main differences are the much larger spacing between the wells and the absence of droplets in the background of the chip. Water is only present in the droplets contained within the wells.

Fig. 8.3 shows the evolution of the droplets over a time period of 16 hours. In this situation, the droplets clearly show signs of shrinking. Some of the water they contained could have escaped through the PDMS, and another portion could have dissolved into the surrounding oil.

However, they still maintain a decent size after several hours, which would not have happened if the chip had not been immersed.

An important clarification concerns the setup of this experiment, as the chip was only immersed in water at the very end. Evaporation is further limited if the chip is saturated with water prior to the experiment. Specifically, a certain amount of time is required to saturate the PDMS near the wells with water. The water needs to diffuse from the outside to saturate the PDMS near the structures and channels. It is more effective to start with a chip that is already saturated with water to minimize evaporation.

As a final remark, some articles use techniques based on droplet shrinking to release them[81, 85, 101, 106]. Indeed, up until now, the assumption has been made that the volume of the droplets remains constant. However, this experiment clearly shows that this is not always the case. It is possible to take advantage of this phenomenon since the trapping force will vary depending on the geometrical parameters. Under these conditions, it is possible to change the trapping regime. The example in Fig. 8.3a shows flattened droplets as their diameter exceeds the sum of the chamber's height and the depth of the well. On the other hand, Fig. 8.3b shows small spherical droplets that are small enough to be released by chip flipping. Thus, the regime has transitioned from a capillary regime to an Archimedes regime.

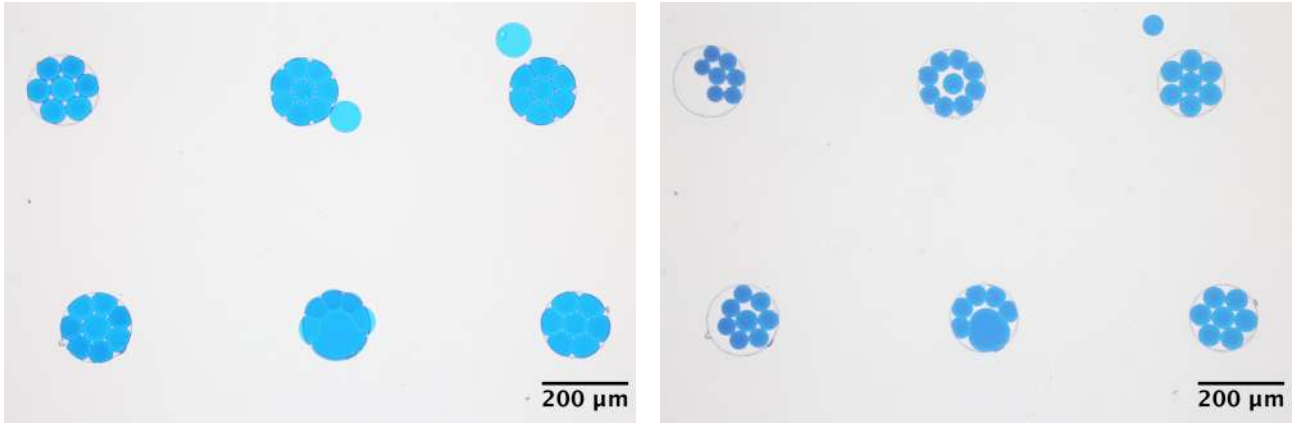

(a) (b)

Figure 8.3: Experimental image showing the evaporation of water within the chip when immersed. In this situation, the chamber has been emptied of excess droplets, and the spacing between the wells has been increased to $i = 400$ [μm]. The characteristic dimensions of the chip are: $H = 30$ [μm] and $W = 30$ [μm]. (a) Photograph taken at the initial moment of chip shutdown, showing the droplets within the wells with an average estimated volume of $V \approx 105$ [pL] inside a specific well (bottom right). (b) Photograph taken 16 hours after chip shutdown, with the same droplets showing a reduced volume estimated at $V \approx 35$ [pL].

To provide an order of magnitude for the evaporation phenomenon, it is interesting to consider how much PDMS a water droplet is capable of saturating. Starting from Fig. 8.3a and focusing on a droplet located in the chamber,
its volume can be evaluated as $V \approx 137$ [pL]. Since it is water, the mass of liquid corresponding to this volume is determined as $m_w = 137 \times 10^{-9}$ [g]. Knowing that the molar mass of water is $M = 18$ [g/mol], the corresponding number of moles is determined as $N = 7.6 \times 10^{-9}$ [mol].

Let's now consider the ideal gas law:

$$P_v V_v = NRT \tag{8.1}$$

Where p_v and V_v correspond to the saturation vapor pressure and associated volume. The saturation vapor pressure of water at 20° [C] is $p_v = 2339$ [Pa]. Since the ideal gas constant is given by $R = 8.3145$ [J mol^{-1} K^{-1}], it is then possible to evaluate the associated volume. This volume amounts to $V_v = 7.92 \times 10^9$ [μm^3]. Thus, the disappearance of a droplet allows for reaching the saturation vapor pressure within a volume of approximately $V_v \approx [2000\mu\text{m}^3]$. Considering that the wells are separated by a distance of 400 [μm] with a chip thickness of about 5 [mm] between the inside and outside, this order of magnitude seems reasonable and somewhat justifies the reduction in droplet volume. It should also be noted that the surrounding oil could also drain some of the water. Indeed, it is slightly permeable to water until it reaches saturation. Given the significantly larger quantity of oil compared to water, a non-negligible fraction of the droplets could potentially be used for this.

As a note, a huge approximation was made in this calculation since it considered air saturation with water vapor rather than that of PDMS and oil. The goal was merely to try to find an order of magnitude. However, it would be necessary to refine this result. Nonetheless, it was not trivial to find this information on water vapor saturation for these materials.

Chapter 9

Fails

This section aims to present a sample of the main issues encountered during this master thesis. It is evident that this part is not exhaustive as the number of failures far exceeds the number of successful tests. Fig. 9.1 shows some of these failures.

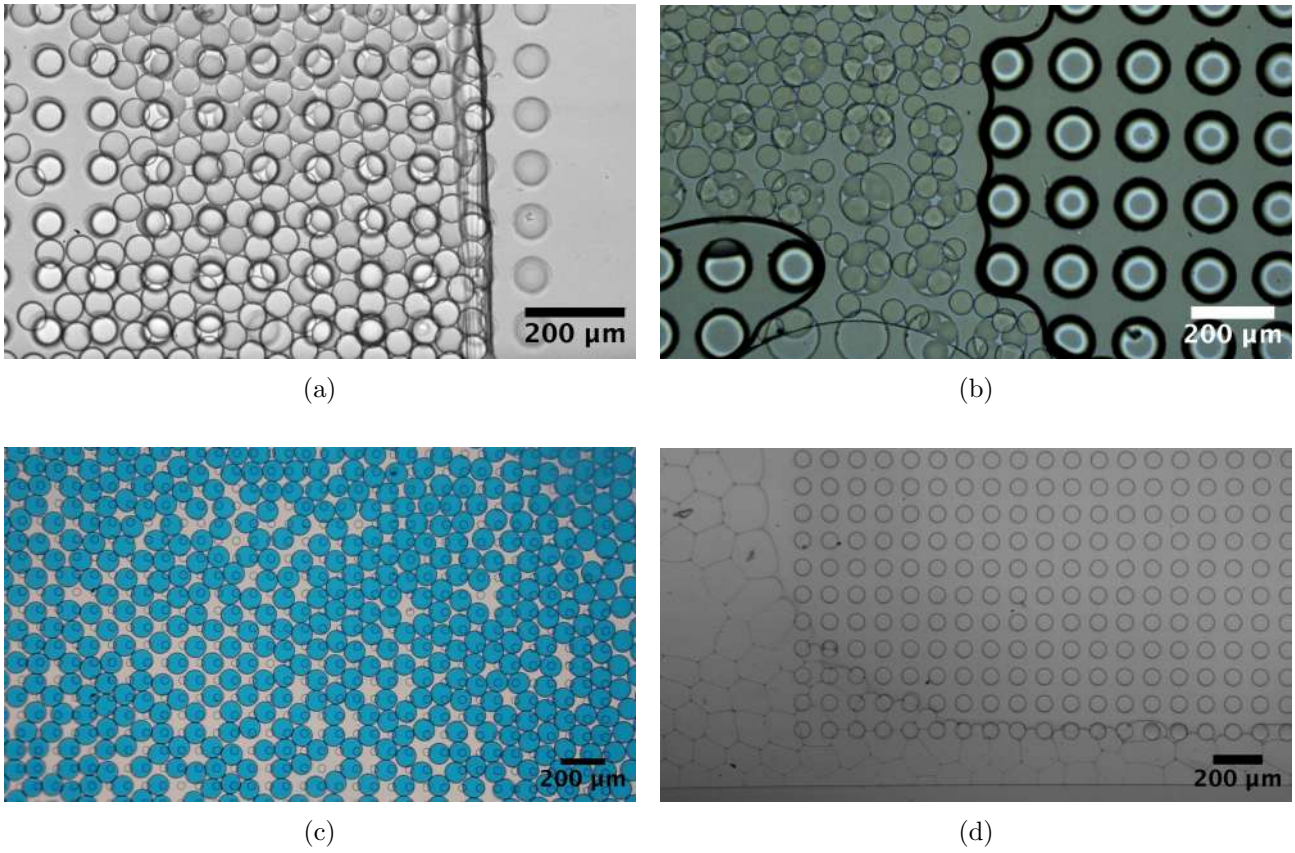

(a) (b)

(c) (d)

Figure 9.1: Experimental image showing the main failures encountered in this master's thesis. (a) Using the deeper chamber, the droplets cannot collapse to the characteristic height of the 30 [μm] channels to flow towards the intended outlet. (b) Trapped air within the chip hinders its proper functioning. (c) Incorrect droplet size can lead to experimental failure. (d) A fabrication error resulted in the collapse of the chamber roof and its adhesion to the lower chip. In these conditions, the droplets follow the chamber walls and flow directly towards the outlet without interacting with the wells.

Part IV

Conclusion

Chapter 10

Trials on other trapping regimes

This section will illustrate the trapping techniques found in the literature, which differ significantly from well-based trapping and therefore will not be presented in the main document.

1 Oil flow trapping

The first chip studied is based on a popular design from the literature that was attempted to be replicated [18, 24, 33, 42, 60, 71–81]. This type of trapping only requires a single chip (Fig. 10.1). The goal is to trap the droplets using an oil flow. The trap operates like a sieve. It is constructed in the shape of a funnel to allow the oil to pass around and inside it. This enables the droplets to enter the trap. However, the narrowing of the junction prevents them from continuing their path. They would need to deform and enter the channel to proceed further. Nevertheless, the oil flow is not sufficient to allow this scenario. A major disadvantage of this trap is that a low oil flow rate must be maintained to prevent the droplet from reversing and escaping; this can also lead to a reduction in droplet size. Unfortunately, the experiment with this chip design was a failure. The size of the structures was not adapted for the microfabrication process at `Technifutur`. They could not be properly printed, resulting in their almost complete inefficiency. The design was exactly the same for all the structures on the chip, therefore no results could be obtained from it.

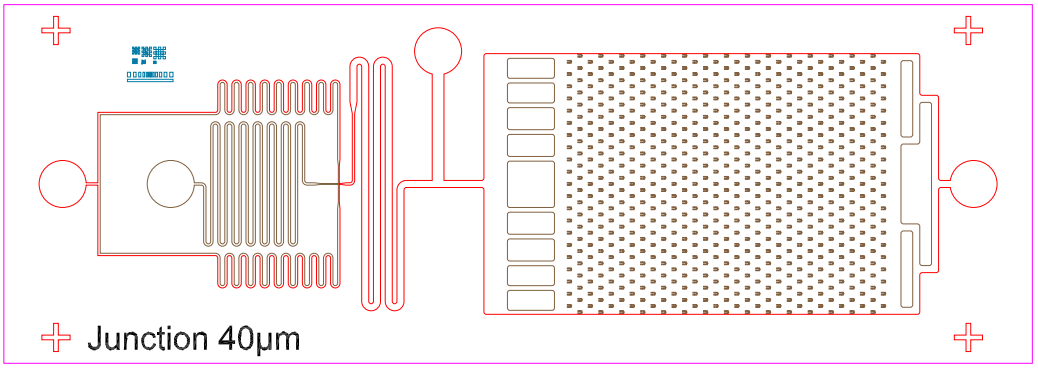

Figure 10.1: Schematic of a chip design for oil flow trapping. The dimensions of the structures are 180 [μm] in length and 120 [μm] in width. The height of the channels and structures is set to $H = 30$ [μm]. The spacing between two structures is set approximately between $i \approx (300 - 400)$ [μm] depending on the direction.

The result of this chip in operation (Fig. 10.2). The structures serve as anchors to some extent

but do not fulfill their initial role due to their insufficient height. By correcting the latest design, it would be possible to make this type of trap functional and study them.

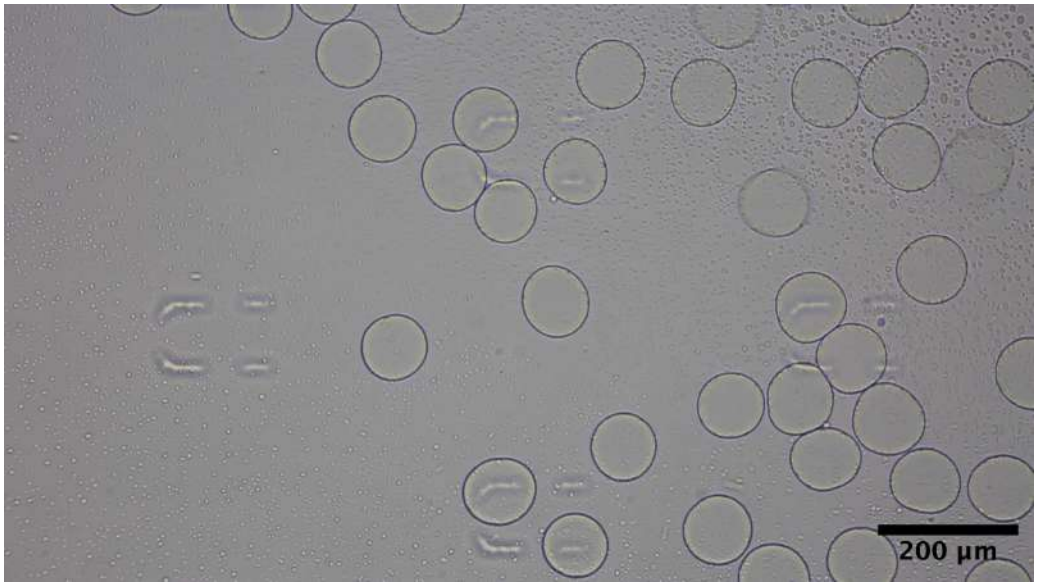

Figure 10.2: Experimental image illustrating the failure of oil flow trapping due to poor microfabrication resolution. The volume of the drops is estimated to be $V = 180$ [pL]. The height of the structures and channels is set to $H = 30$ [μm].

2 Pillars trapping

Another trapping technique that deserves further investigation is the pillar-based trapping [83–85] introduced in section 7. The interest lies in the unconventional nature of this trapping method. The capture of the droplet is ensured by the surrounding pillars. However, the displacement of the droplet is still possible through deformation.

Unfortunately, the tests with this chip also turned out to be failures. The pillars were too small and were not properly printed during microfabrication. The droplets had very little interaction with them, so there was little hope of them influencing the droplet behavior (Fig. 10.3).

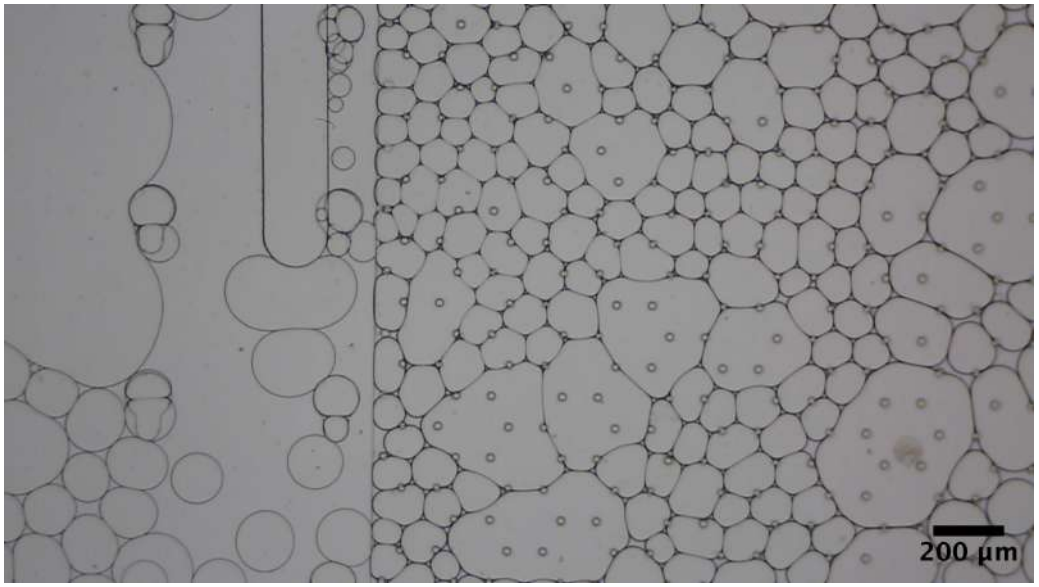

Figure 10.3: Experimental picture illustrating the unsuccessful trapping using pillars, attributed to the inadequate resolution of the microfabrication process. The chamber height is set to $H = 60$ [μm].

3 Dropspots

This type of trapping only requires a single chip (Fig. 10.4). Circular spots, large enough to accommodate a droplet, are separated from each other by channels. The droplet must deform to enter the channel and will preferentially stay in the spot as long as nothing forces it to move. The arrival of a new droplet in the limited-sized spot will force the existing droplet to enter the channel and in turn push the droplet in the next spot to take its place. The addition of channels was a personal choice, as the article directly connected the spots one after another [86]. The goal, as with the wells, was to make the trapping zones independent of each other. The article specified that with adjacent spots, the arrival of a new droplet would require shifting the entire queue of droplets to make room. The channels separating the spots aimed to limit this phenomenon so that the new droplet only had to displace the droplet in the spot it intended to occupy. It is worth noting that each channel contains spots of identical size, but there is a gradient of spot sizes between each channel.

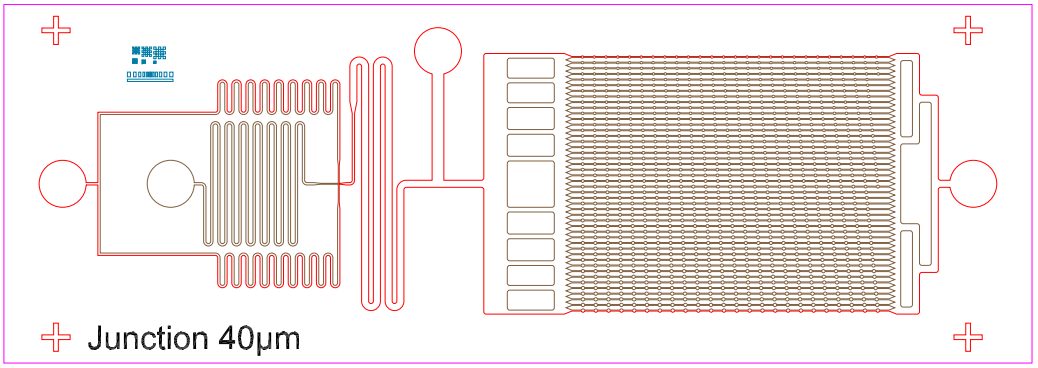

Figure 10.4: Schema of a chip design for trapping using the dropspots technique. The spot size remains constant along a channel but varies from one channel to another. The diameter of the spots starts at 100 [μm] and increases by 1 [μm] between each channel, reaching 145 [μm]. The height of the spots and channels is set to $H = 30$ [μm]. The spacing between two spots within a channel is $i = 400$ [μm].

The result of this Dropspots chip in operation (Fig. 10.5d). Only a surface study could be conducted. Certain regimes have been identified, but their detailed analysis will need to be the subject of future work.

The chip in operation with a wide field of view (Fig. 10.5a). The first important information to note is the regularity of the pattern. With an appropriate droplet size and a sufficiently low flow within the chip, a first regime is reached. The droplets are trapped within the spot. The oil manages to bypass the droplet and flow into the channel. In the depth direction, the droplet does not completely obstruct the flow as it adopts a nodoid shape while the walls of the channels remain straight. Under these conditions, only the arrival of a new droplet can release the droplet already present in the spot. The advantage of having channels between the spots is to make this process independent from one spot to another. In other words, the newly arrived droplet does not need to displace the entire queue of trapped droplets within the spots, but only the droplet it comes into contact with. As a result, the droplets can move within the channels while other droplets remain stationary in the spot. Their motion is triggered only by contact with another droplet.

A more detailed insight into this droplet collision phenomenon can be observed thanks to the addition of dye and the use of a more suitable objective (Fig. 10.5b).

In addition to this technical detail, a remark was made about the potential issue of the introduced channels, as they could contain droplets once the chip is stopped. By stopping the droplet generation and controlling the oil flow appropriately, it is possible to gradually evacuate the remaining droplets until the chip is composed of only one droplet per spot. This type of trapping allows for the capture of the last produced droplets, contrasting with the previous results where only trapping using an anchor described in section 1.1.1.2 allowed for the same. It is indeed possible to trap only one droplet per spot by removing the residual droplets in the channels (Fig. 10.5d). The tests were conducted on the 80 [μm] chip with the goal of forming spheroids. The result of the 80 [μm] chip thickness was also observed on the 30 [μm] chip. Furthermore, even though the viewing angle is very close, this pattern is consistent throughout the length of the chip's channels, as evidenced by a video.

In the next picture, the blur is due to the higher speed of the droplets (Fig. 10.5c). When the flow rate is increased, a different trapping regime appears. The capture within the spots becomes more random, with empty spots potentially appearing. The middle channel also provides an indication of the regime shift, as the droplets are smaller compared to the size of the spot and centered. In the previous regime, the droplets were more attached to the walls or stuck at the exit of the spot, unable to deform enough to enter the channel. The high oil flow rate causes the droplet to center within the spot. A disturbance can lead to the release of the droplet from the spot as the oil flow rate is sufficient to deform the droplet and allow it to enter the channels. In theory, a droplet could traverse the entire length of the channel with minimal deceleration caused by the spots and successive deformations in the channels. However, this occurs only if the droplet has not successfully stabilized within the spot. In this situation, it is accelerated by the oil flow and no longer interacts significantly with the spots it encounters. Conversely, if the droplet is sufficiently slow, the spot represents a stable equilibrium zone in which the droplet can stabilize. The droplet tends to re-center within the spot despite disturbances.

A relevant question would be to understand the advantage of this chip compared to the others

tested so far. The interest lies in the control of the droplets. Until now, the dispersion in the chamber was subject to random behavior. On the contrary, this chip allows for greater control over the positioning and release of the droplets. In the chamber, droplets that insert themselves into areas with lower flow rates are very difficult to dislodge. Unwanted clusters can form with limited control over the droplets composing them. Significantly increasing the flow rate can result in either partial unttraping or, at worst, a leakage in the chip due to pressure constraints. This solution is therefore limited. Dropspots enable the positioning of droplets at predetermined locations. Since all the channels have a smaller cross-section than the chamber, the flow rate can be better controlled. These reasons are behind the interest generated by dropspots.

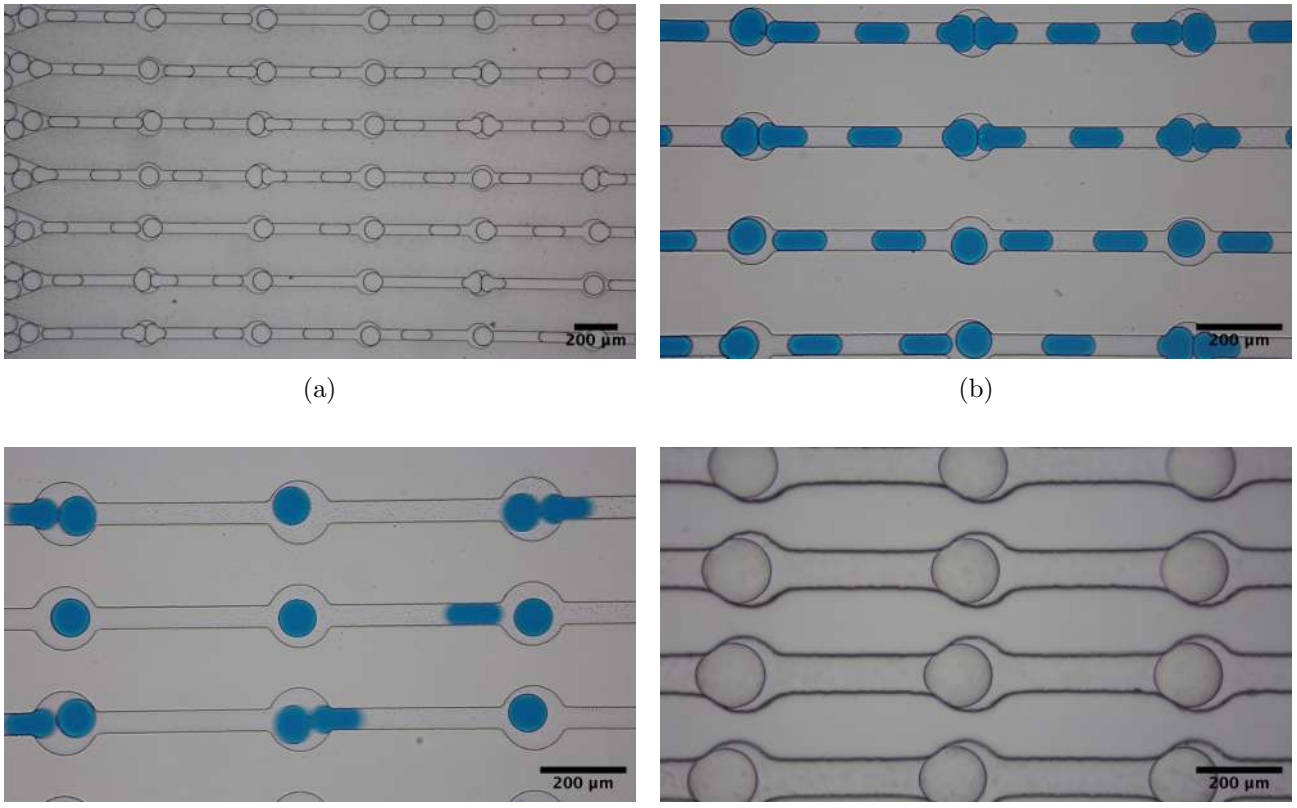

(a) (b)

(c) (d)

Figure 10.5: Experimental pictures depicting trapping phenomena within dropspots. The captured snapshots showcase various scenarios: (a) an overview image demonstrating trapping at $H = 30$ [μm] with an estimated volume of $V \approx 170$ [pL], (b) a close-up image highlighting trapping at $H = 30$ [μm] with an estimated volume of $V \approx 145$ [pL], (c) an image illustrating a transition in trapping behavior under increased oil flow at $H = 30$ [μm] with an estimated volume of $V \approx 160$ [pL], and (d) an image showcasing trapping at $H = 80$ [μm] with an estimated volume of $V \approx 1170$ [pL] for spheroid formation.

Thanks to the gradient in spot sizes, it is possible to observe a trapping regime where two droplets are present within each spot (Fig. 10.6). The experiment was conducted multiple times, and this phenomenon was observed on each occasion. The overall view of the results (Fig. 10.6a), and close-up version using a dye to differentiate the droplets (Fig. 10.6b).

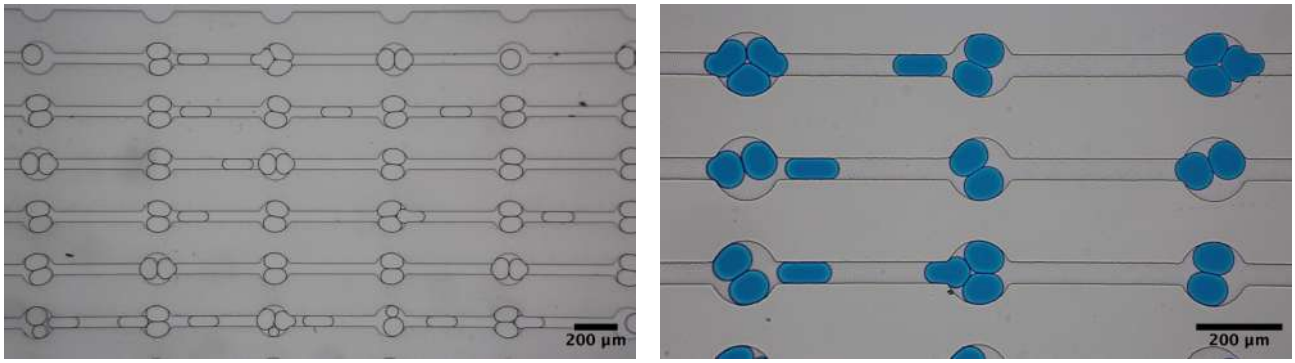

(a) (b)

Figure 10.6: Experimental pictures illustrating the trapping of two droplets within each dropspot. The height of the spots and channels is set to $H = 30$ [μm]. (a) Overall image depicting trapping with an estimated volume of $V \approx 175$ [pL]. (b) Close-up image showcasing trapping with a volume of $V = 150$ [pL].

Finally, after multiple attempts, it was possible to achieve a situation where three droplets were trapped within a single spot (Fig. 10.7a). The transition from one droplet per spot to two droplets per spot was observed in the chip (Fig. 10.7b). However, it should be noted that this is the exception rather than the rule. In general, it was observed that trapping one, two, or three droplets within a spot was only possible within a specific range of spot sizes. Outside of this range, most of the time, the droplets would pass through the channel with minimal interactions with the spots they encountered (Fig. 10.7a).

The quantity of droplets present at the entrance of the channel is an important variable for all regimes. Too many droplets or an inappropriate size can lead to the obstruction of the channel. On the contrary, if there are not enough droplets, the resistance of the channel is reduced, the flow is significant, and the droplets pass through the channel at a too high velocity to be trapped.

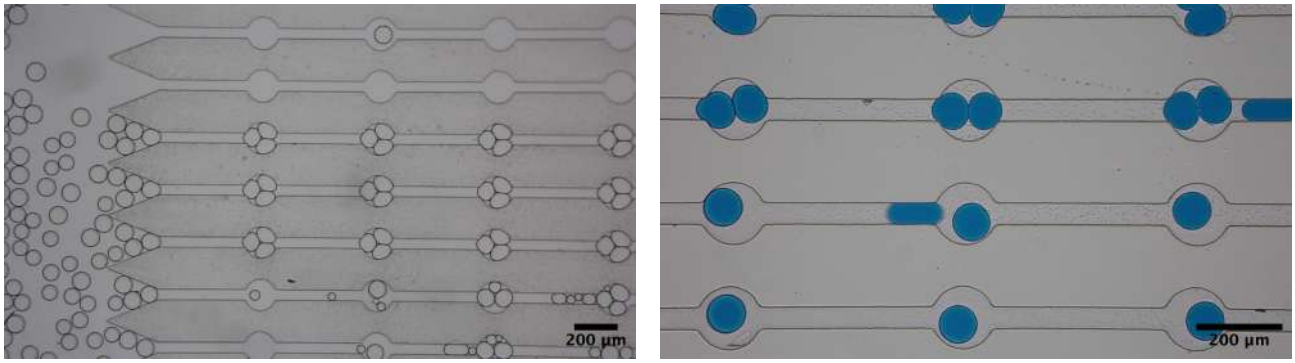

(a) abc (b) abc

Figure 10.7: The following experimental image depicts dropspots with a spot and channel height of $H = 30$ [μm]. (a) Illustration of trapping three droplets within a single spot, with a droplet volume of approximately $V \approx 140$ [pL]. (b) Illustration of a transition in trapping behavior between channels with spots of different sizes, with a droplet volume of approximately $V \approx 160$ [pL].

To complete this study and attempt to capture two distinct droplet populations per spot, a well array was overlaid onto the dropspot chip (Fig. 10.8). The idea was to capture the first

population of droplets, which were significantly smaller than the spot size but suitable for the well size, allowing for capture through buoyancy. Since the chip designs were not originally intended for this purpose, a chip with a high density of wells was needed so that locally, a well could overlap with a spot. It was also necessary to choose the smallest possible well size to contrast with the spot size. The goal of the capture is based on the size asymmetry between the two droplet populations. However, the well needed to be wide enough to allow for capture of the smaller droplets achievable with the junction through buoyancy. These constraints were satisfied by using a well array chip3.3 with a well diameter $D = 60$ [μm] and a depth of 30 [μm]. The dropspot chip10.4, had a thickness of 30 [μm].

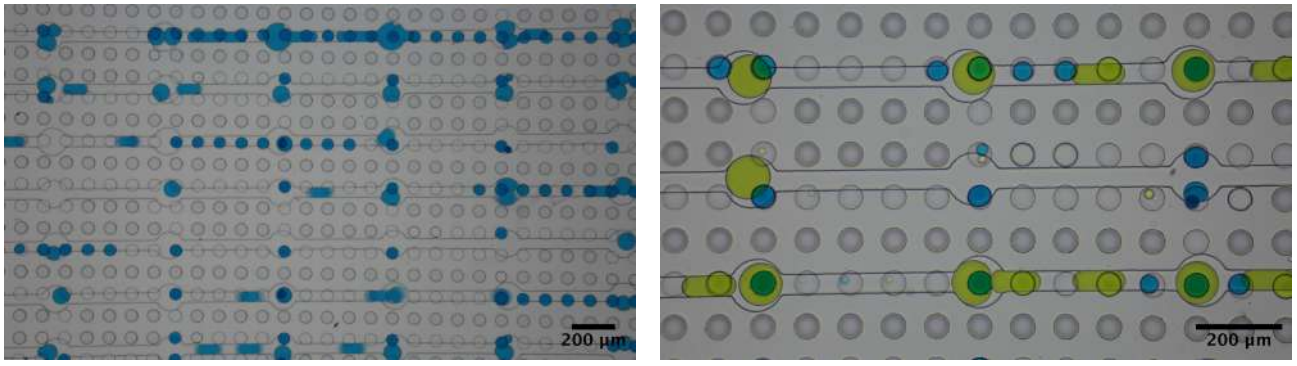

(a) abc (b) abc

Figure 10.8: Trapping of two distinct droplet populations using dropspots. A well array was superimposed onto the dropspot chip. Chip dimensions: $H = 30$ [μm], $W = 30$ [μm]. (a) Global image illustrating trapping of the first droplet population, suited for wells, colored blue, volume $V \approx 125$ [pL]. (b) Close-up image illustrating trapping of the second droplet population, suited for dropspots, colored yellow, volume $V \approx 210$ [pL].

Fig. 10.8a shows the result of the first droplet production. The majority of the wells are obviously left empty as they are obstructed. Only those overlaid with the channels and spots may potentially accommodate a droplet if it is not too fast. Unfortunately, the alignment is not perfect as it was done manually.

This test is primarily based on a personal idea, has not been replicated, and is intended to be quite adventurous. The result after generating a second population of droplets (Fig. 10.8b). They stabilize well within the spot as desired. The trapping of two droplet populations within a spot is thus successful. The small droplets that can be seen are from cleaning the chip after the experiment failed in the first test. The overall pattern suffered from various errors, but by zooming in on certain regions of interest, as shown in the figure, the initial idea seems to be confirmed. The operation is quite similar to anchor trapping studied in section 1.1.1.2. The advantage here is the independence of trapping zones and droplet control through the channels. By adapting the design, there may be a possibility to place electrodes in the PDMS regions separating the channels to facilitate fusion. Fusion using PFO could also be possible in this situation due to the independence of the wells. Unlike anchor trapping, there is no mystery regarding the arrival of the first droplet in the well, as it is driven by buoyancy. This technique thus combines two trapping techniques, through buoyancy and dropspots.

3.1 Spheroids

To test this chip with dropspots in a more concrete case, an attempt to form spheroids was made (Fig. 10.9). The cell concentration used for this test is around 200 cells per droplet. The incubation time for spheroid formation is 24 hours for this experiment. The temperature was maintained at 37°C throughout.

Figure 10.9: Experimental picture showing the formation of a spheroid within the dropspot chip. The height is set at $H = 80$ [μm]. The approximate volume of the droplet is estimated to be 1000 [pL].

Chapter 11

Conclusion

This work has illustrated the various trapping methods possible within a microfluidic chip. To achieve this, a large number of ingenious ideas from the literature were used. Emphasis was placed on those that were most likely to lead to the efficient capture of two types of droplet populations.

Initially, this work focused on the physics behind droplet trapping within circular wells. The essential parameters necessary for studying the problem were identified. Various models were developed to estimate as accurately as possible the volume and shape of the droplets in each of the encountered trapping scenarios. Depending on the height of the chamber and the droplet volume, two major trapping types were distinguished: capillary trapping and buoyancy trapping. In both situations, the analysis of experimental results allowed the determination of parameter values marking the transition between specific trapping regimes.

Subsequently, this master thesis focused on a more exploratory phase where the goal was to achieve the capture of two types of droplet populations. To accomplish this, the shape of the wells was adapted by moving away from a circular geometry. This part relied on various trapping techniques encountered so far and on results from the literature. One of the most successful trapping techniques, involving the trapping of one population by capillarity and another by anchoring, was successfully reproduced.

To best summarize all the obtained results, a comparative figure (Fig. 11.1) and table (Tab.11.1) of trapping methods are presented.

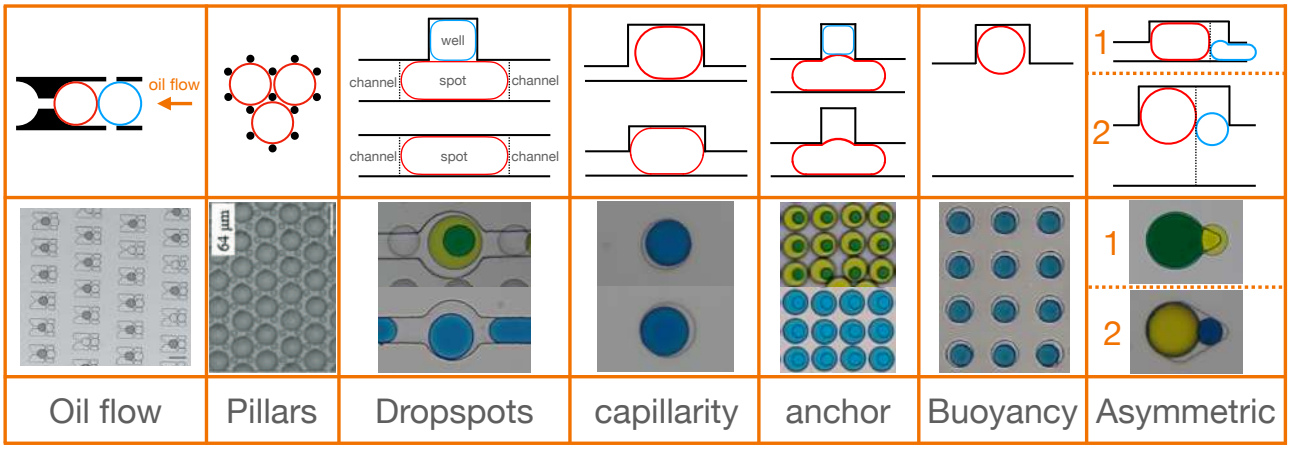

Figure 11.1: Diagrams illustrating, in particular, cross-sectional views of various structures dedicated to a trapping method. Illustration using experimental images of these same trapping methods. For the *Oil flow* the image is sourced from [60, 79], and for *Pillars*, the image is derived from [83].

	Oil flow	Pillars	Dropspots	Capillarity	Anchor	Buoyancy	Asymmetric wells
Droplets trapped	first	first	last	first	last	first	first
Releasing	easy	easy	easy	hard	easy	easy	(1): hard (2): easy
Population trapped	two	one	two	one	two	one+	two
PFO merging	easy	hard	hard	easy	hard+	easy	easy
Pattern homogeneity	/	/	excellent	good - excellent	excellent - perfect	perfect	(1): good+ (2): poor+
Trapping force	low	low	low - middle	middle	low	high	(1): middle/low (2): high/low
releasing after gelation	easy	hard	hard	hard	hard	easy	(1): hard (2): easy

Table 11.1. Table summarizing all types of trapping. Only the major trends could be presented. The shaded cells represent trapping techniques that could not be fully tested. The provided data merely reflects what is mentioned in the literature. The symbol "+" in this Table indicates that the result could potentially be easily improved based on the tests conducted. For *Asymmetric wells*, the numbers correspond to the two tested regimes, respectively: capillary regime (1) or by buoyancy force (2). *Droplets trapped* indicates whether it is the first or the last generated droplets that are trapped. *Releasing* expresses the level of difficulty in releasing the trapped droplets. *Population trapped* expresses the possibility of trapping one or two distinct populations of droplets. The notation "one+" indicates that encouraging results potentially allow for trapping two populations. *PFO merging* expresses the level of difficulty in independently merging droplets by PFO within each well. *Pattern homogeneity* expresses the overall quality of trapping and the homogeneity of trapping across all the wells on the chip. *Trapping force* gives an idea of the magnitude of the force that enables trapping.

This master's thesis aimed to successfully trap an initial population of droplets containing cells to form spheroids. Subsequently, a second population of droplets containing drugs for testing was intended to be trapped at the same location and merged with the first population to enable large-scale testing. These objectives were achieved through fragmented approaches. One of the primary outcomes is the capillary and anchor trapping of each population within the asymmetric wells, with successful fusion using PFO. Spheroid formation was accomplished within the dropspots chip, as presented in the corresponding section 3. Thus, this work was able to replicate, analyze, compare, adapt, and ultimately select certain results from the literature to pave the way to extensive drug screening and testing.

Chapter 12

Perspectives and further improvements

In the context of this work on droplet trapping, it is also important to pave the way for future research directions.

Regarding the results from the section 6 on trapping using circular wells, some promising designs deserve further exploration. In particular, certain configurations appear to enable the trapping of two distinct populations of droplets. It would be necessary to investigate the range of well sizes that allow for this possibility. The phenomenon of capturing both populations of droplets through anchor in the section 1.1.1.2 was rather unexpected and warrants a more in-depth study.

The asymmetric wells developed in the section 7 were chosen to be close to the designs found in the literature to ensure some level of results. However, tests on more innovative geometries could be conducted. It would also be interesting to explore the use of multilayers to incorporate multiple depths within the same well. This manuscript has mentioned missteps that have led to limitations in results during experiments. Correcting these errors would allow the results to be fully realized. The objective would be to make this trapping process more robust for the desired applications. Furthermore, these trapping techniques vary significantly among themselves and may be useful for biological studies other than spheroids.

An essential aspect that has been relatively unexplored in this work is the fusion of droplets. In this master's thesis, only tests using PFO have been conducted. It was the simplest and most affordable means to merge droplets in this particular case. However, there are many other techniques available, and it would be interesting to explore all these methods. While PFO is effective, its impact on cells remains uncertain. Furthermore, its use forces all the droplets in the chip to undergo fusion, without allowing localized fusion on a limited number of droplets.

The next steps of this work would naturally involve further investigation into the physics of trapping. Developing analytical models would be relevant in understanding the shape adopted by the droplets. It would also help to identify and characterize the various forces at play, especially in the anchor regime, and thus justify the trapping quality.

Another part of further projects will be the management of evaporation. This problem has been recurrently identified during incubation steps in microfluidic chips. Various approaches have been tested in order to reduce its impact, however, none is universal. It would be relevant to quantify this evaporation and infer its origin to better mitigate it.

Studies have been conducted on trapping using oil flow, pillar trapping, and dropspots. Among these additional tests, interesting behaviors have been highlighted and would deserve further investigation in future studies.

Another aspect not explored in this work is the difference in trapping speed between droplets trapped by capillarity and those trapped by buoyancy. Since this difference is significant, additional studies in this area could be relevant.

One topic that was omitted in this master thesis is the trapping efficiency. Depending on the type of well, it would be relevant to know the percentage of traps containing droplets in the desired configuration. Addressing this aspect would provide valuable insights into the performance of different trapping methods.

Finally, a cross-cutting idea for this project would be to use trapping to co-encapsulate droplets. Each type of droplet population is subject to a Poisson distribution, and encapsulating two different populations results in a very low effective yield. This limits the number of relevant droplets for future experiments (Fig. 12.1). The idea would be to use the trapping approach to capture one droplet from each population at the same location. It would thus be possible to co-encapsulate one droplet of each type, drastically increasing the number of relevant droplets and overcoming the Poisson distribution [3, 6, 17, 33, 95, 121, 136–138].

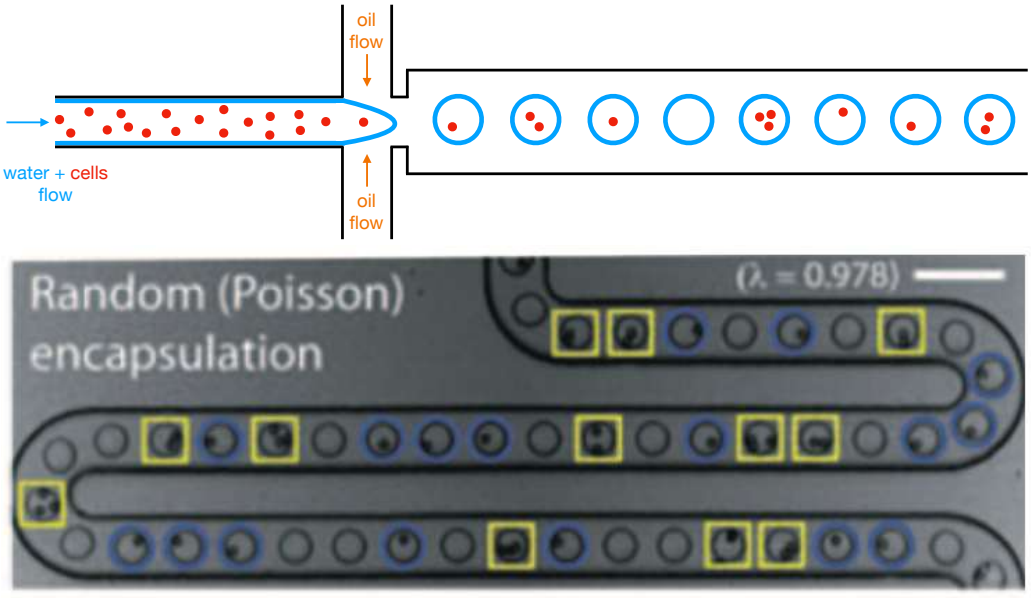

Figure 12.1: Schematic and experimental illustration of random encapsulation of cells inside droplets following a Poisson distribution [17, 33, 138].

Bibliography

[1] Eric Brouzes et al. "Droplet microfluidic technology for single-cell high-throughput screening". In: *Proceedings of the National Academy of Sciences* 106.34 (Aug. 2009), pp. 14195–14200. DOI: 10.1073/pnas.0903542106. URL: https://doi.org/10.1073/pnas.0903542106.

[2] Tomasz S. Kaminski, Ott Scheler, and Piotr Garstecki. "Droplet microfluidics for microbiology: techniques, applications and challenges". In: *Lab on a Chip* 16.12 (2016), pp. 2168–2187. DOI: 10.1039/c6lc00367b. URL: https://doi.org/10.1039/c6lc00367b.

[3] Todd P Lagus and Jon F Edd. "A review of the theory, methods and recent applications of high-throughput single-cell droplet microfluidics". In: *Journal of Physics D: Applied Physics* 46.11 (Feb. 2013), p. 114005. DOI: 10.1088/0022-3727/46/11/114005. URL: https://doi.org/10.1088/0022-3727/46/11/114005.

[4] Mira T. Guo et al. "Droplet microfluidics for high-throughput biological assays". In: *Lab on a Chip* 12.12 (2012), p. 2146. DOI: 10.1039/c2lc21147e. URL: https://doi.org/10.1039/c2lc21147e.

[5] Raphaël F.-X. Tomasi et al. "Individual Control and Quantification of 3D Spheroids in a High-Density Microfluidic Droplet Array". In: *Cell Reports* 31.8 (May 2020), p. 107670. DOI: 10.1016/j.celrep.2020.107670. URL: https://doi.org/10.1016/j.celrep.2020.107670.

[6] Sébastien Sart et al. "Cell Culture in Microfluidic Droplets". In: *Chemical Reviews* 122.7 (Feb. 2022), pp. 7061–7096. DOI: 10.1021/acs.chemrev.1c00666. URL: https://doi.org/10.1021/acs.chemrev.1c00666.

[7] C.-W. Park and G. M. Homsy. "Two-phase displacement in Hele Shaw cells: theory". In: *Journal of Fluid Mechanics* 139 (Feb. 1984), pp. 291–308. DOI: 10.1017/s0022112084000367. URL: https://doi.org/10.1017/s0022112084000367.

[8] Isha Shukla et al. "Film thickness distribution in gravity-driven pancake-shaped droplets rising in a Hele-Shaw cell". In: *Journal of Fluid Mechanics* 874 (July 2019), pp. 1021–1040. DOI: 10.1017/jfm.2019.453. URL: https://doi.org/10.1017/jfm.2019.453.

[9] Lailai Zhu and François Gallaire. "A pancake droplet translating in a Hele-Shaw cell: lubrication film and flow field". In: *Journal of Fluid Mechanics* 798 (June 2016), pp. 955–969. DOI: 10.1017/jfm.2016.357. URL: https://doi.org/10.1017/jfm.2016.357.

[10] Benjamin Reichert, Isabelle Cantat, and Marie-Caroline Jullien. "Predicting droplet velocity in a Hele-Shaw cell". In: *Physical Review Fluids* 4.11 (Nov. 2019). DOI: 10.1103/physrevfluids.4.113602. URL: https://doi.org/10.1103/physrevfluids.4.113602.

[11] S. R. K. Maruvada and C.-W. Park. "Retarded motion of bubbles in Hele-Shaw cells". In: *Physics of Fluids* 8.12 (Dec. 1996), pp. 3229–3233. DOI: 10.1063/1.869113. URL: https://doi.org/10.1063/1.869113.

[12] Prof. John W. M. Bush. *Interfacial Phenomena, Fall 2010*. Course webpage. Apr. 2021. URL: https://thales.mit.edu/bush/index.php/2021/04/10/18-357-interfacial-phenomena/.

[13] Peter A. Kralchevsky and Kuniaki Nagayama. *Particles at fluids interfaces and membranes: Attachment of colloid particles and proteins to interfaces and formation of two-dimensional arrays*. Elsevier, 2001.

[14] Pierre-Gilles de Gennes, Françoise Brochard-Wyart, and David Quéré. *Capillarity and wetting phenomena: Drops, bubbles, pearls, waves*. Springer, 2010.

[15] Kwangseok Seo, Minyoung Kim, and Do Hyun Kim. "Re-derivation of Young's Equation, Wenzel Equation, and Cassie-Baxter Equation Based on Energy Minimization". In: *Surface Energy*. InTech, Dec. 2015. DOI: 10.5772/61066. URL: https://doi.org/10.5772/61066.

[16] Ralf Seemann et al. "Droplet based microfluidics". In: *Reports on Progress in Physics* 75.1 (Dec. 2011), p. 016601. DOI: 10.1088/0034-4885/75/1/016601. URL: https://doi.org/10.1088/0034-4885/75/1/016601.

[17] Ashleigh B. Theberge et al. "Microdroplets in Microfluidics: An Evolving Platform for Discoveries in Chemistry and Biology". In: *Angewandte Chemie International Edition* 49.34 (June 2010), pp. 5846–5868. DOI: 10.1002/anie.200906653. URL: https://doi.org/10.1002/anie.200906653.

[18] Philip H. King et al. "Interdroplet bilayer arrays in millifluidic droplet traps from 3D-printed moulds". In: *Lab Chip* 14.4 (2014), pp. 722–729. DOI: 10.1039/c3lc51072g. URL: https://doi.org/10.1039/c3lc51072g.

[19] Yun Chen, Shweta Narayan, and Cari S. Dutcher. "Phase-Dependent Surfactant Transport on the Microscale: Interfacial Tension and Droplet Coalescence". In: *Langmuir* 36.49 (Dec. 2020), pp. 14904–14923. DOI: 10.1021/acs.langmuir.0c02476. URL: https://doi.org/10.1021/acs.langmuir.0c02476.

[20] Etienne, Gianluca Nicolas. "Fluorinated surfactants in droplet-based microfluidics: Influence of their composition on the properties of emulsion drops". en. In: (2019). DOI: 10.5075/EPFL-THESIS-9304. URL: http://infoscience.epfl.ch/record/263787.

[21] Jenifer Clausell-Tormos et al. "Droplet-Based Microfluidic Platforms for the Encapsulation and Screening of Mammalian Cells and Multicellular Organisms". In: *Chemistry & Biology* 15.5 (May 2008), pp. 427–437. DOI: 10.1016/j.chembiol.2008.04.004. URL: https://doi.org/10.1016/j.chembiol.2008.04.004.

[22] C. Holtze et al. "Biocompatible surfactants for water-in-fluorocarbon emulsions". In: *Lab on a Chip* 8.10 (2008), p. 1632. DOI: 10.1039/b806706f. URL: https://doi.org/10.1039/b806706f.

[23] Jean-Christophe Baret. "Surfactants in droplet-based microfluidics". In: *Lab Chip* 12.3 (2012), pp. 422–433. DOI: 10.1039/c1lc20582j. URL: https://doi.org/10.1039/c1lc20582j.

[24] Arjen Pit, Michèl Duits, and Frieder Mugele. "Droplet Manipulations in Two Phase Flow Microfluidics". In: *Micromachines* 6.11 (Nov. 2015), pp. 1768–1793. DOI: 10.3390/mi6111455. URL: https://doi.org/10.3390/mi6111455.

[25] Pingan Zhu and Liqiu Wang. "Passive and active droplet generation with microfluidics: a review". In: *Lab on a Chip* 17.1 (2017), pp. 34–75. DOI: 10.1039/c6lc01018k. URL: https://doi.org/10.1039/c6lc01018k.

[26] Nachiket Shembekar et al. "Droplet-based microfluidics in drug discovery, transcriptomics and high-throughput molecular genetics". In: *Lab on a Chip* 16.8 (2016), pp. 1314–1331. DOI: 10.1039/c6lc00249h. URL: https://doi.org/10.1039/c6lc00249h.

[27] Jiu-Sheng CHEN and Jia-Huan JIANG. "Droplet Microfluidic Technology: Mirodroplets Formation and Manipulation". In: *Chinese Journal of Analytical Chemistry* 40.8 (Aug. 2012), pp. 1293–1300. DOI: 10.1016/s1872-2040(11)60567-7. URL: https://doi.org/10.1016/s1872-2040(11)60567-7.

[28] Charles N. Baroud, Francois Gallaire, and Rémi Dangla. "Dynamics of microfluidic droplets". In: *Lab on a Chip* 10.16 (2010), p. 2032. DOI: 10.1039/c001191f. URL: https://doi.org/10.1039/c001191f.

[29] Andrew S. Utada et al. "Dripping to Jetting Transitions in Coflowing Liquid Streams". In: *Physical Review Letters* 99.9 (Aug. 2007). DOI: 10.1103/physrevlett.99.094502. URL: https://doi.org/10.1103/physrevlett.99.094502.

[30] Levent Yobas et al. "High-performance flow-focusing geometry for spontaneous generation of monodispersed droplets". In: *Lab on a Chip* 6.8 (2006), p. 1073. DOI: 10.1039/b602240e. URL: https://doi.org/10.1039/b602240e.

[31] Shia-Yen Teh et al. "Droplet microfluidics". In: *Lab on a Chip* 8.2 (2008), p. 198. DOI: 10.1039/b715524g. URL: https://doi.org/10.1039/b715524g.

[32] Shelley L. Anna, Nathalie Bontoux, and Howard A. Stone. "Formation of dispersions using "flow focusing" in microchannels". In: *Applied Physics Letters* 82.3 (Jan. 2003), pp. 364–366. DOI: 10.1063/1.1537519. URL: https://doi.org/10.1063/1.1537519.

[33] Shaojiang Zeng et al. "Basic Technologies for Droplet Microfluidics". In: *Microfluidics*. Springer Berlin Heidelberg, 2011, pp. 69–90. DOI: 10.1007/128_2011_149. URL: https://doi.org/10.1007/128_2011_149.

[34] Derek Y. C. Chan, Evert Klaseboer, and Rogerio Manica. "Film drainage and coalescence between deformable drops and bubbles". In: *Soft Matter* 7.6 (2011), pp. 2235–2264. DOI: 10.1039/c0sm00812e. URL: https://doi.org/10.1039/c0sm00812e.

[35] Xize Niu et al. "Pillar-induced droplet merging in microfluidic circuits". In: *Lab on a Chip* 8.11 (2008), p. 1837. DOI: 10.1039/b813325e. URL: https://doi.org/10.1039/b813325e.

[36] Nicolas Bremond, Abdou R. Thiam, and Jérôme Bibette. "Decompressing Emulsion Droplets Favors Coalescence". In: *Physical Review Letters* 100.2 (Jan. 2008). DOI: 10.1103/physrevlett.100.024501. URL: https://doi.org/10.1103/physrevlett.100.024501.

[37] Rogier M. Schoeman et al. "High-throughput deterministic single-cell encapsulation and droplet pairing, fusion, and shrinkage in a single microfluidic device". In: *ELECTROPHORESIS* 35.2-3 (Sept. 2013), pp. 385–392. DOI: 10.1002/elps.201300179. URL: https://doi.org/10.1002/elps.201300179.

[38] Michele Zagnoni, Charles N. Baroud, and Jonathan M. Cooper. "Electrically initiated upstream coalescence cascade of droplets in a microfluidic flow". In: *Physical Review E* 80.4 (Oct. 2009). DOI: 10.1103/physreve.80.046303. URL: https://doi.org/10.1103/physreve.80.046303.

[39] Michele Zagnoni, Guillaume Le Lain, and Jonathan M. Cooper. "Electrocoalescence Mechanisms of Microdroplets Using Localized Electric Fields in Microfluidic Channels". In: *Langmuir* 26.18 (Aug. 2010), pp. 14443–14449. DOI: 10.1021/la101517t. URL: https://doi.org/10.1021/la101517t.

[40] Craig Priest, Stephan Herminghaus, and Ralf Seemann. "Controlled electrocoalescence in microfluidics: Targeting a single lamella". In: *Applied Physics Letters* 89.13 (Sept. 2006). DOI: 10.1063/1.2357039. URL: https://doi.org/10.1063/1.2357039.

[41] Keunho Ahn et al. "Dielectrophoretic manipulation of drops for high-speed microfluidic sorting devices". In: *Applied Physics Letters* 88.2 (Jan. 2006), p. 024104. DOI: 10.1063/1.2164911. URL: https://doi.org/10.1063/1.2164911.

[42] Ansgar M. Huebner et al. "Monitoring a Reaction at Submillisecond Resolution in Picoliter Volumes". In: *Analytical Chemistry* 83.4 (Jan. 2011), pp. 1462–1468. DOI: 10.1021/ac103234a. URL: https://doi.org/10.1021/ac103234a.

[43] Etienne Fradet et al. "Combining rails and anchors with laser forcing for selective manipulation within 2D droplet arrays". In: *Lab on a Chip* 11.24 (2011), p. 4228. DOI: 10.1039/c1lc20541b. URL: https://doi.org/10.1039/c1lc20541b.

[44] Charles N. Baroud, Matthieu Robert de Saint Vincent, and Jean-Pierre Delville. "An optical toolbox for total control of droplet microfluidics". In: *Lab on a Chip* 7.8 (2007), p. 1029. DOI: 10.1039/b702472j. URL: https://doi.org/10.1039/b702472j.

[45] Etienne Fradet et al. "Parallel measurements of reaction kinetics using ultralow-volumes". In: *Lab on a Chip* 13.22 (2013), p. 4326. DOI: 10.1039/c3lc50768h. URL: https://doi.org/10.1039/c3lc50768h.

[46] Paul Abbyad et al. "Sickling of red blood cells through rapid oxygen exchange in microfluidic drops". In: *Lab on a Chip* 10.19 (2010), p. 2505. DOI: 10.1039/c004390g. URL: https://doi.org/10.1039/c004390g.

[47] Sébastien Sart et al. "Multiscale cytometry and regulation of 3D cell cultures on a chip". In: *Nature Communications* 8.1 (Sept. 2017). DOI: 10.1038/s41467-017-00475-x. URL: https://doi.org/10.1038/s41467-017-00475-x.

[48] Gabriel Amselem et al. "Universal microfluidic platform for bioassays in anchored droplets". In: *Lab on a Chip* 16.21 (2016), pp. 4200–4211. DOI: 10.1039/c6lc00968a. URL: https://doi.org/10.1039/c6lc00968a.

[49] Charles N. Baroud et al. "Thermocapillary valve for droplet production and sorting". In: *Physical Review E* 75.4 (Apr. 2007). DOI: 10.1103/physreve.75.046302. URL: https://doi.org/10.1103/physreve.75.046302.

[50] Caroline Frot, Nicolas Taccoen, and Charles N. Baroud. "Frugal Droplet Microfluidics Using Consumer Opto-Electronics". In: *PLOS ONE* 11.8 (Aug. 2016). Ed. by Arum Han, e0161490. DOI: 10.1371/journal.pone.0161490. URL: https://doi.org/10.1371/journal.pone.0161490.

[51] Emilie Verneuil et al. “Laser-Induced Force on a Microfluidic Drop: Origin and Magnitude”. In: *Langmuir* 25.9 (Apr. 2009), pp. 5127–5134. DOI: 10.1021/la8041605. URL: https://doi.org/10.1021/la8041605.

[52] Raphaël F.-X. Tomasi et al. “Studying 3D cell cultures in a microfluidic droplet array under multiple time-resolved conditions”. In: (Sept. 2018). DOI: 10.1101/407759. URL: https://doi.org/10.1101/407759.

[53] Ilke Akartuna et al. “Chemically induced coalescence in droplet-based microfluidics”. In: *Lab on a Chip* 15.4 (2015), pp. 1140–1144. DOI: 10.1039/c4lc01285b. URL: https://doi.org/10.1039/c4lc01285b.

[54] Jonathan Tullis, Chong L. Park, and Paul Abbyad. “Selective fusion of anchored droplets via changes in surfactant concentration”. In: *Lab Chip* 14.17 (2014), pp. 3285–3289. DOI: 10.1039/c4lc00558a. URL: https://doi.org/10.1039/c4lc00558a.

[55] Qiyue Luan et al. “Microfluidic systems for hydrodynamic trapping of cells and clusters”. In: *Biomicrofluidics* 14.3 (May 2020). DOI: 10.1063/5.0002866. URL: https://doi.org/10.1063/5.0002866.

[56] Swastika S. Bithi and Siva A. Vanapalli. “Behavior of a train of droplets in a fluidic network with hydrodynamic traps”. In: *Biomicrofluidics* 4.4 (Dec. 2010), p. 044110. DOI: 10.1063/1.3523053. URL: https://doi.org/10.1063/1.3523053.

[57] Swastika S. Bithi et al. “Coalescing drops in microfluidic parking networks: A multifunctional platform for drop-based microfluidics”. In: *Biomicrofluidics* 8.3 (May 2014). DOI: 10.1063/1.4885079. URL: https://doi.org/10.1063/1.4885079.

[58] Weiwei Shi et al. “Microfluidic Platform for the Study of Caenorhabditis elegans”. In: *Microfluidics*. Springer Berlin Heidelberg, 2011, pp. 323–338. DOI: 10.1007/128_2011_145. URL: https://doi.org/10.1007/128_2011_145.

[59] Weiwei Shi et al. “Droplet-based microfluidic system for individual Caenorhabditis elegans assay”. In: *Lab on a Chip* 8.9 (2008), p. 1432. DOI: 10.1039/b808753a. URL: https://doi.org/10.1039/b808753a.

[60] Rebecca R. Pompano et al. “Microfluidics Using Spatially Defined Arrays of Droplets in One, Two, and Three Dimensions”. In: *Annual Review of Analytical Chemistry* 4.1 (July 2011), pp. 59–81. DOI: 10.1146/annurev.anchem.012809.102303. URL: https://doi.org/10.1146/annurev.anchem.012809.102303.

[61] Meng Sun, Swastika S. Bithi, and Siva A. Vanapalli. “Microfluidic static droplet arrays with tuneable gradients in material composition”. In: *Lab on a Chip* 11.23 (2011), p. 3949. DOI: 10.1039/c1lc20709a. URL: https://doi.org/10.1039/c1lc20709a.

[62] Wei Wang, Chun Yang, and Chang Ming Li. “On-demand microfluidic droplet trapping and fusion for on-chip static droplet assays”. In: *Lab on a Chip* 9.11 (2009), p. 1504. DOI: 10.1039/b903468d. URL: https://doi.org/10.1039/b903468d.

[63] Wei-Heong Tan and Shoji Takeuchi. “A trap-and-release integrated microfluidic system for dynamic microarray applications”. In: *Proceedings of the National Academy of Sciences* 104.4 (Jan. 2007), pp. 1146–1151. DOI: 10.1073/pnas.0606625104. URL: https://doi.org/10.1073/pnas.0606625104.

[64] Matthew Courtney et al. “Droplet Microfluidic System with On-Demand Trapping and Releasing of Droplet for Drug Screening Applications”. In: *Analytical Chemistry* 89.1 (Dec. 2016), pp. 910–915. DOI: 10.1021/acs.analchem.6b04039. URL: https://doi.org/10.1021/acs.analchem.6b04039.

[65] Si Hyung Jin et al. “Programmable Static Droplet Array for the Analysis of Cell–Cell Communication in a Confined Microenvironment”. In: *Analytical Chemistry* 89.18 (Sept. 2017), pp. 9722–9729. DOI: 10.1021/acs.analchem.7b01462. URL: https://doi.org/10.1021/acs.analchem.7b01462.

[66] Heon-Ho Jeong et al. “A highly addressable static droplet array enabling digital control of a single droplet at pico-volume resolution”. In: *Lab on a Chip* 16.9 (2016), pp. 1698–1707. DOI: 10.1039/c6lc00212a. URL: https://doi.org/10.1039/c6lc00212a.

[67] Hakim Boukellal et al. “Simple, robust storage of drops and fluids in a microfluidic device”. In: *Lab Chip* 9.2 (2009), pp. 331–338. DOI: 10.1039/b808579j. URL: https://doi.org/10.1039/b808579j.

[68] Longxiang Zhang et al. “Trapping a moving droplet train by bubble guidance in microfluidic networks”. In: *RSC Advances* 8.16 (2018), pp. 8787–8794. DOI: 10.1039/c7ra13507f. URL: https://doi.org/10.1039/c7ra13507f.

[69] Zenon Toprakcioglu and Tuomas P. J. Knowles. “Sequential storage and release of microdroplets”. In: *Microsystems & amp Nanoengineering* 7.1 (Sept. 2021). DOI: 10.1038/s41378-021-00303-9. URL: https://doi.org/10.1038/s41378-021-00303-9.

[70] Andreas Grimmer et al. “Simulation before fabrication: a case study on the utilization of simulators for the design of droplet microfluidic networks”. In: *RSC Advances* 8.60 (2018), pp. 34733–34742. DOI: 10.1039/c8ra05531a. URL: https://doi.org/10.1039/c8ra05531a.

[71] Kartik Totlani et al. “Scalable microfluidic droplet on-demand generator for non-steady operation of droplet-based assays”. In: *Lab on a Chip* 20.8 (2020), pp. 1398–1409. DOI: 10.1039/c9lc01103j. URL: https://doi.org/10.1039/c9lc01103j.

[72] Jing Xu et al. “Droplet-based microfluidic device for multiple-droplet clustering”. In: *Lab Chip* 12.4 (2012), pp. 725–730. DOI: 10.1039/c2lc20883k. URL: https://doi.org/10.1039/c2lc20883k.

[73] Alison M Skelley et al. “Microfluidic control of cell pairing and fusion”. In: *Nature Methods* 6.2 (Jan. 2009), pp. 147–152. DOI: 10.1038/nmeth.1290. URL: https://doi.org/10.1038/nmeth.1290.

[74] James Ryley and Olivia M. Pereira-Smith. “Microfluidics device for single cell gene expression analysis in Saccharomyces cerevisiae”. In: *Yeast* 23.14-15 (2006), pp. 1065–1073. DOI: 10.1002/yea.1412. URL: https://doi.org/10.1002/yea.1412.

[75] Dino Di Carlo, Liz Y. Wu, and Luke P. Lee. “Dynamic single cell culture array”. In: *Lab on a Chip* 6.11 (2006), p. 1445. DOI: 10.1039/b605937f. URL: https://doi.org/10.1039/b605937f.

[76] Donald Wlodkowic et al. “Microfluidic Single-Cell Array Cytometry for the Analysis of Tumor Apoptosis”. In: *Analytical Chemistry* 81.13 (June 2009), pp. 5517–5523. DOI: 10.1021/ac9008463. URL: https://doi.org/10.1021/ac9008463.

[77] Vigneswaran Narayanamurthy et al. "Microfluidic hydrodynamic trapping for single cell analysis: mechanisms, methods and applications". In: *Analytical Methods* 9.25 (2017), pp. 3751–3772. DOI: 10.1039/c7ay00656j. URL: https://doi.org/10.1039/c7ay00656j.

[78] Xiaoming Chen and Carolyn L. Ren. "A microfluidic chip integrated with droplet generation, pairing, trapping, merging, mixing and releasing". In: *RSC Advances* 7.27 (2017), pp. 16738–16750. DOI: 10.1039/c7ra02336g. URL: https://doi.org/10.1039/c7ra02336g.

[79] Yunpeng Bai et al. "A double droplet trap system for studying mass transport across a droplet-droplet interface". In: *Lab on a Chip* 10.10 (2010), p. 1281. DOI: 10.1039/b925133b. URL: https://doi.org/10.1039/b925133b.

[80] Burak Dura et al. "Profiling lymphocyte interactions at the single-cell level by microfluidic cell pairing". In: *Nature Communications* 6.1 (Jan. 2015). DOI: 10.1038/ncomms6940. URL: https://doi.org/10.1038/ncomms6940.

[81] Ansgar Huebner et al. "Static microdroplet arrays: a microfluidic device for droplet trapping, incubation and release for enzymatic and cell-based assays". In: *Lab Chip* 9.5 (2009), pp. 692–698. DOI: 10.1039/b813709a. URL: https://doi.org/10.1039/b813709a.

[82] Laurent Mugherli et al. "Quantifying the sol–gel process and detecting toxic gas in an array of anchored microfluidic droplets". In: *Lab on a Chip* 20.2 (2020), pp. 236–243. DOI: 10.1039/c9lc00750d. URL: https://doi.org/10.1039/c9lc00750d.

[83] Yu He et al. "A photofabricated honeycomb micropillar array for loss-free trapping of microfluidic droplets and application to digital PCR". In: *Lab on a Chip* 21.20 (2021), pp. 3933–3941. DOI: 10.1039/d1lc00629k. URL: https://doi.org/10.1039/d1lc00629k.

[84] Jared Kehe et al. "Massively parallel screening of synthetic microbial communities". In: *Proceedings of the National Academy of Sciences* 116.26 (June 2019), pp. 12804–12809. DOI: 10.1073/pnas.1900102116. URL: https://doi.org/10.1073/pnas.1900102116.

[85] Simon F. Berlanda et al. "Recent Advances in Microfluidic Technology for Bioanalysis and Diagnostics". In: *Analytical Chemistry* 93.1 (Nov. 2020), pp. 311–331. DOI: 10.1021/acs.analchem.0c04366. URL: https://doi.org/10.1021/acs.analchem.0c04366.

[86] Christian H. J. Schmitz et al. "Dropspots: a picoliter array in a microfluidic device". In: *Lab Chip* 9.1 (2009), pp. 44–49. DOI: 10.1039/b809670h. URL: https://doi.org/10.1039/b809670h.

[87] Jon F. Edd et al. "Nucleation and solidification in static arrays of monodisperse drops". In: *Lab on a Chip* 9.13 (2009), p. 1859. DOI: 10.1039/b821785h. URL: https://doi.org/10.1039/b821785h.

[88] Sarah Köster et al. "Influence of Internal Capsid Pressure on Viral Infection by Phage λ". In: *Biophysical Journal* 97.6 (Sept. 2009), pp. 1525–1529. DOI: 10.1016/j.bpj.2009.07.007. URL: https://doi.org/10.1016/j.bpj.2009.07.007.

[89] Alireza Karbalaei Baba. "A Theoretical, Numerical, and Experimental Study of Trapped Droplet Coalescence and Mixing, Passively and Under Electric Field". Electronic Theses and Dissertations. University of Central Florida, 2019. URL: https://stars.library.ucf.edu/etd/6847.

[90] Zehang Gao et al. “Droplets isolated array: A universal platform of delaying molecule cross-contamination between microdroplets for digital enzyme-based immunoassay”. In: *Sensors and Actuators B: Chemical* 324 (Dec. 2020), p. 128716. DOI: 10.1016/j.snb.2020.128716. URL: https://doi.org/10.1016/j.snb.2020.128716.

[91] Rémi Dangla, Sungyon Lee, and Charles N. Baroud. “Trapping Microfluidic Drops in Wells of Surface Energy”. In: *Physical Review Letters* 107.12 (Sept. 2011). DOI: 10.1103/physrevlett.107.124501. URL: https://doi.org/10.1103/physrevlett.107.124501.

[92] Gabriel Amselem et al. “Breaking Anchored Droplets in a Microfluidic Hele-Shaw Cell”. In: *Physical Review Applied* 3.5 (May 2015). DOI: 10.1103/physrevapplied.3.054006. URL: https://doi.org/10.1103/physrevapplied.3.054006.

[93] Mathias Nagel, P.-T. Brun, and François Gallaire. “A numerical study of droplet trapping in microfluidic devices”. In: *Physics of Fluids* 26.3 (Mar. 2014), p. 032002. DOI: 10.1063/1.4867251. URL: https://doi.org/10.1063/1.4867251.

[94] Paul Abbyad et al. “Rails and anchors: guiding and trapping droplet microreactors in two dimensions”. In: *Lab Chip* 11.5 (2011), pp. 813–821. DOI: 10.1039/c0lc00104j. URL: https://doi.org/10.1039/c0lc00104j.

[95] Meng Ting Chung et al. “Deterministic droplet-based co-encapsulation and pairing of microparticles via active sorting and downstream merging”. In: *Lab Chip* 17.21 (2017), pp. 3664–3671. DOI: 10.1039/c7lc00745k. URL: https://doi.org/10.1039/c7lc00745k.

[96] Margaux Duchamp et al. “Microfluidic Device for Droplet Pairing by Combining Droplet Railing and Floating Trap Arrays”. In: *Micromachines* 12.9 (Sept. 2021), p. 1076. DOI: 10.3390/mi12091076. URL: https://doi.org/10.3390/mi12091076.

[97] Adrien Saint-Sardos et al. “High-throughput measurements of intra-cellular and secreted cytokine from single spheroids using anchored microfluidic droplets”. In: (Sept. 2020). DOI: 10.1101/2020.09.25.312900. URL: https://doi.org/10.1101/2020.09.25.312900.

[98] Manibarathi Vaithiyanathan et al. “Luminescent nanomaterials for droplet tracking in a microfluidic trapping array”. In: *Analytical and Bioanalytical Chemistry* 411.1 (Nov. 2018), pp. 157–170. DOI: 10.1007/s00216-018-1448-1. URL: https://doi.org/10.1007/s00216-018-1448-1.

[99] Nora Safa et al. “Population-based analysis of cell-penetrating peptide uptake using a microfluidic droplet trapping array”. In: *Analytical and Bioanalytical Chemistry* 411.12 (Mar. 2019), pp. 2729–2741. DOI: 10.1007/s00216-019-01713-5. URL: https://doi.org/10.1007/s00216-019-01713-5.

[100] Ayako Yamada et al. “Trapping and release of giant unilamellar vesicles in microfluidic wells”. In: *Soft Matter* 10.32 (June 2014), p. 5878. DOI: 10.1039/c4sm00065j. URL: https://doi.org/10.1039/c4sm00065j.

[101] Marie R. G. Kopp et al. “Microfluidic Shrinking Droplet Concentrator for Analyte Detection and Phase Separation of Protein Solutions”. In: *Analytical Chemistry* 92.8 (Apr. 2020), pp. 5803–5812. DOI: 10.1021/acs.analchem.9b05329. URL: https://doi.org/10.1021/acs.analchem.9b05329.

[102] Miriam Linsenmeier et al. “Analysis of biomolecular condensates and protein phase separation with microfluidic technology”. In: *Biochimica et Biophysica Acta (BBA) - Molecular Cell Research* 1868.1 (Jan. 2021), p. 118823. DOI: 10.1016/j.bbamcr.2020.118823. URL: https://doi.org/10.1016/j.bbamcr.2020.118823.

[103] Weiwei Shi et al. “Droplet microfluidics for characterizing the neurotoxin-induced responses in individual Caenorhabditis elegans”. In: *Lab on a Chip* 10.21 (2010), p. 2855. DOI: 10.1039/c0lc00256a. URL: https://doi.org/10.1039/c0lc00256a.

[104] Gustave Ronteix et al. “High resolution microfluidic assay and probabilistic modeling reveal cooperation between T cells in tumor killing”. In: *Nature Communications* 13.1 (June 2022). DOI: 10.1038/s41467-022-30575-2. URL: https://doi.org/10.1038/s41467-022-30575-2.

[105] A. Barizien et al. “Growing from a few cells: combined effects of initial stochasticity and cell-to-cell variability”. In: *Journal of The Royal Society Interface* 16.153 (Apr. 2019), p. 20180935. DOI: 10.1098/rsif.2018.0935. URL: https://doi.org/10.1098/rsif.2018.0935.

[106] Jung-uk Shim et al. “Control and Measurement of the Phase Behavior of Aqueous Solutions Using Microfluidics”. In: *Journal of the American Chemical Society* 129.28 (June 2007), pp. 8825–8835. DOI: 10.1021/ja071820f. URL: https://doi.org/10.1021/ja071820f.

[107] Hongxing Hu, David Eustace, and Christoph A. Merten. “Efficient cell pairing in droplets using dual-color sorting”. In: *Lab on a Chip* 15.20 (2015), pp. 3989–3993. DOI: 10.1039/c5lc00686d. URL: https://doi.org/10.1039/c5lc00686d.

[108] Kaston Leung et al. “A programmable droplet-based microfluidic device applied to multiparameter analysis of single microbes and microbial communities”. In: *Proceedings of the National Academy of Sciences* 109.20 (Apr. 2012), pp. 7665–7670. DOI: 10.1073/pnas.1106752109. URL: https://doi.org/10.1073/pnas.1106752109.

[109] Louai Labanieh et al. “Floating Droplet Array: An Ultrahigh-Throughput Device for Droplet Trapping, Real-time Analysisand Recovery”. In: *Micromachines* 6.10 (Sept. 2015), pp. 1469–1482. DOI: 10.3390/mi6101431. URL: https://doi.org/10.3390/mi6101431.

[110] Aude I. Segaliny et al. “Functional TCR T cell screening using single-cell droplet microfluidics”. In: *Lab on a Chip* 18.24 (2018), pp. 3733–3749. DOI: 10.1039/c8lc00818c. URL: https://doi.org/10.1039/c8lc00818c.

[111] Syung Hun Han et al. “Photoactivated Selective Release of Droplets from Microwell Arrays”. In: *ACS Applied Materials and Interfaces* 12.3 (Jan. 2020), pp. 3936–3944. DOI: 10.1021/acsami.9b17575. URL: https://doi.org/10.1021/acsami.9b17575.

[112] Feng Shen et al. “Digital PCR on a SlipChip”. In: *Lab on a Chip* 10.20 (2010), p. 2666. DOI: 10.1039/c004521g. URL: https://doi.org/10.1039/c004521g.

[113] Wenbin Du et al. “SlipChip”. In: *Lab on a Chip* 9.16 (2009), p. 2286. DOI: 10.1039/b908978k. URL: https://doi.org/10.1039/b908978k.

[114] Piotr M. Korczyk et al. “Microfluidic traps for hard-wired operations on droplets”. In: *Lab on a Chip* 13.20 (2013), p. 4096. DOI: 10.1039/c3lc50347j. URL: https://doi.org/10.1039/c3lc50347j.

[115] Yang Shi et al. “High throughput generation and trapping of individual agarose microgel using microfluidic approach”. In: *Microfluidics and Nanofluidics* 15.4 (Feb. 2013), pp. 467–474. DOI: 10.1007/s10404-013-1160-6. URL: https://doi.org/10.1007/s10404-013-1160-6.

[116] Riëlle de Ruiter et al. “Electrostatic potential wells for on-demand drop manipulation in microchannels”. In: *Lab on a Chip* 14.5 (2014), p. 883. DOI: 10.1039/c3lc51121a. URL: https://doi.org/10.1039/c3lc51121a.

[117] Nadia Vertti-Quintero et al. “Time-resolved microfluidics unravels individual cellular fates during double-strand break repair”. In: *BMC Biology* 20.1 (Dec. 2022). DOI: 10.1186/s12915-022-01456-3. URL: https://doi.org/10.1186/s12915-022-01456-3.

[118] Luis M. Fidalgo, Chris Abell, and Wilhelm T. S. Huck. “Surface-induced droplet fusion in microfluidic devices”. In: *Lab on a Chip* 7.8 (2007), p. 984. DOI: 10.1039/b708091c. URL: https://doi.org/10.1039/b708091c.

[119] Benjamin J. Hindson et al. “High-Throughput Droplet Digital PCR System for Absolute Quantitation of DNA Copy Number”. In: *Analytical Chemistry* 83.22 (Oct. 2011), pp. 8604–8610. DOI: 10.1021/ac202028g. URL: https://doi.org/10.1021/ac202028g.

[120] Aniruddha M. Kaushik et al. “Accelerating bacterial growth detection and antimicrobial susceptibility assessment in integrated picoliter droplet platform”. In: *Biosensors and Bioelectronics* 97 (Nov. 2017), pp. 260–266. DOI: 10.1016/j.bios.2017.06.006. URL: https://doi.org/10.1016/j.bios.2017.06.006.

[121] Linas Mazutis et al. “Single-cell analysis and sorting using droplet-based microfluidics”. In: *Nature Protocols* 8.5 (Apr. 2013), pp. 870–891. DOI: 10.1038/nprot.2013.046. URL: https://doi.org/10.1038/nprot.2013.046.

[122] Deniz Pekin et al. “Quantitative and sensitive detection of rare mutations using droplet-based microfluidics”. In: *Lab on a Chip* 11.13 (2011), p. 2156. DOI: 10.1039/c1lc20128j. URL: https://doi.org/10.1039/c1lc20128j.

[123] Sébastien Sart et al. “Mapping Structure and Biological Functions within Mesenchymal Bodies using Microfluidics”. In: (Jan. 2019). DOI: 10.1101/514158. URL: https://doi.org/10.1101/514158.

[124] Ouriel Caen. “Droplet microfluidics for cancer cell evolution”. PhD thesis. Université Sorbonne Paris Cité, 2016.

[125] John Oprea. *Differential Geometry and Its Applications*. American Mathematical Society, 2007. DOI: 10.1090/clrm/059. URL: https://doi.org/10.1090/clrm/059.

[126] M. A. Verges, M. C. Larson, and R. Bacou. “Force and shapes of liquid bridges between circular pads”. In: *Experimental Mechanics* 41.4 (Dec. 2001), pp. 351–357. DOI: 10.1007/bf02323929. URL: https://doi.org/10.1007/bf02323929.

[127] Franck Luthon. “Initiation au traitement d’images”. Master. Lecture. France, June 2019. URL: https://hal.science/cel-01477225.

[128] Caroline A. Schneider, Wayne S. Rasband, and Kevin W. Eliceiri. “NIH Image to ImageJ: 25 years of image analysis”. In: *Nature Methods* 9.7 (2012), pp. 671–675. DOI: 10.1038/nmeth.2089.

[129] Ya Gai et al. “Amphiphilic nanoparticles suppress droplet break-up in a concentrated emulsion flowing through a narrow constriction”. In: *Biomicrofluidics* 11.3 (May 2017). DOI: 10.1063/1.4985158. URL: https://doi.org/10.1063/1.4985158.

[130] Olaf Wagner et al. "Biocompatible fluorinated polyglycerols for droplet microfluidics as an alternative to PEG-based copolymer surfactants". In: *Lab on a Chip* 16.1 (2016), pp. 65–69. DOI: 10.1039/c5lc00823a. URL: https://doi.org/10.1039/c5lc00823a.

[131] Michael J. Owen. "Silicone Surface Fundamentals". In: *Macromolecular Rapid Communications* 42.5 (Sept. 2020), p. 2000360. DOI: 10.1002/marc.202000360. URL: https://doi.org/10.1002/marc.202000360.

[132] Shazia Bashir et al. "Dynamic wetting in microfluidic droplet formation". In: *BioChip Journal* 8.2 (June 2014), pp. 122–128. DOI: 10.1007/s13206-014-8207-y. URL: https://doi.org/10.1007/s13206-014-8207-y.

[133] Sindhu Vudayagiri, Michael Daniel Junker, and Anne Ladegaard Skov. "Factors affecting the surface and release properties of thin polydimethylsiloxane films". In: *Polymer Journal* 45.8 (Jan. 2013), pp. 871–878. DOI: 10.1038/pj.2012.227. URL: https://doi.org/10.1038/pj.2012.227.

[134] Fabienne Courtois et al. "An Integrated Device for Monitoring Time-Dependent in vitro Expression From Single Genes in Picolitre Droplets". In: *ChemBioChem* 9.3 (Feb. 2008), pp. 439–446. DOI: 10.1002/cbic.200700536. URL: https://doi.org/10.1002/cbic.200700536.

[135] Andrew C. Hatch et al. "1-Million droplet array with wide-field fluorescence imaging for digital PCR". In: *Lab on a Chip* 11.22 (2011), p. 3838. DOI: 10.1039/c1lc20561g. URL: https://doi.org/10.1039/c1lc20561g.

[136] Adam R. Abate et al. "Beating Poisson encapsulation statistics using close-packed ordering". In: *Lab on a Chip* 9.18 (2009), p. 2628. DOI: 10.1039/b909386a. URL: https://doi.org/10.1039/b909386a.

[137] Keshvad Shahrivar and Francesco Del Giudice. "Beating Poisson stochastic particle encapsulation in flow-focusing microfluidic devices using viscoelastic liquids". In: *Soft Matter* 18.32 (2022), pp. 5928–5933. DOI: 10.1039/d2sm00935h. URL: https://doi.org/10.1039/d2sm00935h.

[138] Jon F. Edd et al. "Controlled encapsulation of single-cells into monodisperse picolitre drops". In: *Lab on a Chip* 8.8 (2008), p. 1262. DOI: 10.1039/b805456h. URL: https://doi.org/10.1039/b805456h.

[139] Henrik Bruus. *Theoretical microfluidics*. Vol. 18. Oxford university press, 2007.

Part V

Annexe

Chapter 1

Microfluidic resistance

One of the fundamental equations of microfluidics concerns the flow of fluids in small channels. This flow problem is well known in physics and was first studied by Poiseuille. The hydraulic resistance can be established in a relatively simple way for a channel with a circular section. Indeed, the latter has the advantage of having an axial symmetry of revolution which greatly simplifies the equations. However, the approach to this problem in the case of a rectangular section is much more technical to implement. However, microfluidic chips almost exclusively have channels with a rectangular cross section. Therefore, it may be interesting to remind the theoretical model which demonstrate the origin of the fluidic resistance in this case. This section will be dedicated to explaining the main steps of demonstrating the fluid flow within a rectangular cross-sectional channel [139]. To begin with, the flow of a fluid can be modelled by the Navier-Stokes equation. This is given by:

$$\frac{\partial \boldsymbol{v}}{\partial t} + (\boldsymbol{v} \cdot \nabla)\boldsymbol{v} = -\frac{1}{\rho}\nabla p + \nu \Delta \boldsymbol{v} + \boldsymbol{b}. \tag{1.1}$$

At the microfluidic scale Re $<<$ 1, which means that viscosity overcomes inertia. Therefore, the convective acceleration term in the Navier-Stokes equations can be neglected. Furthermore, the flow varies little with time and the liquid can be considered stationary. This can be seen through $\alpha << 1$. The local acceleration term is thus approximated to zero. Once these assumptions are made, it is possible to write the so-called Stokes equation:

$$0 = \mu \Delta \boldsymbol{v} - \nabla p. \tag{1.2}$$

For the considered problem of flow in a rectangular section, the velocity has a component only along the x axis. Moreover, it is only a function of the $y$and$z$ directions. The Stokes partial differential equation can be reduced to:

$$\begin{cases} (\partial_y^2 + \partial_z^2) v_x(y,z) = \dfrac{1}{\mu}\nabla p & \text{for } -w/2 < y < w/2,\ 0 < z < h, \\ v_x(y,z) = 0 & \text{for } y = \pm w/2,\ z = 0,\ z = h. \end{cases} \tag{1.3}$$

As a first step, it is conventional to look at the pressure gradient in the right hand side. If one rewrite the equation in its different components:

$$\begin{bmatrix} \partial_x p(x,y,z) \\ \partial_y p(x,y,z) \\ \partial_z p(x,y,z) \end{bmatrix} = \begin{bmatrix} (\partial_y^2 + \partial_z^2) v_x(y,z) \\ 0 \\ 0 \end{bmatrix}. \tag{1.4}$$

Thus, integrating along y and z, the pressure gradient is constant along these two spatial directions. Thanks to the initial conditions, this constant is evaluated at zero. It is therefore possible to write that $p_y = p_z = 0$. This also means that the pressure gradient is a function of x only. Since the left-hand side is only a function of y and z, it is a constant according to x.If the constant is called A, the equation becomes:

$$(\partial_y^2 + \partial_z^2)v_x(y,z) = A = \partial_x p(x). \tag{1.5}$$

Solving the relation on the right leads to:

$$p(x) = Ax + B. \tag{1.6}$$

The initial conditions are given by $p(0) = p_0 + \Delta p$ and $p(L) = p_0$. Using these boundary conditions, it is possible to evaluate the pressure equation univocally:

$$p(x) = \frac{\Delta p}{L}(L - x) + p_0. \tag{1.7}$$

Starting from the Eq. 1.5, and injecting the solution found for the pressure gradient, the real complex part of the problem appears through the equation:

$$(\partial_y^2 + \partial_z^2)\underbrace{\boxed{v_x(y,z)}}_{\textcircled{1}} = \frac{-\Delta p}{\mu L} \cdot \underbrace{\boxed{1}}_{\textcircled{2}}. \tag{1.8}$$

It is possible to develop the two boxed terms into Fourier series. By expanding this Fourier series according to z, the first term can be written as:

$$\textcircled{1} = v_x(y,z) = \sum_{n=1}^{\infty} f_n(y) \sin\left(\frac{n\pi z}{h}\right). \tag{1.9}$$

The second term to be expanded is simply the constant function 1. The objective this time will be to determine explicitly the value of the Fourier coefficients. As a reminder, the Fourier series expansion is given by:

$$f(z) = a_0 + \sum_{n=1}^{\infty} a_n \cos\left(\frac{n\pi z}{L}\right) + \sum_{n=1}^{\infty} b_n \sin\left(\frac{n\pi z}{L}\right). \tag{1.10}$$

The value of the coefficients can be evaluated through the integrals:

$$a_0 = \frac{1}{2L}\int_{-L}^{L} f(z)\,\mathrm{dz}, \quad a_n = \frac{1}{L}\int_{-L}^{L} f(z)\cos\left(\frac{n\pi z}{L}\right)\,\mathrm{dz}, \qquad b_n = \frac{1}{L}\int_{-L}^{L} f(z)\sin\left(\frac{n\pi z}{L}\right)\,\mathrm{dz}. \tag{1.11}$$

To decompose our function into a Fourier series, we must exploit symmetry and therefore make it periodic. It is necessary to consider a continuous function by piece. Therefore, $f(z) = 1$ on $[0, h]$ and $f(z) = -1$ on $[0, -h]$. The interval is then $L = h$ which correspond to the half of one period. Once all these conditions are met, the calculation of the Fourier coefficient a_0 is given by:

$$a_0 = \frac{1}{2h}\left(\int_{-h}^{0} -1\,\mathrm{dz} + \int_{0}^{\mathrm{h}} 1\,\mathrm{dz}\right) = 0. \tag{1.12}$$

The coefficient a_n is given by:

$$a_n = \frac{1}{h}\left(\int_{-h}^{0} -\cos\left(\frac{n\pi z}{h}\right)\,\mathrm{dz} + \int_{0}^{\mathrm{h}} \cos\left(\frac{\mathrm{n\pi z}}{\mathrm{h}}\right)\,\mathrm{dz}\right) = 0. \tag{1.13}$$

And finally, the coefficient b_n is evaluated as:

$$b_n = \frac{1}{h}\left(\int_{-h}^{0} -\sin\left(\frac{n\pi z}{h}\right)\,\mathrm{dz} + \int_{0}^{\mathrm{h}} \sin\left(\frac{\mathrm{n\pi z}}{\mathrm{h}}\right)\,\mathrm{dz}\right) = \frac{2}{n\pi}\left(1-(-1)^n\right) = \begin{cases} 0 & \text{if } n \text{ even}, \\ \dfrac{4}{n\pi} & \text{if } n \text{ odd}. \end{cases} \tag{1.14}$$

By re-injecting the value of the coefficients into Eq. 1.10, here comes the fourier series decomposition of the desired constant function:

$$\textcircled{2} = 1 = f(z) = \frac{4}{\pi}\sum_{n_{\mathrm{odd}}} \frac{1}{n}\sin\left(\frac{n\pi z}{h}\right) = \frac{4}{\pi}\sum_{n=1}^{\infty}\frac{1}{2n+1}\sin\left(\frac{(2n+1)\pi z}{h}\right). \tag{1.15}$$

By injecting the Fourier series obtained into the main differential equation, it follows that:

$$(\partial_y^2 + \partial_z^2)\sum_{n=1}^{\infty} f_n(y)\sin\left(\frac{n\pi z}{h}\right) = \frac{-4\Delta p}{\mu L\pi}\sum_{n_{\mathrm{odd}}}\frac{1}{n}\sin\left(\frac{n\pi z}{h}\right), \tag{1.16}$$

$$\iff \sum_{n=1}^{\infty}\left(\frac{\mathrm{d^2f_n(y)}}{\mathrm{dy^2}} - \frac{n^2\pi^2}{h^2}f_n(y)\right)\sin\left(\frac{n\pi z}{h}\right) = \frac{-4\Delta p}{\mu L\pi}\sum_{n_{\mathrm{odd}}}\frac{1}{n}\sin\left(\frac{n\pi z}{h}\right). \tag{1.17}$$

By separating the equation according to parity, it is possible to write that:

$$\begin{cases} f_n(y) = 0 & \text{for } n \text{ even}, \quad (1.18a) \\ \dfrac{\mathrm{d^2f_n(y)}}{\mathrm{dy^2}} - \dfrac{n^2\pi^2}{h^2}f_n(y) = -\dfrac{4\Delta p}{\mu L\pi n} & \text{for } n \text{ odd}. \quad (1.18b) \end{cases}$$

Focusing on the Eq. 1.18b, it can be seen that it is in fact a linear differential equation with constant coefficients of order two. Therefore, the solution is written as the sum of the homogeneous and the particular solution:

$$f_n(y) = f_n^h(y) + f_n^p(y). \tag{1.19}$$

Focusing on the homogeneous solution, simply equating the independent term to zero, it follows that:

$$\frac{\mathrm{d^2f_n^h(y)}}{\mathrm{dy^2}} - \frac{n^2\pi^2}{h^2}f_n^h(y) = 0, \tag{1.20}$$

$$\iff f_n^h(y) = A\cosh\left(\frac{n\pi y}{h}\right) + B\sinh\left(\frac{n\pi y}{h}\right). \tag{1.21}$$

where the integration constants A and B can be determined via the initial conditions $f_n\left(\frac{w}{2}\right) = f_n\left(-\frac{w}{2}\right) = 0$. Solving the system of equations gives the value of the constants A and B:

$$A = \frac{-4h^2\Delta p}{\mu L\pi^3 n^3\cosh\left(\frac{n\pi w}{2h}\right)}, \qquad B = 0. \tag{1.22}$$

$$\implies f_n^h(y) = \frac{-4h^2\Delta p}{\mu L \pi^3 n^3 \cosh\left(\frac{n\pi w}{2h}\right)} \cosh\left(\frac{n\pi y}{h}\right). \tag{1.23}$$

The particular solution is a little more subtle to achieve. The idea to find it is to remember that it represents in most situations the long term evolution of the system. Thus, once equilibrium is reached, it represents the stable state of the system. A good rule of thumb is to consider the case where the derivatives cancel out when this steady state is reached. There is, a priory, no more variation of the function. This technique leads to consider the differential Eq. 1.18b by setting the second derivative to zero. One has:

$$-\frac{n^2\pi^2}{h^2} f_n^p(y) = -\frac{4\Delta p}{\mu L \pi n}, \tag{1.24}$$

$$\iff f_n^p(y) = \frac{4h^2\Delta p}{\mu L \pi^3 n^3}. \tag{1.25}$$

The combination of the homogeneous and particular solution gives the final solution:

$$f_n(y) = \frac{4h^2\Delta p}{\mu L \pi^3 n^3}\left[1 - \frac{\cosh\left(\frac{n\pi y}{h}\right)}{\cosh\left(\frac{n\pi w}{2h}\right)}\right]. \tag{1.26}$$

By injecting the solution found in the Eq. 1.9, we deduce the expression of the speed:

$$v_x(y,z) = \sum_{n_{\text{odd}}} \frac{4h^2\Delta p}{\mu L \pi^3 n^3}\left[1 - \frac{\cosh\left(\frac{n\pi y}{h}\right)}{\cosh\left(\frac{n\pi w}{2h}\right)}\right] \sin\left(\frac{n\pi z}{h}\right). \tag{1.27}$$

The Fig. 1.1 illustrates the velocity profile obtained from Eq. 1.27 in a rectangular cross-section channel.

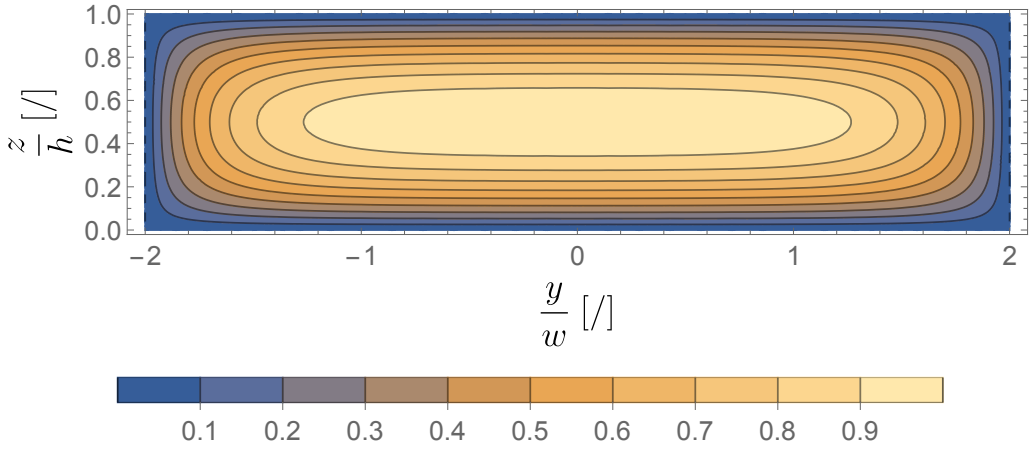

Figure 1.1: Contour plot illustrating the velocity profile of a liquid in a rectangular cross-section channel. The parameters used are $h = l = p = 1$, $w = 4$, $\mu = 0.001$. This velocity profile has been normalized by the maximum velocity in the channel.

Once the velocity expression is known, the preliminary step of evaluating the flow rate is completed. Indeed, it is now sufficient to integrate the velocity over the entire cross-section through which the fluid flows. The application of this reasoning leads to:

$$Q = 2\int_0^{w/2}\int_0^{h} v_x(y,z)\,\mathrm{dz}\,\mathrm{dy}, \tag{1.28}$$

$$= 2\int_0^{w/2}\int_0^{h}\sum_{n_{\text{odd}}}\frac{4h^2\Delta p}{\mu L\pi^3 n^3}\left[1-\frac{\cosh\left(\frac{n\pi y}{h}\right)}{\cosh\left(\frac{n\pi w}{2h}\right)}\right]\sin\left(\frac{n\pi z}{h}\right)\mathrm{dz}\,\mathrm{dy}, \tag{1.29}$$

$$= \sum_{n_{\text{odd}}}^{\infty}\frac{8\Delta p h^2}{\mu L\pi^3 n^3}\int_0^{w/2}\left[1-\frac{\cosh\left(\frac{n\pi y}{h}\right)}{\cosh\left(\frac{n\pi w}{2h}\right)}\right]\mathrm{dy}\int_0^{\mathrm{h}}\sin\left(\frac{\mathrm{n}\pi\mathrm{z}}{\mathrm{h}}\right)\mathrm{dz}, \tag{1.30}$$

$$= \sum_{n_{\text{odd}}}^{\infty}-\frac{8\Delta p h^3}{\mu L\pi^4 n^4}\left[\frac{w}{2}-\frac{h}{n\pi}\frac{\sinh\left(\frac{n\pi w}{2h}\right)}{\cosh\left(\frac{n\pi w}{2h}\right)}\right]\left((-1)^n-1\right), \tag{1.31}$$

$$= \frac{8h^3\Delta p w}{\mu L\pi^4}\left(\boxed{\sum_{n_{\text{odd}}}^{\infty}\frac{1}{n^4}}-\sum_{n_{\text{odd}}}^{\infty}\frac{2h}{\pi w n^5}\tanh\left(\frac{n\pi w}{2h}\right)\right), \tag{1.32}$$

$$= \frac{h^3 w\Delta p}{12\mu L}\left(1-\sum_{n_{\text{odd}}}^{\infty}\frac{1}{n^5}\frac{192h}{\pi^5 w}\tanh\left(\frac{n\pi w}{2h}\right)\right). \tag{1.33}$$

The red boxed term is an infinite series whose solution can be calculated analytically. The development can be summarised as follows:

$$\sum_{n_{\text{odd}}}^{\infty}\frac{1}{n^4}=\sum_{n=1}^{\infty}\frac{1}{n^4}-\sum_{n_{\text{even}}}^{\infty}\frac{1}{n^4}=\sum_{n=1}^{\infty}\frac{1}{n^4}-\sum_{n=1}^{\infty}\frac{1}{(2n)^4}=\sum_{n=1}^{\infty}\frac{1}{n^4}-\frac{1}{16}\sum_{n=1}^{\infty}\frac{1}{n^4}=\zeta(4)\frac{15}{16}. \tag{1.34}$$

The last equality uses the Riemann zeta function which is defined as follows:

$$\zeta(x)=\sum_{n=1}^{\infty}\frac{1}{n^x}. \tag{1.35}$$

The rest of the reasoning will consist in evaluating the value of this function $\zeta(4)$. To do this, it is useful to recall Parseval's theorem which will be used in the rest of the demonstration:

$$\frac{1}{\pi}\int_{-\pi}^{\pi}\left(f(x)\right)^2\,\mathrm{dx}=2a_0^2+\sum_{n=1}^{\infty}(a_n^2+b_n^2). \tag{1.36}$$

In this case the different fourier coefficients are defined as follows:

$$a_0=\frac{1}{2\pi}\int_{-\pi}^{\pi}f(x)\,\mathrm{dx},\quad a_n=\frac{1}{\pi}\int_{-\pi}^{\pi}f(x)\cos(nx)\,\mathrm{dx},\qquad b_n=\frac{1}{\pi}\int_{-\pi}^{\pi}f(x)\sin(nx)\,\mathrm{dx}. \tag{1.37}$$

Now that this theoretical reminder has been given, it is possible to concentrate on solving the main problem through $\zeta(4)$. To do this, the function $f(x)=x^2$ is considered for a Fourier series expansion given in Eq. 1.10. The different Fourier coefficients are evaluated at:

$$a_0=\frac{1}{2\pi}\int_{-\pi}^{\pi}x^2\,\mathrm{dx}=\frac{\pi^2}{3},\quad a_n=\frac{1}{\pi}\int_{-\pi}^{\pi}x^2\cos(nx)\,\mathrm{dx}=\frac{4(-1)^{\mathrm{n}}}{\mathrm{n}^2},\qquad b_n=\frac{1}{\pi}\int_{-\pi}^{\pi}x^2\sin(nx)\,\mathrm{dx}=0. \tag{1.38}$$

Where integration by parts has been used to evaluate the value of the coefficient a_n. The calculation of b_n can be done directly, remembering that the integration of an odd function over a

symmetric interval is zero.

Now apply Parseval's theorem to Eq. 1.36. This allows to write:

$$\frac{1}{\pi}\int_{-\pi}^{\pi} x^4 \,\mathrm{dx} = \frac{2\pi^4}{9} + \sum_{n=1}^{\infty}\frac{16}{n^4}, \tag{1.39}$$

$$\iff \frac{2\pi^4}{5} = \frac{2\pi^4}{9} + \sum_{n=1}^{\infty}\frac{16}{n^4}, \tag{1.40}$$

$$\iff \zeta(4) = \sum_{n=1}^{\infty}\frac{1}{n^4} = \frac{\pi^4}{90}. \tag{1.41}$$

This gives the desired result. If the expression for the flow rate in Eq. 1.33 is considered again, it can be noted that one term shows $\zeta(5)$. However, after multiple searches, no analytical solution could be found. Indeed, this result always seems to be linked to some open problems in mathematics. This lead seems to be far from the main research topic of this master's thesis and from the simple student knowledge of the writer. However, it is possible to obtain a more elegant expression of the Eq. 1.9 if the channel is considered as flat and wide. From then on, the ratio $\frac{h}{w} \longrightarrow 0$ and thus $\frac{h}{w}\tanh\left(\frac{w}{h}\right) \longrightarrow \frac{h}{w}$. By a reasoning analogous to that provided by Eq. 1.34, it is possible to obtain:

$$\sum_{n_{\text{odd}}}^{\infty}\frac{1}{n^5} = \sum_{n=1}^{\infty}\frac{1}{n^5} - \sum_{n_{\text{even}}}^{\infty}\frac{1}{n^5} = \sum_{n=1}^{\infty}\frac{1}{n^5} - \sum_{n=1}^{\infty}\frac{1}{2n^5} = \sum_{n=1}^{\infty}\frac{1}{n^5} - \frac{1}{32}\sum_{n=1}^{\infty}\frac{1}{n^5} = \frac{31}{32}\zeta(5). \tag{1.42}$$

Using a numerical approximation for the value of $\zeta(5)$, the approximation of the flow rate in the case of channels such that $h < w$ is finally given by:

$$Q \approx \frac{h^3 w \Delta p}{12\mu L}\left(1 - 0.63\frac{h}{w}\right) = R\Delta p. \tag{1.43}$$

This is indeed the formula commonly found in the literature. This last relation thus concludes the demonstration.

1 Parseval's theorem

The Parseval's theorem proves the following equality:

$$\int_{-\pi}^{\pi} \left(f(x)\right)^2 \,\mathrm{dx} = \int_{-\pi}^{\pi} a_0 + \sum_{n=1}^{\infty}\left(a_n\cos(nx) + b_n\sin(nx)\right)^2 \,\mathrm{dx}. \tag{1.44}$$

Knowing that $f(x)^2$ can be expanded as:

$$\begin{aligned}(f(x))^2 &= \left(a_0 + \sum_{n=1}^{\infty}(a_n\cos(nx) + b_n\sin(nx))\right)\left(a_0 + \sum_{n=1}^{\infty}(a_n\cos(nx) + b_n\sin(nx))\right), \\ &= a_0^2 + 2a_0\sum_{n=1}^{\infty}(a_n\cos(nx) + b_n\sin(nx)) \\ &\quad + \sum_{n=1}^{\infty}\sum_{m=1}^{\infty}(a_n a_m\cos(nx)\cos(mx) + a_n b_m\cos(nx)\sin(mx) \\ &\qquad + a_m b_n\sin(nx)\cos(mx) + b_n b_m\sin(nx)\sin(mx)).\end{aligned} \tag{1.45}$$

The integration of this term can be written as:

$$\begin{aligned}\int_{-\pi}^{\pi}(f(x))^2\,\mathrm{dx} &= \int_{-\pi}^{\pi}a_0^2\,\mathrm{dx}+\int_{-\pi}^{\pi}2\mathrm{a}_0\sum_{\mathrm{n}=1}^{\infty}(\mathrm{a_n}\cos(\mathrm{nx})+\mathrm{b_n}\sin(\mathrm{nx}))\,\mathrm{dx}\\ &\quad+\int_{-\pi}^{\pi}\sum_{n=1}^{\infty}\sum_{m=1}^{\infty}(a_na_m\cos(nx)\cos(mx)+a_nb_m\cos(nx)\sin(mx)\\ &\quad+a_mb_n\sin(nx)\cos(mx)+b_nb_m\sin(nx)\sin(mx))\,\mathrm{dx},\\ &= 2\pi a_0^2+0+\sum_{n=1}^{\infty}\sum_{m=1}^{\infty}(a_na_m\pi\delta_{nm}+0+0+b_nb_m\pi\delta_{nm}),\\ &= 2\pi a_0^2+\pi\sum_{n=1}^{\infty}(a_n^2+b_n^2). \end{aligned}\tag{1.46}$$

For the second term, the fact that the integral of the sine or cosine over one period is zero was used. For the zeros appearing in the third term, they simply result from the fact that the product of an even function with an odd function gives an odd function and the integral of the latter over a symmetrical domain is zero. The appearance of Kronecker's delta is more subtle to deal with. Here is the proof for the cosine, it is analogous for the sine. In the following development, we assume $m \neq n$. Equality will be considered in the following. One has:

$$\int_{-\pi}^{\pi}\cos(nx)\cos(mx)\,\mathrm{dx} = \int_{-\pi}^{\pi}\frac{1}{2}\cos((m+n)x)\,\mathrm{dx}+\int_{-\pi}^{\pi}\frac{1}{2}\cos((\mathrm{m}-\mathrm{n})\mathrm{x})\,\mathrm{dx},\tag{1.47}$$

$$= \frac{1}{2(m+n)}\int_{\pi(m+n)}^{-\pi(m+n)}\cos u\,\mathrm{du}+\frac{1}{2(\mathrm{m}-\mathrm{n})}\int_{\pi(\mathrm{m}-\mathrm{n})}^{-\pi(\mathrm{m}-\mathrm{n})}\cos\mathrm{v}\,\mathrm{dv},\tag{1.48}$$

$$= \frac{\sin((m+n)\pi)}{m+n}+\frac{\sin((m-n)\pi)}{m-n},\tag{1.49}$$

$$= 0.\tag{1.50}$$

Since $m, n \in \mathbb{N}_0 \Rightarrow m+n \equiv k_1$ and $m-n \equiv k_2$. This implies that $k_1, k_2 \in \mathbb{Z}^0$. Now, $\sin(k_1\pi) = \sin(k_2\pi) = 0$, which demonstrates the last line of the equality.
For the case $m = n$, the integral reduces to:

$$\int_{-\pi}^{\pi}\cos^2(nx)\,\mathrm{dx} = \int_{-\pi}^{\pi}\frac{1}{2}(\cos(2nx)+1)\,\mathrm{dx},\tag{1.51}$$

$$= \int_{-\pi}^{\pi}\frac{1}{2}\cos(2nx)\,\mathrm{dx}+\int_{-\pi}^{\pi}\frac{1}{2}\,\mathrm{dx} = \frac{\sin(2\mathrm{n}\pi)}{2\mathrm{n}}+\pi = \pi.\tag{1.52}$$

Since $n \in \mathbb{N}_0 \Rightarrow \sin(2n\pi) = 0$, which concludes the demonstration.